Real-Time Closed-Loop Control of Microstructure and Geometry in Laser Materials Processing

by

Mohammad Hossein Farshidianfar

A thesis
presented to the University of Waterloo
in fulfillment of the
thesis requirement for the degree of
Doctor of Philosophy
in
Mechanical Engineering

Waterloo, Ontario, Canada, 2017

Examining Committee Membership

The following served on the Examining Committee for this thesis. The decision of the Examining Committee is by majority vote.

External Examiner	NAME: Javad Mostaghimi
	Title: Professor, Mechanical and Industrial Engineering
Supervisor	NAME: Amir Khajepour
	Title: Professor, Mechanical Engineering
Supervisor	NAME: Adrian Gerlich
	Title: Associate Professor, Mechanical Engineering
Internal Member	NAME: Norman Zhou
	Title: Professor, Mechanical Engineering
Internal Member	NAME: Mihaela Vlasea
	Title: Assistant Professor, Mechanical Engineering
Internal-external Member	NAME: Hamid Tizhoosh
	Title: Professor, Systems Design Engineering

AUTHOR'S DECLARATION

I hereby declare that I am the sole author of this thesis. This is a true copy of the thesis, including any required final revisions, as accepted by my examiners.

I understand that my thesis may be made electronically available to the public.

      Mohammad Hossein Farshidianfar

Abstract

Laser Materials Processing (LMP) is currently one of the fastest growing technologies of the 21st century. Different categories of this technology such as Laser Additive Manufacturing (LAM) and Laser Heat Treatment (LHT) have now paved the way for more versatile methods of manufacturing that were not possible through conventional manufacturing methods. The localized laser heat source provides advantages such as minimal dilution, minimal distortion, small heat affected zones, and improved localized geometry and quality. However, these advantages come at a price, which is the number of inputs, outputs and process parameters involved that make the LMP a complex process for mainstream manufacturing. Current industrial LMP platforms require an extensive amount of manual tuning and process knowledge in order to achieve high quality production. Nonetheless, because of process sensitivity and lack of automation in LMP machines, the material and mechanical properties of LMP-manufactured products are highly inconsistent. Therefore, to take advantage of the technology's benefits and to establish LMP into the mainstream manufacturing technology, it is highly essential to develop a fully automated closed-loop LMP process that can intelligently control important output characteristics in real-time.

In this research, an automated real-time closed-loop process will be studied and developed to simultaneously control two of the most important LMP output properties: (1) microstructure and (2) geometry. A multi-objective thermal-geometry monitoring and control module is developed to enable closed-loop control of microstructure and geometry properties of the LMP process. Geometry features such as clad height of the LAM process are directly monitored through a CCD camera. Geometry control is achieved by direct control of absolute geometrical values in real-time. An infrared thermal image acquisition system is integrated with the CCD-based imaging system to monitor real-time thermal dynamics. Thermal dynamics of the process such as the cooling rate, melt pool temperature, and heating rate are recorded directly in real-time through a specific set of thermal image analyses algorithms. Microstructure control is defined as control of consistency and stability of a desired set of microstructures for specific materials correlated with a set of perceived thermal dynamics and thermal signatures offline. Therefore, by directly controlling the desired set of correlated thermal dynamics in real-time, a consistent controlled microstructure is guaranteed during the process. A complete closed-loop control process is developed by integrating the monitoring system, LMP system and a multi-input-multi-output controller system.

LHT and LAM experiments are conducted with thermal monitoring to understand and predict microstructue, hardness and geometry characteristics in real-time. Microstructure features such as martensitic formation and phase transformations are correlated with real-time thermal cooling/heating rates and melt pool temperatures to develop a microstructure prediction method. Important geometry properties such as hardened depth are also correlated with the thermal dynamics to identify a suitable feedback signal for closed-loop control of the depth, which cannot be monitored by a CCD camera. Thermal patterns are identified for online control of the hardness during single-track and multi-track LHT and LAM processes.

Furthermore, an accurate and computationally efficient thermal dynamics model is developed and validated for the LHT and LAM processes for real-time estimation of the thermal dynamics of the process with limited information of the thermal boundaries. The dynamic model is integrated into a state observer feedback control system to provide model-based closed-loop control of the thermal dynamics.

The intelligent closed-loop process is evaluated for different case studies of single-track and multi-track laser heat treatment and laser additive manufacturing. The real-time control of microstructure and hardness is achieved in the LHT process through a closed-loop control of the peak temperature. State observer feedback control of the peak temperature is also evaluated for the LHT process. Single-input-single-output control of the clad height and cooling rate are also incorporated for individual real-time control of the microstructure and geometry. Finally, an integrated microstructure and geometry control of the LAM process is constructed and tested for single-track and multi-track LAM depositions, to provide consistent material properties with controlled clad height.

As a result of the closed-loop multi-input-multi-output control, the consistency and quality of the LMP manufacturing processes have increased significantly. The controller is capable of eliminating the effect of process and environmental disturbances such as irregular workpiece geometries or undesired heat accumulations. As a result, the developed closed-loop system significantly reduces the extensive amount of time and effort required for manual tuning of LMP setups, and automatically adjusts the process inputs to achieve the desired material and geometry properties. In addition, it also provides an essential tool for obtaining in-process knowledge of the LMP manufacturing process.

Acknowledgements

First and foremost, I would like to thank God for giving me this fascinating opportunity to live and experience life alongside so many great people that have helped, supported and inspired me throughout this work.

I would like to express my sincere gratitude and appreciation to Prof. Amir Khajepour whose insightful thinking and fearless approach towards problem solving has been the building blocks of this research, and will always be my greatest takings from this work. A special thanks to Prof. Adrian Gerlich whose support and genuine concern has helped shape and complete the current research.

I would also like to express my deepest gratitude and love to my family and specially my parents Anooshiravan and Maryam, who have taught me how to learn from others and live a happy life.

Last but not least, this work would not have been possible without the never-ending love, passionate care and enduring patience of my loving wife, Faegheh, to whom this work is dedicated to.

Dedication

To Faegheh, whose love and support made this work possible

and our little Behesht, who is the hope in our life.

Table of Contents

List of Figures

List of Tables

Nomenclature

G_T	Melt pool temperature gradient
R_{growth}	Solidification growth rate
d	Secondary dendritic arm spacing
I_i	Intensity of the thermal pixel
P_p	Instantaneous peak temperature pixel in thermal pixel array
P_{f_i}	Fixed spatial point pixel in thermal pixel array
q	Volumetric heat distribution of a moving heat source
T	Temperature
k	Thermal conductivity
α	Thermal diffusivity
ρ	Material density
c_p	Material specific heat
v	CNC machine travelling speed
$\Delta\xi$	Distance between two temperature nodal points
Fo	Fourier number
P_{max}	Laser power
r_B	Laser beam radius
A_{abs}	Laser absorption coefficient
$\tilde{q}$	Laser heat distribution spatial coefficient
$OP(\bar{T}, \bar{P}, \bar{v})$	Nonlinear operating point
k_{eq}	Equivalent thermal conductivity coefficient
T_{bias}	Temperature bias constant
J	Optimal control performance index
H	Hamiltonian

Chapter 1

Introduction

1.1 Motivation

Owing to the discovery of the first laser in 1960 by Ted Maiman [1] at the Hughes Research Laboratories, optical energy has now become one of the most applied energy sources in manufacturing and materials processing technology. The term "laser" is an abbreviation for "Light Amplification by Stimulated Emission of Radiation". The ability to emit light coherently, allows a laser to produce high power beams, which can be focused on a fine spot. Therefore, the energy source which was once dubbed "a solution looking for a problem" [2], is now being widely used in various forms of industrial applications. The more conventional methods of manufacturing such as welding, cutting, forming, surface treatment and rapid manufacturing are now giving way to more efficient and versatile laser technology counterparts such as laser welding, laser cutting, laser forming, laser surface treatment and laser rapid manufacturing. This broad area of laser applications in manufacturing is now being called Laser Materials Processing (LMP). LMP offers several advantages in terms of process optimization and quality of the final product over its' traditional manufacturing counterparts. The high energy density of the laser heat source provides minimal dilution and distortion, smaller heat affected zone, and better surface quality or geometry control. Due to the high cooling rates, fine-grained microstructures are produced during solidification in the LMP process.

Although, LMP is capable of processing a broad range of metals, alloys, ceramics and MMCs, the mechanical properties (geometry, strength, hardness, residual stress) and microstructure characteristics (morphology, grain size, phase precipitation, etc.) of the depositions are difficult to be tailored to a specific application. Process disturbances may even cause variations in the clad properties between reproduced processing cycles performed using the same operating conditions. This poor reproducibility arises from the high sensitivity of LMP processes to small changes in the operating parameters and process disturbances. The process involves complex non-equilibrium physical and chemical metallurgical process, which exhibits multiple modes of heat and mass transfer such as Marangoni flow, buoyancy, convection, and in some instances, chemical reactions. The majority of the current literature

has focused on understanding of the relationships between a material's final microstructure and physical characteristics and conditions of solidification. Reports reveal that the complex metallurgical phenomena during LMP processes are strongly material and process dependent, and are governed by process parameters (e.g. laser power, laser type, traveling speed, spot size, scan line spacing and powder characteristics).

The next big step for the LMP technology is to become fully automated in the sense that all desired material and geometry properties of an LMP product are locally tailored to the needs. There are specific applications with materials ranging from metals, alloys and metal matrix composites (MMCs) that have to meet specific mechanical and metallurgical demands for the aerospace, automotive, rapid tooling, and biomedical industrial sectors. Finding an optimal set of experimental parameters and using them in an open-loop laser cladding process may not result in a good quality clad due to random or periodic disturbances in the system. Therefore, development of an intelligent closed-loop control system with monitoring capability is essential for overcoming the aspects of disturbances in the process.

Control of material properties, which is by far the broadest area of interest in the LMP industry; is only limited to open-loop offline correlations. For sensitive processes like LMP, which are continuously disturbed by process and environmental variables, each specific material operated at a specific configuration requires a separate set of off-line analysis. Furthermore, offline analysis of the microstructure evolution does not guarantee consistent desired properties, due to the presence of real time process disturbances. On the other hand, there have been initial steps taken towards closed-loop control of geometry properties in LMP processes such the clad height in Laser Additive Manufacturing (LAM) and depth of penetration in Laser Heat Treatment (LHT). Nonetheless, for different LMP processes to be established in the mainstream manufacturing, there is the need of automation in terms of microstructure and geometry variations. With the presence of a fully automated LMP process, the technology will gain huge advantages over more conventional manufacturing techniques in a broad area of applications.

The goal of this research is to establish the foundation of an integrated real-time microstructure and geometry control for two of the most important LMP processes: (1) Laser Additive Manufacturing (LAM), and (2) Laser Heat Treatment (LHT). Steps are taken towards understanding the microstructure evolutions in real-time based on online measurements of the thermal dynamics in order to develop an intelligent expert system for a fully automated LAM and LMP process.

1.2 Laser Additive Manufacturing (LAM) Process

Laser Additive Manufacturing (LAM) is a collection of laser technology, computer-aided design and manufacturing (CAD/CAM), actuators, sensors and control, and powder metallurgy that creates parts in a layer-wise fashion. In this process, a stream of metallic powder is fed on to a substrate, a high power laser beam melts the injected powder particles and parts of the substrate. As the laser heats up the substrate, the molten metal is attached to the moving substrate to produce a deposited layer as shown in Figure 1-1. By producing clads beside and on top of each other, a functional component is made in a layer-by-layer fashion. The technology is currently being used in manufacturing and repair, cladding, design of novel alloys or functionally graded materials (FGM), and metallic rapid prototyping.

LAM has specific features, which makes it unique compared to other deposition methods [3], [4] such as reduced dilution, high heating/cooling rates ($10^3 - 10^8\ Ks^{-1}$), improved wear resistance and hardness, reduced thermal distortion, and reduced porosity (particularly in LAM by powder injection). Many research groups around the globe have conducted research on the topic that has led to the development of different forms of machinery setups.
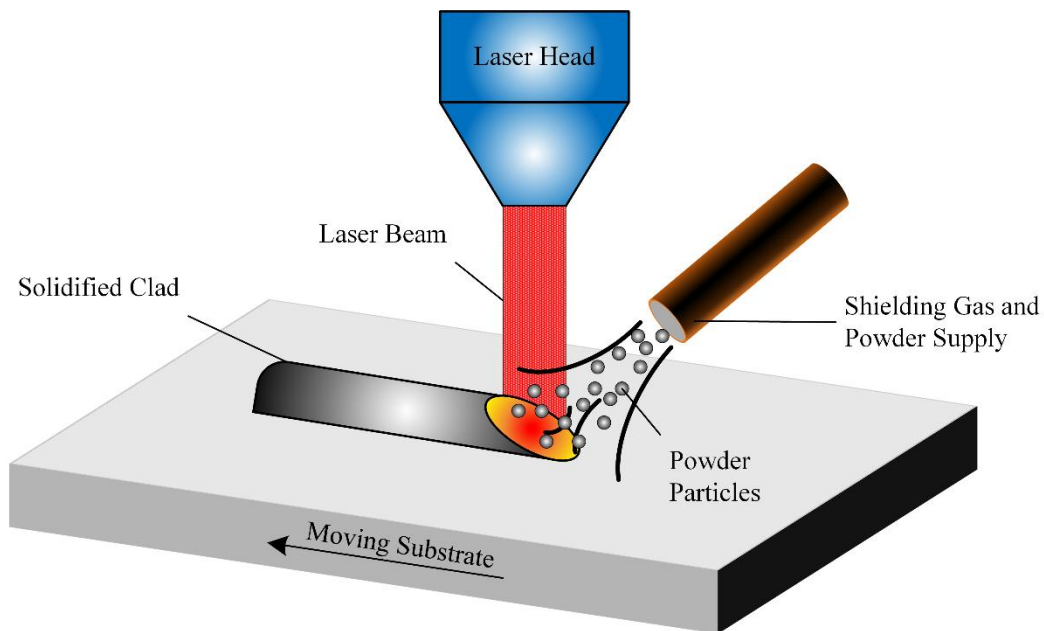
Figure 1-1 Schematic of the Laser Additive Manufacturing (LAM) process.

1.3 Laser Heat Treatment (LHT) Process

Laser Heat Treatment (LHT) or sometimes referred to as laser hardening involves applying the laser as a heat source to improve surface qualities of a component such as the hardness, strength, lubrication wear, and fatigue. LHT produces thin layers on the surface that are heated and cooled rapidly, resulting in very fine microstructures, even in steels with very low hardenability. A schematic of the LHT process is shown in Figure 1-2. Interaction times involved in LHT are an order of magnitude shorter compared to conventional hardening techniques. The surface is heated rapidly to temperatures between the critical solid state transformation and the liquidus temperature, with the adjacent material acting as a heat sink to rapidly cool down the process. As a result of phase transformations such as formation of martensite in ferrous alloys, surface modification such as hardening can be achieved. Although, surface properties are altered in LHT, bulk properties, such as toughness and ductility remain unchanged.
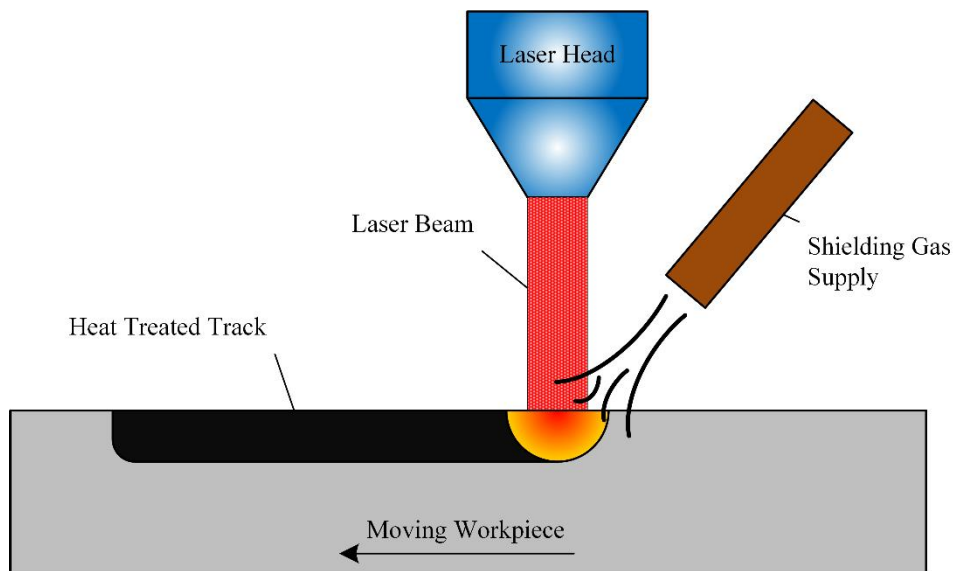
Figure 1-2 Schematic of the Laser Heat Treatment (LHT) process.

1.4 Statement of Objective and Scope

The main objective of this research is to:

"Develop a methodology for integrated real-time microstructure consistency and geometry monitoring and control of the LAM and LHT processes using real-time monitoring of thermal dynamics and process geometry."

To achieve this goal, it is necessary to understand solidification during the LMP processes and how it is affected by thermal dynamics features such as cooling rate, melt pool temperature, and heating rate. An infrared-based thermo-imaging technique is developed to monitor the real-time thermal dynamics of the process i.e. cooling rate, melt pool temperature and the heating rate. A correlation between the thermal dynamics features and processed material properties is obtained and validated through experiments to monitor the microstructure in real-time. Additionally, vision-based monitoring techniques are used to monitor the clad height. These parameters are used in a multi-input-multi-output closed-loop control system to provide a fully automated LMP process. The monitoring and control hardware and software are integrated into a single package in the form of a real-time thermal and geometry monitoring and control module.

This module will enable a fully automated LMP process to significantly increase the consistency and quality of the final product; hence, minimizing the time and cost of post process machining and post manufacturing inspections. In addition, the closed-loop monitoring and control module of the LMP process, will be an effective manufacturing tool for achieving complex desired material and geometry properties with less excessive trial and error experimentation.

1.5 Thesis Overview

The research is divided into seven chapters. **Chapter 2** provides a review of the literature related to the topic of microstructure and geometry control in LMP, to clarify the contribution and novelty of this work. The background of microstructure analysis, continuous cooling and heating transformations (CCT and CHT), phase diagrams and thermal control are also discussed in this chapter.

The experimental setup and development of the multi-objective thermal-geometry monitoring and control module are described in **Chapter 3**. The image and thermal image processing algorithms integrated into the module are explained, including the system architecture of the final closed-loop system.

In **Chapter 4**, a dynamic adaptive thermal model is developed using a finite difference approach. Heat transfer formulations and the dynamic modeling are thoroughly described. Moreover, a model-based optimal linear quadratic tracking controller is designed based on the developed model, to provide closed-loop thermal dynamics.

The design of experiments and predefined laser processing conditions of the samples presented in this research are laid out in **Chapter 5**. The employed materials and material characterization procedures used for post-manufacturing analyses are also described in this chapter.

Chapter 6 presents the results and performance of the current thermal-geometry monitoring and control module. The results are categorized into three groups according to the applications of each section. Initially, results are presented for indirect online microstructure prediction through real-time thermal dynamics monitoring of the LHT and LAM processes. Next, the dynamic thermal model is evaluated and verified experimentally based on real-time thermal dynamics measurements. Finally, the results of closed-loop thermal dynamics and geometry control are discussed for the LHT and LAM procedures. Single-input-single-output control structures are evaluated for controlling the peak temperature during LHT, and the clad height and cooling rate during the LAM process. Offline micrography and hardness measurements are also provided for each sample to analyze the consistency and control of material properties during open-loop and closed-loop conditions. Lastly, a multi-input-multi-output closed-loop control system is investigated for integrated real-time control of the clad height and cooling rate during the LAM process.

The results and the contributions of this research are concluded in **Chapter 7**. Possible future work and enhancements are also proposed to portray the future development of the multi-objective monitoring and control module for the LMP process.

Chapter 2

Literature Review and Background

In this chapter, the existing literature and background on Laser Materials Processing (LMP) technology and the developments on its automation are reviewed. Since LMP is a solidification process, the principles of solidification are described in detail. The chapter focuses on modeling and control of two main LMP processes: (1) Laser Additive Manufacturing (LAM), and (2) Laser Heat Treatment (LHT). It continues with a description on the current microstructure and geometry control schemes during the LAM and LHT processes. Finally, current shortcomings of the automation scheme and its possible solutions are described.

2.1 Principles of Solidification in LMP

Every part produced or processed by any of the LMP procedures has two main properties that are required to be tailored to desired values: (1) geometry, and (2) material properties. The goal is to produce a part with desired geometry and material properties such as specific height and microstructure. In fact, geometry and microstructure are the two most important output criterion for an LMP-manufactured product. Geometry by itself is a defining design criterion, whereas, microstructure is an output metallurgical parameter that defines important mechanical properties such as hardness and wear. Since LMP is a solidification process, to explain the melt pool microstructure and geometry, some basic solidification concepts are required to be understood. These concepts include solute redistribution, solidification mode and size, microstructure growth and nucleation.

2.1.1 Solid Redistribution during Solidification

When a liquid of uniform composition solidifies, the resultant solid is seldom uniform in composition [5]. The redistribution of the solute in the liquid depends on both thermodynamics, that is, the phase diagram, and kinetics, that is, diffusion, undercooling, fluid flow, and so on [5].

As the liquid solidifies at the liquidus temperature T_L, solid phases start to form. In the case of complete diffusion in both the solid and the liquid, both phases are uniform in composition without any segregation. This case is also called "equilibrium solidification" because equilibrium exists in the entire

solid and liquid phase and not just their interface [5]. However, equilibrium solidification is very rare specifically because solid diffusion is limited. Complete diffusion in the liquid requires $D_L t \gg l^2$, where l is the initial length of the liquid, D_L is the diffusion coefficient in the liquid, and t is the time available for diffusion [5]. Similarly, complete diffusion in the solid also requires $D_S t \gg l^2$, where D_S is the diffusion coefficient in the solid [5].

Due to limited diffusion (particularly in the solid), equilibrium solidification rarely occurs during LMP processes. Since LMP has a very short solidification time (t is very small), $D_L t \gg l^2$ and $D_S t \gg l^2$ are hardly achieved during the process. D_S is usually much smaller than D_L, on the other hand, solute redistribution in the liquid is complete only if strong convection is present. Therefore, solid diffusion is negligible and limited liquid diffusion only occurs during LMP. The solute cannot back diffuse into the solid and all the extra solute atoms are rejected to the liquid, creating a transition zone of solute-rich boundary layer. As a result, LMP is a nonequilibrium solidification process that typically leads to segregation of elements in the final microstructure and can produce nonequilibrium phases during solidification. However, these nonequilibrium phases remain in the solid after solidification.

2.1.2 Solidification Mode and Structure Size

Microstructure formation in LMP depends on the solidification process. Hence, to understand and control the microstructure, it is important to analyze the solidification phenomena, its characteristics and the effective physical parameters associated with it.

Prior to discussing the characteristics of a solidification structure, let us first define the two key physical parameters influencing the solidification phenomena: (1) temperature gradient, and (2) growth rate. These two parameters can be described by considering a directional equilibrium solidification inside a metallic rod, with the metal solidifying upwards with a planar S/L interface. The travel speed of the S/L interface is called the growth rate, R_{growth}. The temperature gradient, G_T, in the liquid metal is defined as the tangent of the temperature profile with respect to distance at the S/L interface. The temperature gradient in the LMP case will be defined as the difference between the isotherms inside the melt pool divided by their spatial difference.

As stated earlier, microstructure properties are defined by solidification characteristics. In general, each solidification structure has two main characteristics that define its properties: (1) mode of solidification, and (2) size of solidification structure or so-called morphology. Along with the

composition (and stable solid phases), these two characteristics distinguish solidification microstructures from one another.

2.1.2.1 Solidification Mode (Morphology)

During the solidification of a pure metal, the S/L interface is usually planar, unless severe thermal undercooling is imposed [5]. During the solidification of an alloy, however, the planar S/L interface can break down into cellular or dendritic structures, depending on the solidification condition and the material involved. According to the theory of constitutional super cooling, due to the existence of a non-uniform solute redistribution at the solute-rich boundary layer in alloys, the actual temperature of the transient region in the liquid can fall below the liquidus temperature. Therefore, solid and liquid coexist in this region, resulting in cellular and dendritic growth. The region where dendrites (cellular and dendritic) and the liquid phase coexist is called the mushy zone. Solidification modes are categorized into four groups: (1) planar, (2) cellular, (3) columnar dendritic, and (4) equiaxed dendritic.

According to Kou [5], for a planar S/L interface to be stable at the steady state, the following criterion must be met:

$$\frac{G_T}{R_{growth}} \geq \frac{\Delta T}{D_L} \tag{2.1}$$

in which, ΔT is the temperature difference across the boundary layer, which is the equilibrium freezing range $\Delta T = T_L - T_S$, and D_L is the liquid diffusivity. The travel speed of the S/L interface is called the growth rate, R_{growth}. The temperature gradient, G_T, in the liquid metal is defined as the tangent of the temperature profile with respect to distance at the S/L interface. With an increasing degree of constitutional super cooling, the solidification mode transforms from planar to cellular, from cellular to columnar, and finally from columnar to equiaxed dendritic modes.

It is noteworthy to point out that since LMP has very high cooling rate values, the growth rate R_{growth} is a very large number. On the other hand, since laser is a concentrated heat source, the temperature gradient G_T is very small. Therefore, the ratio G_T/R_{growth} is very small for the LMP process, indicating a non-planar structure, typically leading to formation of either dendritic or equiaxed grains during the LMP process.

2.1.2.2 Size of Solidification Structure

The size of the solidification morphology is another important characteristic of the solidification structure. An initial report by Plaskett et al. [6] and further analysis by Flemings [7] revealed that the cell spacing of the Sn-Pb alloys depends on the product $G_T R_{growth}$. They observed that the size of the cells decreased with increasing $G_T R_{growth}$. Judging from its units, the product $G_T R_{growth}$ (°C/mm × mm/s) is in fact the cooling rate, which is the reduction of solidification temperature over a certain period of time. It has been observed that the higher the cooling rate, that is, the shorter the solidification time, the finer the cellular or dendritic structure becomes [7].

According to a fundamental expression reported by Flemings, the secondary dendrite arm spacing is expressed as follows [7]:

$$d = a t_f^n = b(\varepsilon)^{-n} \tag{2.2}$$

in which d is the secondary dendrite arm spacing, t_f is the local solidification time, ε is the cooling rate, and a and b are proportional constants. Several research groups [8]–[10] have utilized the above equation to estimate cooling rate values based on dendritic arm spacing calculations.

Solidification mode and size are both defined by the temperature gradient G_T and the growth rate R_{growth}. Therefore, G_T and R_{growth} dominate the solidification microstructure. The ratio G_T/R_{growth} determines the mode of solidification (morphology) while the product $G_T R_{growth}$ governs the size of the solidification structure. The LMP microstructure formation is summarized in Figure 2-1. The LMP microstructure is determined by solidification, which has two main characteristics: (1) mode of solidification, and (2) size of solidification structure. These two characteristics are primarily governed by three main physical parameters: (1) temperature gradient, (2) growth rate, and (3) cooling rate. Thus, to control all microstructure properties during the LAM process, online knowledge of these parameters is required. In other words, it is these three parameters that govern the solidified microstructure of an alloy.
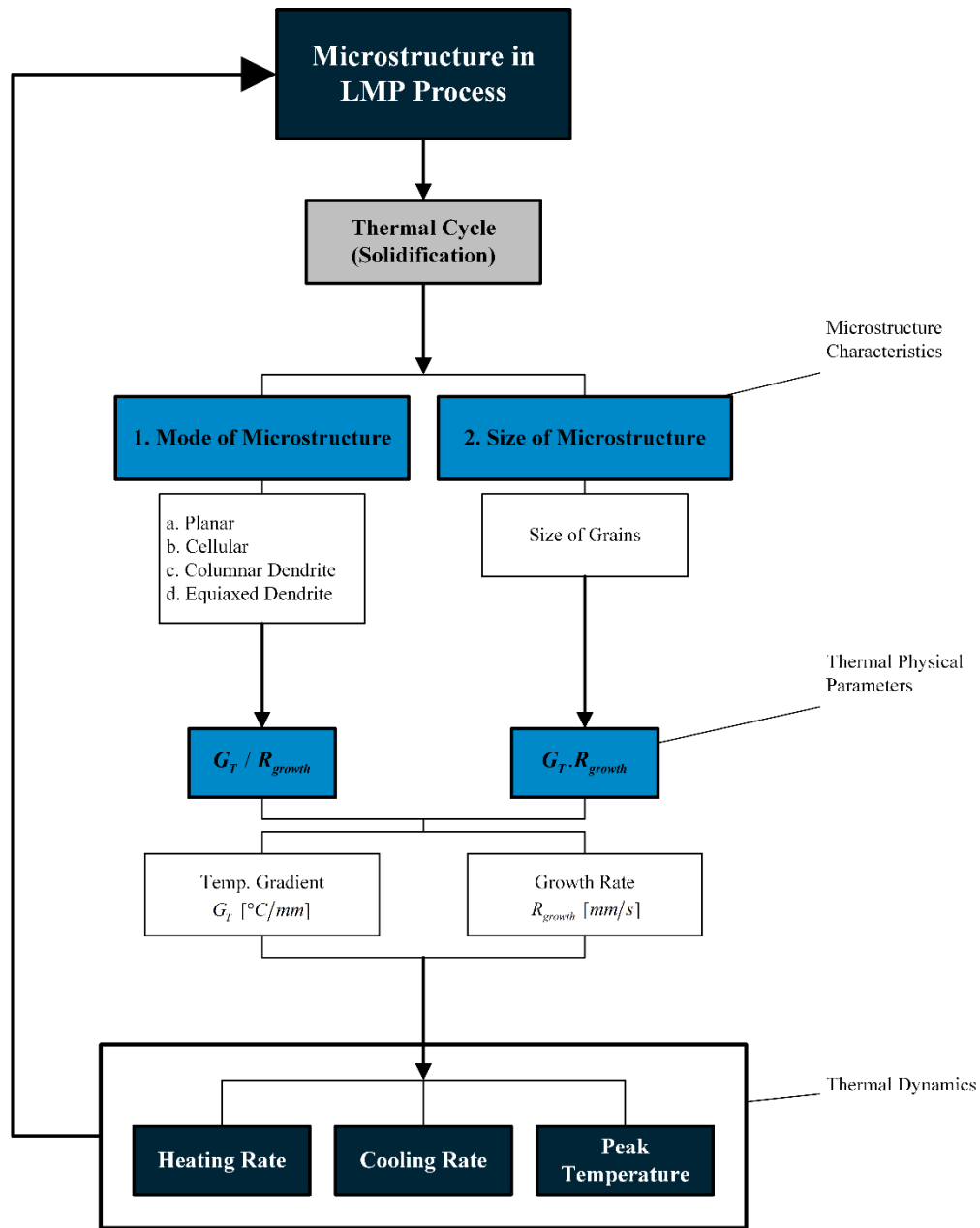
Figure 2-1 Formation of LMP microstructure and its relation with thermal dynamics.

2.2 Material and Thermal dynamics Diagrams

2.2.1 Phase Diagram

In the case of steels, the solidified microstructures are subsequently modified on cooling to room temperature by solid-state phase transformations. Three types of hypoeutectoid steel compositions are

11

used in the later experimentation sections: (1) AISI 1020 low carbon steel, (2) AISI 1018 low carbon steel, and (2) AISI 4340 low alloy steel, which are shown on the iron-carbon equilibrium phase diagram in Figure 2-2. Cooling of an alloy of this composition is represented by moving down the vertical line in Figure 2-2. At about 875 ℃, the microstructure of AISI 1020 and 1018 will consist entirely of grains of austenite. During equilibrium heat treatment from point *c* to *f*, the AISI 1020 material undergoes the following transformations: γ (Austenite) $\rightarrow \gamma + \alpha$ (Austenite + Ferrite) $\rightarrow \alpha + Fe3C$ (Ferrite + Cementite). The equilibrium phase transformations during LAM solidification of AISI 4340 is shown in Figure 2-3, which include: (Liquid) $\rightarrow \gamma$ (Austenite) + (Liquid) $\rightarrow \gamma$ (Austenite) $\rightarrow \gamma + \alpha$ (Austenite + Ferrite) $\rightarrow \alpha + Fe3C$ (Ferrite + Cementite). However, since the LMP process yields rapid cooling conditions with nonequilibrium solidification, some of the resultant nonequilibrium phases produced cannot be predicted by the equilibrium phase diagram.
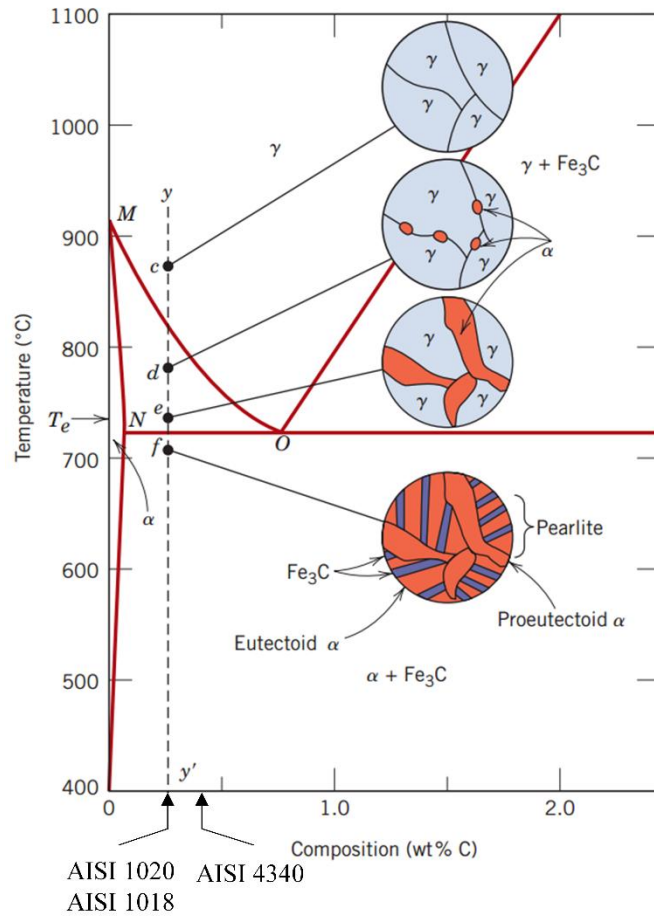
Figure 2-2 Phase diagram of hypoeutectoid iron-carbon alloy with schematic representations of the microstructures as it is cooled from within the austenite phase region to below the eutectoid temperature [11].

AISI 4340
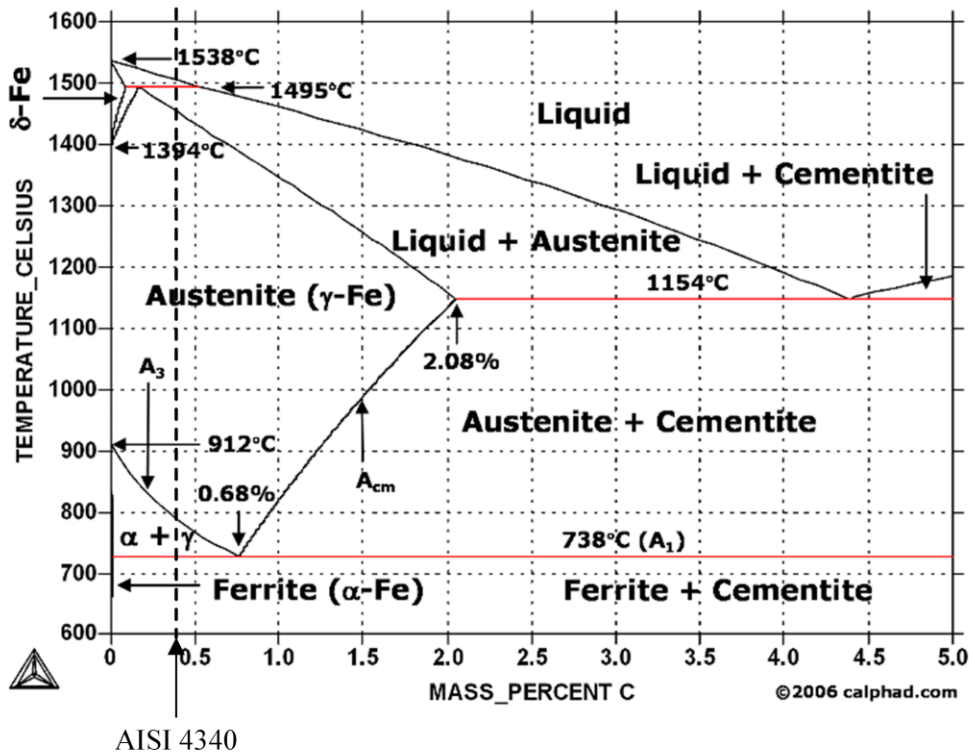
Figure 2-3 Solidification phase transformation diagram of iron and carbon.

2.2.2 Continuous Heating Transformation Diagram

Any heat treatment process consists of three consecutive stages; the heating process, a holding time, and the cooling process. In steels, the heating process is associated with austenitization. The two most important thermal dynamics features affecting the austenization process during heating are the peak temperature and the heating rate. These two features govern the kinetics of austenization and the amount of austenite formation. The Continuous Heating Transformation (CHT) diagram shown in Figure 2-4a describes the austenization process as a function of the heating time and peak temperature. It can be noted that at extremely low heating rates (e.g. $0.22\,℃/s$) to about $775\,℃$, after exceeding the Ac3 temperature after about $1\,h$ all pearlite and ferrite would have been transformed to inhomogeneous austenite [12]. At higher heating rates (e.g. $10\,℃/s$), the inhomogeneous austenization period is reduced to only about $80\,s$. According to such diagrams, the austenization transformation temperatures (A_{c1} and A_{c3}) increase with the heating rate. In fact, for extremely high heating rates of about $1000\,℃/s$, which occur in the LHT process, the range of peak temperature required is between $950-1000\,℃$. Therefore, although rapid heating reduces the austenization time, it makes it more difficult

14

for the austenization to take place because of a higher hardening temperature. According to Figure 2-4b, the heating rate and peak temperature also affect the final hardness in an LHT process. It has been shown, for example, that the maximum hardness would be achieved upon austenizing the steel at 850 °C for about 900 s (or heating at a heating rate of 1 °C/s), which is achieved by forming homogeneous austenite before cooling [12] (see Figure 2-4a).

a)

b)
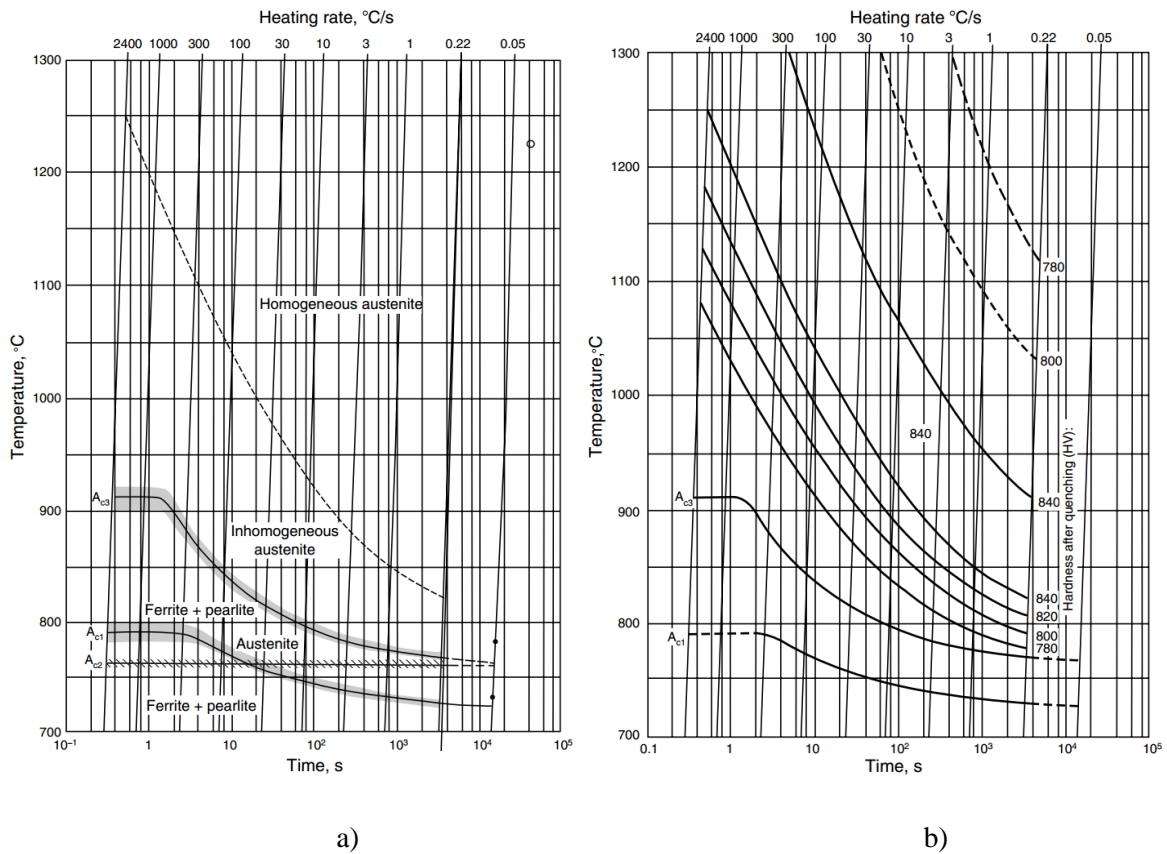
Figure 2-4 (a) Continuous heating transformation diagram, and (b) the achievable hardness in the CHT diagram after heating of the steel grade DIN Ck45 [13].

2.2.3 Continuous Cooling Transformation Diagram

After the heating has taken place during LMP, the holding time is negligibly short, and the cooling process immediately begins. Most heat treatment of steels are conducted under continuous cooling conditions, which is similar to the solidification of the LMP process. Similar to the heating section, there are Continuous Cooling Transformation (CCT) diagrams for various steel alloys that describe the phase formations as a function of the cooling time and cooling temperature. These depend on the alloy

15

chemistry and capture the role of cooling rate on both the diffusion controlled and a thermal (martensitic) transformations that occur in the steel, and allow one to schematically represent the final microstructure and hardness in a simple graphical format. The CCT diagram for AISI 4340 steel is shown in Figure 2-5b. It can be seen that the resultant phases and final microstructure are dependent on the cooling rate. It is observed that under nonequilibrium conditions, the formation of nonequilibrium phases such as martensite and bainite is possible specifically at high cooling rates. For the continuous cooling of a steel alloy, a critical cooling rate is required which represents the minimum rate that will produce a totally martensitic structure [11]. This critical cooling rate, when included in the continuous transformation diagram, will just avoid the start of the bainite transformation. As seen in Figure 2-5, the minimum temperature to avoid pearlite formation for AISI 1045 and 4340 is 10 $℃/s$ and 0.02 $℃/s$, respectively. Moreover, the maximum rate to avoid martensitic microstructure for AISI 1045 and 4340 is 60 $℃/s$ and 8.3 $℃/s$, respectively. Therefore, it is clear that AISI 4340 steel has a high hardenability value compared to 1020 or 1045 low carbon steels, since they require much higher cooling rates to produce a martensitic microstructure. With less carbon or addition of other alloying elements, the start temperature, or transformation 'nose' shifts further towards shorter times on the left of the diagram, requiring higher cooling for formation of a fully martensitic microstructure. Figure 2-5c illustrates the resulted hardness values after the cooling process. The maximum hardness is achieved at the highest cooling rate, where a complete martensitic microstructure is present. Thus, if the three thermal dynamics cooling rate, peak temperature, and heating rate are monitored and controlled in real-time, the hardness and hardened depth of an LHT process can be controlled.
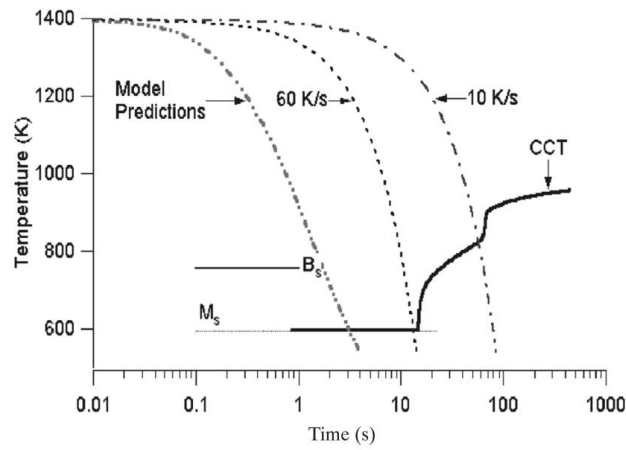
a)
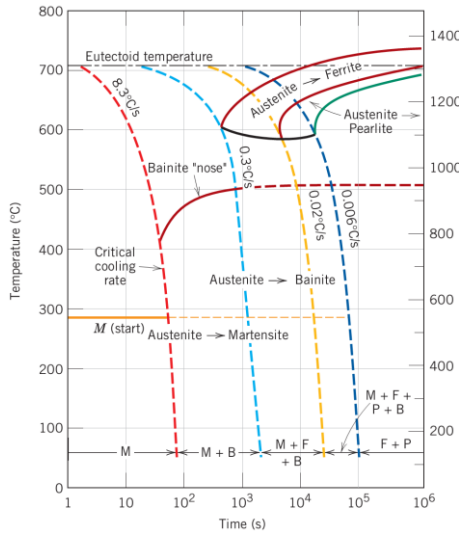
b)
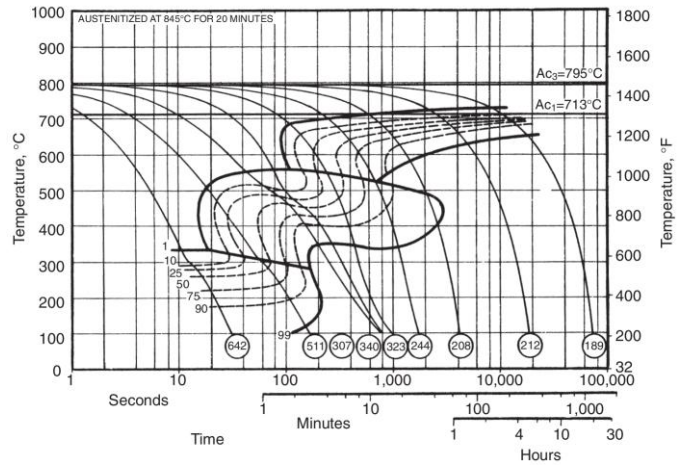
c)

Figure 2-5 (a) Continuous cooling transformation diagram of AISI 1045 [14] (B_s and M_s indicate starting time of bainite and martensite formation), and (b) continuous cooling transformation diagram for 4340 alloy steel [11], and (c) the achievable hardness in the CCT diagram after cooling of 4140 steel [15].

2.3 Thermal Modeling in LMP

As discussed above, basically the thermal dynamics of the LMP process govern its microstructure. In order to control and analyze the microstructure in LMP processes, an in-depth understanding of these thermal dynamics is required. High temperature gradients must be recorded in very short time intervals in order to measure the cooling rate during rapid solidification of the molten pool. According to Figure 2-1, cooling rate and temperature gradient values will define the morphology and size of a microstructure. However, there are limited instrumental facilities available to perform these measurements during the process. On the other hand, development of a fully automated turn-key LMP process generalized for all materials and processes is not achievable only through expensive time consuming experimental observations. A comprehensive thermal model relives the requirement of taking expensive and difficult steps to integrate the LMP process with high-tech instruments for controlling microstructure properties. There are extensive numerical models available in literature, which describe the LAM and LHT thermal processes in detail, however, numerical models are much more time consuming and complex to be used for real-time control purposes. Therefore, analytical models are the best option for understanding the fundamentals of thermal history and microstructure evolutions, and at the same time a good basis for development of comprehensive real-time controllers.

Rosenthal [16] published one of the earliest analytic solutions for temperature distributions applicable to welding, in which a point source moved relative to an infinite material. A one-dimensional (1-D) transient model for predicting the temperature distribution in the vicinity of a moving laser spot was developed by Gregson [17] using Carslaw and Jaeger's [18] semi-infinite analytical plate solution for a uniform heat source. One-dimension heat models are only suitable for simple cases, whereas, two- or three-dimension heat equations are required for more accurate solutions. Cline and Anthony [19] analyzed a 3-D thermal distribution from a moving Gaussian source over a large range of conditions from simple heat treating to deep-penetration (melting) welding. Relationship between cooling rate, temperature, power, melt depth, and laser spot size were compared with experiments. 2-D heat flow models with the temperature dependence of surface absorptivity and the thermal dynamics of the material were presented for cylindrical bodies [5] and for a uniform strip heat source moving along the semi-infinite body for laser hardening of steels [14-15].

The simplified 3-D conduction model provided by Ashby and Easterling [22] served as a basis for many researchers [17-18] to develop more accurate thermal models integrated with microstructure kinetics equations. They developed a combined approximate solution for the temperature held with

18

equations describing the kinetics of structural changes in steel. They predict the structure and hardness of the transformed surface as a function of depth below the treated surface. Their results were assembled into diagrams which show the structure and hardness of as a function of the energy density and interaction time. More recently, Dehoff et al. [25] used the Ashby equations to analyze and control crystallographic grain orientation through electron beam additive manufacturing.

Since thermal properties of carbon steels are closely related to temperature, choosing the correct value for these properties has always been a big issue in analytical models, where only one value can be used. Isenberg and Malkin [26], along with and Kou et al. [27] studied the effect of changing thermal conductivity with temperature. They realized the errors will be minimal as long as the thermal conductivity value is taken close to the transformation hardening temperature (or melt pool temperature) and not room temperature. Komanduri and Hou [28] developed general equations in both transient and quasi steady-state forms considering boundary condition effects. They plotted the variation of temperature from transient to steady-state condition and calculated the time required to reach such a state. An innovative method for estimation of cooling rate in a welded section was presented by Poorheydari et al. [29]. The method was based on applying a weighting factor to the Rosenthal analytical solutions for thick and thin plates to yield specific numbers very close to those obtained experimentally

Although, all the above attempts to obtain analytical models have been validated experimentally, there are major shortcomings in terms of reliability and adaptability when applied to real-time monitoring and control. First, validation of analytical models has been mainly carried out by comparing only melt pool temperature values or temperature values of points below the melt pool. None of the models available in literature have been validated based on real-time temperature gradient and cooling rate measurements. Cooling rate values were only validated indirectly through first and secondary dendritic arm spacing measurements as formulated in Eq. (2.2). Therefore, temperature gradient and cooling rate values provided by the current analytical models are not realistic or reliable. Moreover, due to the simple nature of these models, they are only limited to specific materials or process conditions. As a result, the current analytical models lack in terms of adaptability and robustness to be applied for real-time control purposes.

19

2.4 Current Microstructure Control Schemes in LMP

Material properties are the most important output parameters of the LMP process. Mechanical and material characteristics such as yield strength [30], elongation [31] and tribology [32], are significantly defined by microstructure properties. Li et al. [33] observed exceptionally low Coefficient of Thermal Expansion (CTE), reasonable ductility, high hardness, and significantly improved yield strength in laser fabrication of Invar and TiC metal matrix composites. Griffith et al. [34] reported 1-10 micron grain sizes for LAM-processed Stainless Steel (SS) 316 against the 40 micron of the wrought SS 316. They obtained a yield strength double that of the wrought alloy, while retaining a ductility of nearly 50% [34]. Apart from microstructure analysis based on thermal modeling there has been extensive research on experimental microstructure control to achieve desired properties.

In general, a fine equiaxed morphology is preferred in the fusion zone since it has two main advantages. First, the fine grains help reduce susceptibility to cracking during deposition [5], as shown by Mitzner et al. [35] in LAM. Second, fine grains can improve mechanical properties of the deposition, such as the ductility and fracture toughness in the case of steels and stainless steels [5]. While a broad list of material properties are required to be controlled and tailored to specific engineering specifications, because of the nonequilibrium and sensitive conditions of the LMP process, a great amount of inconsistency is observed in standard LMP procedures. As a result, a broad range of post materials processing techniques are used to modify material characteristics to desired engineering values. In addition, much effort has been made to passively control the microstructure morphology and grain size of the LMP process directly. There are currently a couple of principle microstructure control techniques available in solidification processes that have been applicable to LMP processes with some restrictions, which are mentioned below.

2.4.1 Grain Refinement

These techniques were originally developed for casting to reduce grain size and enhance mechanical properties such as yield strength and elongation. One of the most well-known grain refinement techniques that have been used to control the melt pool grain structure is inoculation. Inoculation involves the addition of nucleating agents or inoculants to the liquid metal to be solidified [5]. As a result of inoculation, heterogeneous nucleation is promoted and the liquid metal solidifies with very fine equiaxed grains [36], [37], [38]. Although, inoculation is a well-known process in casting and welding, it is not widely used in LMP. However, the fiber contents in metal matrix composites produced by LAM have a similar effect of inoculating agents. During the production of Fe-TiC composites,

20

Emamian et al. [39] realized that by changing the volume percentage of the TiC content, the grain size changed drastically. Dynamic stimulation is another method of grain refinement, in which heterogeneous nucleation is promoted. Grabas [40] used vibration-assisted laser surface texturing of AISI 304 to increase surface hardness and enhance critical heat flux.

These methods are widely used in the welding and casting industries, whereas, they are only ideal for bulk material of low dimensional tolerances, and not suitable for local microstructure control. Furthermore, all grain structure control techniques are open-loop, meaning that they cannot be monitored online and adapted accordingly. Yet again, the need for a generalized microstructure control method that can locally control the grain size is required in LMP.

2.4.2 Offline Correlation of Process Parameters

This technique is by far the most widely used technique for microstructure analysis and control in LMP. Since online monitoring of the cooling rate, temperature gradient and the growth rate are difficult, researchers tend to use offline correlation techniques to directly match process parameters with offline observation of microstructure evolutions. Bhattacharya et al. [41] laser deposited an 8-layer thin wall of AISI 4340 on mild steel using the LAM technology. It was observed that the clad micro- hardness decreased from the top (7th layer) to the bottom (alloy) layer corresponding to the degree of tempering of the martensite phase, which increased from top to the bottom layers. The lattice parameters of the phases identified using LAM were shorter as compared to the lattice parameters for the same phases reported in literature due to the rapid cooling rate [41], similar to what Putatunda [42] observed by comparing laser hardening of 300M steel with induction hardening. Qiu et al. [43] compared the microhardness and microstructure of laser hardened rolled steel, quenched and tempered steel, annealed alloyed steel and conventionally through hardened steel. The grain size of rolled ferritic–pearlitic steels had distinct effect on microhardness [43]. Lee and Su [44] investigated the mechanical properties and microstructures of AISI 4340 laser hardened alloy steel under different tempering conditions. The results indicated that strength and hardness of tempered martensite dropped as the tempering temperature and holding time were increased whereas the ductility increased. Fastow et al. [45] reported the presence of traces of retained austenite phase along with martensite phase in the microstructure of laser surface alloyed AISI 4340 steel. An increase in the scanning speed and a decrease in laser power resulted in a finer microstructure and higher microhardness, and a reduction in the amount of overlap improved the overall microhardness [45].

21

Though, all the above reports offer a good insight into microstructure variations during LAM and LHT, each only cover microstructure analysis of a specific material inside a specific region of process parameters. In other words, none of the above research developed a general methodology towards understanding and control of material properties during LMP, which is suitable for all types of materials and process conditions. Finally, since most of these methods are passive, they require extensive trial and error experimentation, which is time consuming and expensive.

2.4.3 Evaluating Process Parameters

Due to the wide range of variables in LAM, a great deal of effort has been made to evaluate the influence of process parameters. A common method to analyze this is to conduct "process mapping" of outcomes in terms of process variables by means of numerical results for single parameters, usually in terms of non-dimensional quantities. Since it is hard to measure the temperature gradient and the cooling rate online, numerical techniques are used to calculate these two parameters based on theoretical models. Later, these numerical values are correlated with process parameters and offline microstructure observations to develop process maps of the process.

In the work on transient melt pool response, numerically determined melt pool response times are used to establish a lower bound on the response times of thermal feedback control systems for LENS [46]. The first attempt to predict and control microstructure in laser deposition processes based on thermal conditions at the onset of solidification was carried out by Bontha and Klingbeil [47] in 2003. Bontha and Klingbeil [47] extracted cooling rates and thermal gradients at the onset of solidification numerically from the Rosenthal solution throughout the depth of the melt pool, and developed dimensionless process maps for both thin-wall and bulky deposits. They obtained solidification maps for Ti-6Al-4V, which provided insight into the effects of process variables on grain morphology. Cao [48] developed a process model of microstructure evolution that indicated it is not the mass transfer but the heat transfer in the melt pool that dominates the solidification process [48]. Ki and So [49] developed a process map for carbon steels in terms of laser intensity and interaction time using a one-dimension heat conduction model. They obtained two most important factors in heat treatment; carbon diffusion time in austenite and cooling time, and plotted them in the heat treatable region. The maps were then validated accordingly based on laser hardening of AISI 1020 and 1035 samples by measuring their hardness and depth of penetration values. While the process mapping technique is less costly compared to other methods of microstructure analysis and control, it cannot be implemented for more complex materials or LMP procedures due to restrictions in numerical modeling.

22

2.4.4 Thermal Monitoring

Although, the above conventional methods have been widely applied in the industry for grain structure control in casting and welding processes, they have major drawbacks for sensitive LMP processes such as LAM and LHT. One of the most significant disadvantages of the later techniques is the fact that they are only suitable for bulk microstructure control and not local microstructures. For production of highly sensitive aerospace or turbine parts, where specific material properties are required at different locations of a unified body with resolutions as high as millimeters, the conventional techniques are limited. Currently, such parts are produced separately and joined together by different joining techniques to come up with specific desired properties throughout the final part. The introduction of joining techniques to the final part brings its own mechanical and material setbacks. On the other hand, all of the conventional microstructure control methods are passive and not active, in the sense that their controlling effect is evaluated after the process and not online during the process. This characteristic is because there are currently no online monitoring systems to provide real-time knowledge of the microstructure development at the onset of solidification. The absence of an online monitoring device also makes all the conventional techniques open-loop. Since there are no feedback signals during the solidification, there has been no success in developing a closed-loop control scheme.

Since LAM is a solidification process, the initial step towards achieving a fully controlled material property is to understand the thermal behavior [7], [50]. Current reports on monitoring systems using pyrometers [51]–[56] indicate their feasibility in observing changes in LAM and their application to real-time process control; they also highlight the complexity of the process. By understanding the coupling between the thermal and microstructure evolutions, precise locally tailored microstructures can be fabricated through graded deposition of single or multi-materials and optimized process parameters.

Melt pool temperature monitoring and correlation with microstructure has been the major area of research in LMP thermal monitoring. In 1999, Griffith et al. [57] used a thermocouple for measuring the melt pool temperature at different passes of a hollow block during LAM. Although, in-situ thermal measurements were acquired, no correlation was obtained for microstructure evolutions with the thermal behavior. In a later study, Griffith and Hofmeister [58] used CCD thermal imaging to understand microstructure variations during LENS processing of 316 stainless steel and H13 tool steel. Spatial temperature gradients were measured online and later used to indirectly obtain the cooling rate since, it was difficult to measure online cooling rate values. Doubenskaia et al. [51], [59], [60] used

pyrometers and infrared cameras to measure melt pool temperatures for monitoring laser cladding, however, no microstructure analysis was carried out. Hua et al. [61] found a relationship between the molten pool temperature and the cladding thickness. Zhang et al. [62] indicated that the thermal history of a deposition has an important effect on the microstructure, and consequently on the final properties of a multi-layer stainless steel 410 (SS 410) thin wall. Lhospitalier et al. [63] calibrated thermal imaging of a charge coupled device camera equipped with infrared filters by a set of tungsten (W5-type) thermocouples. They measured the temperature distribution in the weld pool and near the melted zone. Bi et al. [64] observed that variation of the melt pool temperature and cooling rate of stainless steel 316L thin walls results in dimension error, inhomogeneous microstructure and hardness. Vasudevan et al. [65] carried out real-time monitoring of the weld pool using infrared thermography during gas tungsten arc welding (GTAW). For 316LN stainless steel weld joints, IR thermal signatures were acquired for various weld defects, such as lack of fusion, lack of penetration and tungsten inclusions, for use as reference signatures for on-line monitoring during GTA welding [65].

Kim at al. [66] studied thermal deformation of thick boron steel and dual phase steel specimen using different type of heat sinks. It was observed that thermal deformation can be significantly decreased by the use of a heat sink. They also observed that the HAZ depth is an important parameter for analyzing thermal deformation. Hence, it was concluded that thermal deformation can be effectively controlled through all LMP processes. Lusquinos [67] used a pyrometer to both monitor and control the melt pool temperature during laser hardening of AISI 1045. They realized that the hardness increases with an increase in the austenization temperature and travelling speed. However, the increased speed had an upper limit for increasing the hardness since at very high speeds the small time of exposition to the laser beam did not allow the complete transformation into austenite. In their numerical modeling they observed changes in the melt pool temperature even when processing parameters were kept fixed through the process, which caused variations in hardness. These fluctuations were addressed by integrating a closed-loop temperature control using the laser power as the control action to keep the hardness value within the required range. Shiue [68] analyzed the influence of travelling speed and tempering treatment of AISI 4340 on the hardness profile and microstructure. A lower tempering temperature of the alloy produced a deeper hardened zone and a narrower transition zone in the hardness profile [68]. Furthermore, faster travelling speeds resulted in smaller martensite grain sizes and higher hardness. Qiu [43] investigated the surface hardening of AISI 4340 by linear oscillation scanning, achieving a higher overall hardness value compared to the case without oscillation. Pantsar [69] measured the surface hardness of tool steel with a dual wavelength pyrometer increasing the travelling

speed from 1.1 mms^{-1} to 33.3 mms^{-1}. Highest hardness values were achieved at slow travelling speeds and high surface temperatures due to slow diffusion rate of the chromium atoms, which required longer austenization time. Santhanakrishnan [70] showed that the case depth hardness uniformity of multi-pass LHT was highly influenced by the tempering temperature and the change of cooling rate. The tempering temperature was dependent on the heat management defined by the size of overlap and length of scan.

Many researchers have also focused on monitoring the cooling rate during the LMP process. Elmer et al. [71], [72] were the first to characterize the effects of different processing conditions on the LAM microstructure using the cooling rate in an electron beam deposition process. They indicated that mainly the cooling rate and chemical composition that influence the mode of solidification, solid distribution and nucleation. Their cooling rates were obtained indirectly offline [72], using secondary and primary dendritic arm spacing measurements and Eq.(2.2). The resulting cooling rates were shown to vary from 7 $°C/s$ to 7.5 $\times 10^6$ $°C/s$. Griffith et al. [58] reported cooling rate values ranging from 200– 6000 Ks^{-1} at the solid-liquid interface of the LENS process by using an indirect calculation approach using melt pool temperature measurements. The grain sizes and modes of solidification were correlated with temperature measurements and indirect cooling rate measurements. Mazumder et al. [73] also obtained the cooling rate offline based on the secondary dendrite arm spacing values. Wang et al. [74] characterized the thermal behavior of the LENS process for SS 410 single wall build by using a two-wavelength imaging pyrometer. They calculated a maximum offline cooling rate (based on melt pool temperature measurements) on the order of 10^3 $°Cs^{-1}$. It was observed that the molten pool size and cooling rate significantly depend on the travel velocity and the laser power. Yamashita et al. [75] developed a novel temperature measurement method during laser welding by using two high-speed cameras and a two-color thermometry method. Both temperature distribution and history were measured precisely although, the cooling rate was quite high during laser welding. Yu et al. [76] used two kinds of methods on temperature measurement for AISI 304: (1) real-time tracking for online measurement of the melt pool, in which the sensor moved together with the laser head and aimed at the molten pool, and (2) fixed-point monitoring for offline measurement of the cooling rate, in which the sensor aimed at the midpoint of the track without moving. They analyzed multi-layer depositions on a wall. The cooling time decreased with decreasing the powder feeding rate and increasing the laser power and scanning velocity in single layer deposition process. In the multi-layer deposition process, the cooling rate increased with increasing the number of the deposition layers.

Miokovic et al. [68-69] provide an in-depth study of the effects of cooling and heating rates on the microstructure, amount of retained austenite and surface hardness of laser hardened AISI 4140 in quenched and tempered conditions. It is shown that the amount of dissolving carbides and the distribution of carbon content in previously inhomogeneous austenitized areas lead to widely varying amounts of retained austenite in the hardened zone with increasing number of cycles during laser surface hardening with cyclic austensite–martensite transformation [77].

Few research groups have implemented closed-loop controllers to control the melt pool temperature in their cladding process. Song and Mazumder [79] presented a model predictive control system that controls the melt pool temperature. A dual-color pyrometer was used to monitor the melt pool temperature. The compensation for the lack of deposition with the closed-loop controller was demonstrated by cladding on a stepped surface. The controller successfully compensated for the lack of deposition by adjusting the laser power during laser cladding process. Salehi and Brandt [80] developed a PID-based controller to monitor and control melt pool temperature during laser cladding. The quality of clad layer in terms of its dilution and the extent of HAZ was investigated, and it was shown that control of temperature alone will not produce desired cladding results. They indicated that controlling the melt pool size with another operating parameter such as translation speed is also required to effectively control the process and quality of clad layer under a wide range of operating conditions [80]. More recently, Dehoff et al. [25] achieved site specific control of the crystallographic orientation of Inconel 718 grains during electron beam deposition. They were able to produce disoriented micron scale grains outlining the letter D, O and E, through the thickness of a 25.4 mm tall bulk block comprised of primarily columnar oriented grains. However, they achieved this microstructure variation through offline optimization of the travel speed based on a simplified analytical model.

In general, while numerous attempts have been made to obtain some reasonable online understanding of microstructure evolutions through real-time thermal monitoring, they have all been unsuccessful because of limitations in extracting the complete thermal information online. Most noticeably, no thermal monitoring device has been developed up to date, for monitoring and extracting the cooling rate and heating rate of the LMP process in real-time. All thermal monitoring information are restricted to recordings of the melt pool temperature, in spite of the fact that melt pool temperature is only one of the three main thermal dynamics affecting the final microstructure, as indicated in Figure 2-1.

2.5 The Need for Real-time Microstructure Monitoring and Control

Despite the progress on studying the solidification and thermal behavior of the LMP process, none of the above methods were successful to develop an online monitoring and controlling methodology for the microstructure. Furthermore, the described conventional methods are not automated and generalized for different materials and process parameters. On the other hand, LMP is a very sensitive process with a concentrated heat source and very high cooling rate. Therefore, it has the key capability of producing very sensitive parts with locally tailored microstructures. However, such advanced applications and process benefits are only feasible using a closed-loop LMP process that can monitor the microstructure in real-time, and actively control material properties locally.

To control the whole solidification microstructure, one has to monitor and control the ratio and product of the growth rate and the temperature gradient. Going from one solidification mode to another requires great variations inside the LMP process, whereas, the size of the morphology is very sensitive to process parameters. It is evident that the product of the temperature gradient and growth rate $G_T R_{growth}$ (℃/s), is in fact the cooling rate that defines the size of the grains. As indicated in previous studies [58], [72], apart from the grain size, the cooling rate also affects the solidification mode. Therefore, there exists a great possibility that by measuring the cooling rate and correlating its variations with microstructure development, one could easily understand and control the local microstructure formation in real-time. However, since in-situ real-time cooling rate measurements are difficult to achieve [58], no researcher has obtained a generalized logic on how to obtain optimized process parameters in order to obtain desired material properties. Having such a methodology, one could acquire controlled solidification characteristics, such as grain size control, locally and at the onset of solidification.

In a series of prior work leading to the current study [81]–[85], the feasibility of real-time thermal monitoring has been studied along with the correlation to microstructures in the LAM process. An infrared-based thermal imaging system was developed to monitor the LAM thermal process in real-time. The developed system was capable of capturing the real-time cooling rate and melt pool temperature. A basic PID closed-loop control system was also developed to control the cooling rate in real-time using the laser travelling speed as the control action. It was observed that microstructure characteristics such as grain size and volumetric phase percentage are well correlated with online variations of the cooling rate. The results were limited and required further detailed investigations, since

microstructure control resulted in deviations in the clad geometry. Thus, this real-time thermal extracting methodology will provide the bases of the developed microstructure control technique.

2.6 Current Geometry Control Schemes in LMP

Apart from the microstructure properties of an LMP product, the geometry properties are also a limiting factor that require monitoring and control. The geometry and microstructure together form the two most important output properties of an LMP product. In contrast to the absence of a closed-loop microstructure controller, there have been numerous successful attempts in achieving a closed-loop geometry control system for different LMP processes. Each LMP process has its own specific geometry characteristics. For example, the clad height and width are important during LAM depositions, whereas, the hardened and width are the two most important geometry properties of the LHT process. Geometry control of the LMP processes is achieved through two main schemes: (1) direct control through measurement and control of geometry properties, and (2) indirect control through measurement and control of thermal dynamics.

Meriaudeau et al. [86] were one of the first to integrate a system of two CCD cameras to directly measure the clad height and width in LAM. Mazumder et al. [66-67] used a bang-bang controller for the laser power to control the height of deposition in LAM. Toyserkani and Khajepour [88] used a CCD-based image system to obtain a discrete model for the clad height in a PID-based controller to control the height in a closed-loop system using the laser power as the control action. Fathi et al. [89] used a similar approach to control the clad height using a feedforward PID controller with the laser travelling speed. Other various type of controllers such as fuzzy logic [70-71] and adaptive sliding mode [92] were also developed by researchers to control the clad height during LAM depositions. Although direct measurement of the clad geometry through CCD-based imagery is a routine way to develop closed-loop control systems for the LAM process, such a direct approach is not applicable for measuring the depth of penetration in LHT.

Hu and Kovacevic [93] used a CCD camera with an integrated infrared filter to capture an infrared image of the melt pool. They were able to obtain the size of the melt pool through measuring the pixel number of the melt pool in the infrared image. A closed-loop controller was designed to produce a 60 layer thin wall with a consistent melt pool geometry. Song and Mazumder [79] used a two color pyrometer to measure the melt pool temperature. They utilized a model predictive control for the melt pool temperature to compensate for the lack of deposition in cladding on a stepped surface.

28

Considering the existing literature, there are numerous reports available on indirect control of the LHT geometry (hardening depth and width) through melt pool temperature control. Grum and Kek [94] used an IR photodiode to correlate IR voltage signal and hardened depth and width. Although, they were able to obtain empirical process maps for voltage-depth and voltage-width relations, no controller was developed. Similarly, Xu [95] also developed a relation between output DC voltage of an IR monitor with the hardness and depth of laser hardened ferrous alloys. Qiu [43] realized that the hardened depth of AISI 4340 could be increased by applying high oscillation frequency on the laser travelling speed. However, Homberg and Weiss [96] showed that a prescribed hardening depth with no surface melting cannot be achieved only through melt pool temperature control. They observed fluctuations in hardening depth and melting during a closed-loop melt pool temperature control process in a substrate with changing thickness. They noticed changes of temperature at depths below the surface in their numerical model, indicating a change in the cooling rate. Since they were not able to measure the actual subsurface temperatures with a pyrometer for control purposes, they obtained an optimal melt pool temperature corresponding to a uniform subsurface temperature and cooling rate through a numerical model. This optimal temperature profile obtained offline served as the setpoint for the PID-controlled melt pool temperature to provide a uniform hardened depth.

2.7 The Need for Integrated Microstructure and Geometry Control

Although, a broad range of closed-loop control systems have been developed for clad height control, nearly all of them result in deviations in the microstructure and material properties because of in-process deviation of process inputs. The same goes for microstructure control techniques, which result in inconsistencies in the deposition geometry. As a result, all current LMP setups including LAM and LHT machines require a great deal of manual calibration and engineering time to produce products with specific engineering design criteria. Despite all the manual tuning and calibration, great amount of inconsistency still exists in the quality of the final LMP product, because of the sensitive nature of the process. Consequently, numerous passive inspection procedures are currently being implemented in the industry to identify and correct the manufacturing defects of an LMP-manufactured part. These setbacks in process control have prevented the implementation of LMP manufacturing systems in mainstream manufacturing. Hence, development of a closed-loop LMP system that can provide online information of both microstructure and geometry properties, is highly crucial for the advancement of LMP technologies. Utilization of these online monitoring data inside an integrated closed-loop system will also result in higher quality products and increased efficiency of the LMP manufacturing process.

Overall, the development of an integrated LMP microstructure and geometry monitoring and controlling technique will be increasingly important for time and cost savings in the manufacturing industry.

2.8 Summary

In this chapter, the literature of microstructure and geometry modeling and control in LMP processes were discussed. It was denoted that LMP is a nonequilibrium solidification process that can promote the formation of nonequilibrium phases such as martensite and bainite in steels. As shown in Figure 2-1, the microstructure of the solidification was found to be in direct contact with the thermal dynamics of the process, specifically the cooling rate and temperature gradient. Since thermal dynamics are the governing nature of the LMP microstructure, there have been several attempts to model them analytically for the purpose of microstructure prediction and control. A variety of these models were studied in Section 2.3. However, due to limitations in development of a real-time thermal monitoring device, none of these models were found to be validated experimentally based on actual cooling rate data or temperature gradient measurements.

Apart from modeling, current microstructure control techniques in LMP processes were also studied in Section 2.4. The three conventional methods of microstructure control were found to be limited to bulk control of specific materials and at the same time, time and cost consuming. The broad work on thermal monitoring of the LMP processes was also discussed in detail in Section 2.4.4. It was observed that although there are numerous reports on the monitoring of the melt pool temperature and its correlation with the microstructure, there are no real-time cooling rate measurements and correlations. This lack of real-time cooling rate data during the LMP process has limited the understanding and control of the microstructure evolutions during the process. In general, all of the current microstructure control techniques are passive and offline. Thus, they require an extensive amount of experimentation time and effort.

Finally, the current research on geometry control of the LMP processes was discussed in Section 2.6. The microstructure and geometry where identified as two of the most important output properties of a LAM product. However, it was observed that there is currently no monitoring and control scheme available in the industry that can simultaneously provide the integrated real-time control of the microstructure and geometry. The current single-input-single-output closed-loop thermal or geometry control systems, result in inconsistent properties for the uncontrolled outputs. Therefore, no control

system is available that is capable of controlling the microstructure and geometry simultaneously in real-time. This lack of full automation, has limited the applications and implantation of LMP systems in mainstream manufacturing.

Chapter 3

Multi-objective Thermal-Geometry Monitoring and Control Module

An automated Laser Materials Processing (LMP) system is composed of several sophisticated components. However, in order to improve production consistency and achieve desired engineering properties during the LMP process, it is essential to monitor and control the most critical of these properties in real-time. A standalone module is developed to monitor and control microstructure and geometry properties in real-time. The module utilizes thermal and optical image processing techniques, which will be discussed in the current chapter. The chapter begins with a description of the LMP setup integrated at the Automated Laser Fabrication (ALFa) lab at the University of Waterloo. Additional information is provided on how the geometry and thermal dynamics of the LMP process are monitored in real-time using machine vision and thermal image processing. The development of the automated closed-loop LMP process that monitors and controls multi-objective geometry and microstructure properties in real-time is also clarified.

3.1 Laser Materials Processing Setup

A schematic view of the integrated closed-loop LMP setup used in this research is illustrated in Figure 3-1.
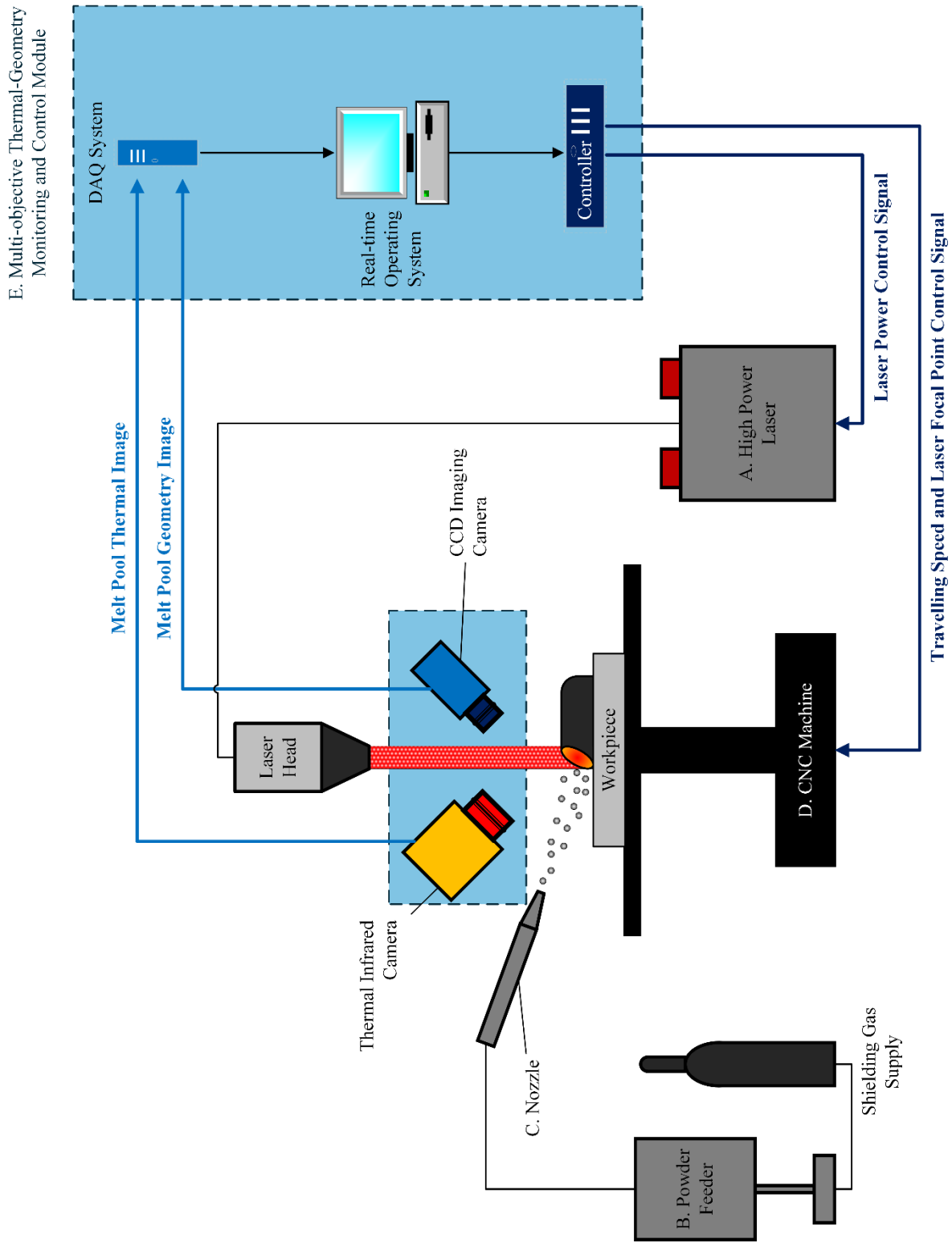
Figure 3-1 Schematic of the closed-loop automated LMP system.

Each piece of equipment is described briefly as follows.

A. **High power laser:** An IPG fiber laser YLR-1000-IC operated in continuous mode with a maximum power of $1.1\ kW$ is utilized as the energy source. The fiber laser operates at a wavelength of $1070\ nm$.

B. **Powder feeder:** A Sulzer Metco TWIN 10-C powder feeder with two $1.5\ L$ hoppers are used to control the powder mass feed rate and the flow of argon shielding gas. The feed rate and flow rate are controlled manually using the onboard controllers installed on the system. A wide range of particle sizes can be sprayed at feed rates varying from $2\ g/min$ to $150\ g/min$.

C. **Nozzle:** The powder is fed through a lateral nozzle onto the substrate with inside diameter $1.6\ mm$ and outside diameter $3.1\ mm$. The nozzle is installed on a mechanism with four degrees of freedom, providing good positioning for focusing the powder onto the laser beam spot.

D. **CNC machine:** A 5-axes CNC machine is used as the positioning device. Two additional rotational axes were installed on a 3-axes Fadal VMC 3016 to produce the required motions. An additional moving axis was also installed on the laser head, vertically aligning the head in order to control the laser spot size in real-time.

E. **Multi-objective thermal-geometry monitoring and control module:** An integrated vision-based monitoring system captures the melt pool shape and thermal history in real-time. A CCD-based camera (Teledyne Dalsa Genie M1020) captures the shape and profile of the melt pool. Additionally, an infrared thermal camera (Jenoptik IR-TCM 384) records real-time thermal maps of the melt pool and surrounding area of the deposition. These recorded images are processed in a standalone operating system using NI LabVIEW and its' modules to provide feedback of important process parameters such as the clad height, melt pool temperature, cooling rate and heating rate in real-time. Process inputs such as the CNC travelling speed, laser power and laser focal point are controlled by the operating system inside LabVIEW. The input control commands are sent to the system through an NI PCI-7342 motion controller device.

As shown in Figure 3-1, the laser beam is transferred to the laser head installed on the CNC machine through the fiber optics. The beam is then shot on to the workpiece increasing the temperature and producing a melt pool (transformation of solid into liquid) during the LAM process or only a heated region (remaining in solid state and no liquid transformation) during the LHT process. During the LAM process the powder feeder sprays the required amount of metallic powder onto the melt pool, also

feeding argon shielding gas to prevent oxidation, whereas during the LHT process only a shielding gas is supplied on the heated region without any additive material. As the powder particles and a thin layer of workpiece are melted, a layer is deposited on the substrate. Due to rapid cooling rates and localized heat zones, a strong bond is formed between the deposited layer and the workpiece (in the case of a LAM process), and unstable phases such as martensite may be formed on the substrate (in the case of an LHT process). The CNC machine moves the workpiece, producing the required track profile on the workpiece. This setup can be used for a variety of applications such as cladding, coating and rapid prototyping and hardening. An image of the closed-loop LMP system, which was developed in the ALFa lab is shown in Figure 3-2.

Figure 3-2 Image of the closed-loop LMP system developed in the ALFa lab.

All other industrial LMP machines (e.g. laser cutting and laser welding) found in the manufacturing industry have a system architecture similar to the above setup. While, limited systems such as the

machines provided by DM3D [97] provide limited monitoring of geometrical characteristics, the majority of the LMP machine configurations found in the industry are "open-loop" systems and do not have any thermal-geometry monitoring and control module (discussed above in Figure 3-1). Thus, most industrial LMP machines cannot provide any online information of how the LMP process is changing during operation. Additionally, these open-loop setups cannot overcome and control process disturbances, which are highly effective on the final product properties. Therefore, all current inspection and quality control procedures are passive and conducted after production, resulting in a manufacturing process that is inconsistent, time consuming, and requires great expertise and extensive hours of manual calibration.

3.2 Multi-objective Thermal-Geometry Monitoring and Control Module

As explained in Chapter 2, the microstructure and geometry of an LMP-manufactured part are the two most important characteristics that are inspected after production and require to meet specific engineering needs. However, there is currently no device available to monitor and control these two properties simultaneously in real-time. Therefore, a standalone module was designed and developed to provide real-time information of integrated microstructure and geometry variations during the LMP process, in order to construct an active online inspection and control procedure. The final module will assist with the development of a "closed-loop" LMP process that controls the consistency of final material properties.

Generally, the part, or workpiece, processed by the LMP thermal process defined above, has two sets of properties:

- **Mechanical properties** including, but not limited to, geometry, strength, hardness and residual stress

- **Microstructure properties** including, but not limited to, morphology, grain size and phase precipitation.

The objective of any LMP process is to obtain enhanced material properties of the workpiece or additive material, such as enhanced hardness, yield strength and wear. Each of these properties relate to the microstructure characteristics of the finished part. It is also beneficial to achieve specific geometry dimensions and tolerances of the finished part produced by the LMP process. Therefore, monitoring and controlling microstructure and geometry properties of the workpiece during any LMP

process is of importance for industrial applications. This may be achieved by monitoring the thermal dynamics variables, such as the cooling rate or the heating rate of the thermal cycle in real-time.

Since the LMP procedure is typically a thermal process defined by a thermal cycle, the microstructure and geometry properties of the finished part are governed by the dynamics of this thermal cycle (as shown in Figure 2-1). Measuring and monitoring most geometry properties during the LMP procedure is convenient to achieve through normal image acquisition and processing. Some examples include measuring the clad height or width of deposition during laser additive manufacturing (LAM) or width of hardened track during laser heat treatment (LHT). However, measurement and monitoring of microstructure properties and certain geometry properties including but not limited to, hardening depth during heat treatment processes, are generally not achievable through normal image acquisition and processing techniques.

The developed module utilizes two types of imaging-based sensors to extract geometry and thermal information from the LMP process. A normal imaging sensor such as a CCD/CMOS-based camera is used to actively measure physical geometry values (e.g. height or width of deposition and width of hardened track). Additionally, a thermal imaging sensor such as an infrared (IR) camera is used to record thermal maps of the process and obtain the real-time thermal dynamics values of the peak temperature, cooling rate and heating rate.

The schematic of the developed multi-objective monitoring and control module is highlighted in Figure 3-1. The system architecture of the developed module comprises of three main subsystems: (1) geometry monitoring system, (2) thermal monitoring system, and (3) integrated closed-loop control system. An image of the thermal and imaging cameras is shown in Figure 3-3. The two imaging-based sensors record real-time images and thermal images of the process. These images are transferred to the operating system in order to visualize the process actively online. The images are analyzed and processed online in order to provide feedback from geometry and microstructure variations in real-time. The module later utilizes these feedback signals to automatically adjust process parameters in order to produce consistent material properties with consistent quality. The following sections provide a detailed description of the module subsystems that develop in a complete closed-loop automated LMP process.

Figure 3-3 Integrated CCD and thermal infrared monitoring of the LMP process.

3.2.1 Geometry Monitoring with CCD/CMOS Imaging

An optical-based imaging system is used to provide online images of the LMP process and the melt pool region. CCD-based imagery is used for online monitoring of the shape and profile of the melt pool. In the current research, a Teledyne Dalsa Genie M1020 CCD-based camera with a resolution of 1024 X 768 pixels was used to record images of the melt pool with a frequency of $60\ Hz$. The spatial resolution of the camera during measurement was $0.004\ \frac{mm}{pixel}$. In the melt pool process zone, the high temperature of the melt pool, plasma and vaporized metal emit lights with high intensities. In order to prevent image saturation, an ND filter (No. 6) is used to reduce the melt pool image intensity. These images are transferred into LabVIEW for additional image processing and analyses. The greyscale images provided by the camera are used for image processing to obtain the clad height.

Figure 3-4 illustrates two examples of the image processing method used to extract the clad height in real-time from the original melt pool images. In the first step, a series of image processing functions are implemented to transform the original image into a binary image of the melt pool. In this image the melt pool is clearly identified by the white pixels. In the second step, the vertical pixels of the melt pool that represent the clad height are measured and converted into real-time clad height measurements.

Original Image

Original Image

Processed Binary Image

Processed Binary Image

Measured Clad Height Pixels

Measured Clad Height Pixels

clad height pixels

clad height pixels

removed heat affected zone pixels

removed heat affected zone pixels
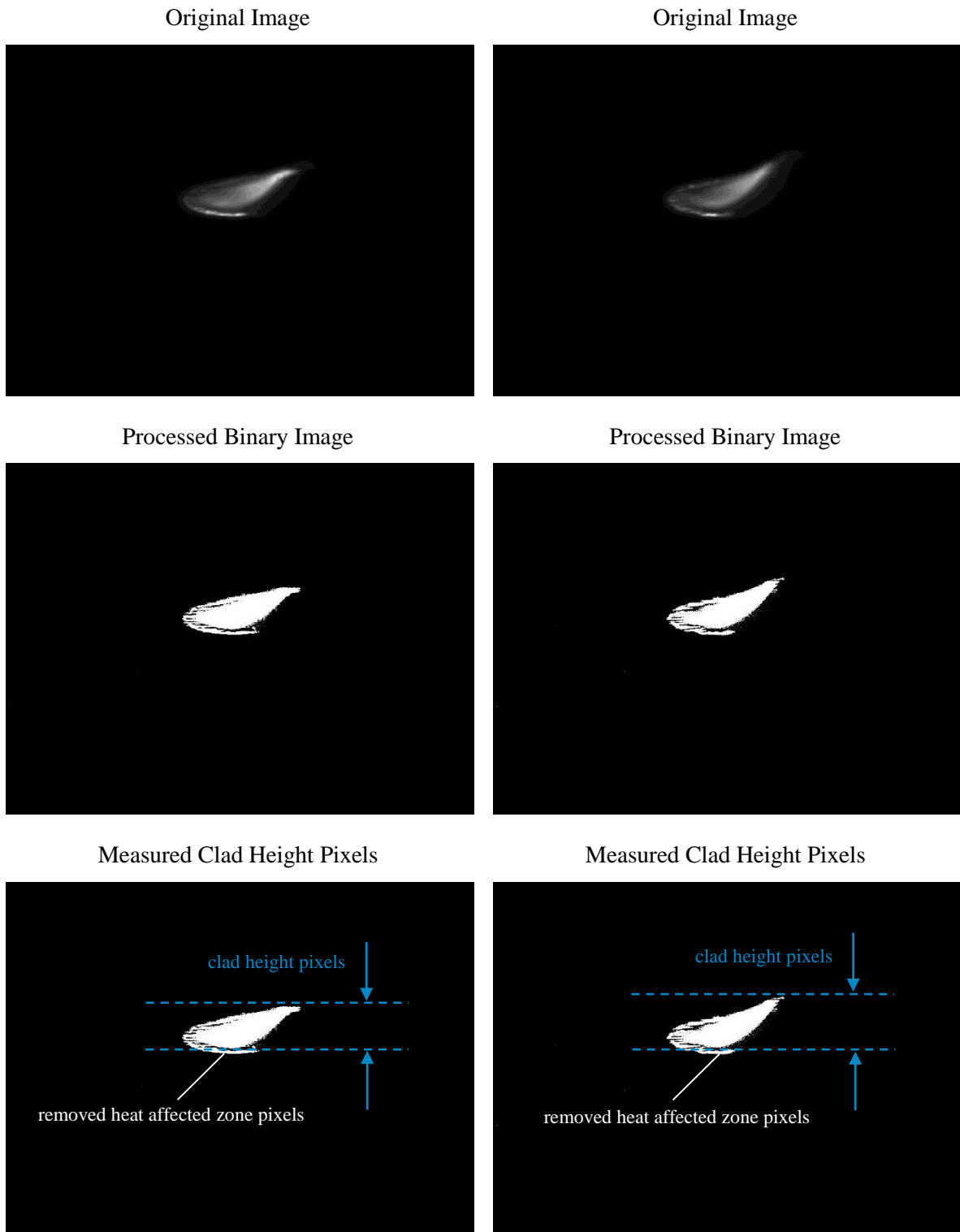
Figure 3-4 Examples of clad height measurement image processing scheme.

The general developed pattern recognition methodology is similar to the method implemented by Toyserkani [88] and Iravani [98]. However, in the current developed technique clad height measurement is achieved by using a combination of edge filters to define and remove the pixels representing the heat affected zone at the bottom of the melt pool. The final vertical clad height pixels are calculated by removing these excessive pixels from the total vertical pixels, as shown in Figure 3-4.

3.2.2 Thermal Dynamics Monitoring with Infrared Thermal Imaging

Microstructure properties cannot be monitored directly during the LMP thermal process. However, according to the summary provided in Figure 2-1, the microstructure is governed by the real-time thermal dynamics of the process. Therefore, through real-time thermal dynamics monitoring, one can predict the microstructure evolutions to an acceptable level of accuracy in real-time. However, in order to understand which thermal dynamics are required to be monitored for online microstructure predictions, it is necessary to investigate the LMP thermal process. During the LMP process, the materials undergo a thermal cycle in order to achieve enhanced materials properties. In effect, this is changing the microstructure of the workpiece or the additive material as shown in Figure 3-5. During the process, the heating energy and translational movement of the workpiece, produce a rapid thermal cycle, which includes three main stages:

- The first stage may be seen as a **heating stage** which may include the rapid heating of a pre-defined location on the workpiece or of additive material fed (or preplaced) by the concentrated laser heat source. During the LMP heating process, the workpiece or additive metallic material may transform from its original solid state to another state, such as a liquid (solidification) or liquid-solid (partial solidification) state or may remain solid during the thermal cycle.

- The second stage may be seen as a **translational movement** whereby the workpiece is moved with respect to the heat source by the motion system.

- The final stage may be seen as a **cooling stage**, which includes a rapid cooling of the heated region of the heating stage. This cooling may be performed via the translational movement between the workpiece and the heat source and/or exposure of the heated region to a cooling source, such as the shielding gas supply.
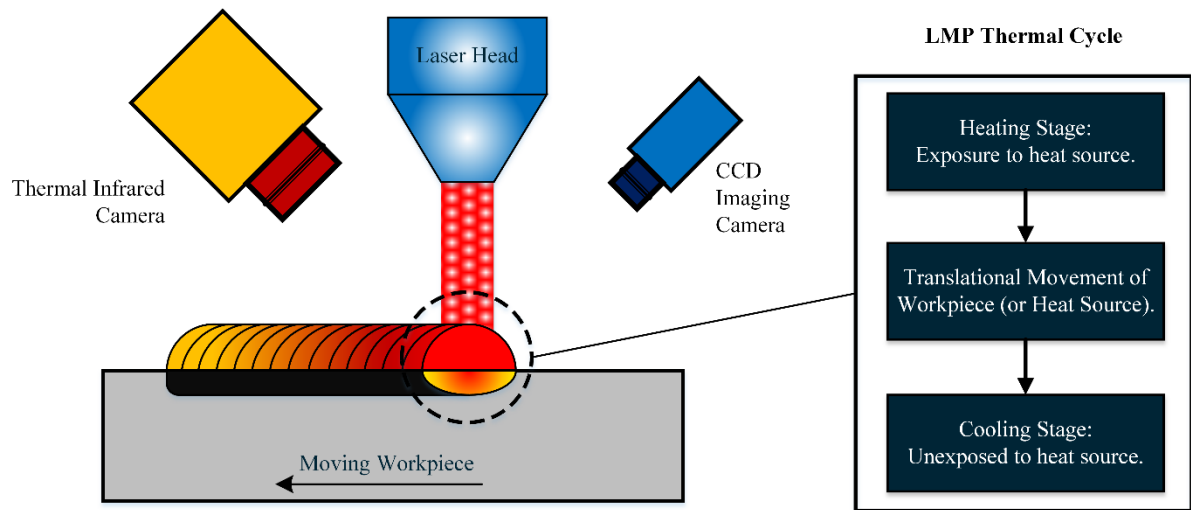
Figure 3-5 LMP process thermal cycle.

To control the resulting microstructure of an LMP product, complete knowledge of the process thermal cycle is required. The thermal cycle described in Figure 3-5, is in most cases a solidification process. As illustrated in Figure 2-1, the heating rate, cooling rate and peak temperature of the workpiece or additive material are three thermal dynamics variables that govern the microstructure of a solidified part. These variables tend to be the most significant variables that provide comprehensive information of the LMP thermal cycle and each of its three stages. The heating rate provides information of how fast the material is initially heated at the beginning of the cycle, while the melt pool temperature represents the amount of actual energy absorbed during the thermal cycle. Finally, the cooling rate defines how the fast the material is cooled down and the total duration of the thermal cycle. Therefore, by having real-time values of the three main thermal dynamics, the heating rate, melt pool temperature and cooling rate, one can obtain complete information of the LMP thermal cycle, which can thus predict the developed microstructure. In order to monitor these variables during solidification, a great amount of thermal information is required from the melt pool and its boundaries.

There are a variety of devices including thermocouples, pyrometers, and thermal infrared cameras that can provide thermal information of a system. Considering their methods of implementation and applications, these instruments can be categorized into specific sub-categories such as; contact and non-contact measuring devices or point, line and area scan measurement devices. Infrared thermal cameras have several advantages compared to other contact and non-contact techniques that are specifically suitable for the LMP application. These thermal cameras can provide a thermal image over a large area of pixels rather than single pixel calculations (which is provided by thermocouples or pyrometers). This

41

property provides the capability to capture real-time cooling rates and heating rates, which require multiple point temperature measurements rather than single-point measurements. Additionally, infrared image acquisition is non-contact and non-destructive, which is suitable for the high temperature melt pool of the LMP process. These two characteristics enable measurement of the melt pool temperature and more importantly the cooling and heating rates of the LMP thermal cycle.

Considering these advantages, a high temperature thermal infrared camera was used in the multi-objective monitoring and control module to provide information of the process thermal dynamics. The integrated setup of the infrared thermal and CCD cameras are shown in Figure 3-3. A Jenoptik IR-TCM 384 camera with a resolution of 384×288 pixles and a temperature measuring accuracy of $\pm 2\%$ is used to monitor the thermal behavior of the LMP process with a frequency of $30\ Hz$. The infrared imaging is used to directly measure the temperature of the melt pool and cooling/heating rates in real time.

Two sample thermal images captured during the LHT and LAM processes are shown in Figure 3-6 and Figure 3-7, respectively. Zoomed-in images of the original image are also shown in these figures. Thermal images taken using an infrared camera only provide temperatures of each pixel and thus, require processing and analysis to be functional for exact microstructure analyses and control applications. The intensity of each pixel is directly related to its temperature, the greater the RGB value (the brighter the pixel) the higher the temperature. The camera was located at a distance of $20\ cm$ from the substrate that provided a resolution of $0.35\ \frac{mm}{pixel}$. It can be seen in Figure 3-6c and Figure 3-7c that the melt pool occupies an average of 5 to 10 pixels (depending to the size of laser beam), making it difficult for exact thermal measurements. Zoomed-in images of Figure 3-6b-c cover a total area of $26.95 \times 14.30\ mm$ and $14.30 \times 7.70\ mm$, respectively. The original image array (Figure 3-6a and Figure 3-7a) has a size of $X \times Y$ in which X is the total number of pixel rows (384 pixels) and Y is the total number of pixel columns (288 pixels) of the image. Each element of the array has an assigned row r, and column c, with a position vector (c, r). The size of each element $I_{c,r}$ is equal to the RGB value of the equivalent pixel.
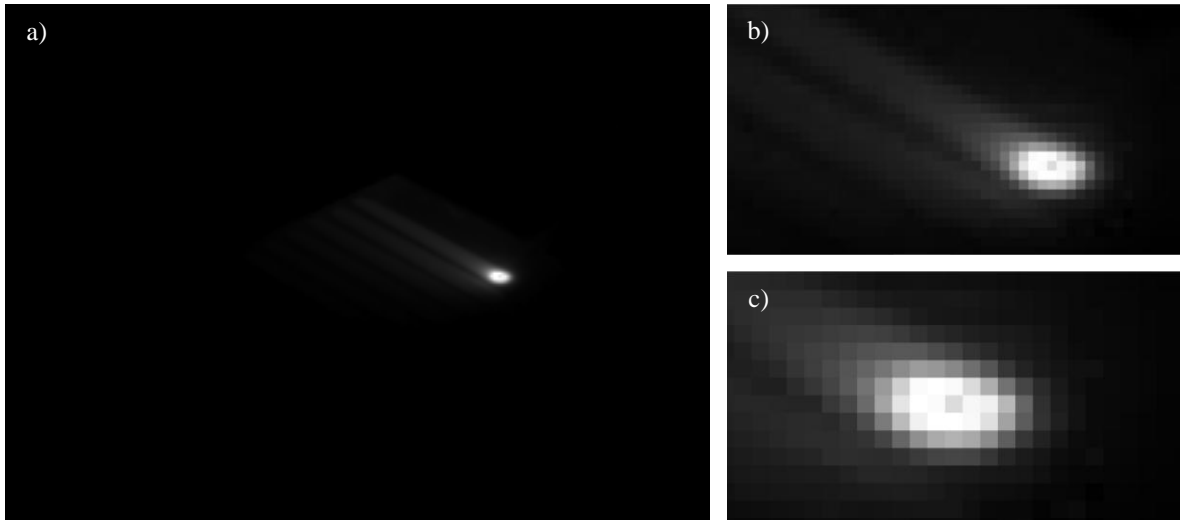
Figure 3-6 Greyscale thermal image captured by the thermal infrared camera during LHT (2.5 mm laser beam diameter). (a) actual size image (384×288 pixels), (b) zoomed-in image (49×26 pixels), and (c) zoomed-in image (26×14 pixels).
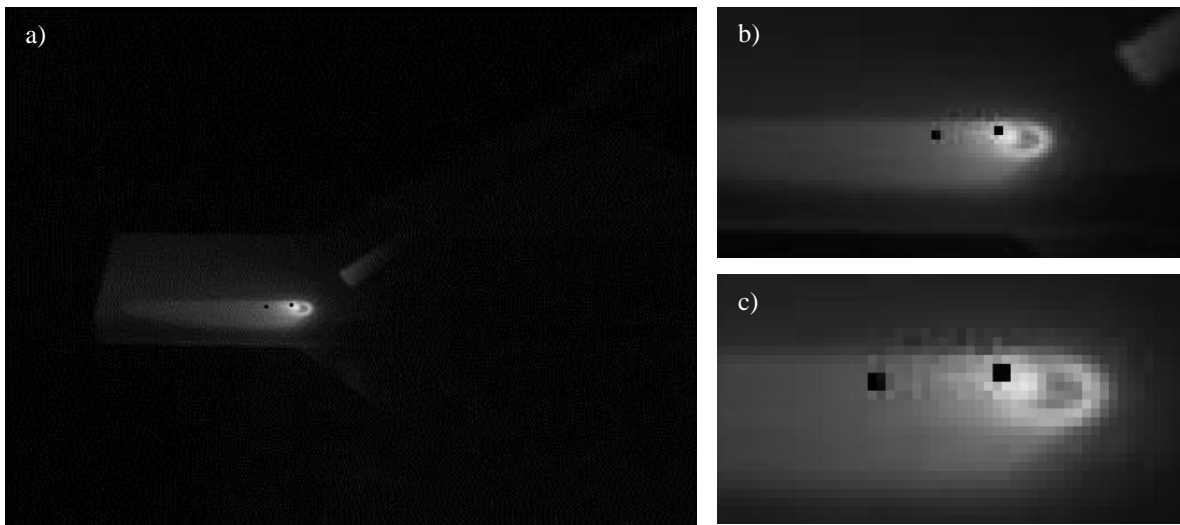
Figure 3-7 Greyscale thermal image captured by the thermal infrared camera during LAM (2 mm laser beam diameter). (a) actual size image (384×288 pixels), (b) zoomed-in image (104×56 pixels), and (c) zoomed-in image (52×28 pixels).

As stated earlier, to be capable of monitoring changes in the solidification mode and structure size, it is required to have in-process knowledge of the LMP thermal cycle, which is represented by the thermal dynamics variables. The cooling rate, which is the product of the temperature gradient and growth rate, has direct influence on the solidification mode and solidification structure size. Therefore, controlling microstructure during the LMP process requires a complete knowledge of the real-time cooling rate values as well as other thermal dynamics such as the melt pool temperature and heating rate. A general description of the thermal algorithm that extracts these thermal dynamics is discussed in the following sections.

3.2.2.1 Real-time Measurements of Thermal Dynamics

The current methodology is directed at a method and system to obtain or determine real-time measurements of the three main thermal dynamics variables during an LMP process: melt pool temperature (or peak temperature), cooling rate, and heating rate. In order to understand the method and system, one needs to consider the heated surface of the workpiece (including the additive material) as a 2-dimensional (X and Y) array of pixels (or grids), as shown in Figure 3-8. Since the thermal camera is installed on the laser head (shown in Figure 3-5), the XY thermal array coordinate system is fixed with respect to the global coordinate system. Therefore, the location of the instantaneous melt pool pixel is fixed within the XY coordinate system, whereas, all other floating points on the workpiece move with the translational movement (shown in Figure 3-5) within the XY coordinate system. Each spatial point P_i (or pixel) on the workpiece has an intensity I and a position vector (c, r) in the array at time t, which is represented by $I_i^t(c_i^t, r_i^t)$. The intensity of each pixel I_i^t, can be converted to an actual temperature of that pixel T_i^t, through the infrared thermal monitoring camera. The current thermal camera has been calibrated for a temperature range of $-40\ °C$ to $2700\ °C$.

In order to demonstrate the calculation of peak temperature, cooling rate and heating in real-time, a schematic of two thermal images at two different time frames is illustrated in Figure 3-8. This figure illustrates two thermal pixel arrays at times $t_1 = t_0$ and $t_2 = t_0 + n\tau$, in which τ is the sampling time and n is the total number of sampling times elapsed after initial time t_0. Let us define two important thermal points inside the thermal pixel array:

- **Point P_p^t** is the **"instantaneous peak temperature"** of the LMP process. This point will always be the element with the maximum intensity inside the thermal array. At any time t, P_p^t is represented by intensity and position vector $I_p^t(c_p^t, r_p^t)$, with temperature T_p^t. For

example, $P_p^{t_1}$ represents the peak temperature at time t_1, with the intensity and position vector $I_p^{t_1}(c_p^{t_1}, r_p^{t_1})$.

- **Point $P_{f_i}^t$** is a **"fixed spatial point"** on the workpiece (or deposition). This point, which will be later used for cooling rate calculations, represents any consistent fixed spatial point f_i on the workpiece. At any time t, $P_{f_i}^t$ is represented by intensity and position vector $I_{f_i}^t(c_{f_i}^t, r_{f_i}^t)$, with temperature $T_{f_i}^t$. For example, at time t_1, the fixed spatial point $P_{f_i}^{t_1}$ has an intensity and a position vector $I_{f_i}^{t_1}(c_{f_i}^{t_1}, r_{f_i}^{t_1})$, with temperature $T_{f_i}^{t_1}$.
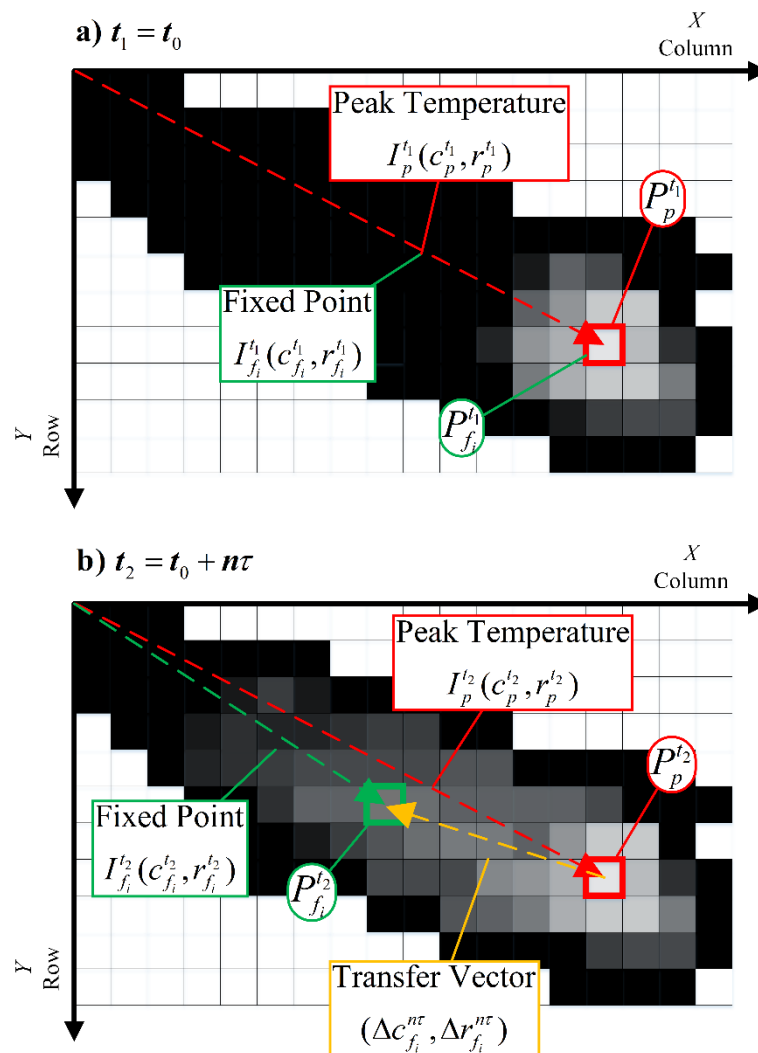
Figure 3-8 Schematic view of two thermal images at two consecutive time frames for a processed straight line during the LMP process.

45

After a translational movement has been performed on the workpiece, at time t_2, the fixed spatial point $P_{f_i}^t$ moves with the translational motion inside the thermal pixel array resulting in a new intensity and position vector $I_{f_i}^{t_2}(c_{f_i}^{t_2}, r_{f_i}^{t_2})$, and a cooled temperature $T_{f_i}^{t_2}$. The transfer vector $(\Delta c_{f_i}^{n\tau}, \Delta r_{f_i}^{n\tau})$, which is denoted in Figure 3-8, is the distance travelled by point $P_{f_i}^t$ from time t_1 to t_2. The thermal infrared camera can collect the thermal information shown in Figure 3-8 by capturing two thermal images at two different time frames. After these thermal information of points P_p^t and $P_{f_i}^t$ are collected in each time frame, the thermal dynamics are calculated in three steps:

- **STEP 1- Melt pool temperature (or peak temperature) identification:** The first step in identifying the real-time thermal dynamics is to identify the location and value of the peak or melt pool temperature. The instantaneous melt pool temperature T_p^t, indicates the amount of heat input supplied to the system during the process. When a thermal image is taken at each time frame, the pixel with the maximum intensity inside the thermal array represents the melt pool, or in other words $I_p^t = I_{max}^t$. Thus, the center of the melt pool and temperature is found by identifying the location and value of the maximum element in the 2-D array of thermal pixels.

- **STEP 2- Cooling rate identification:** The cooling rate of a single point on the workpiece, which is represented by $C_{f_i}^t$, indicates how fast the temperature of point f_i reduces in time. The calculation of the cooling rate may be enhanced using the thermal dynamics algorithm shown in Figure 3-9. According to this algorithm, the cooling rate of any point f_i on the workpiece can be monitored in real-time. It can be seen in Figure 3-8a that at time t_1, $P_{f_i}^{t_1}$ can also be chosen as the melt pool temperature pixel, so that $T_{f_i}^{t_1} = T_p^{t_1}$. Hence, it is recommended that point f_i be selected as the instantaneous peak temperature at time t_1, which is $P_p^{t_1}$. When resetting point f_i to f_{i+1} at the end of each cooling rate calculation in thermal dynamics algorithm shown in Figure 3-9, the new peak temperature pixel at time t_2 (which is $P_p^{t_2}$) is selected as the new f_{i+1}. Therefore, the real-time cooling rate of the instantaneous peak temperature, C_p^t may be calculated at each sample time. However, it has to be noted that point f_i can be any fixed spatial point on the workpiece (or deposition). Therefore, this method can be used to measure the real-time cooling or the real-time heating rate of any point on the workpiece (or deposition).

46

- **STEP 3: Heating rate identification:** The heating rate shows how fast a point on the substrate absorbs energy. The heating rate of the heat source denoted by $H_{f_i}^t$ is also measured through the thermal information provided in Figure 3-8. The real-time heating rate is monitored by defining the spatial temperature gradient of the pixels in front of the fixed point f_i and dividing it by the instantaneous travelling speed at time t_1. Similar to the cooling rate, for the heating rate calculation the fixed point f_i can be chosen as the instantaneous melt pool pixel so that $H_{f_i}^{t_1} = H_p^{t_1}$.
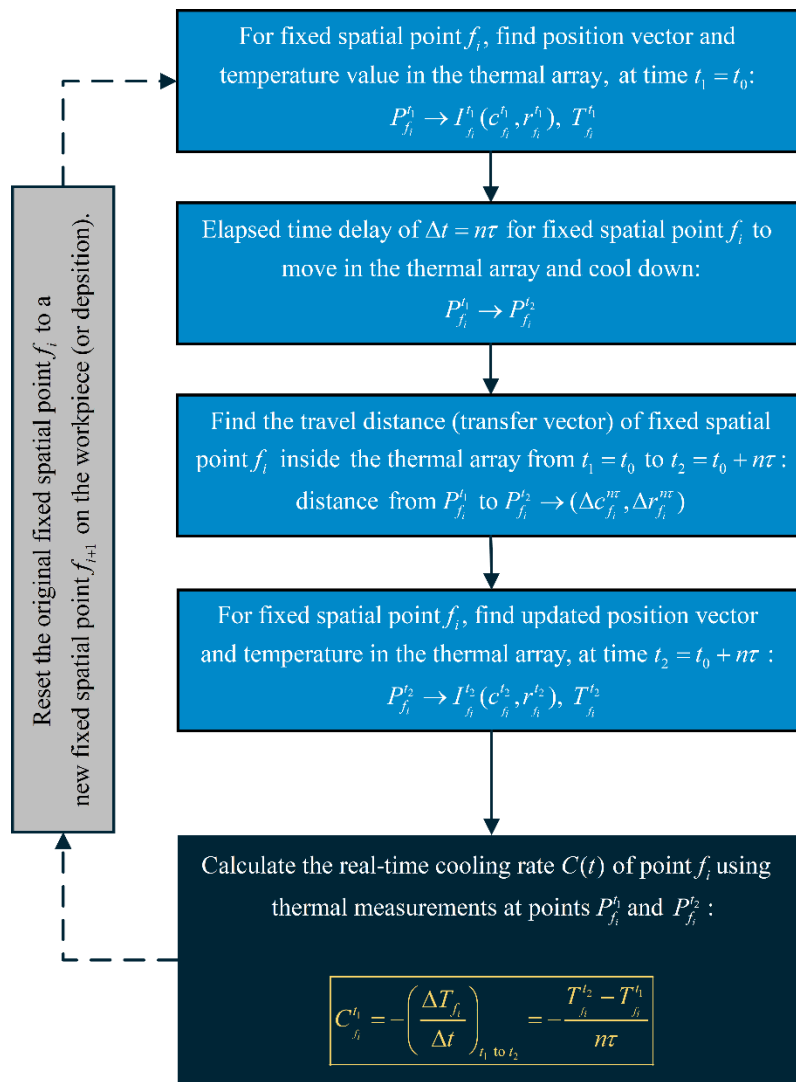
Figure 3-9 Thermal dynamics algorithm for identification of the cooling rate.

It has to be noted that in order to reduce measurement noise in all of the above thermal dynamics calculations, temperature calculations of each thermal pixel was averaged with the three maximum neighboring pixels surrounding it. More details on the thermal dynamics algorithms are provided in prior works [77-91].

3.2.2.2 Emissivity Value and Thermal Signature Measurements

A thermal infrared camera defines the real temperature of an object using a constant emissivity value ε. The emissivity of metallic powders deposited during LAM (such as stainless steel and titanium) are highly dependent on temperature, especially at the elevated temperatures of the LMP process ($800 - 2200\,°C$). The change of emissivity with temperature in steel is mainly attributed to the formation of an oxide layer on the surface of the steel as its temperature increases [99]. This change of emissivity may lead to errors in capturing the real body temperature as high as $100\,°F$ [100]. However, in the current application thermal dynamics values from the infrared cameras are compared and correlated with microstructures for comparative analyses. Since a comparative study of the thermal dynamics values is enough for indirect monitoring and controlling of the microstructure, actual true temperature measurements are not required as long as relative (or comparative) measurements are provided by the infrared camera. Hence, an average emissivity is calculated for each material being deposited and this emissivity is kept constant throughout the whole process and real-time temperature calculations. The emissivity values of all of the LAM and LHT samples in this research were taken as 0.55.

Using a constant emissivity value results in real-time measurement of a thermal signature rather than the "true temperatures" during the process. However, as stated earlier, since the current module only requires a comparative study of the thermal dynamics, this issue would not be of concern for the final microstructure control and prediction applications. Therefore, while the current infrared thermal camera has been accurately calibrated for temperature measurements of up to $2700\,°C$, note that all individual temperature measurements provided in the current research provide variations in the thermal signature signal rather than true temperatures of the process, which is still valid for microstructure control purposes.

In conclusion, a thermal monitoring system such as a thermal infrared camera can be used to extract the thermal information illustrated in Figure 3-8. The complete thermal pixel array information can then be inserted into the thermal dynamics algorithm shown in Figure 3-9 to obtain real-time peak temperature T_p^t, cooling rate $C_{f_i}^t$ and heating rate $H_{f_i}^t$. In order to obtain the main thermal dynamics

variables, including the calculation of the cooling rate and/or heating rate, these values may be obtained in real-time using a real-time thermal dynamics monitoring scheme shown schematically in Figure 3-10.
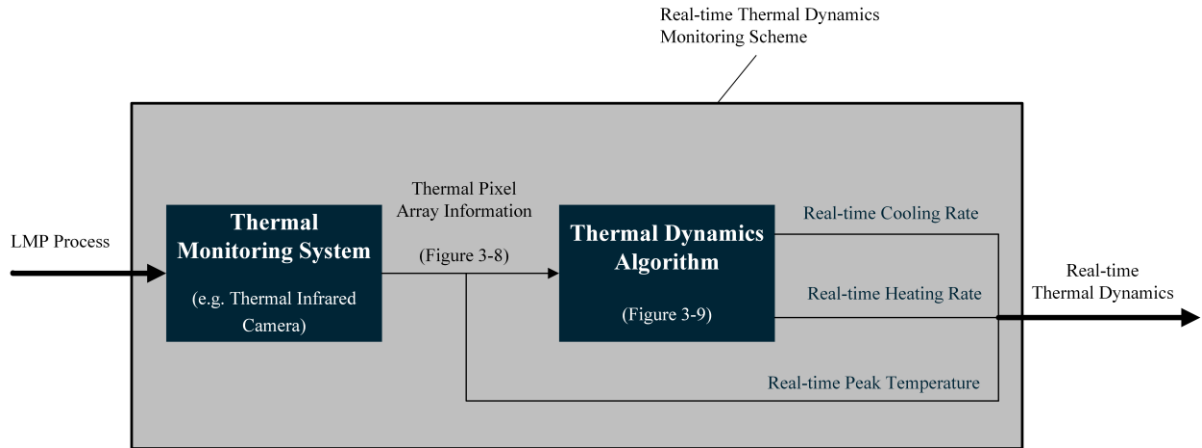
Figure 3-10 Block diagram of the thermal dynamics monitoring scheme.

3.2.2.3 Indirect Real-time Microstructure/Geometry Monitoring Scheme

As explained earlier, the goal of an automated LMP process, is to obtain consistent microstructure characteristics. Due to the harsh environment and rapid thermal cycles typically present during an LMP procedure, direct monitoring of microstructure properties during the process is difficult. As a result, conventional microstructure monitoring and analysis systems such as Scanning Electron Microscopy (SEM) machines, are either not suited for the LMP environment or very expensive. Moreover, some geometry properties of certain LMP processes such as the hardening depth during LHT process cannot be directly obtained by normal imaging. As a result, the real-time thermal dynamics monitoring scheme described above are utilized to "indirectly" predict microstructure properties and certain geometry values.

A breakdown of the indirect microstructure/geometry identification scheme is shown in Figure 3-11. Since both microstructure and geometry properties of the process are indirectly defined by the thermal dynamics, thermal models or look-up tables can be developed for microstructure and geometry prediction, which provide microstructure and geometry properties based on real-time thermal dynamics variations. When the thermal-microstructure model and thermal-geometry models or relations are developed, they can be integrated together to construct a combined microstructure/geometry model as shown in Figure 3-11. The thermal-microstructure and thermal-geometry models can be initially

49

developed using different methods including empirical, analytical and numerical methods. The general knowledge of thermal-microstructure and thermal-geometry relations for LMP procedures can be obtained through correlation of the real-time thermal dynamics variables with output properties. As an example, offline correlations between microstructure phase percentages, hardness or hardening depth and thermal dynamics recorded data can be used to develop the combined microstructure/geometry model based on the thermal dynamics variables. Another suggested method is to construct a process map for the model, relating the thermal dynamics variables to the microstructure/geometry. As an example, a microstructure map similar to continuous cooling transformation (CCT) and continuous heating transformation (CHT) diagrams can be developed offline where the different microstructure phases are predicted based on the cooling rate, heating rate and the peak temperature.
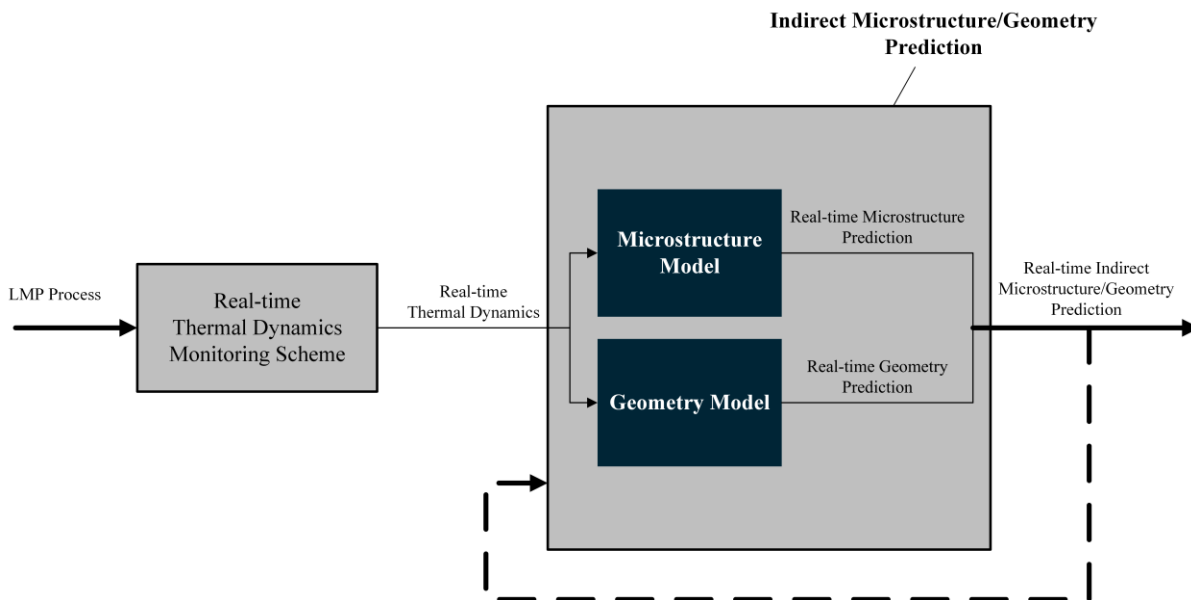
Figure 3-11 Indirect microstructure/geometry identification scheme.

As shown in Figure 3-11, integrating the real-time thermal dynamics monitoring scheme and microstructure/geometry models provides an indirect real-time microstructure/geometry prediction scheme for implementation in the closed-loop LMP process. According to this method, initially, the real-time thermal dynamics variables of the LMP process are recorded, or determined, by the real-time thermal dynamics monitoring scheme, and then fed into the microstructure/geometry model to obtain predictions of changes in the microstructure and geometry. Since the thermal dynamics variables are recorded in real-time, the outputs of the microstructure/geometry model provide real-time information of how the microstructure or geometry are evolving during the LMP process.

50

Finally, the microstructure/geometry model can be updated online with the real-time microstructure and geometry models data during the process (dotted feedback signal in Figure 3-11). An adaptive scheme is developed if the model is updated online. Therefore, a generalized real-time adaptive microstructure/geometry monitoring scheme for LMP processes can be achieved through the indirect thermal dynamics approach shown in Figure 3-11. This monitoring scheme will provide an understanding of how the microstructure and geometry of the materials of the LMP process are changing with the process inputs, during the process and in real-time.

3.2.3 MIMO Thermal and Geometry Controller System

The final subsystem of the developed thermal-geometry monitoring and control module is a real-time controller system. As described in the previous two sections, measurement of geometry and thermal dynamics characteristics such as the clad height, melt pool temperature, cooling rate and heating rate are obtained by using the CCD and thermal infrared cameras. These output parameters of the process govern the mechanical and material characteristics of the LMP product. The final piece in achieving a fully automated closed-loop LMP process is to include a real-time controller system for online adjustment of process variables based on these feedback signals. This controller will receive the thermal dynamics and geometry feedbacks from the CCD and thermal infrared cameras, and subsequently define the values of LMP process inputs to achieve the desired mechanical and material properties. Since two type of feedback signals are provided to the controller, the control system can be designed in the form of a Single-Input-Single-Output (SISO) or Multi-Input-Multi-Output (MIMO) control architecture.

3.3 Automated LMP Process

The developed thermal-geometry monitoring and control module can be integrated into any LMP process to develop a fully automated closed-loop system. A block diagram of the final closed-loop LMP process is illustrated in Figure 3-12. The three main components of the multi-objective thermal-geometry monitoring and control module are highlighted in light blue. In addition to the thermal and geometry monitoring systems, the closed-loop system includes the MIMO controller system to provide controlled microstructure and geometry.
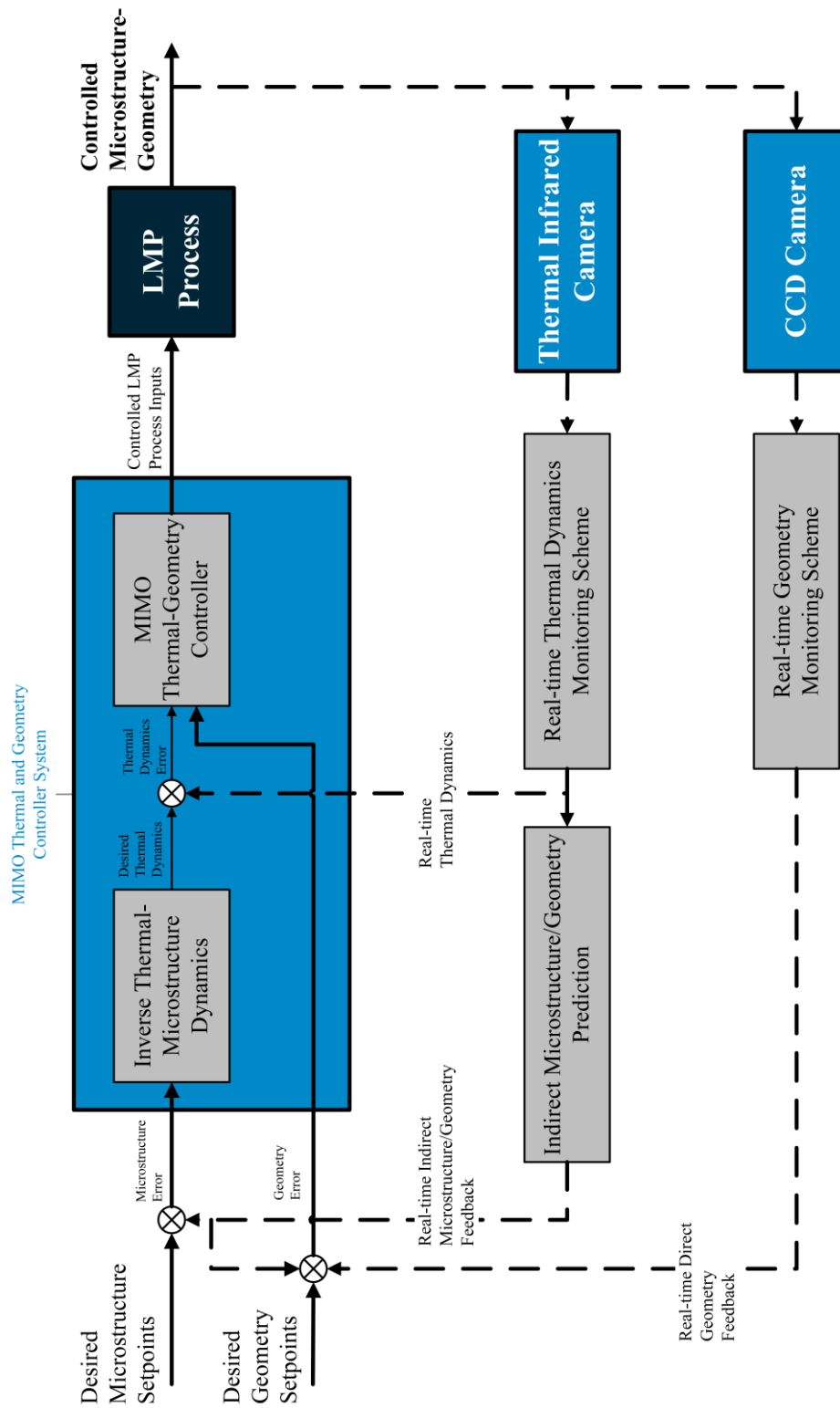
Figure 3-12 Schematic of the integrated closed-loop microstructure and geometry LMP process.

Each of the integrated hardware and software in the developed closed-loop system have a specific operating frequency. However, in order to ensure consistent closed-loop operation, all feedback (including image collection) and output control signals were collected and sent under the lowest available operating frequency, which was mainly governed by the program. The final closed-loop system operated at a frequency of about 10 Hz. Thus, real-time optical and thermal images were also collected at a frequency of 10 Hz, although they could provide a higher operational frequency.

Two feedback signals are obtained in the closed-loop LMP process. The first is provided by the "thermal infrared camera" and the second is obtained from the "CCD camera". The images captured by the CCD camera are directly fed into the "real-time geometry monitoring scheme" described in Section 3.2.1, to obtain the real-time values of the clad height. The thermal images however, are first fed into the "real-time thermal dynamics monitoring scheme" described in Section 3.2.2, to obtain the thermal dynamics. In order to convert the real-time thermal dynamics recordings into meaningful microstructure information, the indirect microstructure/geometry prediction approach discussed in Section 3.2.2.3 is used to provide real-time predictions of microstructure and certain geometry evolutions. The real-time microstructure predictions and geometry measurements are compared to a set of predefined desired properties, to understand the current process output deviation and error. To minimize this error, the "MIMO controller" block adjusts a set of process inputs such as the laser power or travelling speed, accordingly.

By utilizing only one of the feedback signals in this closed-loop LMP process, one can achieve single-input-single-output control of either microstructure or geometry properties. Activating both feedback signals, however, will result in an integrated multi-input-multi-output control of both the microstructure and geometry of the LMP process. Depending on the primary goal of the controlling scheme, any of the microstructure or geometry controllers can act as the primary controller and the other controller can be utilized as the secondary controlling method. When both controllers are needed, the two controllers may be integrated and activated simultaneously to control multiple microstructure and geometry properties at the same time.

3.4 Summary

This chapter summarized all of the experimental apparatus and algorithms required to construct an automated closed-loop LMP process. The development of a multi-objective thermal-geometry monitoring and control module was discussed in detail. The core elements of the module including the

geometry monitoring system, thermal monitoring system, and the MIMO controller were described. It was shown that geometry characteristics such as the clad height can be measured directly in rea-time using a CCD-based camera. Thermal image processing algorithms were developed to extract real-time feedback signals of the thermal dynamics including the cooling rate, peak temperature and heating rate. An indirect method for monitoring microstructure properties of the LMP process in real-time was also described. Finally, the development of an automated closed-loop LMP process was discussed, which will provide integrated microstructure and geometry control.

Chapter 4

Thermal Dynamics Modeling and

State Observer Feedback Control

The focus of this chapter is on the development of a novel thermal dynamics model and design of model-based control systems for the LMP thermal process. The chapter begins with finite difference modeling of the moving heat source problem, which can provide computationally fast solutions for real-time applications. The developed model identifies the temperature of each thermal pixel in the recorded thermal image. An optimal Linear Quadratic Tracking (LQT) control system is also designed based on the state space formulation of the thermal model to provide model-based feedback control of the peak temperature during the LMP process.

4.1 Thermal Modeling in LMP

In general, a model is a mathematical formulation of a physical phenomenon that provides predictions of future behavior based on current observed behavior of a process. Since LMP is a thermal process, thermal modeling has been used to better understand the LMP phenomena. Due to the absence of a comprehensive thermal monitoring system, it has been extremely difficult or impossible for researchers to visualize and understand important physical and thermal phenomena such as cooling rates, heating rates, or microstructure formation during experimental conditions. Consequently, thermal modeling and mathematical calculations have been the main route for better understanding of the LMP thermal process. Researchers have used different forms of mathematical formulations to extract theoretical thermal dynamics characteristics such as thermal gradients, cooling rates or solidification rates. Based on these calculations, they have responded to important questions such as why and how the microstructure has been formed or what has been the optimum operating range of parameters. Nonetheless, most of the developed thermal models have been lacking a fundamental criteria, which is experimental validation of modeling results. The lack of a proper thermal monitoring system has been a great obstacle in the verification process of different thermal models and the justification of their physical assumptions.

55

The development of the multi-objective thermal-geometry monitoring and control module enables us to provide an experimental benchmark for verification of any thermal model. Since the module is capable of extracting several important thermal dynamics features including the peak temperature, cooling rate and heating rate, it will be a reliable comprehensive source, for online or offline validation of thermal mathematical formulation.

4.2 Thermal Dynamics Control

A reliable thermal model will be highly valuable for the closed-loop automated LMP process, specifically during the design and tuning process of the MIMO controller shown in Figure 3-12. Controllers are designed and tuned in either two different methods:

4.2.1 Empirical Error-based Controllers

In the empirical error-based design, the controller is implemented and tuned during operation without the use of any theoretical or analytical justifications. These types of controllers control a process adequately without full information of the process characteristics or transfer functions. This is usually achieved by experimental tuning, which could be done manually or automatically by a tuning or optimization algorithm. While, most industrial controllers in the industry are designed and tuned using this method, the different types of empirical error-based controllers are very limited. The most well-known method amongst this group of controllers are Proportional-Integral-Derivative (PID) controllers. PID controllers are the most widely used controllers in the industry, mainly because of ease of use, which results in shorter implementation times.

Nonetheless, in a PID controller all three gains have to be tuned and balanced in order to impact the whole system, which may compromise the transient response, such as settling time, overshoots and transient oscillations. The tuning process is time consuming and experimentally expensive since it requires numerous experiments and testing conditions. More importantly, PID controllers are not robust enough for control of "black box" models with unknown system parameters and high levels of disturbance. This requires further tuning for each processing window and implementation of gain scheduling and look-up table techniques. Although, PID gains can be well-designed and tuned for a process, the PID controller is still less robust compared to robust model-based controllers when it comes to a highly sensitive LMP process under uncertainty and process disturbance.

4.2.2 Model-based Controllers

On the other hand, model-based controllers utilize mathematical and analytical methods to assist with the control of more complex dynamic systems. These types of controllers are highly dependent on a verified model for calculation and theoretical justifications. While, their design and implementation process is longer compared to error-based controllers, they can be extremely versatile and robust towards process disturbance, and can be designed and tuned during simulations rather than real testing conditions. These controllers are also broader in type and methods of implementation, which makes them more versatile towards different applications. Examples of model-based controllers include optimal control, Model Predictive Control (MPC), model identification adaptive control (MIAC), and model reference adaptive control (MRAC) techniques.

While, these techniques have several advantages compared to empirical error-based controllers, their performance is highly dependent upon the accuracy of the base model. Thus, to be capable of using model-based controllers in the closed-loop LMP process developed in the previous chapter, a reliable thermal model of the LMP process is required. The closed-loop LMP process can benefit from several advantages of a model-based controller if such a dynamic model is available. However, this thermal model should meet specific criteria in order to be useful for implementation inside the closed-loop LMP control process. The LMP thermal model should satisfy the following conditions:

- Represent a dynamic model

- Verifiable by the multi-objective thermal-geometry monitoring and control module

- Provide predictions of the measured thermal dynamics (melt pool temperature, cooling rate and heating rate).

The above criteria enable the correct use of the thermal model inside the closed-loop integrated microstructure and geometry control scheme. The first criterion enables the thermal model to be used by a model-based controller since controllers are only able to control dynamic models. This dynamic model should also be computationally fast in order to be applicable and responsive for real-time control purposes. The second criterion develops a highly reliable model through actual experimental verification, which will also enhance the performance of the controller and identification process. The third criterion enables the thermal model to be used for microstructure identification and control inside the developed closed-loop integrated microstructure and geometry control process.

In the case of using predictive control techniques, the derived microstructure/geometry model can be used as the reference model. The MIMO microstructure-geometry controller architecture can also have different architectures or combinations, including but not limited to, integration with a feedforward controller for eliminating the effect of disturbance. In the case of using feedforward control techniques, the thermal model can be used as the reference model for the feedforward controller.

In conclusion, development of a responsive dynamic thermal model, which can predict important thermal dynamics characteristics such as the peak temperature, cooling rate and heating rate is highly beneficial during the identification and control process of microstructure and geometry properties. In addition to all of the above advantages, a reliable verified model can significantly reduce the number of experiments required for identification and control purposes. Therefore, it is increasingly beneficial to have a reliable thermal model for the LMP process. The following section describes the novel development process of a dynamic thermal model, which can be implemented inside a closed-loop thermal process in real-time.

4.3 Dynamic Thermal Modelling of the LMP Process

Thermal modeling can be carried out in different forms and methods including empirical, analytical and/or numerical modeling. The correct choice of modeling technique is critically important in order to obtain a highly responsive and accurate controlled process. Meanwhile, empirical and analytical models are widely used in literature for design of LMP experiments or parametric offline control of the process, even though they do not provide a detailed understanding of the system physics. These are usually restricted to simple geometries and boundary conditions, and often require numerous simplifications. However, more often than not, the LMP thermal problem contains process and environmental complexities that exceed such circumstances. In these conditions, the better alternative are numerical models that provide a richer and more accurate understanding of complex thermal systems. Additionally, numerical models can be easily extended to two or three-dimensional problems. However, one has to be careful in choosing a numerical model for real-time control applications since these type of models usually come along with an extensive amount of computational time and complex mathematical formulations. In order to benefit from the accuracy of numerical modeling while remain computationally fast for control applications, a basic numerical technique is used to model the LMP process. The "finite difference method" is a basic numerical modeling technique that is easy to implement and requires less computational memory and time, compared to other numerical techniques

such as the finite element method. The following sections present the mathematical derivation of an adaptive dynamic finite difference model for the LMP process.

4.3.1 Moving Heat Source Problem

In the first step, a mathematical formulation of a moving laser heat source is developed under transient heating conditions. A schematic of the LMP heat transfer problem is shown in Figure 4-1, which illustrates the geometry and coordinates of a moving heat source. During the LMP process, the moving laser beam heats up the system with a volumetric heat distribution $q(x, y, z, t)$, with units of (W/m^3). The movement of the workpiece is in the positive x-direction with a constant travelling speed of v, which results in a transient (time-dependent) heat transfer problem.
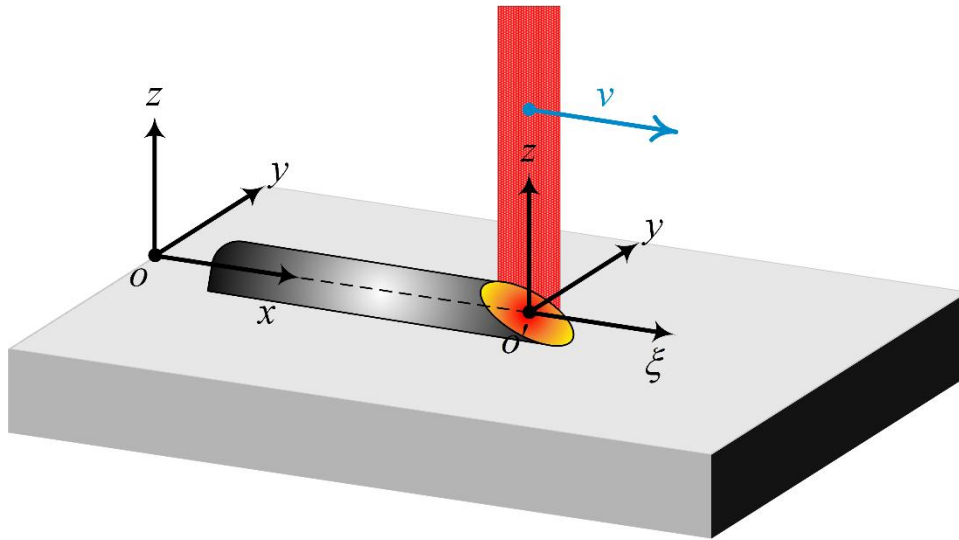
Figure 4-1 Schematic of the LMP moving heat source problem.

In Figure 4-1, the xyz coordinate system represents the global fixed coordinate system. The LMP thermal process involves all three forms of heat transfer including conduction, convection and radiation. However, since the conduction mode has the most significant role in altering the system's thermal dynamics, one only needs to consider the conduction mode of the LMP process. Assuming a homogenous material and consistent properties with time and temperature variations, the three-dimensional heat conduction equation in the fixed xyz coordinate system is taken as:

$$\frac{\partial^2 T}{\partial x^2} + \frac{\partial^2 T}{\partial y^2} + \frac{\partial^2 T}{\partial z^2} + \frac{1}{k} q(x, y, z, t) = \frac{1}{\alpha} \frac{\partial T}{\partial t} \tag{4.1}$$

in which $\alpha = \dfrac{k}{\rho c_p}$. In the above equation t is the respective time, $T(x, y, z, t)$ represents the temperature distribution on the surface, k is the thermal conductivity $(W/m.K)$, α is the thermal diffusivity (m^2/s), ρ is the density of the material (kg/m^3), and c_p is the specific heat of the material (J/kgK).

4.3.1.1 Transformation of the Origin

Since the thermal infrared camera of the multi-objective monitoring and control module is fixed with respect to the moving heat source, it is more convenient to have a moving coordinate system for the model, which moves with the heat source. This transformation will simplify the verification and calculation process of a moving heat source problem. The following transformation is achieved by introducing a new coordinate ξ defined by [101]:

$$\xi = x - vt \tag{4.2}$$

The moving coordinate system ξyz that moves with the heat source is illustrated in Figure 4-1. Using the chain rule of differential equations, the heat conduction equation Eq. (4.2), is transformed from the fixed coordinate system xyz with fixed origin O, to the moving coordinate system ξyz with a moving origin O'. By applying the chain rule, the transformed transient portion of the heat conduction equation becomes [101]:

$$\frac{1}{\alpha}\frac{\partial T(\xi, y, z, t)}{\partial t} = \frac{1}{\alpha}\left[\frac{\partial T}{\partial \xi}\frac{\partial \xi}{\partial t} + \frac{\partial T}{\partial y}\frac{\partial y}{\partial t} + \frac{\partial T}{\partial z}\frac{\partial z}{\partial t} + \frac{\partial T}{\partial t}\frac{\partial t}{\partial t}\right]. \tag{4.3}$$

Since $\dfrac{\partial T}{\partial y}\dfrac{\partial y}{\partial t} = \dfrac{\partial T}{\partial z}\dfrac{\partial z}{\partial t} = 0, \dfrac{\partial t}{\partial t} = 1$, and $\dfrac{\partial \xi}{\partial t} = -u$, the final form of the above equation becomes:

$$\frac{1}{\alpha}\frac{\partial T(\xi, y, z, t)}{\partial t} = \frac{1}{\alpha}\left[-u\frac{\partial T}{\partial \xi}\frac{\partial \xi}{\partial t} + \frac{\partial T}{\partial t}\right]. \tag{4.4}$$

The transformed first and second partial derivatives with respect to the x-direction are also defined by the chain rule as:

$$\frac{\partial T(\xi, y, z, t)}{\partial x} = \frac{\partial T}{\partial \xi}\frac{\partial \xi}{\partial x} + \frac{\partial T}{\partial y}\frac{\partial y}{\partial x} + \frac{\partial T}{\partial z}\frac{\partial z}{\partial x} + \frac{\partial T}{\partial t}\frac{dt}{dx} = \frac{\partial T}{\partial \xi} \tag{4.5}$$

$$\frac{\partial T^2(\xi, y, z, t)}{\partial x^2} = \frac{\partial^2 T}{\partial \xi^2} \tag{4.6}$$

in which it is assumed that $\frac{\partial y}{\partial x} = \frac{\partial z}{\partial x} = \frac{dt}{dx} = 0$. Substituting Eqs. (4.4) and (4.6) in the original heat conduction equation Eq. (4.1), the final transformed three-dimensional heat conduction equation in the moving coordinate system ξyz is given by [101]:

$$\frac{\partial^2 T}{\partial \xi^2} + \frac{\partial^2 T}{\partial y^2} + \frac{\partial^2 T}{\partial z^2} + \frac{1}{k} q(\xi, y, z, t) = \frac{1}{\alpha} \left[\frac{\partial T}{\partial t} - v \frac{\partial T}{\partial \xi} \right]. \tag{4.7}$$

4.3.1.2 Transformed Two-dimensional Heat Conduction Equation

Since the current model is developed for the purpose of real-time estimation and control, it needs to be computationally fast and highly responsive. Therefore, to reduce computational time, the three-dimensional heat conduction equation was reduced to a two-dimensional model in the xy-coordinate system, which is shown in Figure 4-2. In order to reduce the three-dimension model from the ξyz coordinate system to two-dimensional conditions in ξy coordinate system, the conduction rate is assumed for a unit depth along the z-direction, which results in the following two-dimensional nonlinear heat conduction equation:

$$\frac{\partial^2 T}{\partial \xi^2} + \frac{\partial^2 T}{\partial y^2} + \frac{1}{k} q(\xi, y, t) = \frac{1}{\alpha} \left[\frac{\partial T}{\partial t} - v \frac{\partial T}{\partial \xi} \right]. \tag{4.8}$$

4.3.2 Finite Difference Solution

Eq. (4.8) is a partial differential equation, which is usually solved analytically through rigorous mathematical calculations. However, analytical solution of the above equation does not always yield a closed-form exact solution and often results in a complex term in the form of parametric surface integration. Numerical calculation of the above equation is an alternative method of solving partial differential heat conduction equations, which simplifies the complex formulations and calculations, but demands greater computational memory and time. Consequently, one can use the finite difference numerical method to obtain the temperature distribution of the two-dimensional heat conduction equation.
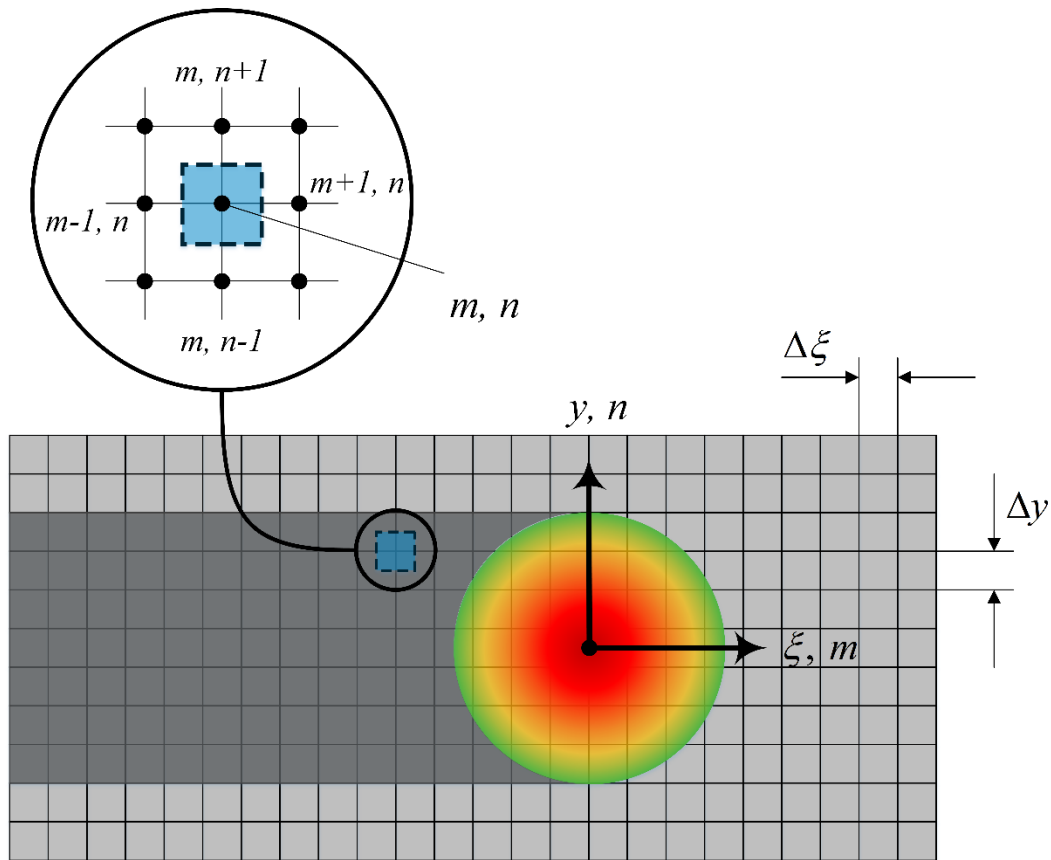
Figure 4-2 Schematic nodal network of the two-dimensional LMP heat conduction problem.

4.3.2.1 The Nodal Network

In contrast to analytical solutions, which determine the temperature at any continuous point in the medium, numerical techniques allow for temperature determination at only discrete points. The first step in any numerical analysis is to discretize the medium of interest into a number of small regions and assigning a reference point, which represents each region or element. The reference point is usually defined as a nodal point, and the collective points are identified as a nodal network, gird, or mesh. The nodal network of the two-dimensional LMP problem is illustrated in Figure 4-2. The ξ and y axes of the two-dimensional heat conduction problem are represented by the m and n indices in the new nodal network, respectively.

The nodal points are spaced at equal spacing of $\Delta\xi$ and Δy along the ξ and y directions, respectively. Each node of the nodal network represents a certain region, and its temperature is an average

representative measure of the region's temperature. As an example, the temperature of node $(m.n)$ which is denoted by $T_{m,n}$, represents the temperature of the shaded region in Figure 4-2.

4.3.2.2 Discretization of the Heat Equation

The next step in the finite difference formulation is the finite difference approximation or discretization of the heat conduction equation partial derivatives. Using the Taylor series expansion, the finite difference approximation of the first and second-order derivatives of a function $f(x)$ using the central-difference derivative are expressed as:

$$f_i' = \frac{f_{i-1} - f_{i+1}}{2h} + O(h^2) \tag{4.9}$$

$$f_i'' = \frac{f_{i-1} - 2f_i + f_{i+1}}{h^2} + O(h^2). \tag{4.10}$$

To obtain the finite difference form of the heat conduction equation, we will apply the above central-difference approximation to spatial derivatives prescribed by Eq. (4.8). Considering the enlarged detailed nodal structure in Figure 4-2, the discretized equations of space in the mn nodal network are given as follows:

$$\frac{\partial^2 T}{\partial \xi^2}\Big|_{m,n}^p = \frac{T_{m-1,n}^p - 2T_{m,n}^p + T_{m+1,n}^p}{(\Delta \xi)^2} \tag{4.11}$$

$$\frac{\partial^2 T}{\partial y^2}\Big|_{m,n}^p = \frac{T_{m,n-1}^p - 2T_{m,n}^p + T_{m,n+1}^p}{(\Delta y)^2} \tag{4.12}$$

$$\frac{\partial T}{\partial \xi}\Big|_{m,n}^p = \frac{T_{m+1,n}^p - T_{m-1,n}^p}{2\Delta \xi} \tag{4.13}$$

in which, the integer p denotes the current time instance at which the temperature distribution is discretized and is derived from:

$$t = p\Delta t. \tag{4.14}$$

In the above equation, t is the discretized time vector and Δt is the time interval between two successive time frames, which is also known as the "sampling time". Similar to being restricted to discrete spatial points, finite difference solutions are also restricted to discrete times. Therefore, finite difference calculations are performed at successive time frames t^p and t^{p+1}, separated by the time interval Δt.

In the finite difference approximation, the heat conduction problem must also be discretized in time in addition to being discretized in space. The nature of the finite difference solution depends on the

specific time frame at which the spatial derivative discretization is taken place. Since all of the spatial finite difference approximations are calculated at the current time frame (p), the finite difference approximation of the time derivative should also include the temperature of the current time frame. Consequently, the forward-difference approximation is used to discretize the first-order time derivate, which is given by:

$$f_i' = \frac{f_{i+1} - f_i}{h} + O(h) \tag{4.15}$$

Using the forward-difference approximation, the discretized form of the first-order time derivative in Eq. (4.8) is given as:

$$\frac{\partial T}{\partial t}\Big|_{m,n}^p = \frac{T_{m,n}^{p+1} - T_{m,n}^p}{\Delta t}. \tag{4.16}$$

In the above discretized formulations, the temperature of each node T, is identified with a subscript and superscript. The subscripts indicate the spatial location of the temperature node in the mn nodal network, while the superscript p is also used to express the time dependence of T. Accordingly, the time derivative is defined in terms of temperature difference between future $(p + 1)$ and current (p) time frames.

Substituting the discretized spatial and time partial derivatives prescribed by Eqs. (4.11)-(4.13) and Eq. (4.16), respectively, in the two-dimensional heat conduction equation Eq. (4.8), the initial form of the discretized heat conduction equation is obtained:

$$\frac{T_{m-1,n}^p - 2T_{m,n}^p + T_{m+1,n}^p}{(\Delta\xi)^2} + \frac{T_{m,n-1}^p - 2T_{m,n}^p + T_{m,n+1}^p}{(\Delta y)^2} + \frac{1}{k}q_{m,n}^p$$
$$= \frac{1}{\alpha}\left[\frac{T_{m,n}^{p+1} - T_{m,n}^p}{\Delta t} - v_{m,n}^p \frac{T_{m+1,n}^p - T_{m-1,n}^p}{2\Delta\xi}\right]. \tag{4.17}$$

Considering equal spacing between the nodal points along the m and n-directions of the nodal network $(\Delta\xi = \Delta y)$, the above formulation is simplified to:

$$(T_{m-1,n}^p - 2T_{m,n}^p + T_{m+1,n}^p) + (T_{m,n-1}^p - 2T_{m,n}^p + T_{m,n+1}^p) + \frac{(\Delta\xi)^2}{k}q_{m,n}^p$$
$$= \frac{(\Delta\xi)^2}{\alpha\Delta t}\left[(T_{m,n}^{p+1} - T_{m,n}^p) - \frac{\Delta t}{2\Delta\xi}(T_{m+1,n}^p - T_{m-1,n}^p)v_{m,n}^p\right]. \tag{4.18}$$

4.3.2.3 Nonlinear Finite Difference Heat Conduction Formulation

Solving for the unknown nodal temperature at the future time frame $(P + 1)$, and moving all of the known nodal temperatures at the current time frame (P), to the other side, the final finite difference approximation of the two-dimensional heat conduction problem is expressed in the following nonlinear form:

$$T_{n,m}^{p+1} = Fo[T_{n,m-1}^p + T_{n,m+1}^p + T_{n-1,m}^p + T_{n+1,m}^p] + (1 - 4Fo)T_{n,m}^p + K_1 q_{n,m}^p$$
$$+K_2[T_{n,m+1}^P - T_{n,m-1}^P]v^P$$

$$\begin{cases} K_1 = \dfrac{\alpha \Delta t}{k} \\ K_2 = \dfrac{\Delta t}{2\Delta \xi} \end{cases} \tag{4.19}$$

where Fo is also the finite-difference form of the Fourier number:

$$Fo = \frac{\alpha \Delta t}{(\Delta \xi)^2}. \tag{4.20}$$

The above formulation is the result of an explicit method of solution, since the unknown nodal temperatures of the future time frame $(p + 1)$, are entirely identified by the known nodal temperatures at current time frame (p). By having all of the initial nodal temperatures $(T_{n,m}^0)$ and process inputs $(q_{n,m}^0$ and $v^0)$ at the initial time $t = 0$ $(p = 0)$, the temperature calculations of the next time frame $(T_{n,m}^1)$, at time $t = \Delta t$ $(p = 1)$, are obtained by applying the two-dimensional finite difference heat conduction formulation Eq. (4.19), to each node. After the first iteration is carried out and the nodal temperatures are calculated for the first time frame $(T_{n,m}^1)$, the calculation of the next time frame at $(p = 2)$ is carried out by having the process inputs at the previous time $(q_{n,m}^1$ and $v^1)$. Similarly, the nodal temperatures at any desired time $t = p\Delta t$, are obtained by iteratively solving the finite difference heat conduction equation up to iteration p.

The accuracy of the finite difference solution depends on the size of $\Delta \xi$ and Δt. Smaller $\Delta \xi$ and Δt will result in a higher accuracy, while also increasing the required computational time and memory. The choice of $\Delta \xi$ is totally arbitrarily, however, since in the current research the model is verified and updated by comparison with measured thermal pixels of the infrared thermal camera, the size of $\Delta \xi$ should always be greater or equal to the size of each thermal pixel. For the sake of easier calculation and verification process, the size of $\Delta \xi$ is always chosen equal to the size of each thermal pixel.

Once $\Delta\xi$ is assigned, however, the size of Δt cannot be arbitrarily chosen and is instead, determined by stability criteria. One major drawback of numerical solutions and specifically the explicit methodology is that they are not always stable during the iteration calculations. In a transient heat transfer problem such as the LMP moving heat source equation, after a transition period, the nodal temperatures reach a final steady state solution. However, when using the explicit method, calculations may lead to numerically-induced oscillations, which might result in an unstable diverging solution. To prevent this instability, the size of Δt should be restricted to a minimum value. This stability criterion is determined by requiring that "*the coefficient associated with the node of interest at the current time is greater than or equal to zero*" [102]. This is done by collecting all terms involving $T_{n,m}^p$, and equaling them to zero. For the two-dimensional heat conduction equation Eq. (4.19), the stability criterion is satisfied by $(1 - 4Fo) \geq 0$, which results in:

$$Fo \leq \frac{1}{4}. \tag{4.21}$$

With predefined values of $\Delta\xi$ and α, the minimum value of Δt is determined from the stability criterion expressed in Eq. (4.21). Therefore, by defining the correct values of $\Delta\xi$ and Δt according to the stability criterion, one can obtain the final steady state solution of the two-dimensional heat conduction equation in an iterative manner.

4.3.3 Laser Heat Distribution

The finite difference heat conduction formulation expressed by Eq. (4.19), includes two processing input variables (v^p and $q_{n,m}^p$) that are required to be defined before each iteration of the solution. v^p is the profile of the CNC travelling speed, which is only a function of time and is defined by a single value at each time frame. On the other hand, the volumetric heat distribution $q_{n,m}^p$, is a function of both space and time. The volumetric heat distribution of a laser beam during an LMP process is often represented by a circular Gaussian distribution. Therefore, the spatial heat distribution of a laser beam in three-dimensions is expressed as:

$$q_{\xi,y} = \frac{A_{abs}P_{max}}{\pi r_B^2 \Delta z} \exp - \left(\frac{\xi^2 + y^2}{r_B^2} \right) \tag{4.22}$$

In which, P_{max} is the laser power, r_B is the laser beam radius and A_{abs} is the laser absorption coefficient. Eq. (4.22) represents the spatial profile of the volumetric heat distribution in the continuous two-dimensional coordinate system ξy, whereas the heat conduction equation Eq. (4.19), is defined in the

66

discrete mn nodal network. In order to discretize the volumetric heat distribution and transform the working space from the ξy coordinate to the mn nodal network, one has to calculate the total amount of volumetric heat for the region (or element) represented by each nodal point. Turning back to the magnified nodal network shown in Figure 4-2, this is achieved by integrating the continuous heat distribution profile Eq. (4.22), over the shaded region of each node, which is:

$$q_{n,m} = \frac{P_{max} \int_{\left(n\Delta y - \frac{\Delta y}{2}\right)}^{\left(n\Delta y + \frac{\Delta y}{2}\right)} \int_{\left(m\Delta\xi - \frac{\Delta\xi}{2}\right)}^{\left(m\Delta\xi + \frac{\Delta\xi}{2}\right)} \frac{A_{abs} \exp - \left(\frac{\xi^2 + y^2}{r_B^2}\right)}{\pi r_B^2 \Delta z} d\xi dy}{(\Delta y \Delta \xi)} \qquad \textbf{(4.23)}$$

Considering the analytical solution to the exponential integral, the above integration simplifies to the following:

$$q_{n,m}^p = \tilde{q}_{n,m} P_{max}^p . \qquad \textbf{(4.24)}$$

P_{max}^p is the laser power value at each time frame (p). For each nodal point (m, n) the constant spatial term $\tilde{q}_{n,m}$, is defined as:

$$\tilde{q}_{n,m}$$

$$= \frac{\left(\frac{A_{abs}}{4}\right) \left[\text{erf}\left(\frac{m\Delta\xi + \frac{\Delta\xi}{2}}{r_b}\right) - \text{erf}\left(\frac{m\Delta\xi - \frac{\Delta\xi}{2}}{r_b}\right) \right] \left[\text{erf}\left(\frac{n\Delta\xi + \frac{\Delta\xi}{2}}{r_b}\right) - \text{erf}\left(\frac{n\Delta\xi - \frac{\Delta\xi}{2}}{r_b}\right) \right]}{(\Delta\xi^2 \Delta z)} . \qquad \textbf{(4.25)}$$

Since the heat conduction of the two-dimensional problem is considered in a unit depth along the z-direction (described in Section 4.3.1.2), the volumetric heat distribution is also reduced to a surface heat flux with unit depth $(\Delta z = 1mm)$. In general, Eq. (4.19) is solved using the discrete Gaussian heat distribution expressed in Eq. (4.24) as the laser beam heat profile.

4.3.4 Linearization

The finite difference heat conduction equation Eq. (4.19), can be solved numerically in an iterative manner, nonetheless, since this equation consists of nonlinear terms $(K_2[T_{n,m+1}^p - T_{n,m-1}^p]v^p)$, it cannot be implemented in linear control structures. Moreover, linear calculation techniques cannot be used to solve this equation. Therefore, in order to simplify the calculation process and also extend the type of prescribed controllers, it is required to linearize the two-dimensional finite difference heat conduction equation around its' operating point.

Utilizing the Taylor series expansion, one can linearize a nonlinear discrete function in the form of $X^{p+1} = f(x_1^p, x_2^p, ..., x_i^p)$, around its' operating point $\bar{X} = f(\bar{x}_1, \bar{x}_2, ..., \bar{x}_i)$, using the following expression:

$$\Delta X^{p+1} = f(\bar{x}_1, \bar{x}_2, ..., \bar{x}_i) + (\frac{\partial f}{\partial x_1^p}|_{\substack{x_1^p=\bar{x}_1 \\ x_2^p=\bar{x}_2 \\ ... \\ x_i^p=\bar{x}_i}}) \Delta x_1^p + (\frac{\partial f}{\partial x_2^p}|_{\substack{x_1^p=\bar{x}_1 \\ x_2^p=\bar{x}_2 \\ ... \\ x_i^p=\bar{x}_i}}) \Delta x_2^p + \cdots$$

$$+ (\frac{\partial f}{\partial x_i^p}|_{\substack{x_1^p=\bar{x}_1 \\ x_2^p=\bar{x}_2 \\ ... \\ x_i^p=\bar{x}_i}}) \Delta x_i^p.$$

(4.26)

in which $(\Delta X^{p+1}, \Delta x_1^p, \Delta x_2^p, ..., \Delta x_i^p)$, are perturbation variables around the operating point, expressed as:

$$\begin{cases} \Delta X^{p+1} = X^{p+1} - \bar{X} \\ \Delta x_1^p = x_1^p - \bar{x}_1 \\ \Delta x_2^p = x_2^p - \bar{x}_2 \\ ... \\ \Delta x_i^p = x_i^p - \bar{x}_i \end{cases} .$$

(4.27)

Using the above linearization formulation for nodal temperatures of the nonlinear finite difference heat conduction equation Eq. (4.19), one will extract the linearized form of the two-dimensional heat conduction equation around the operating point as follows:

$$\Delta T_{n,m}^{p+1} = (Fo)\Delta T_{n-1,m}^p + (Fo - K_2\bar{v}^p)\Delta T_{n,m-1}^p + (1 - 4Fo)\Delta T_{n,m}^p +$$
$$(Fo + K_2\bar{v}^p)\Delta T_{n,m+1}^p + (Fo)\Delta T_{n+1,m}^p + (K_1\bar{q}_{n,m})\Delta P_{max}^p + [K_2(\bar{T}_{n,m+1}^p - \bar{T}_{n,m-1}^p)]\Delta v^p$$

(4.28)

in which the perturbation variables are defined by:

$$\begin{cases} \Delta T_{n,m}^{p+1} = T_{n,m}^{p+1} - \bar{T}_{n,m} \\ \Delta T_{n-1,m}^p = T_{n-1,m}^p - \bar{T}_{n-1,m} \\ \Delta T_{n,m-1}^p = T_{n,m-1}^p - \bar{T}_{n,m-1} \\ \Delta T_{n,m}^p = T_{n,m}^p - \bar{T}_{n,m} \\ \Delta T_{n,m+1}^p = T_{n,m+1}^p - \bar{T}_{n,m+1} \\ \Delta T_{n+1,m}^p = T_{n+1,m}^p - \bar{T}_{n+1,m} \\ \Delta P_{max}^p = P_{max}^p - \bar{P}_{max} \\ \Delta v^p = v^p - \bar{v} \end{cases} .$$

(4.29)

In the previous equations, $\bar{T}_{n,m}, \bar{T}_{n-1,m}, \bar{T}_{n,m-1}, \bar{T}_{n,m+1}, \bar{T}_{n+1,m}$ are known nodal temperatures at the operating point, and $\bar{P}_{n,m}$ and $\bar{v}$ are also the known laser power and travelling speed at the operating

68

point,   respectively.   Therefore,   by   defining   an   operating   point $OP(\bar{T}_{n,m}, \bar{T}_{n-1,m}, \bar{T}_{n,m-1}, \bar{T}_{n,m+1}, \bar{T}_{n+1,m}, \bar{P}_{max}, \bar{v})$, the linearized heat conduction problem is solved iteratively using Eqs. (4.28) and (4.29).

4.3.5 Restricted Nodal Network

Since the linearized model is to be implemented for control purposes, calculation time is a critical factor in the responsiveness and accuracy of the controller. Although, the linearized model denoted by Eq. (4.28) can provide computationally fast solutions at each iteration, it will be relatively slow for real-time control process if one wants to calculate the complete nodal network temperatures on the whole workpiece surface (measured duration of each iteration between $1 - 10\ s$). Moreover, the main goal of the thermal modeling is to predict the thermal behavior of the system in and around the melt pool area, whereas, conducting thermal calculations over the whole surface of the workpiece will result in calculation of nodal areas that are unnecessary and inessential.

An alternate method is to restrict the nodal network to a certain region of interest in and around the melt pool as shown in Figure 4-3. The region of interest is always chosen so that its centerline along the y-axis is always superimposed on the y-axis centerline of the melt pool region. This way, it is only necessary to calculate half of the nodes in any region of interest since the heat condition model is symmetric with respect to the ξ-axis. For example in Figure 4-3, the model nodes that require calculation are highlighted in black. Therefore, the complete heat conduction model is reduced to a restricted half nodal network of size M by N, which will result in savings in computational time and memory.
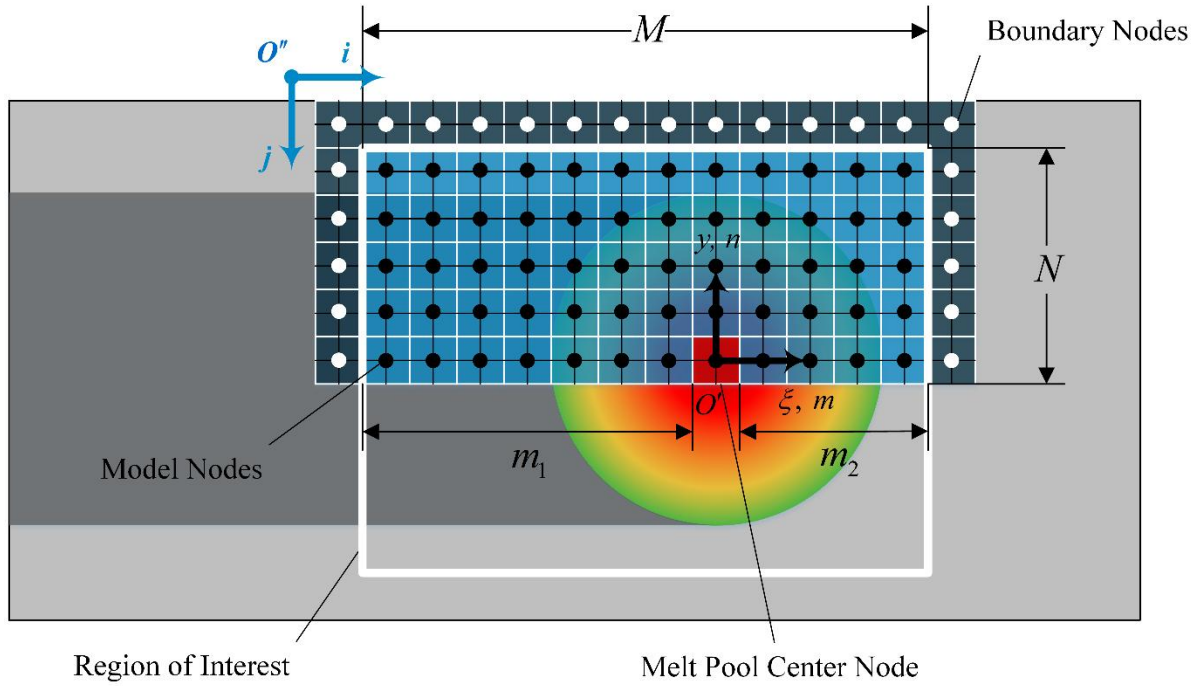
Figure 4-3 Restricted nodal network of the dynamic heat conduction model.

As shown in Figure 4-3, the original discrete mn coordinate system of Eqs. (4.19) and (4.28), has an origin O', located on the melt pool center node, which is not centric with respect to the nodal network of the region of interest. To simplify the calculation and implementation of the model in the restricted region of interest, it is more convenient to transform the coordinate system to a new ij coordinate system with an origin at O''. The relationship between the two coordinate systems is expressed as follows:

$$\begin{cases} i = m - (m_1 + 2) \\ j = (N + 1) - n \end{cases}.$$

(4.30)

in which, $M = m_1 + m_2 + 1$. The above coordinate transformation will be used for the final model calculations.

4.3.6 Adaptive Model

The current dynamic model is primarily used for online and offline identification and control of the LMP system. It is critically important for a dynamic model to precisely exemplify the dynamics and behavior of its represented system outputs with respect to time and process input variations. Thus, it is highly essential for the current thermal model to provide exact predictions of the LMP thermal

dynamics behavior. The developed model prescribed by Eqs. (4.19) and (4.28), delivers a correct dynamic representation of the LMP thermal system, since it considers the main mode of heat transfer during the LMP thermal cycle and it also formulates the fundamental thermal relations between the fine temperature nodes in the system. Nonetheless, due to the simplifying assumptions of the heat transfer problem, the model may contain errors in the final predicted values. These simplifying assumptions are described as follows:

- The current model only considers the main heat conduction mode of the heat transfer problem, whereas, during the LMP process, heat convection and radiation are also influential. For example, in the current modeling scheme, the effect of external cooling systems such as the shielding gas air supply, which introduces extra cooling through heat convection, has not been considered.

- The LMP process is a complex Multiphysics phenomena that contains other modes of mass and momentum transfer. These Multiphysics, introduce other phenomena such as the Marangoni heat flow that affect the final heat transfer and thermal dynamics values.

- The model assumes constant material and thermal properties such as material density, specific heat and thermal conductivity, whereas, these values change with respect to temperature and direction of heat transfer.

The above assumptions will introduce undesired deviations and errors into the nonlinear and linear models of Eqs. (4.19) and (4.28), which require to be addressed in the formulation process. In order to correct these final value errors while keeping the accurate dynamic representation, a modification is applied to the model material properties and the final reported temperatures.

4.3.6.1 Equivalent Thermal Conductivity

In Eqs. (4.19) and (4.28), the material density ρ, specific heat capacity c_p, and thermal conductivity k, are the three material properties affecting the predictions of the two-dimensional heat condition model. The material density is defined as the amount of mass contained in a unit volume. The specific heat capacity is described by the amount of heat required to increase the temperature of one kilogram of material by one degrees Kelvin. The thermal conductivity is also a material property describing the ability to conduct heat. Thermal conductivity can be defined as "the quantity of heat transmitted through a unit thickness of a material - in a direction normal to a surface of unit area - due to a unit temperature

gradient under steady state conditions" [102]. In general, the rate of heat transfer is higher in materials with higher thermal conductivity compared to materials with lower thermal conductivity.

In the current modelling solution, these material properties have been considered to be independent of any variables, whereas, in reality, they are dependent on the material temperature, direction of heat transfer and other environmental conditions. Variations in these parameters will affect the final model temperature matrix, however, it will not affect the overall dynamic behavior of the model. Therefore, a suitable method for overcoming the model errors is to tune (or adjust) one or more of the material properties, in order to compensate for the physical assumptions in the model. Such a tuning requires careful selection of the correct parameter, which can embody the thermal effects of the simplified assumptions in the model, through appropriate deviations from its original value.

Among the three material properties, the material density and specific heat capacity are more reliant on the type of material than the heat transfer conditions. Therefore, when the material of the LMP system remains unchanged, it is safe to consider a constant material density and specific heat capacity for the model. In addition, variations of these two parameters do not represent any significant physical meaning in terms of direct heat transfer modifications. Alternatively, the thermal conductivity is a parameter that is highly dependent on the temperature and heat transfer conditions of the medium. More importantly, by definition, variations in the thermal conductivity, indicate a direct change in the rate and amount of heat transfer. Therefore, one can replace the constant material thermal conductivity k, in Eqs. (4.19) and (4.28), with an adaptive equivalent thermal conductivity coefficient $\hat{k}_{eq}$, to include the effects of the simplifying assumptions in the final modified model. This term will be adaptively tuned in the model verification process to provide an accurate prediction of the system.

4.3.6.2 Temperature Bias

Although, the transformation of the original thermal conductivity value to an equivalent value does not affect the dynamics of Eq. (4.31) significantly, it will offset the final predicted temperature matrix by a constant amount. In order to cancel out the output offset caused by the equivalent thermal conductivity, an adaptive temperature bias term $\hat{T}_{bias}$, is introduced in the final model. The temperature bias, is a constant amount added to or subtracted from the final temperature matrix only at the end of each calculation iteration. To avoid altering the dynamic behavior of the current model, the temperature bias term $\hat{T}_{bias}$, is only implemented for the final reported temperature values, and it will not be affective in the model calculation process.

Considering the adaptive equivalent thermal conductivity coefficient described in Section 4.3.6.1 and the new coordinate system transformation denoted by Eq. (4.30), the final transformed two-dimensional "adaptive nonlinear" form of the heat conduction equation (Eq. (4.19)) is given by:

$$
\boxed{
\begin{aligned}
T_{j,i}^{p+1} = Fo\left[T_{j,i-1}^p + T_{j,i+1}^p + T_{j-1,i}^p + T_{j+1,i}^p\right] + (1 - 4Fo)T_{j,i}^p + \widehat{K}_{1_{eq}}q_{j,i}^p \\
+ K_2[T_{j,i+1}^p - T_{j,i-1}^p]v^p
\end{aligned}
}
$$

$$
\begin{cases}
\widehat{K}_{1_{eq}} = \dfrac{\hat{\alpha}_{eq}\Delta t}{\hat{k}_{eq}} \\
K_2 = \dfrac{\Delta t}{2\Delta\xi}
\end{cases}.
$$

(4.31)

For which the "modified nonlinear temperature matrix" is reported at the end of each iteration by:

$$
\left(T_{j,i}^p\right)_{modified} = T_{j,i}^p - \widehat{T}_{bias}.
$$

(4.32)

The final transformed two-dimensional "adaptive linearized" form of the heat conduction equation (Eq. (4.28)) close to the operating point $(\bar{T}_{j,i}, \bar{T}_{j-1,i}, \bar{T}_{j,i-1}, \bar{T}_{j,i+1}, \bar{T}_{j+1,i}, \bar{P}_{max}, \bar{v})$, is also given as:

$$
\boxed{
\begin{aligned}
\Delta T_{j,i}^{p+1} = (Fo)\Delta T_{j-1,i}^p + (Fo - K_2\bar{v}^p)\Delta T_{j,i-1}^p + (1 - 4Fo)\Delta T_{j,i}^p + \\
(Fo + K_2\bar{v}^p)\Delta T_{j,i+1}^p + (Fo)\Delta T_{j+1,i}^p + \left(\widehat{K}_{1_{eq}}\bar{q}_{j,i}\right)\Delta P_{max}^p + \left[K_2\left(\bar{T}_{j,i+1}^p - \bar{T}_{j,i-1}^p\right)\right]\Delta v^p
\end{aligned}
}
$$

$$
\begin{cases}
\widehat{K}_{1_{eq}} = \dfrac{\hat{\alpha}_{eq}\Delta t}{\hat{k}_{eq}} \\
K_2 = \dfrac{\Delta t}{2\Delta\xi}
\end{cases}
$$

(4.33)

in which the perturbation variables are defined by:

$$
\begin{cases}
\Delta T_{j,i}^{p+1} = T_{j,i}^{p+1} - \bar{T}_{j,i} \\
\Delta T_{j-1,i}^p = T_{j-1,i}^p - \bar{T}_{j-1,i} \\
\Delta T_{j,i-1}^p = T_{j,i-1}^p - \bar{T}_{j,i-1} \\
\Delta T_{j,i}^p = T_{j,i}^p - \bar{T}_{j,i} \\
\Delta T_{j,i+1}^p = T_{j,i+1}^p - \bar{T}_{j,i+1} \\
\Delta T_{j+1,i}^p = T_{j+1,i}^p - \bar{T}_{j+1,i} \\
\Delta P_{max}^p = P_{max}^p - \bar{P}_{max} \\
\Delta v^P = v^P - \bar{v}
\end{cases}.
$$

(4.34)

For which the "modified linearized temperature matrix" is reported at the end of each iteration by:

$$\left(\Delta T_{j,i}^{p}\right)_{modified} = \Delta T_{j,i}^{p} - \hat{T}_{bias}. \tag{4.35}$$

Finally, the profile of the volumetric heat distribution in the new coordinate system is also given by:

$$q_{j,i}^{p} = \tilde{q}_{j,i} P_{max}^{p} . \tag{4.36}$$

For each nodal point (i,j), the constant spatial term $\tilde{q}_{j,i}$, is defined as:

$$\tilde{q}_{j,i} = \frac{\left(\frac{A_{abs}}{4}\right)\left[\text{erf}\left(\frac{[(i-m1)-\frac{3}{2}]\Delta\xi}{r_b}\right) - \text{erf}\left(\frac{[(i-m1)-\frac{5}{2}]\Delta\xi}{r_b}\right)\right]}{(\Delta\xi^2\Delta z)} \tag{4.37}$$
$$\times\left[\text{erf}\left(\frac{[(N-j)+\frac{3}{2}]\Delta\xi}{r_b}\right) - \text{erf}\left(\frac{[(N-j)+\frac{1}{2}]\Delta\xi}{r_b}\right)\right].$$

in which the volumetric heat distribution is also assumed to be in unit depth ($\Delta z = 1mm$). It is noteworthy to point that both of the two-dimensional linearized finite difference equations are dynamic models, since in these equations, the behavior of the system is described over time.

4.3.7 Boundary and Initial Conditions

To determine the nodal temperatures of the workpiece (or additive material) at each iteration, it is necessary to solve the appropriate nonlinear or linearized form of the finite difference heat conduction equation expressed by Eqs. (4.31) and (4.33). The initial iteration at time $t = 0$ ($p = 0$), depends on the conditions existing in the workpiece at the initial time. The initial temperatures of the nodal network $T_{j,i}^{0}$, is known and assumed to be equal to room temperature. Additionally, the solution at each iteration also depends on the physical and thermal conditions existing at the boundaries of the region of interest represented by $T_{j_{BC},i_{BC}}^{p}$ for which the boundary nodes (i_{BC}, j_{BC}), are defined in $\left(i = 1, 1 \le j \le (N+1)\right)$, $\left(i = (M+2), 1 \le j \le (N+1)\right)$ and $(1 \le i \le (M+2), j = 1)$. The boundary nodes are highlighted in black in Figure 4-3. One can obtain the temperature of these boundary nodes in real-time from the thermal images of the thermal infrared camera.

For comparison reasons we will be using three type of Boundary Conditions (BCs) for Eqs. (4.31) and (4.33):

- **Real-time adaptive boundary conditions:** at every time frame, the location of the boundary nodes are identified in the thermal image and the measured temperatures $\bar{T}_{j_{BC},i_{BC}}^{p}$, are updated

74

for implementation in each iteration. For each iteration calculation, the nodal BC temperatures of the model are updated in real-time, so that $T_{j_{BC},i_{BC}}^p = \bar{T}_{j_{BC},i_{BC}}^p$.

- **Fixed adaptive boundary conditions:** at a specific time frame $t = t_{BC}$ ($p = p_{BC}$), the location of the boundary nodes are identified in the thermal image and the measured temperatures $\bar{T}_{j_{BC},i_{BC}}^{p_{BC}}$, are fixed for implementation in every iteration. For each iteration calculation, the nodal BC temperatures of the model are fixed (in time) to the measured temperature profiles so that $T_{j_{BC},i_{BC}}^p = \bar{T}_{j_{BC},i_{BC}}^{p_{BC}}$.

- **Fixed constant boundary conditions:** For each iteration calculation, all of the nodal BC temperatures of the model are fixed to a constant temperature value $\bar{T}_{BC}$, so that $T_{j_{BC},i_{BC}}^p = \bar{T}_{BC}$.

The real-time adaptive BC is the most accurate of the above BC types, whereas, the fixed constant BC provides the fastest calculation time. The fixed adaptive BC is also a mixture of the other two BC types, which can deliver a reasonable degree of accuracy along with a fast calculation time. The above boundary condition types will be used for temperature calculations in order to evaluate the optimum option.

4.3.8 State Space Formulation

Since the linearized dynamic model (Eq. (4.33)) is going to be implemented in a linear model-based control architecture, it is necessary to re-arrange the numerical formulation into the below dynamic state space formulation:

$$\begin{cases} \Delta \mathbf{x}(p+1) = \mathbf{A}\Delta \mathbf{x}(p) + \mathbf{B}\Delta \mathbf{u}(p) \\ \Delta \mathbf{y}(p) = \mathbf{C}\Delta \mathbf{x}(p) + \mathbf{D}\Delta \mathbf{u}(p) \end{cases} \tag{4.38}$$

where $p = p_0, p_1, \ldots, p_f - 1$, $\Delta \mathbf{x}(p)$ is $(N \times M)^{th}$ order state vector, $\Delta \mathbf{u}(p)$ is 2nd order control vector, $\Delta \mathbf{y}(p)$ is r^{th} order output vector, and $\mathbf{A}$ is $(N \times M) \times (N \times M)$ state, $\mathbf{B}$ is $(N \times M) \times 2$ input, $\mathbf{C}$ is $r \times (N \times M)$ output, and $\mathbf{D}$ is $r \times 2$ transfer matrices. In the developed linearized dynamic model (Eq. (4.33)), the states are the nodal temperatures $\Delta T_{j,i}$, which are represented by a two-dimensional $(N \times M)$ state matrix denoted by:

$$\Delta \mathbf{T}^P = \begin{bmatrix} \Delta T_{2,2}^p & \cdots & \Delta T_{2,M+1}^p \\ \vdots & \ddots & \vdots \\ \Delta T_{N+1,2}^p & \cdots & \Delta T_{N+1,M+1}^p \end{bmatrix}. \tag{4.39}$$

In order to transform the above two-dimension state matrix $\Delta \mathbf{T}^P$ to the one-dimensional state vector $\Delta \mathbf{x}(p)$, we will use the following mapping:

$$\begin{cases} \Delta T_{j,i}^p \rightarrow \Delta x_h(p) \\ h = M(j-1) + (i-1) - M \end{cases}. \tag{4.40}$$

in which $j = 2, \dots, N$ and $i = 2, \dots, M$. The above mapping will result in the following temperature state vector:

$$\Delta \mathbf{x}(p) = \begin{pmatrix} \Delta x_1(p) \\ \Delta x_2(p) \\ \vdots \\ \Delta x_{N\times M}(p) \end{pmatrix} = \begin{pmatrix} x_1(p) - \bar{x}_1 \\ x_2(p) - \bar{x}_2 \\ \vdots \\ x_{N\times M}(p) - \bar{x}_{N\times M} \end{pmatrix} = \begin{pmatrix} \Delta T_{2,2}^p \\ \Delta T_{2,3}^p \\ \vdots \\ \Delta T_{N+1,M+1}^p \end{pmatrix}. \tag{4.41}$$

where the states of the operating point $(\bar{x}_1, \bar{x}_2, \dots, \bar{x}_{N\times M})$ are defined by:

$$\begin{pmatrix} \bar{x}_1 \\ \bar{x}_2 \\ \vdots \\ \bar{x}_{N\times M} \end{pmatrix} = \begin{pmatrix} \bar{T}_{2,2} \\ \bar{T}_{2,3} \\ \vdots \\ \bar{T}_{N+1,M+1} \end{pmatrix}. \tag{4.42}$$

The state space control vector is also expressed as:

$$\Delta \mathbf{u}(p) = \begin{pmatrix} \Delta v^p \\ \Delta P_{max}^p \end{pmatrix}. \tag{4.43}$$

Input and control matrices $\mathbf{A}$ and $\mathbf{B}$, are obtained by substituting the coefficients of the state and control vector elements $((\Delta T_{2,2}^p, \Delta T_{2,3}^p, \dots, \Delta T_{N+1,M+1}^p)$ and $(\Delta v^p, \Delta P_{max}^p))$, from the original two-dimensional linearized heat conduction formulation (Eq. (4.33)) into the stat space formulation Eq. (4.38). Finally, the output vector $\Delta \mathbf{y}(p)$, output matrix $\mathbf{C}$, and transfer matrix $\mathbf{D}$ are prescribed by the total number of outputs required, which is defined arbitrarily according to the application. The current state space formulation of the linearized dynamic heat conduction model will be implemented inside the model-based controller architecture for thermal dynamics control.

4.3.9 Summary of the Dynamic Finite Difference Modeling

In conclusion, a novel adaptive dynamic model of the two-dimensional heat conduction problem with a moving heat source was obtained by Eq. (4.31). While, this model can provide nodal temperatures on the workpiece over time, it is nonlinear and cannot be conveniently implemented in linear model-based control techniques. As a result, the nonlinear model was linearized around an operating point, which yielded a linearized adaptive dynamic model prescribed by Eq. (4.33). The developed dynamic model

satisfies all of the three required conditions prescribed in Section 4.2, and can therefore be utilized for model-based thermal dynamics control and identification. For this purpose, the linear dynamic model was re-arranged into a standard stat space formulation using Eqs. (4.38) and (4.40)-(4.43), for implementation inside a control system.

It is important to note that both of the nonlinear and linear models can provide the similar pixel by pixel thermal information as the ones measured by the thermal infrared camera in each sample time. One can use the exact same procedure prescribed in Section 3.2.2.1, to obtain the three main thermal dynamics; melt pool temperature, cooling rate, and heating rate, from the model nodal temperatures. By obtaining the predictions of thermal dynamics from the finite difference models, one can easily tune and verify the accuracy of the developed model.

4.3.9.1 Thermal Model Validation Process

As described in Sections 4.3.6.1 and 4.3.6.2, the equivalent thermal conductivity $\hat{k}_{eq}$, and temperature bias $\hat{T}_{bias}$, are the two adaptive coefficients that need to be tuned in the model. An adaptive tuning scheme was developed for correct tuning of these two adaptive parameters. The tuning process is carried out offline according to the following schema:

- **STEP 1:** Collection of a set of tuning data through real-time excitation of the LMP system. The thermal infrared camera can be used to collect the real-time thermal dynamics of the excited system.

- **STEP 2:** Tuning of the equivalent thermal conductivity coefficient $\hat{k}_{eq}$, for minimizing the cooling rate error of Eqs. (4.31) and Eq. (4.33), with respect to the tuning data. Since the thermal conductivity constant represents the rate of heat transfer, it is more convenient to tune this parameter with respect to the cooling rate dynamics.

- **STEP 3:** Tuning of the temperature bias coefficient $\hat{T}_{bias}$, for minimizing the melt pool temperature (peak temperature) error of Eqs. (4.31) and Eq. (4.33), with respect to the measured dynamic data. The temperature bias is a constant amount added to or subtracted from the temperature output of the model. Thus, by adjusting this term one can cancel out the offset error of the melt pool temperature and all other nodal temperatures, at the same time, not influencing the cooling and heating rate values.

77

4.4 Thermal dynamics Linear Quadratic Tracking Controller

In this section, the design of an optimal model-based controller is described in order to control the melt pool temperature (or peak temperature) of the LMP process in real-time. The main objective of an optimal control structure is to determine control signals that will drive a system (or plant) from initial state to final state and at the same time extremizing (maximize or minimize) a performance criterion [103].

Let us consider the linear, time invariant thermal dynamics model described by the state space formulation in Eq. (4.38). Assigning the transfer matrix D to zero, the state and output vectors to be controlled are defined by:

$$\begin{cases} \Delta\mathbf{x}(p+1) = \mathbf{A}\Delta\mathbf{x}(p) + \mathbf{B}\Delta\mathbf{u}(p) \\ \qquad\quad \Delta\mathbf{y}(p) = \mathbf{C}\Delta\mathbf{x}(p) \end{cases}. \tag{4.44}$$

The performance index to be minimized is given as:

$$J = \frac{1}{2}\big[\mathbf{C}\Delta\mathbf{x}\big(p_f\big) - \Delta\mathbf{z}\big(p_f\big)\big]'\mathbf{F}\big[\mathbf{C}\Delta\mathbf{x}\big(p_f\big) - \Delta\mathbf{z}\big(p_f\big)\big]$$

$$+ \frac{1}{2}\sum_{p=p_0}^{p_f-1} \left\{ \begin{array}{c} [\mathbf{C}\Delta\mathbf{x}(p) - \Delta\mathbf{z}(p)]'\mathbf{Q}[\mathbf{C}\Delta\mathbf{x}(p) - \Delta\mathbf{z}(p)] + \Delta\mathbf{u}'(p)\mathbf{R}\mathbf{u}(p) + \\ [\Delta\mathbf{u}(p) - \Delta\mathbf{u}(p-1)]'\mathbf{S}[\Delta\mathbf{u}(p) - \Delta\mathbf{u}(p-1)] \end{array} \right\}. \tag{4.45}$$

where one can assume that $\mathbf{F}$ and $\mathbf{Q}$ are $(N \times M) \times (N \times M)$ dimensional positive semidefinite symmetric matrices, and $\mathbf{R}$ and $\mathbf{S}$ are 2×2 positive definite symmetric matrices. The initial state condition is given as $\Delta\mathbf{x}(p_0)$, while the final state condition $\Delta\mathbf{x}(p_f)$ is arbitrarily chosen with p_f fixed. Our goal is to minimize the error $\Delta\mathbf{e}(p) = \Delta\mathbf{y}(k) - \Delta\mathbf{z}(k)$ with a minimum control effort $\Delta\mathbf{u}(p)$ and minimum control action variation $\Delta\mathbf{u}(p) - \Delta\mathbf{u}(p-1)$. The methodology to obtain the solution of the optimal tracking controller is carried out using the following steps.

4.4.1 Formulating the Hamiltonian

The Hamiltonian is formulated as follows:

$$H\big(\Delta\mathbf{x}(p), \Delta\mathbf{u}(p), \boldsymbol{\lambda}(p+1)\big) =$$

$$\frac{1}{2}\sum_{p=p_0}^{p_f-1} \left\{ \begin{array}{c} [\mathbf{C}\Delta\mathbf{x}(p) - \Delta\mathbf{z}(p)]'\mathbf{Q}[\mathbf{C}\Delta\mathbf{x}(p) - \Delta\mathbf{z}(p)] + \Delta\mathbf{u}'(p)\mathbf{R}\mathbf{u}(p) + \\ [\Delta\mathbf{u}(p) - \Delta\mathbf{u}(p-1)]'\mathbf{S}[\Delta\mathbf{u}(p) - \Delta\mathbf{u}(p-1)] + \boldsymbol{\lambda}'(p+1)[\mathbf{A}\Delta\mathbf{x}(p) + \mathbf{B}\Delta\mathbf{u}(p)] \end{array} \right\}. \tag{4.46}$$

in which $\boldsymbol{\lambda}(p)$ is the $(N \times M)^{th}$ order co-state vector.

78

4.4.2 Deriving the state and co-state systems

In terms of the Hamiltonian, the required conditions of the control, co-state and state vectors for an extremum are also given as [103]:

$$\frac{\partial H}{\partial \Delta \mathbf{u}^*(p)} = 0 \tag{4.47}$$

$$\frac{\partial H}{\partial \Delta \mathbf{x}^*(p)} = \boldsymbol{\lambda}^*(p) \tag{4.48}$$

$$\frac{\partial H}{\partial \boldsymbol{\lambda}^*(p+1)} = \Delta \mathbf{x}^*(p+1) \tag{4.49}$$

where $\Delta \mathbf{x}^*(p), \Delta \mathbf{u}^*(p)$ and $\boldsymbol{\lambda}^*(p)$ are the optimal state, control and co-state. Consequently, one obtains the optimal control from Eq. (4.47) as:

$$\Delta \mathbf{u}^*(p) = [\mathbf{R} + \mathbf{S}]^{-1}[\mathbf{S}\Delta \mathbf{u}(p-1) - \mathbf{B}'\boldsymbol{\lambda}^*(p+1)] \tag{4.50}$$

the optimal state from Eq. (4.48) as:

$$\Delta \mathbf{x}^*(p+1) = \mathbf{A}\Delta \mathbf{x}^*(p) + \mathbf{B}\Delta \mathbf{u}^*(p) \tag{4.51}$$

and the optimal co-state from Eq. (4.49) as:

$$\boldsymbol{\lambda}^*(p) = \mathbf{C}'\mathbf{Q}\mathbf{C}\Delta \mathbf{x}^*(p) - \mathbf{C}'\mathbf{Q}\Delta \mathbf{z}(p) + \mathbf{A}'\boldsymbol{\lambda}(p+1). \tag{4.52}$$

The initial condition of the state vector is $\Delta \mathbf{x}(p_0) = \Delta \mathbf{x}_0$, and the final condition of the co-state vector for the case of a free-final point system with fixed final time is obtained from the following boundary condition [103]:

$$\boldsymbol{\lambda}(p_f) = \frac{\partial \left[\frac{1}{2}[\mathbf{C}\Delta \mathbf{x}(p_f) - \Delta \mathbf{z}(p_f)]'\mathbf{F}[\mathbf{C}\Delta \mathbf{x}(p_f) - \Delta \mathbf{z}(p_f)]\right]}{\partial \Delta \mathbf{x}(p_f)}. \tag{4.53}$$

which gives:

$$\boldsymbol{\lambda}(p_f) = \mathbf{C}'\mathbf{F}\mathbf{C}\Delta \mathbf{x}(p_f) - \mathbf{C}'\mathbf{F}\Delta \mathbf{z}(p_f). \tag{4.54}$$

4.4.3 Deriving the Riccati and Vector Equations

From the nature of the co-state final condition given by Eq. (4.54), one may assume the following transformation:

$$\boldsymbol{\lambda}^*(p) = \mathbf{G}(k)\Delta\mathbf{x}^*(p) - \mathbf{g}(p) \tag{4.55}$$

where, $\mathbf{G}(k)$ is the $(N \times M) \times (N \times M)$ dimension Riccati matrix, and $\mathbf{g}(p)$ is an $(N \times M) \times 2$ dimension matrix that are required to be determined. In order to do so one can eliminate the optimal co-state from Eq. (4.51) by replacing $\Delta\mathbf{u}^*(p)$ in Eq. (4.51) with the optimal control equation Eq. (4.50), and then replacing $\boldsymbol{\lambda}^*(p)$ with the above transformation Eq. (4.55), which results in:

$$\Delta\mathbf{x}^*(p + 1) = [I + \bar{\mathbf{E}}\mathbf{G}(p + 1)]^{-1}[\mathbf{A}\Delta\mathbf{x}^*(p) + \bar{\mathbf{E}}\mathbf{g}(p + 1) + \bar{\mathbf{S}}\Delta\mathbf{u}(p - 1)] \tag{4.56}$$

where $\bar{\mathbf{S}} = \mathbf{B}\mathbf{R}_s^{-1}\mathbf{S}$, $\bar{\mathbf{E}} = \mathbf{B}\mathbf{R}_s^{-1}\mathbf{B}'$ and $\mathbf{R}_s = [\mathbf{R} + \mathbf{S}]$.

The next step is to use Eqs. (4.55) and (4.56) in the co-state relation Eq. (4.52) that yields the following:

$$\{-\mathbf{G}(p) + \mathbf{V} + \mathbf{A}'\mathbf{G}(p + 1)[\mathbf{I} + \bar{\mathbf{E}}\mathbf{G}(p + 1)]^{-1}\mathbf{A}\}\Delta\mathbf{x}^*(p)$$
$$+ \{\mathbf{A}'\mathbf{G}(p + 1)[\mathbf{I} + \bar{\mathbf{E}}\mathbf{G}(p + 1)]^{-1}[\bar{\mathbf{E}}\mathbf{g}(p + 1) + \bar{\mathbf{S}}\Delta\mathbf{u}(p - 1)] + \mathbf{g}(p) \tag{4.57}$$
$$- \mathbf{A}'\mathbf{g}(p + 1) - \mathbf{W}\Delta\mathbf{z}(p)\} = 0$$

in which $\mathbf{V} = \mathbf{C}'\mathbf{Q}\mathbf{C}$ and $\mathbf{W} = \mathbf{C}'\mathbf{Q}$.

The previous equation must be true for all values of $\Delta\mathbf{x}^*(p)$, which means that the coefficients of $\Delta\mathbf{x}^*(p)$ and $\Delta\mathbf{u}^*(p)$ must both equal to zero. By equating the coefficient of $\Delta\mathbf{x}^*(p)$ to zero, we obtain:

$$\mathbf{G}(p) = \mathbf{A}'\mathbf{G}(p + 1)[\mathbf{I} + \bar{\mathbf{E}}\mathbf{G}(p + 1)]^{-1}\mathbf{A} + \mathbf{V} \tag{4.58}$$

or:

$$\mathbf{G}(p) = \mathbf{A}'[\mathbf{G}^{-1}(p + 1) + \bar{\mathbf{E}}]^{-1}\mathbf{A} + \mathbf{V} \tag{4.59}$$

which is called the nonlinear, matrix difference Riccati equation. Equating the coefficient of $\Delta\mathbf{u}^*(p)$ to zero also results in:

$$\mathbf{g}(p) = \{\mathbf{A}' - \mathbf{A}'\mathbf{G}(p + 1)[\mathbf{I} + \bar{\mathbf{E}}\mathbf{G}(p + 1)]^{-1}\bar{\mathbf{E}}\}\mathbf{g}(k + 1)$$
$$- \{\mathbf{A}'\mathbf{G}(p + 1)[\mathbf{I} + \bar{\mathbf{E}}\mathbf{G}(p + 1)]^{-1}\bar{\mathbf{S}}\Delta\mathbf{u}(p - 1)\} + \mathbf{W}\Delta\mathbf{z}(p) \tag{4.60}$$

or

$$\mathbf{g}(p) = \{\mathbf{A}' - \mathbf{A}'\mathbf{G}\mathbf{A}'[\mathbf{G}^{-1}(p + 1) + \bar{\mathbf{E}}]^{-1}\bar{\mathbf{E}}\}\mathbf{g}(k + 1)$$
$$- \{\mathbf{A}'[\mathbf{G}^{-1}(p + 1) + \bar{\mathbf{E}}]^{-1}\bar{\mathbf{S}}\Delta\mathbf{u}(p - 1)\} + \mathbf{W}\Delta\mathbf{z}(p) \tag{4.61}$$

which are called the linear, vector difference equation.

The boundary conditions of the above two equations are obtained by comparing Eqs. (4.54) and (4.55), which gives:

$$G(p_f) = \mathbf{C'FC} \tag{4.62}$$

$$\mathbf{g}(p_f) = \mathbf{C'F}\Delta\mathbf{z}(p_f). \tag{4.63}$$

Using the above final conditions, we can solve both of the matrix difference Riccati and vector difference equations in a backwards scheme.

4.4.4 Closed-loop Optimal Control Law

By substituting the transformation of Eq. (4.55) into the optimal control equation Eq. (4.50), one will obtain the following:

$$\Delta\mathbf{u}^*(p) = \mathbf{R}_s^{-1}\big[\mathbf{S}\Delta\mathbf{u}(p-1) - \mathbf{B'}[\mathbf{G}(k+1)\Delta\mathbf{x}^*(p+1) - \mathbf{g}(p+1)]\big] \tag{4.64}$$

and substituting the state form prescribed by Eq. (4.51) in the above equation yields:

$$\Delta\mathbf{u}^*(p) =$$
$$\mathbf{R}_s^{-1}\mathbf{S}\Delta\mathbf{u}(p-1) - \mathbf{R}_s^{-1}\mathbf{B'G}(p+1)[\mathbf{A}\Delta\mathbf{x}^*(p) + \mathbf{B}\Delta\mathbf{u}^*(p)] + \mathbf{R}_s^{-1}\mathbf{B'g}(p+1). \tag{4.65}$$

By multiplying both sides by $\mathbf{R}_s^{-1}$ and solving for the optimal control $\Delta\mathbf{u}^*(p)$ the final closed-loop optimal control law is:

$$\boxed{\Delta\mathbf{u}^*(p) = -\mathbf{L}(p)\Delta\mathbf{x}^*(p) + \mathbf{L}_g(p)\mathbf{g}(p+1) + \mathbf{L}_s(p)\Delta\mathbf{u}(p-1)} \tag{4.66}$$

in which

$$\begin{cases} \mathbf{L}(p) = [\mathbf{R}_s + \mathbf{B'G}(p+1)\mathbf{B}]^{-1}\mathbf{G}(p+1)\mathbf{A} \\ \mathbf{L}_g(p) = [\mathbf{R}_s + \mathbf{B'G}(p+1)\mathbf{B}]^{-1}\mathbf{B'} \\ \mathbf{L}_s(p) = [\mathbf{R}_s + \mathbf{B'G}(p+1)\mathbf{B}]^{-1}\mathbf{S} \end{cases}. \tag{4.67}$$

In the above formulation, $\bar{\mathbf{L}}(p)$ is the feedback gain and $\bar{\mathbf{L}}_g(p)$ is the feedforward gain of the optimal closed-loop control system.

Replacing Eq. (4.66) into Eq. (4.51), the optimal states are expressed as:

$$\boxed{\Delta\mathbf{x}^*(p+1) = [\mathbf{A} - \mathbf{BL}(p)]\Delta\mathbf{x}^*(p) + \mathbf{BL}_g(p)\mathbf{g}(p+1) + \mathbf{BL}_s(p)\Delta\mathbf{u}(p-1)}. \tag{4.68}$$

81

4.4.5 Summary of the LQT Controller System

One can use the above formulations to control the linear thermal dynamics model prescribed in Eq. (4.33) while minimizing the error and control effort through a smooth control action trajectory. In order to implement this controller for thermal dynamics control, one must take the following steps:

- **Step 1:** solve the matrix differential Riccati equation defined by either Eqs. (4.58) or (4.59). However, both of these two formulations contain the inverse of a large matrix, which may result in a nonsingular matrix calculation. In order to prevent such an issue one can re-formulate the matrix differential Riccati equation in the following form:

$$\boxed{\mathbf{G}(p) = \mathbf{A'G}(p+1)[\mathbf{A} - \mathbf{BL}(p)] + \mathbf{V}}. \tag{4.69}$$

  The above matrix differential Riccati equation has to be solved offline in a backwards scheme using the boundary condition prescribed by Eq. (4.62).

- **Step 2:** solve the vector difference equation defined by either Eqs. (4.60) or (4.61). Similar to the Riccati equations, the vector difference equations also contain an inverse term, which may results in a nonsingular matrix calculation. In order to prevent such an issue one can re-formulate the vector difference equation in the following form:

$$\boxed{\mathbf{g}(p) = [\mathbf{A} - \mathbf{BL}(p)]'\mathbf{g}(k+1) - [\mathbf{\bar{S}'L}(p)]'\Delta\mathbf{u}(p-1) + \mathbf{W}\Delta\mathbf{z}(p)}. \tag{4.70}$$

  The above vector difference equation has to be solved offline in a backwards scheme using the boundary condition prescribed by Eq. (4.63).

- **Step 3:** obtain the optimal states in Eq. (4.68).

- **Step 4:** obtain the optimal control law in Eq. (4.66).

The above scheme represents a discrete-time Linear Quadratic Tracking (LQT) control system, which will be used to control the thermal dynamics of the LHT process in real-time. The tuning process of this controller involves tuning of the $\mathbf{F}, \mathbf{Q}, \mathbf{R}$ and $\mathbf{S}$ matrices, which is done offline and during simulations of the closed-loop LMP process.

4.5 Thermal Dynamics State Observer Feedback Control

In empirical error-based controller systems such as PID controllers, the systems' states, which in our case are the LMP thermal dynamics, must be known through real-time measurements, whereas, in many

LMP cases it may not be possible to determine the physical parameters of the thermal dynamics directly through real measurements. Most LMP machines do not have a high-resolution or high-temperature thermal monitoring system such as an infrared thermal camera due to high cost of the hardware. On the other hand, low-temperature and low-cost thermal monitoring apparatus such as thermocouples or low-temperature pyrometers are very common in the industry. Yet, due to technological and implementation limitations, these devices cannot measure temperatures inside the melt pool, and are only able to provide measurements of the low-temperature regions such as the boundary nodes defined in Figure 4-3. Therefore, no real-time thermal PID closed-loop control system can be developed for such setups.

Nonetheless, since the above mentioned thermal measuring instruments deliver some restricted observability of the system, their limited measurements can be used inside an "observer" to provide an estimation of the complete states or temperatures of the system. An observer or sometimes referred to as an "estimator", utilizes observable measurements of the input and output of a real system, to calculate the internal "unobservable" states. The estimated feedbacks can then be used inside a model-based control system to provide real-time closed-loop control.

In the LMP thermal system, one can use the temperature measurements of the boundaries obtained from a low-cost pyrometer or thermal camera, to obtain the unobservable peak temperatures, cooling rates and heating rates in real-time, using the developed thermal model (in Section 4.3) as a reliable observer system. These estimated thermal dynamics can then be used as real-time feedback signals for the constructed model-based LQT controller (in Section 4.4). The thermal dynamics state observer feedback control system is schematically shown in Figure 4-4. The following state observer feedback control system enables closed-loop thermal dynamics control of the LMP process with limited thermal information of the melt pool boundaries rather than the melt pool itself. Compared with the general closed-loop control system illustrated in Figure 3-12, the state observer feedback control has a lower hardware cost, however, it requires the implementation of a highly reliable and accurate observer model.
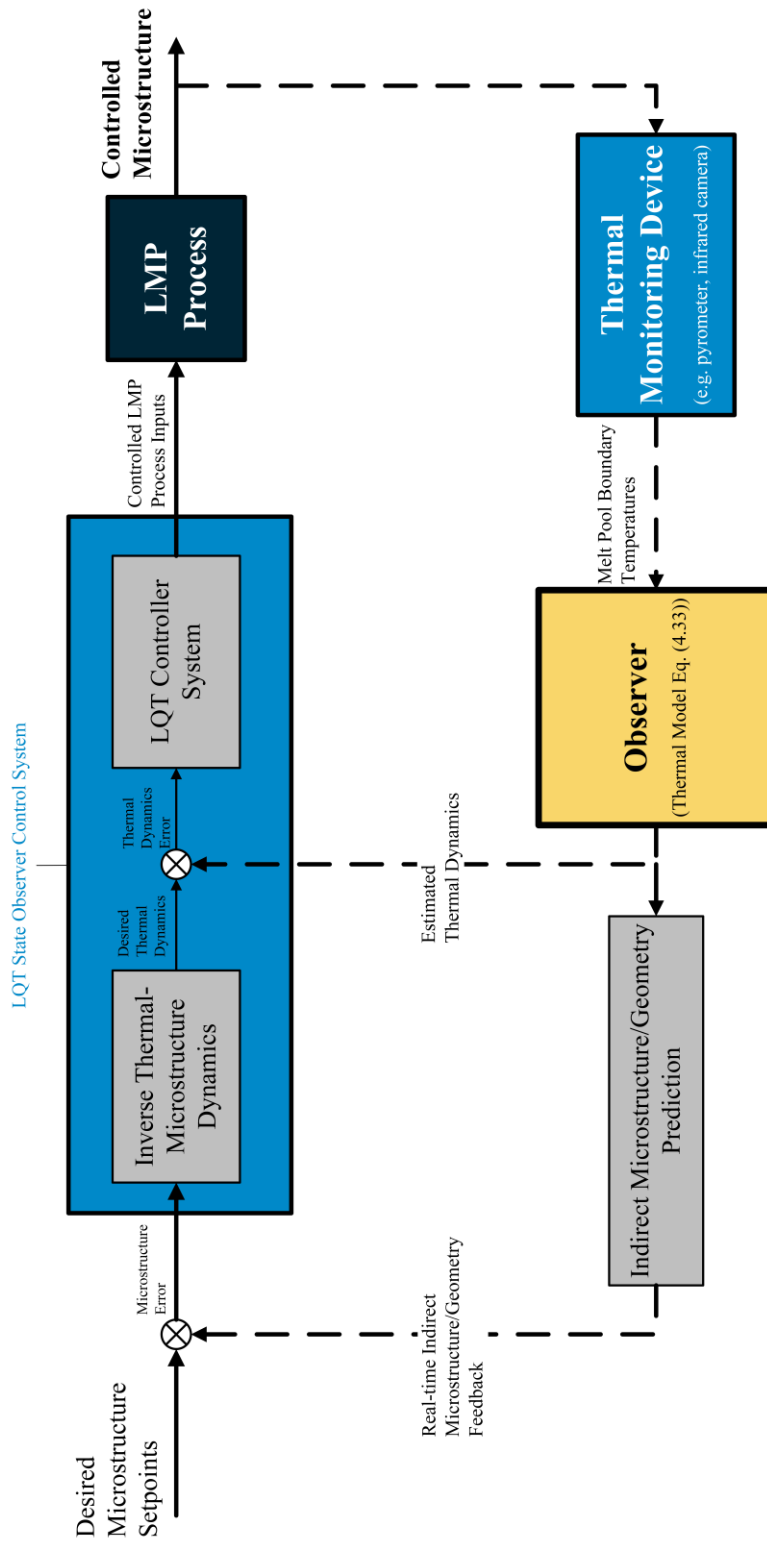
Figure 4-4 Thermal dynamics state observer feedback control system.

4.6 PID Closed-loop Control

In addition to the above model-based LQT state observer control system, one can also utilize Proportional-Integral-Derivative (PID) control systems in the MIMO controller of the general closed-loop LMP process. A PID controller calculates error values of the difference between a measured process output and a desired set point. The controller attempts to minimize the error by adjusting the process through use of a manipulated process variable. The PID algorithm consists of three basic coefficients; proportional (K_P), integral (K_I) and derivative (K_D) which are varied to get optimal response.

A block diagram of the implemented PID control structure in a feedback loop is shown in Figure 4-5. The present error is represented by K_c (proportional gain), the accumulation of past errors is represented by T_i (integral gain), and prediction of future errors is represented by T_d (differential gain), as the error and its rate of change are computed at each step the three actions are summed to adjust the thermal dynamics or process geometry using either of the two process variables laser power ($P_{max}(t)$) or travelling speed ($u(t)$). The PID gains (K_c, T_i and T_d) are expressed in terms of a predefined set of PID coefficients ($\widehat{K}_P, \widehat{K}_I$ and $\widehat{K}_D$) as:

$$\begin{cases} K_c = \widehat{K}_P \\ T_i = \dfrac{K_C}{\widehat{K}_I} \\ T_d = \dfrac{\widehat{K}_D}{K_C} \end{cases}. \tag{4.71}$$
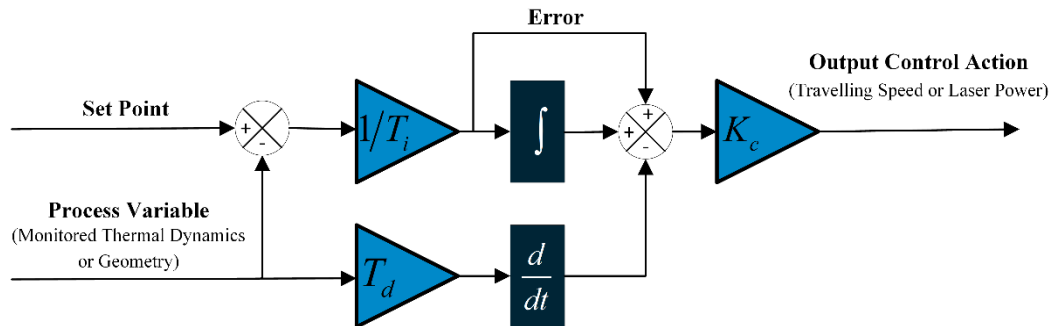
Figure 4-5 Block diagram of the implemented PID control system [104]**.**

In the case of the LMP process, the response of the system to a given control output may change over time or in relation to some variable, which indicates that the process has a nonlinear behavior as already

shown by Eq. (4.31). In such systems the control parameters that produce a desired response at one operating point might not produce a satisfactory response at another operating point [104], which therefore requires further PID control techniques such as gain scheduling and different set of tuned parameters for different operating points.

The described PID control system will be used by the developed thermal-geometry monitoring and control module in order to provide controlled thermal dynamics and process geometry (such as clad height) either in form of a Single Input Single Output (SISO) or Multi Input Multi Output (MIMO) controller architecture. Experiments are required to understand which of the process variables should be used as the control action. An extended set of experiments is also required to tune the PID coefficients for each operating point. These experiments are described in the following chapters.

4.7 Summary

In this chapter, theories of thermal dynamics modeling and optimal controller design of the thermal-geometry monitoring and control module were described. A novel approach was used to develop a finite difference thermal dynamics model of the LMP process, which formulates a two-dimensional heat conduction problem of a moving laser heat source with a Gaussian heat distribution. The formulation develops a nonlinear finite difference model that provides nodal temperatures of a restricted region of interest around the melt pool. The nonlinear model was linearized and re-arranged into a state space formulation in which the temperatures of each node represent the states of the system. A discrete-time linear quadratic tracking control system was also designed for the developed model, which will assist in the model-based control of the thermal dynamics in the closed-loop LMP process.

Finally, a state observer feedback control system was developed for closed-loop control of the thermal dynamics, for setups, which only have limited thermal information of the melt pool boundaries rather that the melt pool thermal dynamics. Low-key thermal measuring instruments that are not capable of measuring the thermal dynamics directly and completely, can be used to provide feedback of the melt pool boundaries. The developed dynamic model is computationally fast, which enables it to be implemented as a real-time "observer system" in an LQT state observer feedback control. The structure of an error-based PID controller system is also described. The PID controller will be used in the closed-loop LMP process in the form of a Single Input Single Output (SISO) or Multi Input Multi Output (MIMO) control architecture in order to control the thermal dynamics and/or geometry process variables in real-time.

86

Chapter 5

Design of Experiments

The current chapter describes the different type of experiments designed in order to evaluate the monitoring and control performance of the developed thermal-geometry monitoring and control module. The experiments are conducted for two types of LMP procedures; the Laser Additive Manufacturing (LAM) and the Laser Heat Treatment (LHT) processes. Experiments are designed for assessing the online microstructure prediction characteristics of the module. Additional experiments are also discussed to validate the accuracy of the developed finite difference thermal model. Finally, open-loop and closed-loop experiments are designed to evaluate the performance of single-input-single-output and multi-input-multi-output control of thermal dynamics and/or geometry. The material preparation process and the materials used for the experimental analyses are also discussed.

5.1 Experimentation Objectives

In order to demonstrate the main objectives of the developed thermal-geometry monitoring and control module, the experimental studies of this research are designed in three categories, which are:

- Indirect online microstructure prediction

- Thermal dynamics model validation

- Closed-loop Microstructure and/or geometry control.

The experiments in each category are evaluated for both LHT and LAM processes to generalize the results of the research for a wide range of LMP procedures. The LHT and LAM samples processed in the following sections are conducted in either six cases (or conditions), which are schematically shown in Figure 5-1. LAM samples are deposited in either single or multi-track straight line profiles on a rectangular workpiece with consistent thickness (Figure 5-1a-d). During LHT experiments, samples are heat treated in either single or multi-track straight lines (Figure 5-1d-f). Additionally, single-track laser heat treatment samples are also prepared in which the thickness of the workpiece is varied during the process, as shown in Figure 5-1f.

(a) single-track LAM

(b) multi-track LAM with overlap

(c) multi-track LAM with offset

(d) single-track LHT

(e) multi-track LHT with adjacent tracks (zero offset)

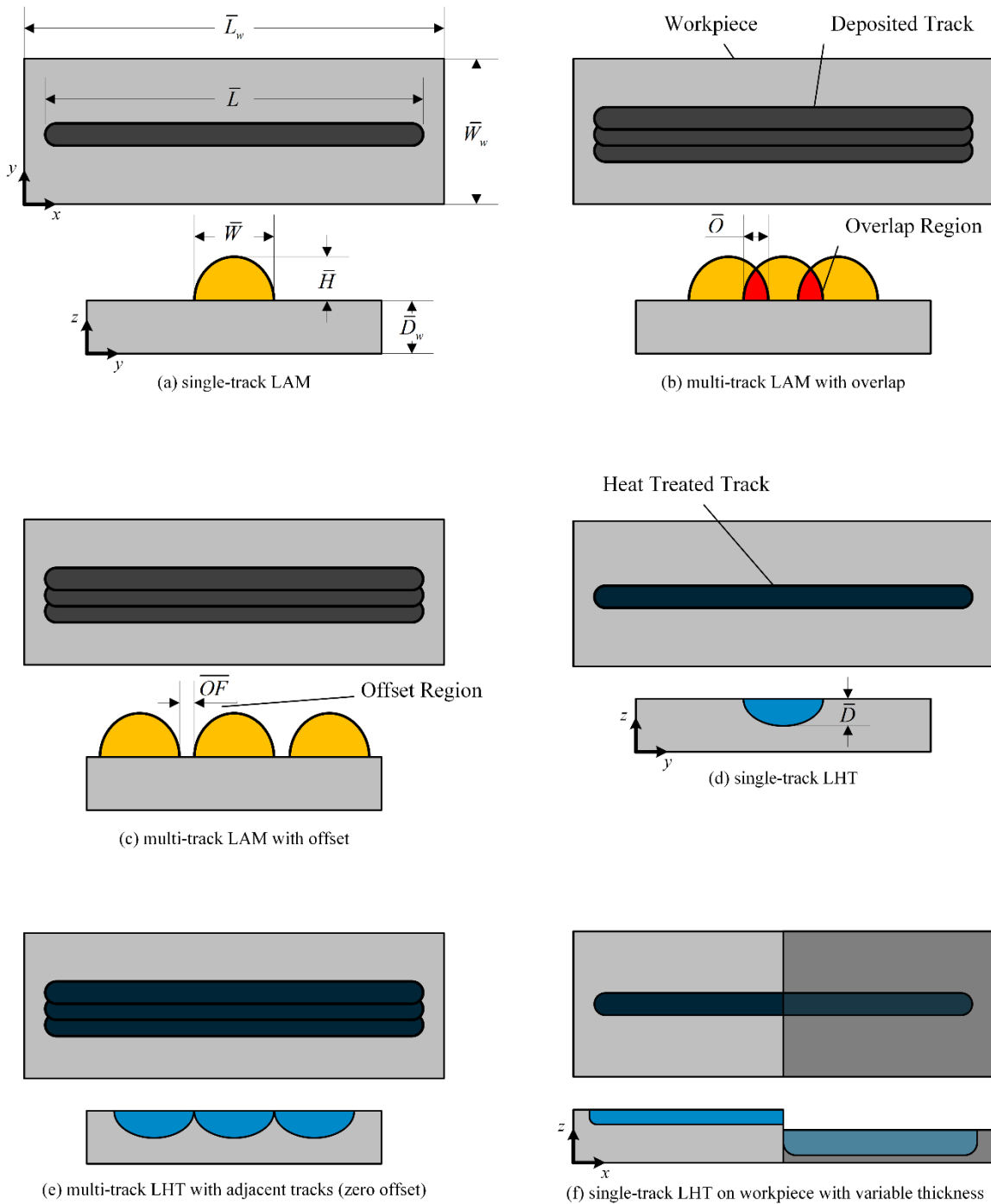(f) single-track LHT on workpiece with variable thickness

Figure 5-1 LHT and LAM experimental cases.

In the above samples, $\bar{L}_w$, $\bar{W}_w$ and $\bar{D}_w$ are the length, width and thickness of the workpiece, respectively, $\bar{L}$ and $\bar{W}$ are the length and width of the deposited or heat treated tracks, $\bar{H}$ is the height of the deposited

88

track in LAM depositions, $\overline{D}$ is the hardened depth of the heat treated track in LHT, and $\overline{O}$ and $\overline{OF}$ are also the overlap percentage and offset distance of two adjacent tracks during multi-track LAM experiments. As schematically indicated in the figure, all of the multi-track samples include three tracks. The following sections provide a detailed description of each designed set of experiments.

5.2 Experimentation for Indirect Online Microstructure Prediction

One of the main capabilities of the developed thermal-geometry monitoring and control module is the indirect online identification of process microstructure and geometry through real-time monitoring of the thermal dynamics, which is represented by the "indirect microstructure/geometry identification" block of Figure 3-12. This indirect identification block is achieved through direct correlation of measured thermal dynamics variables with microstructure evolutions for a set of different process conditions. More importantly, to develop a good controller for microstructure it is essential to determine the most important governing parameter on the microstructure and other mechanical properties. The experiments in this section are conducted in order to understand and construct such correlations. The operating laser conditions in these group of experiments are set such that the laser spot is below the laser focal point.

5.2.1 Laser Heat Treatment Experiments

As explained earlier, output properties such as the hardness depth and hardness values of parts subjected to the LHT process are very much dependent upon thermal dynamics. It is clear that variation of process parameters affects these thermal dynamics and therefore, material and mechanical properties. Moreover, the response of different materials to the LHT process at similar processing conditions are different due to the differences in metallurgical characteristics denoted in the phase diagrams and continuous cooling transformation diagrams. For example, low carbon steels require very high degrees of cooling rate for hardening, whereas, low alloy steels can be hardened more easily at lower cooling rate values. Therefore, two set of experiments *A* and *B* were prepared by changing process parameters such as the travelling speed and laser power to evaluate the effect of these parameters on the thermal dynamics, and consequently on the hardened depth and amount of hardening of AISI 1020 low carbon steel.

The laser power and travelling speed are two of the most influential laser parameters that affect LMP thermal dynamics. Hence, initially a group of *A*-samples are studied to analyze the effect of changing travelling speed on thermal dynamics and indirectly on the microstructure and geometry properties of

low carbon steels. In the *A*-samples the laser power is kept constant at $250\ W$ and the travel speed is increased incrementally between samples. On the other hand, a group of *B*-samples were also studied to analyze the effect of laser power on the thermal dynamics. In the *B*-samples the laser travel speed is kept constant at $500\ mm/min$ and the laser power is increased incrementally. The processing parameters of the *A* and *B*-samples are shown in Table 5-1. The *A* and *B*-samples are all single-track laser heat treated lines as shown in Figure 5-1d, with a track length $\bar{L} = 90\ mm$, laser beam radius $r_b = 1\ mm$ and workpiece dimensions of $\bar{L}_w = 100\ mm, \overline{W}_w = 25\ mm$ and $\overline{D}_w = 6.35\ mm$.

Table 5-1 Laser processing conditions of single-track LHT *A* and *B*-samples.

Sample No.	Laser Power (W)	Travelling Speed (mm/min)
A100	250	100
A300	250	300
A400	250	400
A500	250	500
A600	250	600
A700	250	700
A800	250	800
B175	175	500
B200	200	500
B225	225	500
B250	250	500
B275	275	500
B300	300	500
B400	400	500

5.2.2 Laser Additive Manufacturing Experiments

Similar to the LHT process, the microstructure of the LAM process is also governed by the thermal dynamics, which define mechanical properties such the harness value of each deposited track. The next

set of experiments conducted in the current section were on laser additive manufacturing of AISI 4340 powder. These experiments were designed to evaluate the effect of processing parameters on the real-time thermal dynamics and further evaluation of microstructure analysis based on these thermal variations.

5.2.2.1 Single-track Depositions

In order to study the influence of laser travelling speed on thermal dynamics and microstructures of the LAM process, a set of C-samples were prepared. As shown in Table 5-2, the laser power is constant at $800\ W$ and the travelling speed increases gradually in these samples. The C-samples are all single-track LAM depositions as shown in Figure 5-1a, with a track length $\bar{L} = 90\ mm$, laser beam radius $r_b = 1\ mm$, material feed rate $\bar{F} = 6\ g/min$, and workpiece dimensions of $\bar{L}_w = 100\ mm, \bar{W}_w = 25\ mm$ and $\bar{D}_w = 6.35\ mm$.

Table 5-2 Laser processing conditions of single-track LAM C-samples.

Sample No.	Laser Power (W)	Travelling Speed (mm/min)
C100	800	100
C150	800	150
C200	800	200
C300	800	300
C400	800	400

5.2.2.2 Multi-track Laser Depositions with Overlap

To further study the effects of thermal dynamics of the LAM process on microstructure, a multi-track deposition similar to the schematic shown in Figure 5-1b was built, by overlapping three single-track deposits with a specific overlap percentage. The processing parameters of the D-samples are listed in Table 5-3. A track of length $\bar{L} = 45\ mm$, laser beam radius $r_b = 1\ mm$, material feed rate $\bar{F} = 6\ g/min$, and workpiece dimensions of $\bar{L}_w = 100\ mm, \bar{W}_w = 25\ mm$ and $\bar{D}_w = 6.35\ mm$ were used for these samples.

Table 5-3 Laser processing conditions of multi-track LAM _D_-samples.

Sample No.	Laser power (W)	Travelling Speed (mm/min)	Overlap (%)
_D100_	800	100	25
_D150_	800	150	25
_D200_	800	200	25

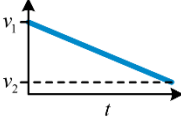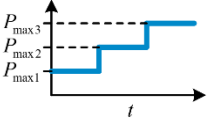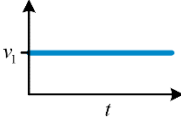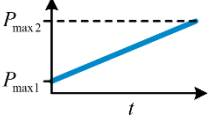## 5.3 Experimentation of Thermal dynamics Model Validation
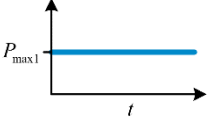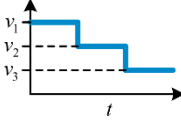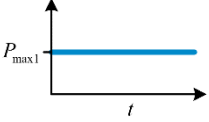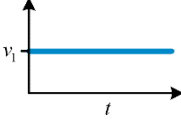
The thermal information provided by the thermal infrared camera, are extremely useful for development and validation of a reliable thermal model. As explained earlier, while numerous models have been developed for thermal prediction of LMP processes, due to the lack of a proper thermal monitoring device, most of these models are unverified and unreliable for real-time implementation. The experiments in this section are designed to provide a validating benchmark for the developed nonlinear and linearized finite difference models prescribed by Eqs. (4.31) and (4.33), respectively. This validation will enable a reliable thermal model that can be used as an "observer" in the thermal dynamics state observer feedback control system developed in Section 4.5. The experiments in this section are conducted in order to provide model verification based on real-time thermal dynamics measurements. The operating laser conditions in these group of experiments are set such that the laser spot is above the laser focal point.

5.3.1 Laser Heat Treatment Experiments

Since laser power and travelling speed are the process control actions used in the model-based controller, it is essential to validate the finite difference model based on variations of these two process inputs. In order to excite all modes of the dynamic system and evaluate the dynamic model over a wide range of process variables, a combination of four set of input signals including constant, step and ramp profiles were used to alter the laser power and travelling speed during the process. The types and values of the different input signal profiles used for model evaluation during the LHT process are schematically shown in Table 5-4. The _E1_ and _E2_ samples are excited by step and ramp signals for the travelling speed, while, the _E3_ and _E4_ samples are excited by step and ramp signals for the laser power. The _E_-samples are all single-track laser heat treated lines as shown in Figure 5-1d, with a track length

$\bar{L} = 150\ mm$, laser beam radius $r_b = 1\ mm$, material feed rate $\bar{F} = 4\ g/min$, and workpiece dimensions of $\bar{L}_w = 152\ mm, \bar{W}_w = 25\ mm$ and $\bar{D}_w = 6.35\ mm$.

Table 5-4 Laser processing conditions of single-track LAM E-samples.

Sample No.	Laser Power (W)			Laser Power Signal Type	Travelling Speed (mm/min)			Travelling Speed Signal Type
	P_{max1}	P_{max2}	P_{max3}		v_1	v_2	v_3	
E1	375	-	-		250	150	90	
E2	375	-	-		250	90	-	
E3	325	375	425		150	-	-	
E4	325	425	-		150	-	-	

5.3.2 Laser Additive Manufacturing Experiments

Similar to the previous experiments described for the LHT process, a range of different travelling speed and laser power signals were used to excite the LAM system in order to verify the dynamic model for the LAM process. The types and values of the different input signal profiles used for these samples are schematically shown in Table 5-5. The *F*-samples are excited by step and ramp signals for the travelling speed. These samples are all single-track LAM depositions as shown in Figure 5-1a, with a track length $\bar{L} = 150\ mm$, laser beam radius $r_b = 1\ mm$, material feed rate $\bar{F} = 4\ g/min$, and workpiece dimensions of $\bar{L}_w = 152\ mm, \bar{W}_w = 25\ mm$ and $\bar{D}_w = 6.35\ mm$.
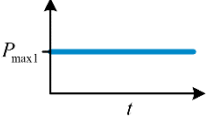
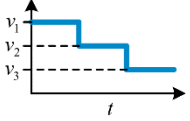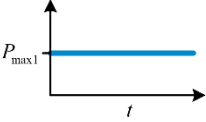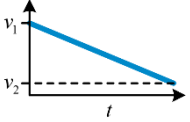**Table 5-5 Laser processing conditions of single-track LAM *F*-samples.**

Sample No.	Laser Power (W)			Laser Power Signal Type	Travelling Speed (mm/min)			Travelling Speed Signal Type
	P_{max1}	P_{max2}	P_{max3}		v_1	v_2	v_3	
F1	800	-	-		200	150	100	
F2	800	-	-		200	100	-	

5.4 Experimentation for Closed-loop Microstructure and/or Geometry Control

The final and ultimate goal of the thermal-geometry monitoring and control module is to develop a closed-loop LMP system that automatically monitors and controls the microstructure (indirectly) and geometry properties of the final product. The experiments conducted in this section will showcase the real-time monitoring and controlling capabilities of the designed module through different case studies. In order to demonstrate the versatility of each mode of the control module, the experiments are designed and implemented in three modes based on the type of controlled process outputs:

- Single Input Single Output (SISO) geometry control

- Single Input Single Output (SISO) thermal dynamics control

- Multi Input Multi Output (MIMO) integrated thermal dynamics and geometry control.

Two type of controller systems are also utilized in the above closed-loop control processes. An empirical error-based PID controller is designed for the SISO and MIMO control of the thermal dynamics and geometry properties. In addition, the develop LQT state observer feedback control system is used to control the peak temperature of the LHT process based on the verified thermal model. In both of these controller systems, the laser power and/or travelling speed are used as the control action(s) of the process.

5.4.1 Laser Heat Treatment Samples

Hardness of a heat treated product is the most critical process output that is always inspected closely and vigorously after the process has been finished. All current LHT hardness monitoring and control techniques are therefore, passive and offline. Using the information obtained from the indirect online microstructure identification experiments (Section 5.2), a closed-loop LHT process is developed to control the peak temperature in real-time in order to achieve a consistent hardness value. The developed control system is evaluated for different case studies including single-track and multi-track laser heat treatments, and heat treatment of a workpiece with a stepped surface. The controller is also evaluated at different setpoint values and profiles such as a constant and multi-step peak temperature profile.

5.4.1.1 Closed-Loop Peak Temperature Control (with PID controller)

In order to evaluate the performance of the PID controller in the closed-loop LHT process, four case studies were designed. Since the goal of these experiments is to evaluate the consistency of the hardness value during the closed-loop process, an identical open-loop experiment is also conducted for each closed-loop case study for comparison reasons. Thus, by comparing the results of the open-loop and closed-loop samples and their measured output properties, one will be able to analyze the control performance and capability of the thermal-geometry monitoring and control module. The experimental conditions of the open-loop and closed-loop *G*-samples are shown in Table 5-6 and Table 5-7, respectively. Sample *G1* is a multi-track laser heat treated surface as shown in Figure 5-1e, with a track length $\bar{L} = 90 \ mm$, laser beam radius $r_b = 1 \ mm$, and workpiece dimensions of $\bar{L}_w = 102 \ mm, \bar{W}_w = 25 \ mm$ and $\bar{D}_w = 6.35 \ mm$. Samples *G2* to *G4* are single-track laser heat treated lines as shown in Figure 5-1f, with a track length $\bar{L} = 150 \ mm$, laser beam radius $r_b = 1 \ mm$, and workpiece dimensions of $\bar{L}_w = 204 \ mm, \bar{W}_w = 25 \ mm, \bar{D}_{w1} = 6.35 \ mm$ and $\bar{D}_{w2} = 3.175 \ mm$. Therefore, the step on the workpiece has a thickness of $3.175 \ mm$.

Table 5-6 Laser processing conditions of open-loop LHT *G*-samples (with constant laser power $P_{max} = 375\ W$).
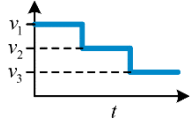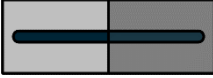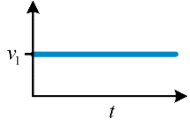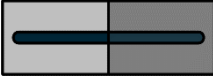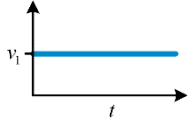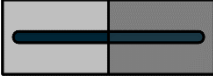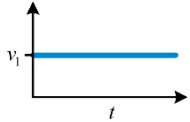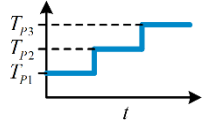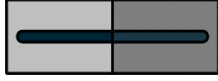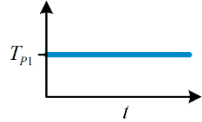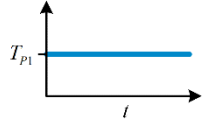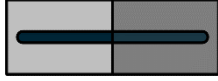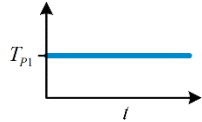
Sample No.	Heat Treatment Conditions	Travelling Speed (mm/min)			Travelling Speed Signal Type (for each track)
		v_1	v_2	v_3	
G1-o	Multi-track LHT	225	170	125	
G2-o	Single-track LHT (on a workpiece with stepped surface)	225	-	-	
G3-o	Single-track LHT (on a workpiece with stepped surface)	170	-	-	
G4-o	Single-track LHT (on a workpiece with stepped surface)	125	-	-	

Table 5-7 Laser processing conditions of closed-loop LHT *G*-samples with controlled peak temperature (with constant laser power $P_{max} = 375\,W$).
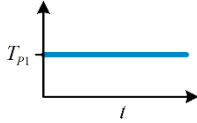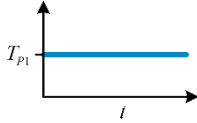
Sample No.	Heat Treatment Conditions	Setpoint Temperature (°C)			Temperature Setpoint Profile (for each track)
		T_{P1}	T_{P2}	T_{P3}	
G1-c	Multi-track LHT	1000	1200	1400	
G2-c	Single-track LHT (on a workpiece with stepped surface)	1000	-	-	
G3-c	Single-track LHT (on a workpiece with stepped surface)	1200	-	-	
G4-c	Single-track LHT (on a workpiece with stepped surface)	1400	-	-	

5.4.1.2 Closed-Loop Peak Temperature Control (with LQT stated observer feedback controller)

In order to evaluate the performance of the LQT state observer feedback control system in the closed-loop control of the LHT peak temperature, three case studies were designed. The experimental conditions of the closed-loop *H*-samples controlled with the LQT controller are shown in Table 5-8.

Sample *H1-c* is a multi-track laser heat treated surface as shown in Figure 5-1e, with a track length $\bar{L} = 45\ mm$, laser beam radius $r_b = 1\ mm$, and workpiece dimensions of $\bar{L}_w = 102\ mm, \bar{W}_w = 25\ mm$ and $\bar{D}_w = 6.35\ mm$. Sample *H2-c* is a single-track laser heat treated lines on a stepped workpiece as shown in Figure 5-1e, with a track length $\bar{L} = 150\ mm$, laser beam radius $r_b = 1\ mm$, and workpiece dimensions of $\bar{L}_w = 204\ mm, \bar{W}_w = 25\ mm, \bar{D}_{w1} = 6.35\ mm$ and $\bar{D}_{w2} = 3.175\ mm$. Therefore, the step on the workpiece has a thickness of $3.175\ mm$.

Table 5-8 Laser processing conditions of closed-loop LHT *H*-samples with controlled peak temperature (with constant laser power $P_{max} = 375\ W$).

Sample No.	Heat Treatment Conditions	Setpoint Temperature (°C)	Temperature Setpoint Profile (for each track)
		T_{P1}	
H1-c	Multi-track LHT	1400	
H2-c	Single-track LHT (on a workpiece with stepped surface)	1400	

5.4.2 Laser Additive Manufacturing Experiments

Experiments in this section are designed to demonstrate the capability of the monitoring and control module in development of consistent microstructure and geometry properties for LAM depositions. The properties to be controlled locally are the clad height, morphology and hardness of each deposited track. Using the information obtained from the indirect online microstructure identification experiments (Section 5.2), a closed-loop LAM process is developed to control the cooling rate and clad height in real-time. In the final set of experiments, the performance of a MIMO closed-loop system is evaluated, which provides integrated microstructure and geometry control with simultaneous adjustments of both the laser power and travelling speed.

98

5.4.2.1 Closed-Loop Clad Height Control (with PID controller)

A multi-track *I1-c* sample is deposited in order to evaluate the performance of the PID controller for closed-loop control of the clad height during LAM depositions. The tracks of the multi-track deposition are deposited with an offset of $\overline{OF} = 1\ mm$, similar to the schematic shown in Figure 5-1c. The experimental conditions of the closed-loop *I* sample is shown in Table 5-9. The *I1-c* sample has a track length $\bar{L} = 45\ mm$, laser beam radius $r_b = 1\ mm$, and workpiece dimensions of $\bar{L}_w = 102\ mm, \bar{W}_w = 25\ mm$ and $\bar{D}_w = 6.35\ mm$.

5.4.2.2 Closed-Loop Cooling Rate Control (with PID controller)

A set of *J*-samples is deposited in order to evaluate the performance of the PID controller for closed-loop control of the cooling rate during LAM depositions. The experimental conditions of the open-loop and closed-loop *J*-samples are shown in Table 5-10 and Table 5-11, respectively. The tracks of the multi-track deposition *J1* are deposited with an offset of $\overline{OF} = 1\ mm$, similar to the schematic shown in Figure 5-1c. The *J*-samples have a track length $\bar{L} = 90\ mm$, laser beam radius $r_b = 1\ mm$, and workpiece dimensions of $\bar{L}_w = 102\ mm, \bar{W}_w = 25\ mm$ and $\bar{D}_w = 6.35\ mm$.

Table 5-9 Laser processing conditions of closed-loop LAM *I*-sample with controlled clad height (with constant laser power $P_{max} = 800\ W$).
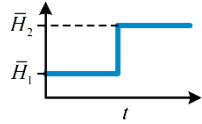
Sample No.	Additive Manufacturing Conditions	Setpoint Clad Height (mm)		Clad Height Setpoint Profile (for each track)
		$\bar{H}_1$	$\bar{H}_2$	
I1-c	Multi-track LAM	0.60	0.90	

Table 5-10 Laser processing conditions of open-loop LAM *J*-sample (with constant laser power $P_{max} = 800\ W$).
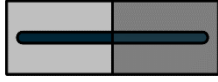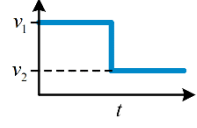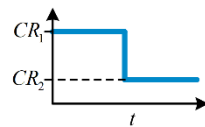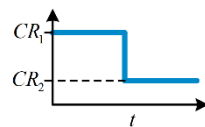
Sample No.	Heat Treatment Conditions	Travelling Speed (mm/min)		Travelling Speed Signal Type (for each track)
		v_1	v_2	
J1-o	Multi-track LAM	150	100	

Table 5-11 Laser processing conditions of closed-loop LAM *J*-samples controlled with PID control system (with constant laser power $P_{max} = 800\ W$).
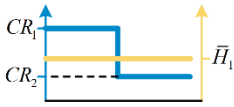
Sample No.	Additive Manufacturing Conditions	Setpoint Cooling Rate (℃/s)		Clad Height Setpoint Profile (for each track)
		CR_1	CR_2	
J1-c	Multi-track LAM	750	350	
J2-c	Single-track LAM	600	400	

5.4.2.3 Integrated Cooling Rate and Clad Height Control with MIMO PID Controller

The final set of experiments conducted in this research are to demonstrate the multi-input-multi-output control capabilities of the thermal-geometry monitoring and control module. In these group of samples the cooling rate and clad height are controlled simultaneously in real-time by adjusting the laser power and travelling speed during the LAM process. The experimental conditions of the closed-loop *K*-samples are shown in Table 5-12. The tracks of the multi-track deposition *K1-c* are deposited with an offset of $\overline{OF} = 1\ mm$, similar to the schematic shown in Figure 5-1c. The *K1-c* and *K2-c*-samples have

a track length $\bar{L} = 90\ mm$ and $\bar{L} = 45\ mm$, respectively. These samples have a laser beam radius $r_b = 1\ mm$, and workpiece dimensions of $\bar{L}_w = 102\ mm, \bar{W}_w = 25\ mm$ and $\bar{D}_w = 6.35\ mm$.

Table 5-12 Laser processing conditions of closed-loop LAM K-samples with integrated control of clad height and cooling rate.

Sample No.	Additive Manufacturing Conditions	Setpoint Cooling Rate (°C/s)		Setpoint Clad Height (mm)	Multi-objective Setpoint Profile (for each track)
		CR_1	CR_2	$\bar{H}_1$	
L1-c	Single-track LAM	600	400	0.6	
L2-c	Multi-track LAM	500	-	0.6	

5.5 Materials and Material Preparation Process

The material characteristics, and material preparation and analysis techniques used in the research are described as follows.

AISI 1020 hot rolled steel is used as sample coupon for the LHT experiments in Section 5.2.1, and workpiece (or substrate) for LAM depositions in Sections 5.2.2, 5.3.2 and 5.4.2. AISI 1018 cold rolled steel is used as sample coupon for the LHT experiments in Sections 5.3.1 and 5.4.1. The powder used for the laser additive manufacturing experiments is AISI 4340 powder, -106 +45 mesh, provided by Sandvik Osprey LTD. The AISI 4340 powder has a composition of 0.40 wt % C, 0.83 wt % Cr, 0.50 wt % Mn, 0.25 wt % Mo, 1.97 wt % Ni, less than 0.007 wt % P, 0.006 wt % S, 0.11 wt % Si, and balance wt % Fe.

Before the LHT and LAM processes all of the substrates were rinsed with ethanol and washed with acetone to remove any contamination. Initial temperature and amount of preheat in all laser heat treated samples and claddings have great influence in microstructure formation. To insure the initial temperature and preheat of each sample was the same for single or multi-track LHT or LAM samples

on one workpiece, after each sample was finished, the workpiece was quenched in washing acetone for 10 s and air dried to reach the initial room temperature.

The specimens were sectioned along the horizontal *y*-direction for microstructure examination. Samples were prepared using SiC grit paper with grit mesh sizes from 240 to 1200, polished with 1, 0.3, 0.1 μm alumina powder. After each polishing step, the samples were placed in an ultrasonic machine to remove contamination and later air dried. Samples were etched in Nital 2% etchant, to expose the grain structure and morphology. The microstructures were analyzed using optical microscopy with images obtained from an Olympus AH microscope. Hardness measurements were also made using micro-hardness tester and the Vickers hardness technique.

5.6 Summary

This chapter summarized all of the LHT and LAM experiments designed for evaluation of the thermal-geometry monitoring and control module. A set of experiments were designed to evaluate the capability of indirect monitoring of microstructure and geometry through thermal monitoring. Another set of experiments were designed to verify the thermal model and state observer feedback control system developed in the previous chapter. A final set of experiments were also described to evaluate the performance and advantages of closed-loop thermal and geometry control. These experiments were designed in open-loop and closed-loop conditions for comparison reasons. Finally, the material preparation process and the materials used for the experimental analysis were also discussed.

Chapter 6

Results and Discussions

This chapter discusses and analyzes the applications and performance of the thermal-geometry monitoring and control module for automated control of the LHT and LAM processes. The chapter first addresses the effects of cooling rate, melt pool temperature (or peak temperature) and heating rate on the formation of the microstructure during the LHT and LAM processes. Based on correlations between the thermal dynamics and microstructure formation, a generalized indirect scheme is developed to understand and control microstructure variations during the LHT and LAM processes through thermal monitoring and control. The module is then used to verify the finite difference thermal dynamics model using different excitation signals for the LHT and LAM processes. Key process parameters and thermal feedback signals are identified for the purpose of closed-loop microstructure and geometry control. Performance of the multi-objective thermal-geometry controller is evaluated through closed-loop experiments for single-input-single-output control of the peak temperature during the LHT process, and single-input-single-output control of the clad height and cooling rate during the LAM process. The developed thermal dynamics state observer feedback control system is also evaluated for real-time peak temperature control. In the final section, results of an automated multi-input-multi-output control system for integrated control of the clad height and microstructure during the LAM process are described.

6.1 Online Prediction of Material and Mechanical Properties

Micrographs, microhardness tests and geometry measurements of the experiments described in Section 5.2 are presented in this section. Furthermore, real-time thermal dynamics of the LHT and LAM processes recorded during these experiments are also reported. These thermal recordings are correlated with microstructure formation and transformation diagrams (Figure 2-4 and Figure 2-5) to identify a closed-loop thermal scheme for the purpose of real-time geometry and microstructure control.

6.1.1 Microstructure Analysis of Laser Heat Treatment Process

The results and discussions presented in Section 6.1.1, which discuss thermal-microstructure and thermal-geometry correlations of the LHT process, have been published by the author in the form of a journal publication, and are therefore being cited from the original publication [84].

6.1.1.1 Effect of Travelling Speed on Thermal Dynamics and Microstructure

"The *A*-samples were designed to show the effect of the laser travelling speed on thermal dynamics of the LHT process. The real-time cooling rate of the *A*-samples are shown in Figure 6-1. As the laser starts to interact with the material, a small delay is required for extracting the cooling rate of the first point (as indicated in the thermal dynamics algorithm of Figure 3-9). After a short period of time, the cooling curve reaches a stable value. There are spikes at the end of each cooling curve, which is the result of laser shut down and movement of the laser head into its original position. Therefore, these spikes are disregarded during the analysis. There are fluctuations present in the real-time cooling curve of the higher cooling rate samples (e.g. *A800*). These fluctuations are a result of the very rapid cooling, which results in very short duration times for cooling rate measurements. Due to the limitation in the capturing frequency and low resolution of the thermal infrared camera, consistent measurements are difficult for short time periods and small melt pools. Hence, higher amount of noise is present at higher cooling rate values, however, the mean values of the cooling at the stable regions is a correct indicator of the cooling values with respect to each other. It is clear from Figure 6-1 that the cooling rate increases with the increasing traveling speed drastically." [84].

"In order to eliminate the effects of noise and have a comparative study of each cooling curve, mean values of each curve at their stable regions are plotted in Figure 6-2. According to this figure, the cooling rate increases with the increasing traveling speed in a cubic manner ($C \propto V^3$). This increasing effect of the travelling speed is justified since the increasing travelling speed results in smaller interaction time of the laser beam during the heating cycle and also provides a greater time span for the cooling cycle." [84]. The cubic model that has been fit to the cooling rate is listed in Table 6-1.
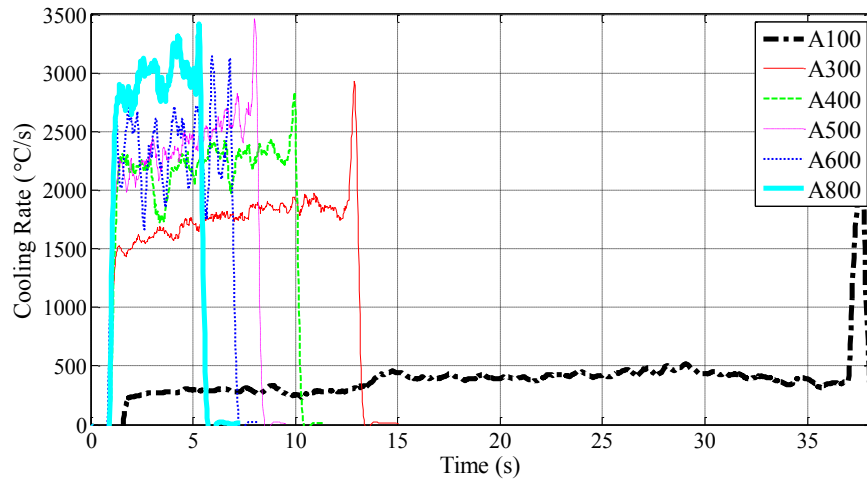
Figure 6-1 Real-time cooling rate of the *A*-samples with constant power ($250\ W$) and changing travelling speed (the number after the letter *A* indicates the travelling speed in mm/min).
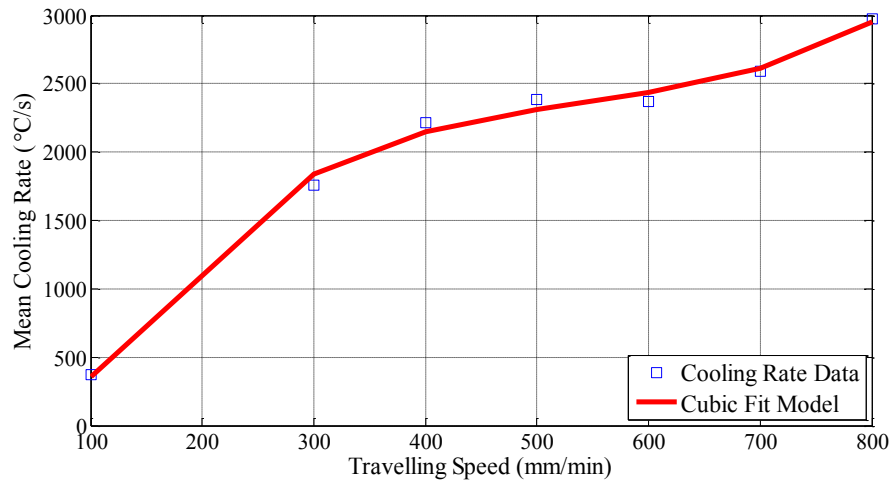
Figure 6-2 Mean cooling rate of the *A*-samples with respect to the travelling speed (constant power at $250\ W$).

"The real-time peak temperature measurements of the A-samples with their mean values with respect to the travelling speed are shown in Figure 6-3 and Figure 6-4, respectively. It is observed that at low travelling speeds (sample A100) due to high interaction times and higher amount of heat accumulation, the peak temperature increases gradually even during the process. In contrast to the cooling rate, the peak temperature decreases with increasing travel speed quadratically ($T_m \propto -V^2$). The decreasing effect of the travelling speed (negative sign) is the result of smaller interaction time during the heating

105

cycle, which results in lower absorbed heat energy. However, as it can be seen in Figure 6-2, the travelling speed has a greater influence on the cooling rate ($C \propto V^3$) compared to the peak temperature ($T_m \propto -V^2$), since for the cooling rate the effect of travelling speed is accumulated during both the heating and cooling stages, whereas the peak temperature is mostly governed by the heating stage." [84].
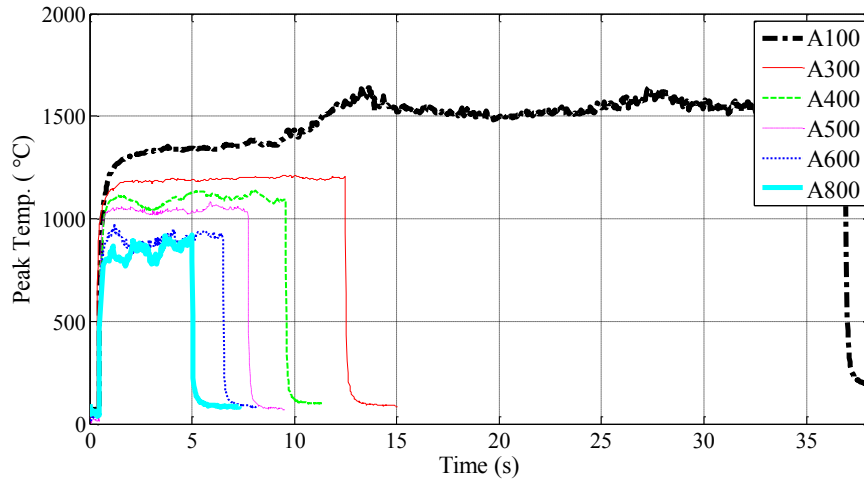
Figure 6-3 Real-time peak temperature of the A-samples with constant power ($250\ W$) and changing travelling speed (the number after the letter A indicates the travelling speed in mm/min).
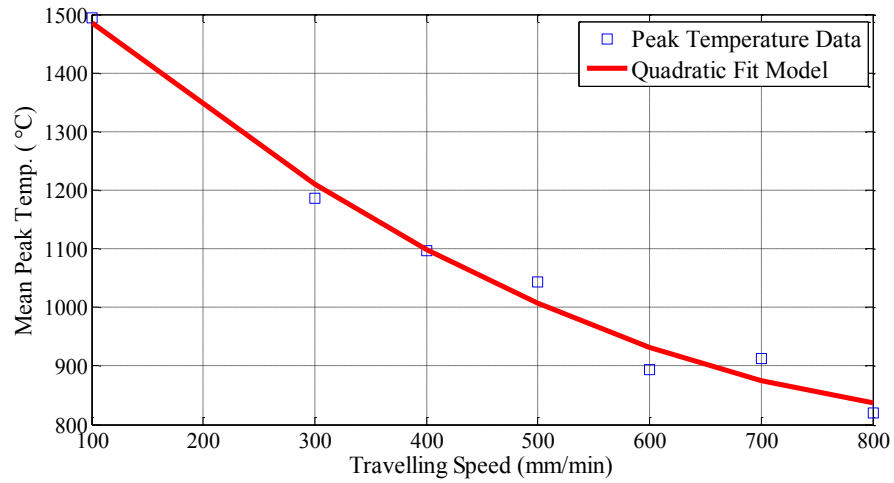
Figure 6-4 Mean peak temperature of the *A*-samples with respect to the travelling speed (constant power at $250\ W$).

"Figure 6-5 illustrates the real-time heating rate of the *A*-samples. For sample *A100,* the heating rate increases after $15\ s$. This observation proves the assumption of accumulated heat at higher interaction times and lower traveling speeds, which results in increasing peak temperature (Figure 6-3). The mean value of the heating rate with respect to the travelling speed is also shown in Figure 6-6. Similar to the previous thermal history, a linear regression model was also proposed to fit to the heating rate (as shown in Table 6-1). Interestingly, the heating rate has a more linear ($H \propto V$) relationship with the travel speed, which is caused by lower heat accumulation during the heating stage resulting in faster rise (heating) and decline (cooling) of the temperature." [84].
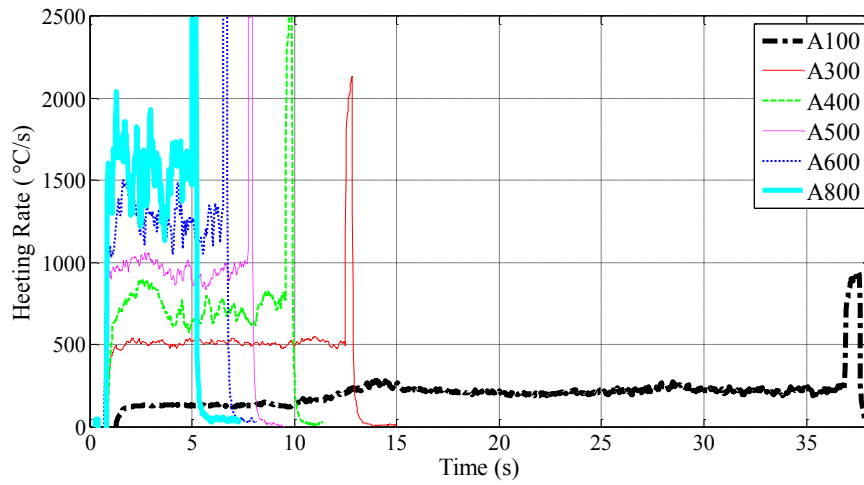
Figure 6-5 Real-time heating rate of the *A*-samples with constant power ($250\ W$) and changing travelling speed (the number after the letter *A* indicates the travelling speed in mm/min)..
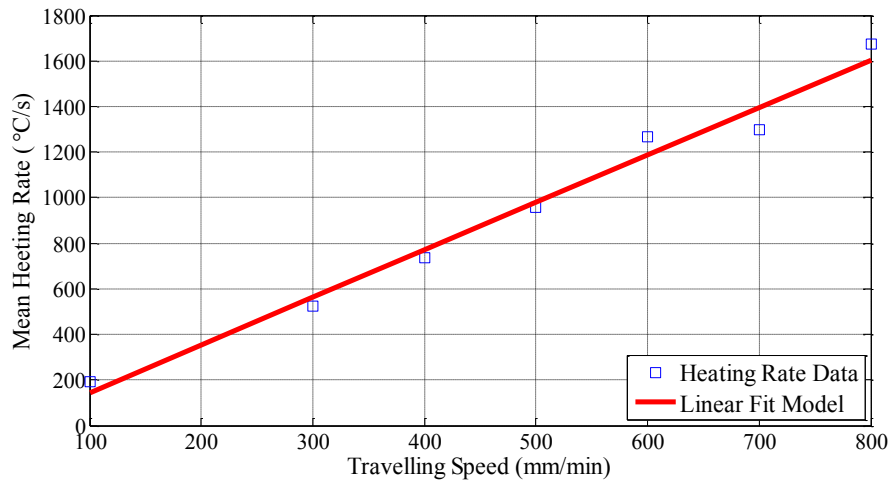
Figure 6-6 Mean heating rate of the *A*-samples with respect to the travelling speed (constant power at $250\ W$).

Table 6-1 Coefficients of the fit models for the cooling rate, peak temperature and heating rates of the *A*-samples as a function of the travelling speed (*V*).

$$y = a_3V^3 + a_2V^2 + a_1V + a_0$$

y	a_3	a_2	a_1	a_0
Cooling Rate	1.7331e-05	-0.0282	16.4452	-1024.8048
Melt Pool Temperature	0	0.0009	-1.7387	1650.5469
Heating Rate	0	0	2.0864	-64.2053

Although observations were obtained in terms of the effect of travelling speed on the cooling rate, peak temperature and heating rate, the correlation of microstructure with these thermal dynamics will be the final piece in developing a closed-loop scheme for microstructure control. In order to analyze the effect of the energy density and interaction time on the general laser heat treated profile, low magnification micrographs ($100 \times$) of samples *A100* (with very high energy density and interaction time), and *A800* (with very low energy density and interaction time) are shown in Figure 6-7. As it can be seen in the figure, due to high energy density and interaction time in sample *A100,* the laser penetrates well into the substrate producing a distinct laser hardening layer with three regions: (1) hardened layer (with fully transformed martensite), (2) heat affected zone (with high amounts of retained austenite) and (3) base metal. However, in sample *A800* because of the low energy density and interaction time, laser penetration is limited and only a narrow heat affected zone is produced with high amounts of retained austenite, rather than a fully transformed martensitic region.
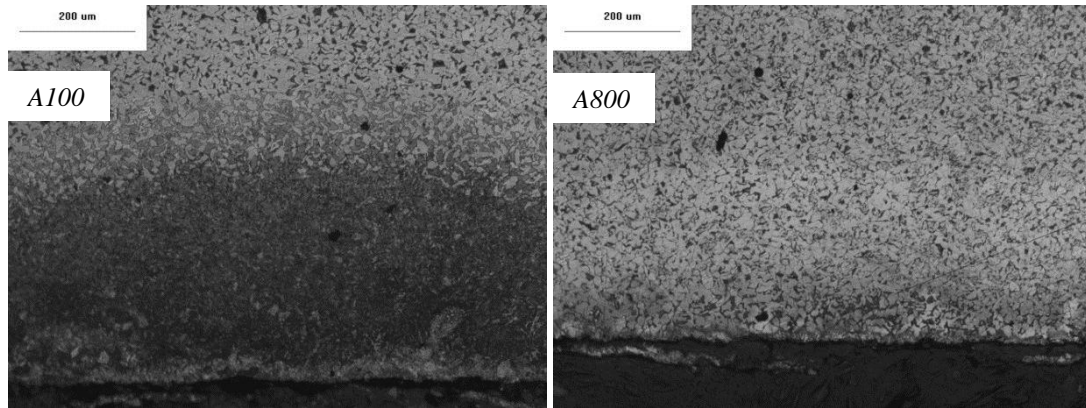
Figure 6-7 Low magnification ($100 \times$) micrographs of samples *A100* and *A800*.

"Figure 6-8, shows the general microstructures in the base metal, Heat Affected Zone (HAZ) and hardened surface of the *A*-samples. Two phases are present in each of the regions: (1) local dark regions,

and (2) light regions with shades of dark in the middle. To further investigate, local hardness measurements were taken from each region. According to Figure 6-8a, the base metal is composed of pearlite in a matrix of ferrite and Fe_3C (light regions). The dark regions of the HAZ also correspond to untransformed pearlite, whereas, the light regions are mainly composed of ferrite. On the other hand, the dark regions in the hardened surface (Figure 6-8b) correspond to martensite due to their high hardness values (489 $HV0.01$), whereas, the lighter regions are partially transformed martensite. Partial martensite transformation may be promoted here by the nonuniform distribution of carbon in the austenite, due to nonhomogenized austenization during rapid heating and cooling." [84].

a) Base Metal and HAZ   *b) Hardened Surface*
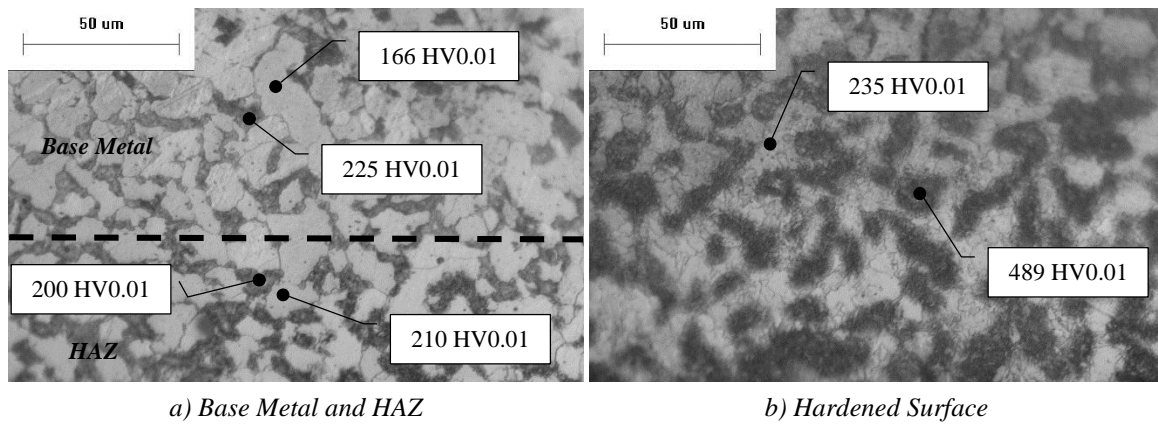
Figure 6-8 Local hardness measurements of dark/light phases from the base metal, HAZ and hardened surface.

"High magnification (500 ×) micrographs of the *A*-samples are shown in Figure 6-9. A fully martensitic morphology is observed in the *A100* specimen in Figure 6-9, as a result of the rapid cooling. Since the rest of the samples have higher cooling rates compared to *A100*, a fully martensitic structure is also expected according to the CCT diagrams shown in Figure 2-5a. However, it is observed that from sample *A300* to *A800* the fully martensitic structure changes to a two micro constituent structure of martensite and ferrite grains. This unexpected reduction of martensite at high cooling rates is a consequence of the rapid heating. Looking at the CHT diagram shown in Figure 2-4a; it was observed that as the heating rate increases during the heating process, higher peak temperatures are required for a homogenous austenization. Whereas, the increased heating rates from sample *A300* to *A800* are associated with a reduction of peak temperature because of increased traveling speeds. As a result, there is insufficient austenite formed during the heating stage to transform into martensite, no matter how high the cooling rate is. Therefore, a high cooling rate at the cooling stage does not always produce the

expected phases and hardness values predicted in a CCT diagram (Figure 2-5) due to the highly non-equilibrium conditions imparted by the rapid thermal cycle. On the other hand, the kinetics of the heating rate and peak temperature during the heating stage also define the final microstructure and its hardness." [84].
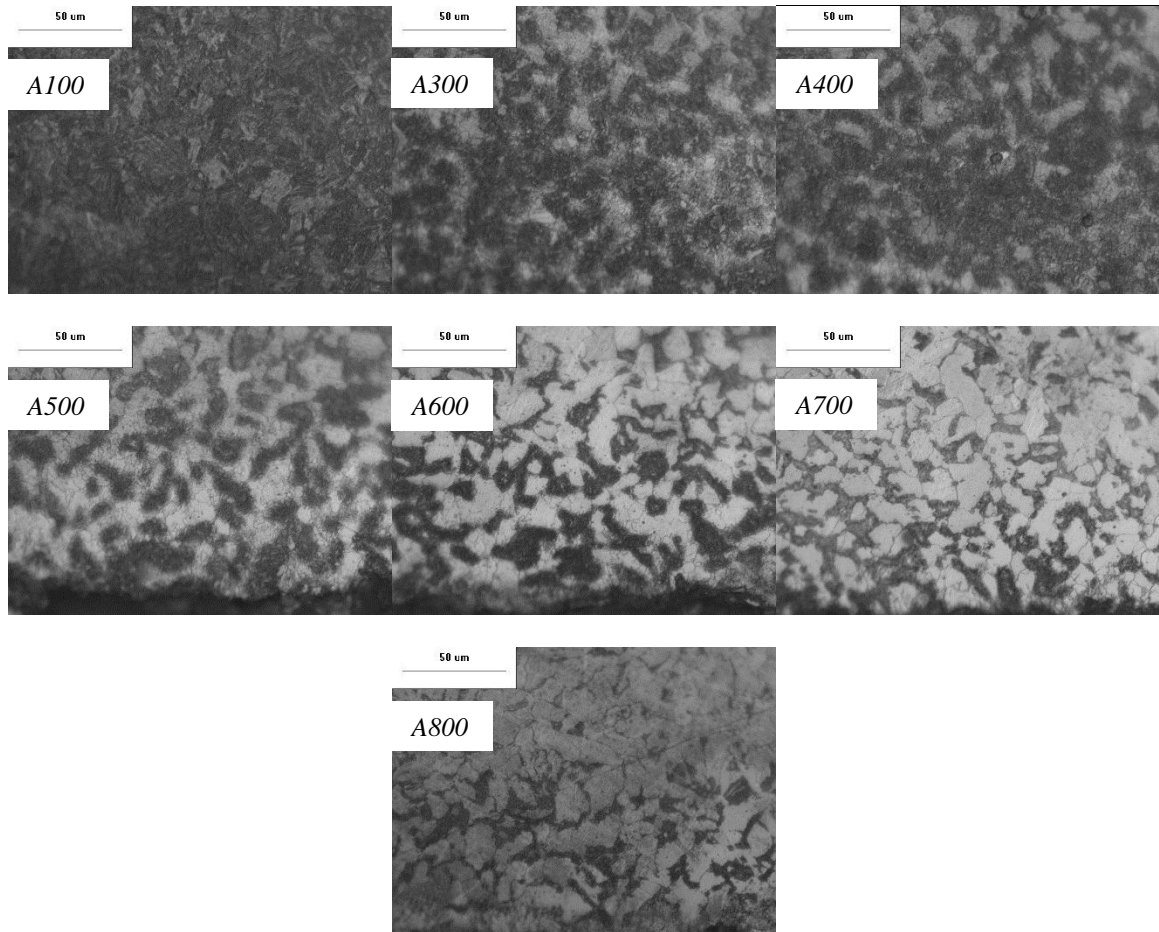
Figure 6-9 High magnification (500 ×) micrographs of *A*-samples.

"Although, the peak temperature for all of the *A*-samples in Figure 6-3 is above the austenization temperature (Section 2.2), the very high heating rates and low peak temperatures achieved in samples *A300-A800* have resulted in a non-homogenized austenization (see CHT diagram of Figure 2-4a). This incomplete austenization process also explains the formation of partially transformed martensite shown in Figure 6-8b. Hence, the reduction of the martensitic region through samples *A100-A800* could be interpreted and correlated to a combination of real-time cooling rate, peak temperature and heating rate data provided by the thermal infrared camera." [84].

111

6.1.1.2 Effect of Laser Power on Thermal Dynamics and Microstructure

"The B-samples were also designed to show the effect of the laser power on thermal dynamics of the LHT process. Figure 6-10, Figure 6-11 and Figure 6-12 illustrate the mean cooling rate, peak temperature and heating rate of the B-samples, respectively. The current measurements show that as the laser power increases in these samples, the cooling rate increases up to $300\,W$ and then suddenly reduces afterwards. Such a cooling reduction can be better understood by considering a similar heating rate trend in Figure 6-12, in which there is a sudden reduction of the heating rate at $300\,W$. This behavior may be due to change in laser absorption coefficient at melting since, the peak temperature for this sample is very close to the melting temperature (see Figure 6-11). Such unpredictable changes of the laser absorption coefficient could only be compensated for through real-time monitoring of the thermal profile. The peak temperature on the other hand, has a more uniform trend; increasing with the laser power. It can be noted that a cubic ($C \propto P^3$) model best describes the cooling rate-laser power relation, whereas, a quadratic model ($T_m \propto P^2$ and $H \propto P^2$) best describe both the peak temperature and heating rate variations with laser power." [84].
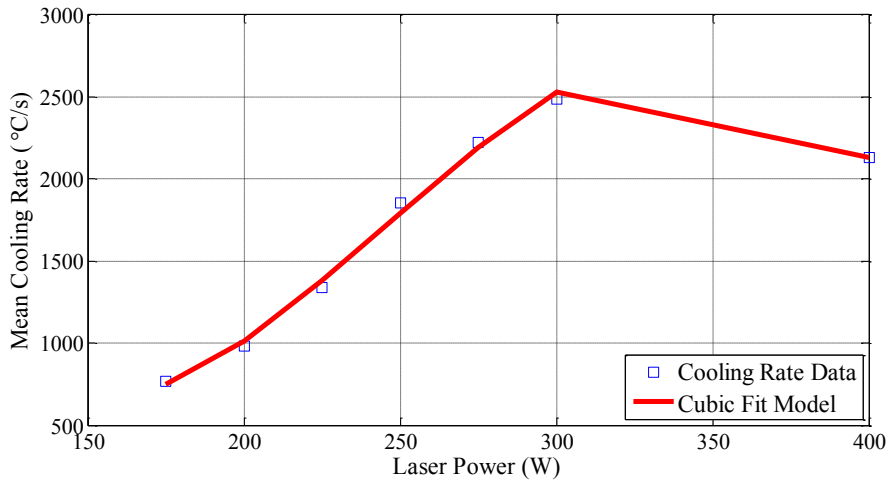
Figure 6-10 Mean cooling rate of the B-samples with respect to the laser power (constant travelling speed at $500\,mm/min$).
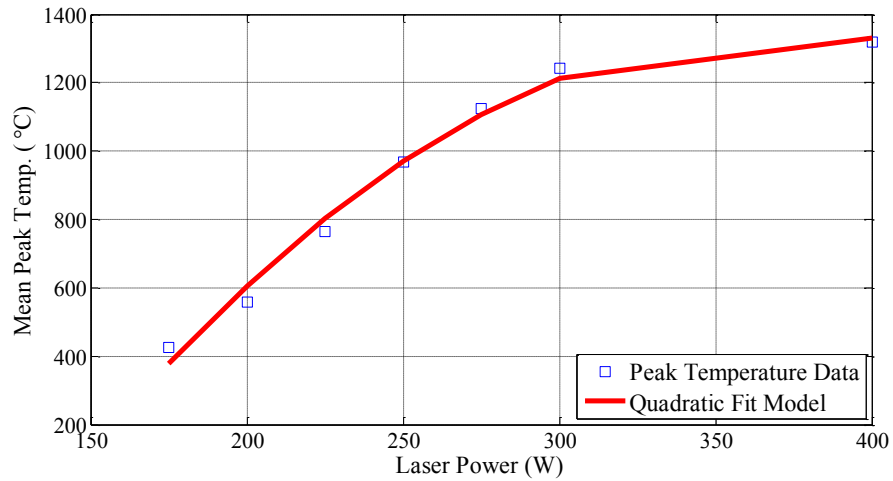
Figure 6-11 Mean peak temperature of the *B*-samples with respect to the laser power (constant travelling speed at 500 mm/min).
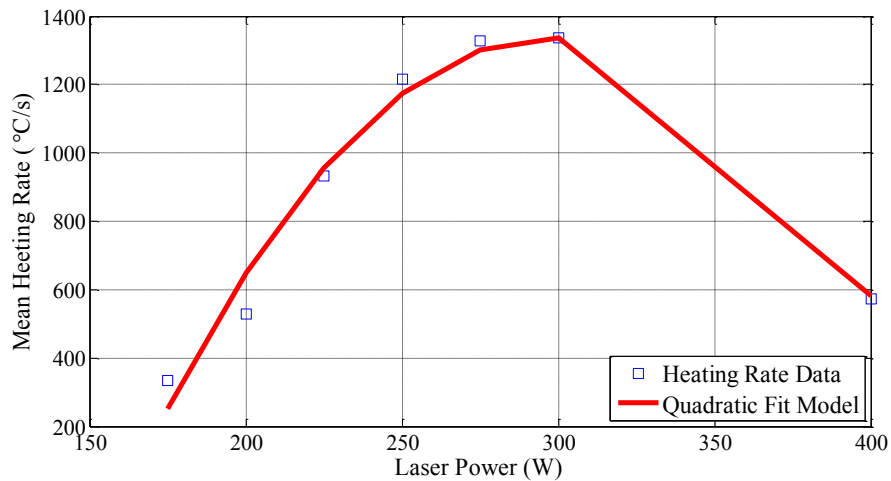
Figure 6-12 Mean heating rate of the *B*-samples with respect to the laser power (constant travelling speed at 500 mm/min).

"Micrographs of the *B*-samples were also investigated. It was observed that only samples *B250-B400* produced a hardened region and samples *B175-B225* did not have enough energy to penetrate into the substrate. Similar to the micrographs shown in Figure 6-9, sample *B400*, which has the highest melt pool temperature had a fully martensitic microstructure, whereas, from samples *B300* to *B250* the

martensite regions reduced. Similar to the *A*-samples, the reduction of the martensite regions from *B300* to *B250* could be anticipated based on non-homogenized austenization as a result of high heating rates and a low peak temperature." [84].

6.1.1.3 Prediction of Hardness via Real-Time Monitoring of the Thermal Dynamics

"The microstructure of a hardened surface determines the final hardness in an LHT process. To further evaluate hardness changes with respect to the correlation between microstructure and thermal history, microhardness measurements of the *A* and *B*-samples are shown in Figure 6-13 and Figure 6-14, respectively. In both cases, the hardness increases as the amount of martensite regions increase with increased peak temperature, while softening occurs at very high cooling and heating rates, as a result of less martensite formation. However, sample *A100*, which has the highest peak temperature has a lower amount of hardening immediately at the surface compared to the lower points of the hardened region. The peak temperatures in sample *A100* ($T_{A100} \approx 1500\,°C$) are very close to the liquidus temperature of AISI 1020, causing partial melting at the top surface and a corresponding reduction in hardness. According to the CCT diagram shown in Figure 2-5b, as the cooling rate decreases, it will get closer to the critical cooling rate value, which reduces the production of unstable martensite phases. Such a behavior is observed in sample *A100*, in which the higher temperature and melting phenomena reduce the cooling rate drastically. Consequently, the amount of martensite formation and hardness are reduced in this sample because of melting. By comparing thermal dynamics of the *A300* and *B300* samples, it is understood that the peak temperature of the two samples are the same $T_{A300} \approx T_{B300} \approx 1200\,°C$, however, the cooling and heating rates of *A300* are much lower compared to *B300*; $C_{A300}(\approx 1750\,°C/s) < C_{B300}(\approx 2500\,°C/s)$ and $H_{A300}(\approx 500\,°C/s) < H_{B300}(\approx 1350\,°C/s)$. Since the cooling and heating rates of *A300* are lower, the austenization is more extensive and homogenous, which allows for more material to transform to martensite, and produce a higher hardness value. Therefore, it is evident that no single parameter plays a defining role during the LHT process. On the other hand, all of the three thermal characteristics (cooling rate, peak temperature and heating rate) are effective and should be monitored and controlled simultaneously to produce a desired hardness values." [84]. Nonetheless, since the peak temperature has a direct effect on both of the austenization and martensite formation processes, it has the major role in defining the value of the hardness. This is confirmed by the positive correlation between the mean peak temperature values of samples *A* and *B* and their respective hardness values. In fact, it is observed that the hardness of each sample increases with increased peak temperature, while the peak temperature is below the melting point.

114
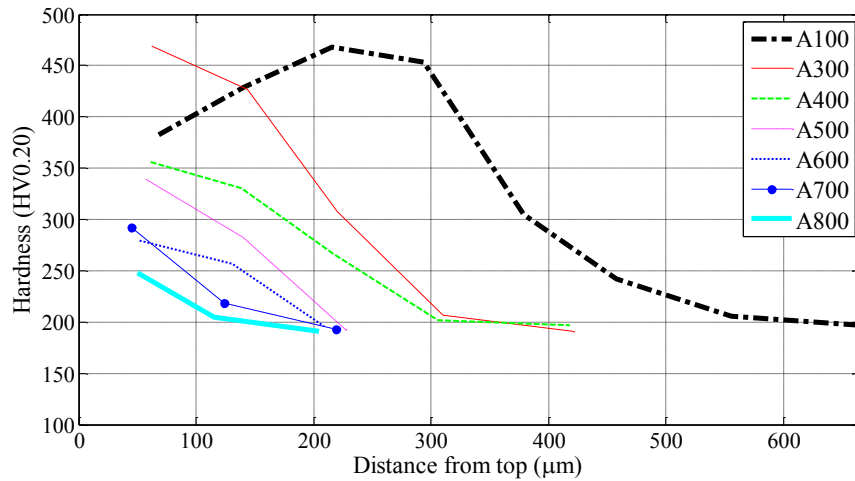
Figure 6-13 Hardness of the *A*-samples with constant laser power (250 *W*) and changing travelling speed (the number after the letter *A* indicates the travelling speed in *mm/min*).
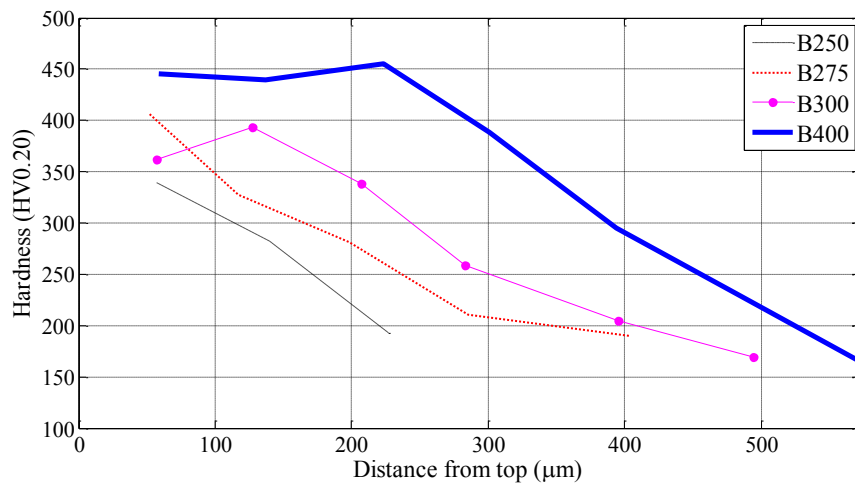
Figure 6-14 Hardness of the *B*-samples with constant travelling speed (500 *mm/min*) and changing laser power (the number after the letter *B* indicates the laser power in *W*).

6.1.1.4 Prediction of Hardening Depth via Real-Time Monitoring of Thermal Dynamics

"The most important geometry characteristic of an LHT process is the hardening depth. Direct measurement of the hardening depth through CCD-based imagery is impossible therefore, the only way to predict the depth is to somehow monitor and correlate the thermal dynamics with the hardened depth. The hardening depth of the *A* and *B*-samples were measured and plotted against their cooling rate and

115

peak temperature values in Figure 6-15 and Figure 6-16, respectively. It is noteworthy that the hardening depth measurements included the HAZ height as well. The cooling rate does not have any positive correlation with the hardening depth whereas, the peak temperature is in direct correlation with the hardening depth. In fact, the hardening depth has a linear relation with the peak temperature, which is an insightful observation for the development of a closed-loop controller for the hardening depth. In other words, controlling the peak temperature will result in an indirect control of the hardening depth."
[84].
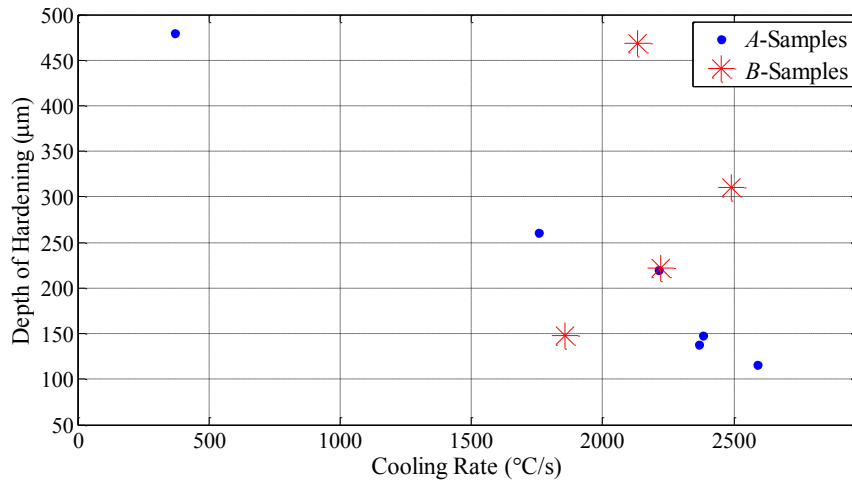
Figure 6-15 Hardening depth of the *A* and *B*-samples with respect to their cooling rate.
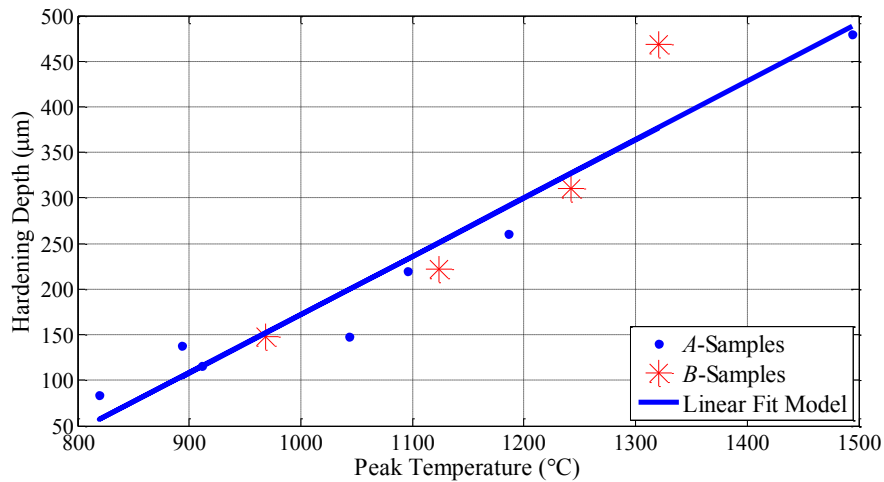
Figure 6-16 Hardening depth of the *A* and *B*-samples with respect to their peak temperature.

116

6.1.2 Microstructure Analysis of Laser Additive Manufacturing Process

Micrographs, microhardness tests and geometry measurements of the experiments discussed in Section 6.1.1 are presented in this section. The real-time thermal dynamics of the LAM process recorded during these experiments are also reported and compared to recordings of the LHT samples. These thermal recordings are correlated with microstructure evolutions to identify a closed-loop scheme for the purpose of real-time microstructure control.

6.1.2.1 Effect of Travelling Speed on Thermal Dynamics and Microstructure

The *C*-samples were designed to show the effect of the laser travelling speed on thermal dynamics of the single-track LAM process and consequently the microstructure. The real-time cooling rates of the *C*-samples with their mean values with respect to the travelling speed are shown in Figure 6-17 and Figure 6-18, respectively. Similar to the LHT samples in the previous section, the cooling rate increases with increasing travelling speed. In addition, it is interesting that in the majority of the LAM samples, the cooling gradually reduces during the deposition as a result of heat accumulation. This cooling reduction as a result of heat accumulation is more evident in the LAM samples compared to the LHT samples.
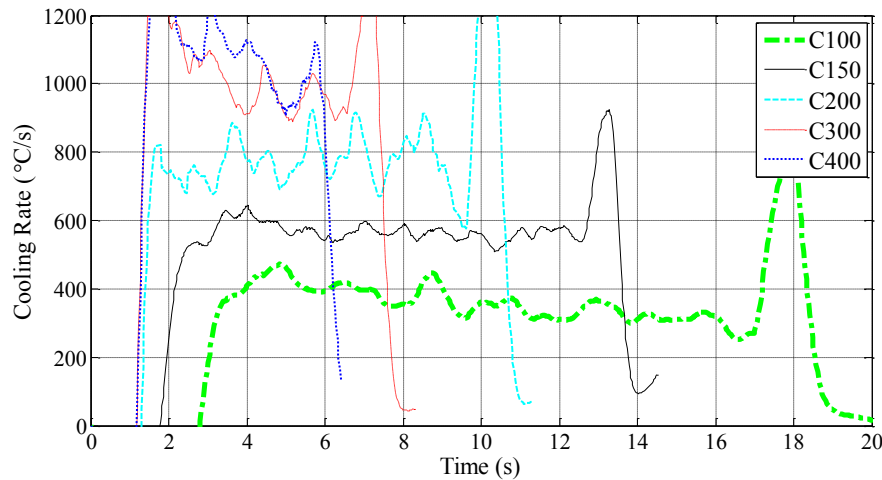
Figure 6-17 Real-time cooling rate of the *C*-samples with constant power ($800\ W$) and changing travelling speed (the number after the letter *C* indicates the travelling speed in mm/min).

117
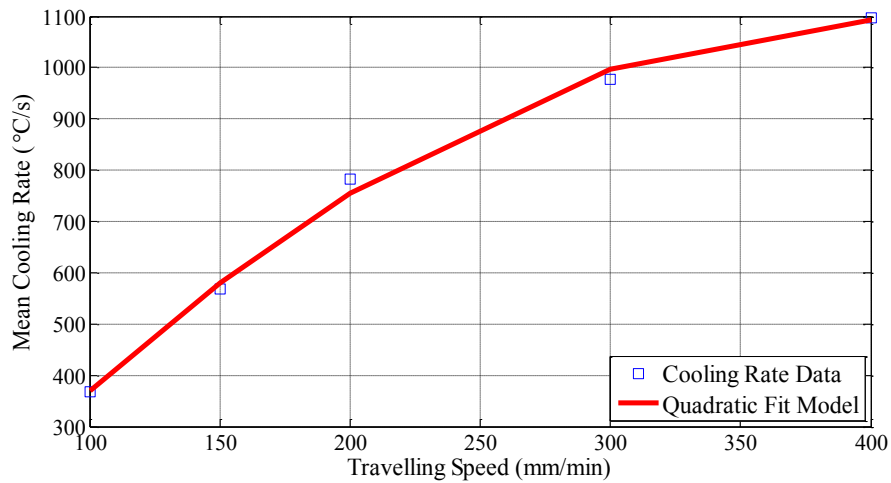
Figure 6-18 Mean cooling rate of the *C*-samples with respect to the travelling speed (constant power at 800 *W*).

The real-time melt pool temperatures of the *C*-samples with their mean values with respect to the travelling speed are shown in Figure 6-19 and Figure 6-20, respectively. In contrast to cooling rate variations, the melt pool temperature variations are not as drastic as the LHT samples during the LAM depositions. However, the general trend is similar to the LHT samples in which the melt pool temperature reduces with increasing travelling speed.
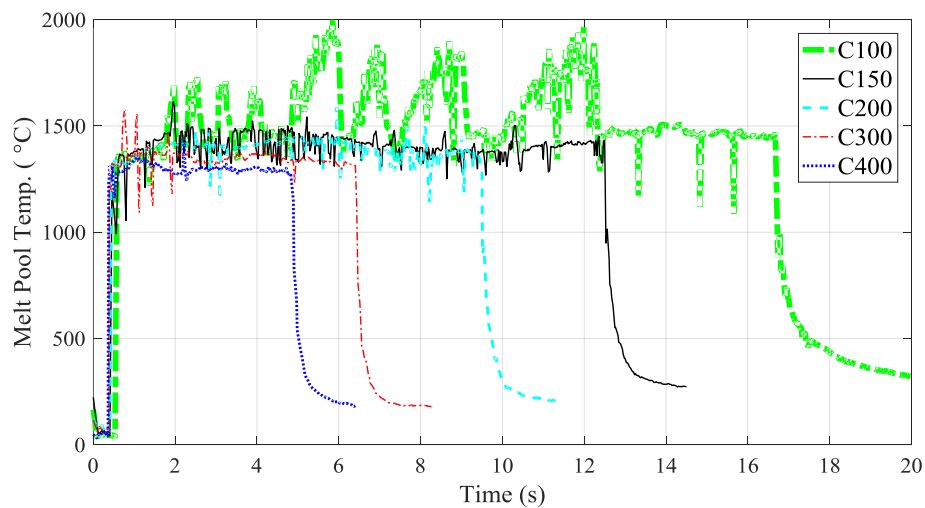
Figure 6-19 Real-time melt pool temperature of the *C*-samples with constant power (800 *W*) and changing travelling speed (the number after the letter *C* indicates the travelling speed in *mm/min*).

118
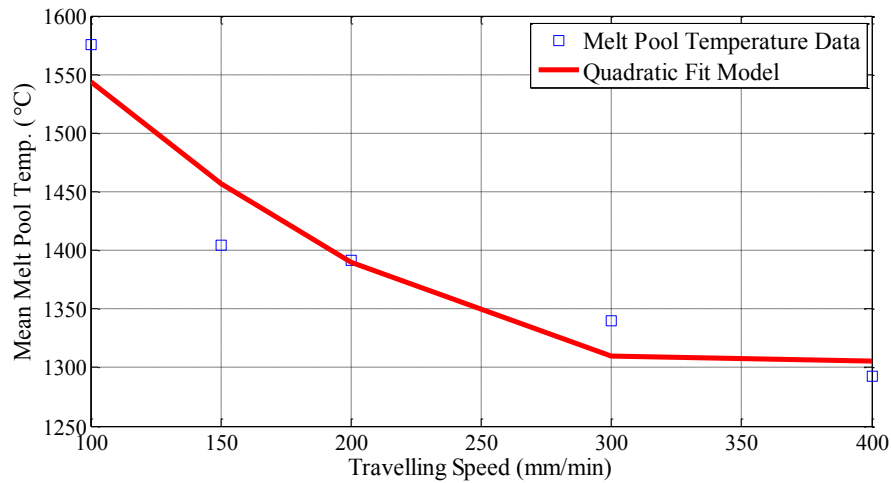
Figure 6-20 Mean melt pool temperature of the *C*-samples with respect to the travelling speed (constant power at 800 *W*).

The microstructures of the *C*-samples are shown in Figure 6-21. During LAM, the AISI 4340 sample undergoes a complete solidification process. The phase changes the steel experiences during this solidification process are indicated in Figure 2-3, which include (Liquid) → γ (Austenite) + (Liquid) → γ (Austenite) → $\gamma + \alpha$ (Austenite + Ferrite) → $\alpha +$ $Fe3C$ (Ferrite + Cementite). However, since the LAM process is a fast cooling non-equilibrium solidification process, it results in non-equilibrium phases such as martensite during solid transformation. Since LAM depositions produce high cooling rates, the martensite phase will be the dominant phase formed during the solid state transformations. In the case of LAM depositions, the rate of solidification can cause some austenite plus ferrite to form, which will reduce the fraction of martensite from the partial austenite. Thus, it can be seen that as the cooling rate of the samples increases and the peak temperature reduces, the amount of martensite reduces likewise. It is predicted that higher cooling rates results in either finer austenite formation or even a mixed ferrite plus austenite structure, which will result in a lower martensite formation and reduced final hardness value. This general change of microstructure can be roughly observed in the micrographs illustrated in Figure 6-21. Therefore, the overall morphology and amount of maretnesite formation in AISI 4340 depositions can be generally predicted in-situ using the real-time thermal dynamics of the cooling rate and melt pool temperature.
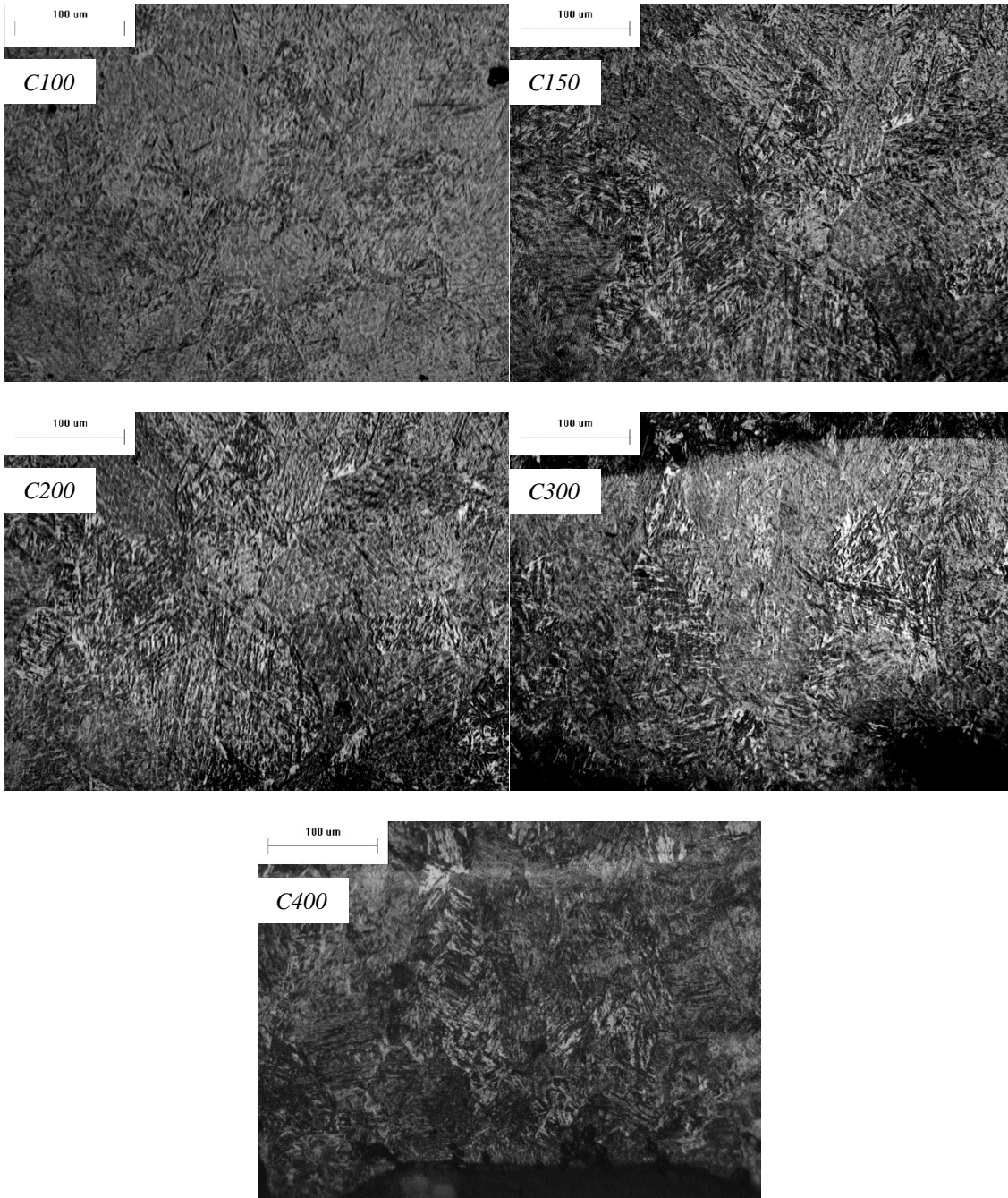
Figure 6-21 High magnification (200 ×) micrographs of *C*-samples.

6.1.2.2 Prediction of Hardness via Real-Time Monitoring of Thermal Dynamics

Microhardness of the *C*-samples with respect to the travelling speed, real-time cooling rate and melt pool temperature are shown in Figure 6-22. In contrast to the AISI 1020 heat treated samples (Figure 6-13 and Figure 6-14), the AISI 4340 depositions of the *C*-samples had a consistent hardness throughout the whole cross section. Similar to LHT samples, the hardness reduces with the increasing traveling speed. The increasing cooling rate from samples *C100* to *C400* increase the chances of martensite formation as outlined by the 4340 CCT diagram of Figure 2-5b. However, similar to the *A* and *B*-samples of the LHT process (Section 6.1.1.3), the lower melt pool temperature and rapid heating rate at higher speeds limits austenization, and corresponding formation of martensite. Therefore, it is observed again that although the high cooling rate of the LMP process satisfies martensite formation, the melt pool temperature and heating rate values of the *C*-samples can limit the hardening process. More importantly, according to Figure 6-22 the cooling rate has a good correlation with the hardness value, whereas, the melt pool temperature does not have a positive correlation with the hardness. Therefore, the real-time cooling rate can be a good indicator of the deposition hardness during the LAM process for online monitoring and control of the hardness.
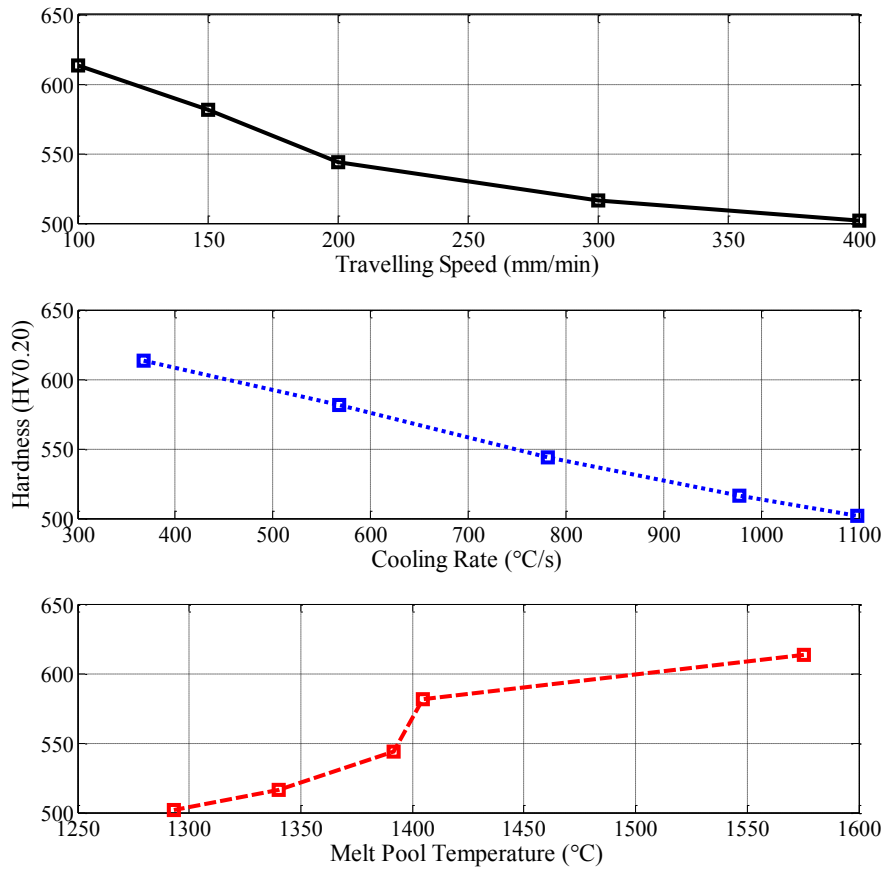
Figure 6-22 Hardness of the *C*-samples with respect to the travelling speed, cooling rate and melt pool temperature (constant power at 800 *W*).

6.1.2.3 Prediction of Hardness in Multi-Track Depositions via Real-Time Monitoring of Thermal Dynamics

The multi-track *D*-samples were designed to study hardness variation of multi-track laser additive manufacturing based on thermal dynamics. The real-time cooling rate and melt pool temperature of the *D*-samples are shown in Figure 6-23 and Figure 6-24, respectively. Each of the three bumps in the recordings indicates the thermal history of each of the three tracks during the deposition of every *D*-sample. It is interesting the melt pool temperature of the three tracks of each sample does not change significantly. On the other hand, for samples *D100* and *D150* that have a lower speed compared to *D200*, the cooling rate drops in the second and third tracks as a result of the preheating caused by prior

depositions. Moreover, at the time of deposition of the second or third tracks the previous tracks will act as a heat sink, increasing the directions of the heat flow and reducing the cooling. In *D200* however, since the travelling speed and cooling rate are higher there is not enough heat accumulated in the substrate to reduce the cooling of the later tracks.
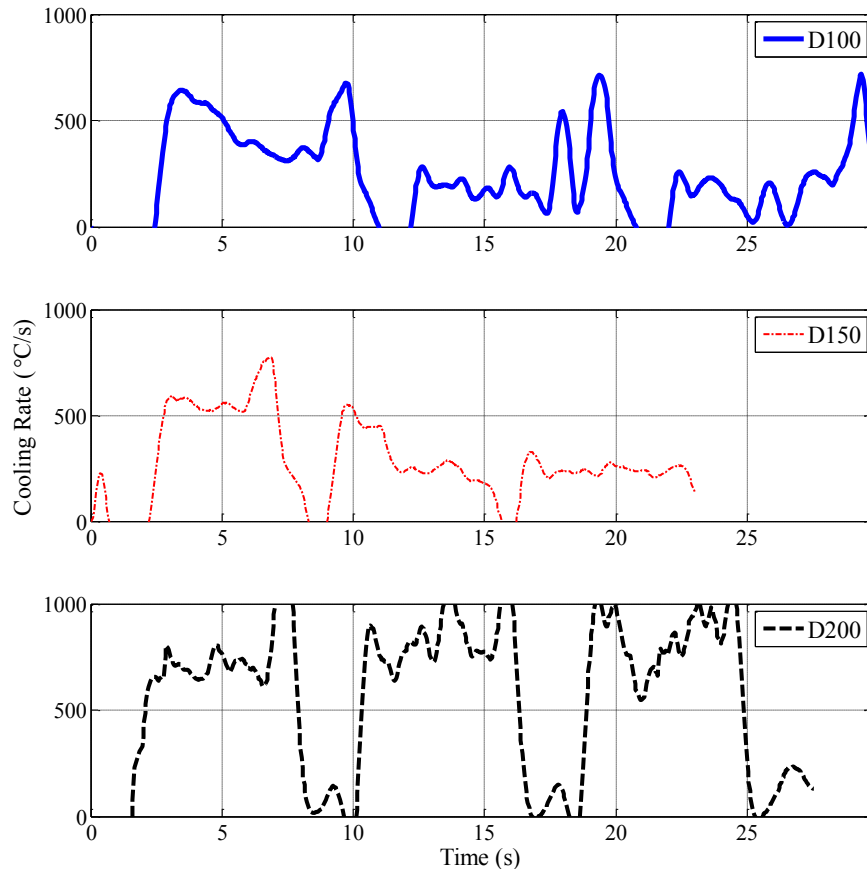
Figure 6-23 Real-time cooling rate of the multi-track *D*-samples (25% overlap) with constant power (800 *W*) and changing travelling speed (the number after the letter *D* indicates the travelling speed in *mm/min*).

The hardness of each track in every *D*-sample is listed in Table 6-2. The second and third tracks in samples *D100* and *D150*, which had a lower cooling rate compared to the first track have higher hardness. The hardness reduction is due to tempering of the first track caused by the later track depositions. However, in sample *D200* all of the three tracks have nearly the same hardness, which is

123

in positive correlation with their similar cooling rate history. Therefore, the hardness of multi-track LAM depositions is in great correlation with the cooling history of each line during depositions, whereas, the melt pool temperature recordings of the lines do not provide any information on the hardness variations. Further evaluation of the cooling rate effect on multi-track LAM process is required to generalize the current conclusion, however, the current cooling rate-hardness correlations could provide a basis for the development of a closed-loop hardness control in LAM based on cooling rate control.
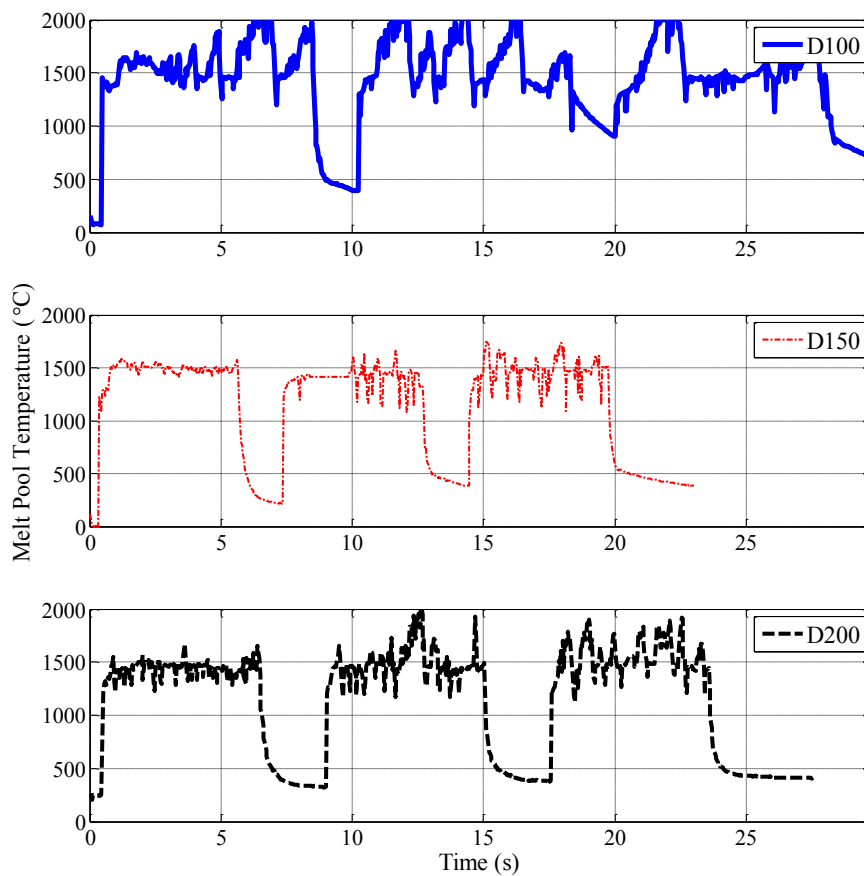
Figure 6-24 Real-time melt pool temperature of the multi-track *D*-samples (25% overlap) with constant power ($800\ W$) and changing travelling speed (the number after the letter *D* indicates the travelling speed in mm/min).

Table 6-2 Hardness of each track in the multi-track LAM depositions of the _D_-samples.

Sample No.	Track 1 (HV0.20)	Track 2 (HV0.20)	Track 3 (HV0.20)
_D100_	450	583	545
_D150_	400	465	520
_D200_	410	475	430

6.2 Adaptive Thermal Dynamics Estimation of Laser Materials Processing

A finite difference approach was used in Section 4.3 to develop an adaptive numerical thermal model for the LMP process, which can be utilized for thermal estimations and model-based controller design. The model can be limited to a restricted region on the workpiece in order to reduce calculation time for real-time estimation and control. In addition, the boundary conditions of the region of interest can be updated online by real-time measurements of the thermal infrared camera, which develops a reliable observer model for any observer state feedback control system. While the numerical model developed has a higher accuracy compared to analytical modeling techniques, it is as computationally fast as an analytical solution. However, before being implemented in actual estimation and control applications, the model must be verified experimentally.

In this section, the results of the experiments designed for thermal model verification (Section 5.3) are discussed in detail. The indirect online microstructure identification experiments described in the previous section indicated that the laser power and travelling speed both have a significant effect on the thermal dynamics and consequently microstructure evolutions. Thus, initially the system dynamics are excited by a variety of different excitation signals for the laser power and travelling speed. The model is verified and tuned based on these dynamics for both of the LHT and LAM processes.

6.2.1 Thermal dynamics Modelling of the Laser Heat Treatment Process

The first step before the model validation process is the selection of an appropriate restricted nodal network defined by the _M_ and _N_ values shown in Figure 4-3. Several LHT tests with different nodal network size were initially conducted during which the temperature of the boundary nodes were recorded. Accordingly, the size of the region of interest (_M_ and _N_), was chosen big enough so that the measured temperatures of the boundary nodes remain consistent with minimum variations during process parameter changes. Consequently, it will be correct to assume fixed boundary conditions in an _M_ by _N_ region of interest. Assigning a restricted nodal network with such dimensions will justify the

correct implementation of fixed boundary conditions through online and offline model calculations. Moreover, by selecting a big enough region of interest with fixed boundary conditions, the dynamic model can provide faster calculations with less required memory. After the selection of an appropriate restricted nodal network (M and N), and defining the material and model parameters ($\rho, c_p, A_{abs}, \Delta t$ and $\Delta \xi$), the equivalent thermal conductivity $\hat{k}_{eq}$ and temperature bias $\hat{T}_{bias}$, have to be tuned.

Since the model is going to be used primarily as an observer for real-time estimation and control, it is significantly important that it represents and predicts the dynamics of the system. In the current LMP system, these dynamics are represented by the thermal dynamics and their variations with respect to input process parameters in time. Therefore, the real-time thermal dynamics measurements provided by the thermal-geometry monitoring and control module is the ideal benchmark for validation of thermal models or simulations. Although, the thermal infrared measurements may not represent the exact actual values of melt pool temperature, cooling rate or heating rate, they do provide a precise recording of the dynamics of these thermal dynamics variables. These dynamics can be used for real-time control or identification of the LMP thermal process.

In order to be applicable for process estimation and control, an LMP thermal model has to represent the total dynamic behavior of the LMP system. Consequently, it is necessary to excite all modes of the LMP dynamic system in order to compare the system response with the predicted model response for obtaining a general verification of the model accuracy and precision. To capture the different dynamic modes of the LHT process, it is required to excite the system with a variety of input signals. It was observed in Section 6.1.1 that the laser power and travelling speed have a high degree of influence on the thermal dynamics of the LHT process. As a result, the *E*-sample experiments were designed for model verification, in which the laser power and travelling speed input signals are changed in time using a variety of step and ramp functions to evaluate the dynamic response of the developed model.

The model was tuned for the LHT thermal process using the verification schema described in Section 4.3.9.1. The thermal dynamics data recorded for the *E1* sample was used as the tuning data. The *E1*-sample is excited by a two-step travelling speed function schematically shown in Table 5-4. This sample is an ideally rich signal for validation, since it will provide the thermal response of the LHT system to three different travelling speeds and in real-time conditions. The parameters of the tuned model are presented in Table 6-3.

Table 6-3 Tuned model parameters for the LHT process.

$\rho\ (\frac{kg}{m^3})$	$c_p\ (\frac{J}{kg.K})$	A_{abs}	$\Delta t\ (s)$	$\Delta \xi\ (m)$	N	M	$\widehat{k}_{eq}\ (\frac{W}{m.K})$	$\widehat{T}_{bias}(°C)$
7850	500	0.30	5.00e-03	3.44e-04	6	17	10	500

The input excitation and real-time response of the LHT process for sample *E1* is illustrated in Figure 6-25. The response of the tuned model is also provided in this figure for both of the nonlinear and linear models represented by Eqs. (4.31) and (4.33). As described in Section 4.3.7, the response of the nonlinear model is evaluated for real-time adaptive and fixed constant boundary conditions, whereas, the linear model is evaluated under fixed adaptive boundary conditions. As prescribed by the verification schema described in Section 4.3.9.1, the real-time peak temperature and cooling rate response are used for model tuning and validation. According to the process and model response provided in Figure 6-25, the developed model precisely tracks and predicts the dynamic behavior of the peak temperature and cooling rate. In fact, the model response is so accurate that for most of the experimental duration it overlies on the real-time process response.

In order to evaluate the precision of the developed modeling technique quantitatively, the Mean Absolute Deviation (MAD) of the model response is calculated based on the below formula:

$$MAD = \frac{1}{p_f} \sum_{j=1}^{p_f} |\hat{y}_{model} - y_{process}| \tag{6.1}$$

in which $\hat{y}_{model}$ is the model estimation, $y_{process}$ is the measured process output, and p_f is the total number of sample times for the whole experiment. The MAD is the average magnitude of deviation from the process output in a set of model predictions. Therefore, the MAD value has the same units of the proposed model response. For the current model, the MAD is calculated for both of the peak temperature and cooling rate predictions.

It is also important to understand the relative error of the model deviation with respect to the absolute value of the measured response. Therefore, the Mean Deviation Error (MDE) of the peak temperature and cooling rate predictions, which is reported in percentage error (%), is calculated based on the following formulation:

$$MDE = \frac{MAD}{\frac{1}{p_f} \sum_{j=1}^{p_f} |y_{process}|}. \tag{6.2}$$

127
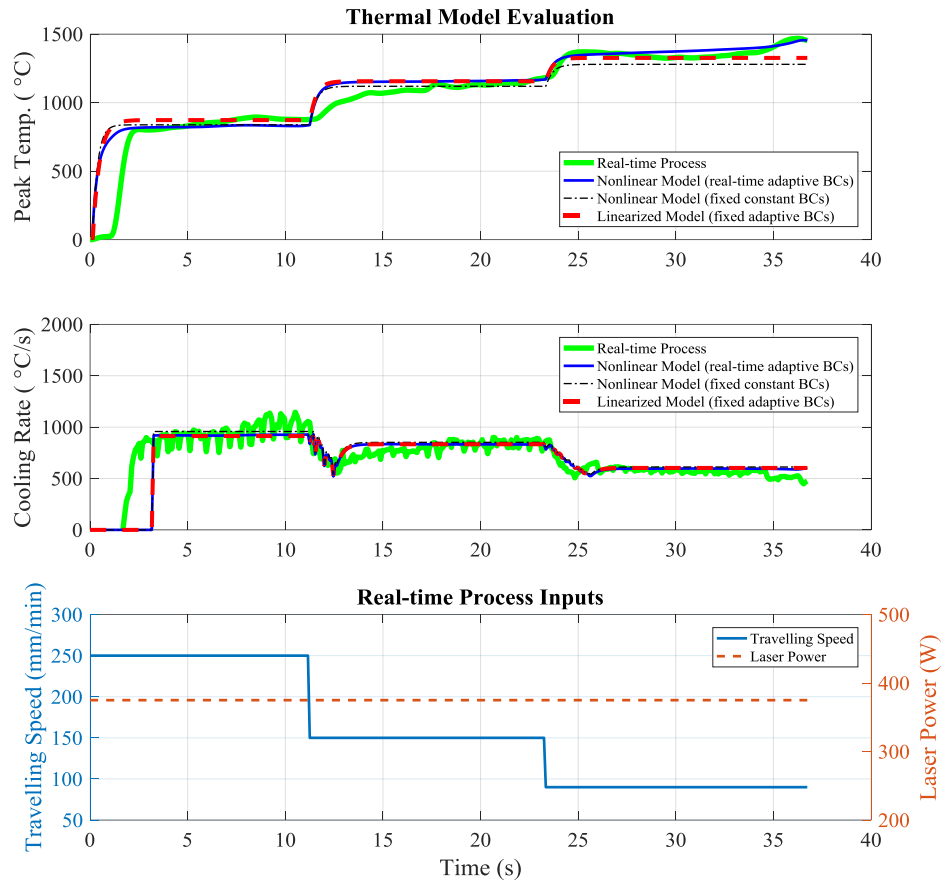
Figure 6-25 Thermal model validation and tuning for LHT sample *E1*.

Table 6-4 Mean Absolute Deviation (MAD) and Mean Deviation Error (MDE) for sample *E1*.

	Nonlinear Model (real-time adaptive BCs)	Nonlinear Model (fixed constant BCs)	Linearized Model (fixed adaptive BCs)
Peak Temperature Deviation (°C)	44.42	52.09	39.20
Peak Temperature Error (%)	3.77	4.42	3.33
Cooling Rate Deviation (°C/s)	55.15	61.12	56.78
Cooling Rate Error (%)	7.49	8.30	7.71

The MAD and MDE of the peak temperature and cooling rate predictions for the tuning data of sample *E1* are calculated and reported in Table 6-4. The range of error for the model peak temperature

estimation for all of the three models with the different BC types is between ± 3.77 % and ± 4.42 %, which indicates a highly accurate modeling when compared to the infrared thermal camera resolution that is ± 2.00 %. Moreover, the range of error for the cooling rate estimations are also between ± 7.49 % and ± 8.30 %, which is again a highly accurate estimation of the system when compared to the resolution of the measured cooling rate data that is ± 4.00 %. In Figure 6-25, it is evident that a great portion of the calculated model deviations and error are due to the noisy oscillations of the real-time process response caused by inconsistent measurement and thermal dynamics calculations. The oscillations of these noise signals are specifically observed for the cooling rate response, which is mainly due to the thermal dynamics algorithm calculations described in Figure 3-9. Nonetheless, the peak temperature and cooling rate predictions overly on the average of the measured oscillations and are therefore, a very good indicator of the denoised response.

According to the MAD data provided in Table 6-4, the mean deviation of the model peak temperature prediction is between $\pm 39.20\,^\circ\text{C}$ and $\pm 52.09\,^\circ\text{C}$, which is completely acceptable for microstructure and geometry identification and control, since these properties do not change significantly within these temperature deviations. The mean deviation of the cooling rate estimation with respect to the real-time process input is also calculated as $\pm 55.15\,^\circ\text{C}/s$ and $\pm 61.12\,^\circ\text{C}/s$, which is also acceptable, since it does not affect the microstructure and geometry prediction and control process.

In order to verify the accuracy of the developed model even further, the tuned model response was evaluated in real-time for unseen processing conditions. The dynamic modes of the LHT thermal system were thoroughly excited using a variety of combined multi-step and ramp signals for the travelling speed and laser power. The thermal dynamics data recorded through samples *E2-E4* (described in Table 5-4) were used for verification of the tuned model. Sample *E2* excites the system with a decreasing ramp signal for the travelling speed from 250 to $90\ mm/min$. Sample *E3* excites the system with an increasing two-step laser power signal at $325, 375$ and $425\ W$. Finally, sample *E4* provides an excitation in the system by an increasing laser power ramp signal from 325 to $425\ W$. The real-time process thermal data and model predictions for samples *E2*, *E3* and *E4* are illustrated in Figure 6-26, Figure 6-27 and Figure 6-28, respectively. The MAD and MDE calculations of the model predictions for these samples are also reported in Table 6-5, Table 6-6 and Table 6-7, respectively.
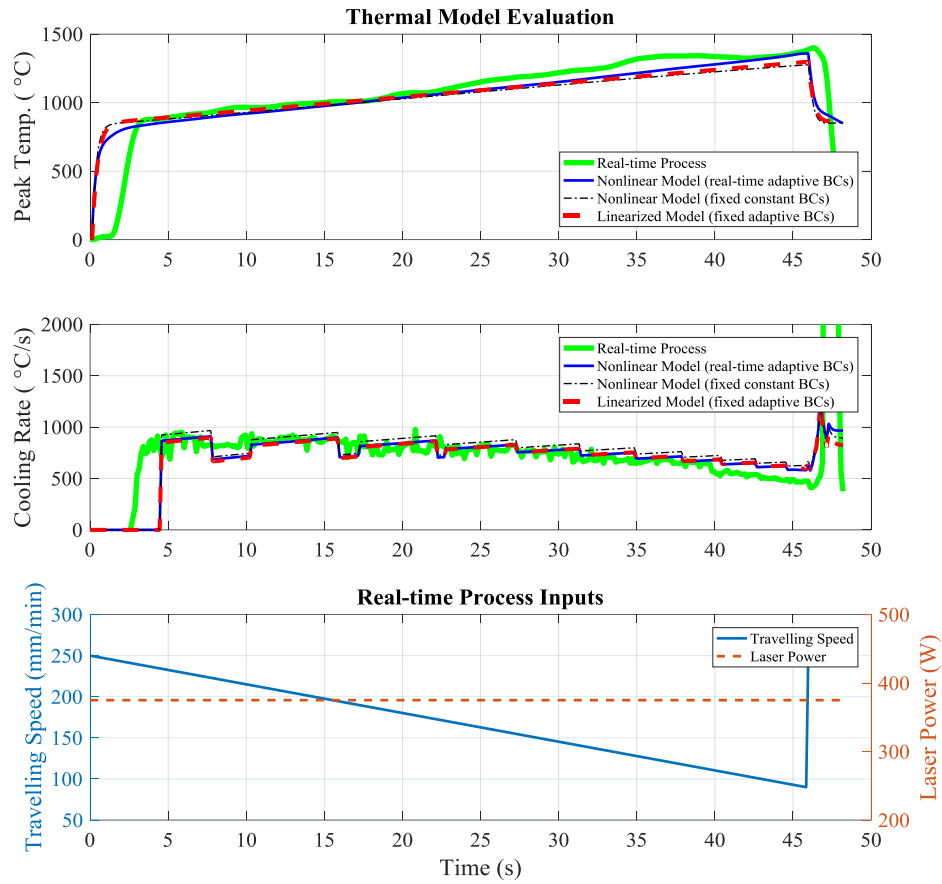
Figure 6-26 Thermal model evaluation for LHT sample *E2*.

Table 6-5 Mean Absolute Deviation (MAD) and Mean Deviation Error (MDE) for sample *E2*.

	Nonlinear Model (real-time adaptive BCs)	Nonlinear Model (fixed constant BCs)	Linearized Model (fixed adaptive BCs)
Peak Temperature Deviation (℃)	65.99	87.78	74.96
Peak Temperature Error (%)	5.55	7.38	6.31
Cooling Rate Deviation (℃/*s*)	48.20	83.11	49.07
Cooling Rate Error (%)	6.46	11.13	6.57

130
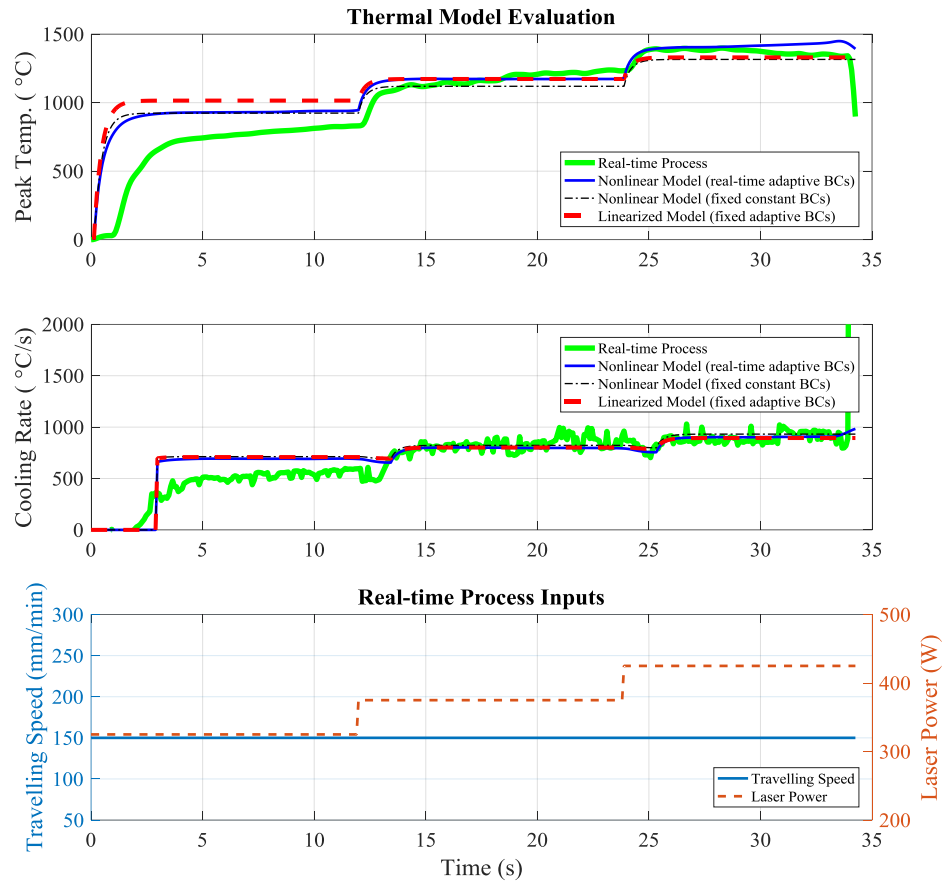
Figure 6-27 Thermal model evaluation for LHT sample *E3*.

Table 6-6 Mean Absolute Deviation (MAD) and Mean Deviation Error (MDE) for sample *E3*.

	Nonlinear Model (real-time adaptive BCs)	Nonlinear Model (fixed constant BCs)	Linearized Model (fixed adaptive BCs)
Peak Temperature Deviation (℃)	48.22	73.08	70.80
Peak Temperature Error (%)	4.09	6.20	6.00
Cooling Rate Deviation (℃/*s*)	67.38	73.31	70.20
Cooling Rate Error (%)	8.71	9.47	9.07
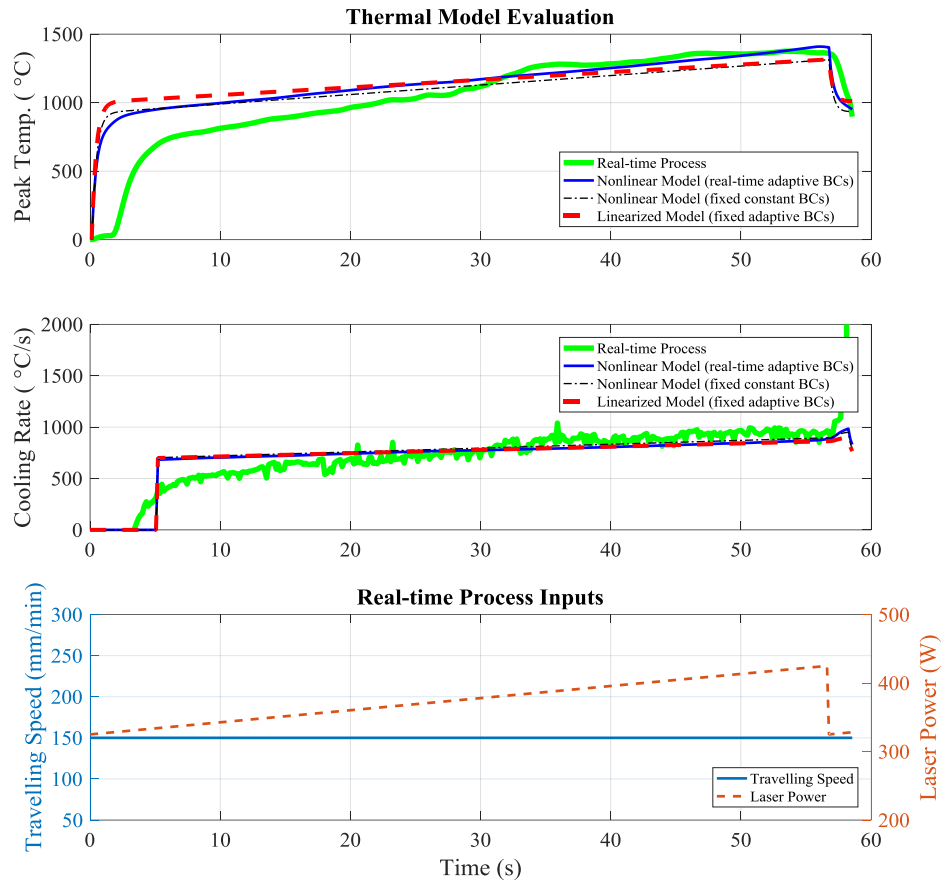
Figure 6-28 Thermal model evaluation for LHT sample *E4*.

Table 6-7 Mean Absolute Deviation (MAD) and Mean Deviation Error (MDE) for sample *E4*.

	Nonlinear Model (real-time adaptive BCs)	**Nonlinear Model** (fixed constant BCs)	**Linearized Model** (fixed adaptive BCs)
Peak Temperature Deviation (℃)	63.32	84.32	89.54
Peak Temperature Error (%)	5.35	7.12	7.56
Cooling Rate Deviation (℃/s)	72.19	66.62	72.70
Cooling Rate Error (%)	9.00	8.30	9.06

The real-time model estimation provided in Figure 6-26, Figure 6-27 and Figure 6-28, illustrated a highly accurate estimation of the LHT thermal process obtained by the nonlinear and linear models

132

prescribed by Eqs. (4.31) and (4.33), respectively. For each excitation signal, the model provides precise estimations of the system dynamics by tracking the variations of the peak temperature and cooling rate signals. The model deviation and error values for the verification experiments, reported in Table 6-5, Table 6-6 and Table 6-7, are also in the same range as the tuning data error and deviation, which specifies a generalized verified model over a broad range of processing parameters. Nonetheless, for the laser power excitation signals (Figure 6-27 and Figure 6-28), the predictions have a respective larger error and deviation in the lower laser powers. Such deviation may be caused by a lower laser absorption A_{abs} at low laser powers, which will result in lower amount of absorbed heat and temperature. These small process variations can be represented in the model by using "real-time adaptive" equivalent thermal conductivity and temperature bias coefficients $\hat{k}_{eq}(t)$ and $\hat{T}_{bias}(t)$, instead of the current fixed adaptive coefficients $\hat{k}_{eq}$ and $\hat{T}_{bias}$. Through adaptive adjustments to the equivalent thermal conductivity coefficient $\hat{k}_{eq}(t)$, in real-time, the lower laser absorptivity and heat accumulation at low laser powers can be embodied in the medium.

Comparing the predictions of the linearized estimation model (Eq. (4.33)) with the original nonlinear model (Eq. (4.31)) in samples *E1-E4*, it is safe to assume the linearized model response as accurate as the nonlinear formulation. The dynamics of both equations are very similar, and the deviation and error values of both modeling techniques are very similar for the peak temperature and cooling rate estimations. Moreover, it is observed that all of the three different boundary conditions types (described in Section 4.3.7), provide eligible and exact predictions. Nevertheless, the fixed constant boundary condition type, which was fixed at $\bar{T}_{BC} = 150\ ^\circ\mathrm{C}$, for all temperature nodes yields the highest error. This high error is understandable since assuming a constant temperature for all of the BC nodes will neglect the temperature gradient in the BC nodes along the direction of movement. Although this assumption introduces an error into the nonlinear model predictions, the results are still completely eligible. This is a highly promising result since, it will justify the implementation of point temperature measurement devices such as a pyrometer instead of a thermal infrared camera, for capturing the temperature of the boundaries. Thus, the model can be used correctly with fixed boundary conditions obtained from a point measurement device such as a pyrometer, as the observer of state observer feedback control system described in Section 4.5.

Furthermore, the "fixed adaptive boundary condition" applied to linearized model introduces very limited error, while reducing the calculation time and effort. In fact a portion of the very small linearized

133

model error compared to the nonlinear model, is attributed to the use of a fixed adaptive boundary condition rather than the linearization error.

6.2.2 Thermal dynamics Modelling of Laser Additive Manufacturing Process

In order to evaluate the generalization of the developed thermal modelling technique for a variety of LMP processes, the thermal model was also tuned and evaluated for the laser additive manufacturing process. The thermal dynamics data recorded for the *F1* sample was used as the tuning data. In this sample, a decreasing two-step signal for travelling speed is used at $200, 150$ and $100\ mm/min$, in order to obtain the dynamic response of the melt pool temperature and cooling rate of the LAM thermal system. The parameters of the tuned model for the LAM system are presented in Table 6-8. It is noteworthy to point that the material properties ρ and c_p, have been kept consistent with respect to the LHT tuned parameters, which is a further validation for the generalization of the model.

Table 6-8 Tuned model parameters for the LAM process.

$\rho\ (\frac{kg}{m^3})$	$c_p\ (\frac{J}{kg.K})$	A_{abs}	$\Delta t\ (s)$	$\Delta\xi\ (m)$	N	M	$\hat{k}_{eq}\ (\frac{W}{m.K})$	$\hat{T}_{bias}(°C)$
7850	500	0.30	3.10e-03	3.44e-04	6	16	37	150

The input excitation and real-time response of sample *F1* is illustrated in Figure 6-29. It is evident from both of the melt pool and cooling rate signals that the model provides a very accurate estimation of the LAM thermal dynamics. The MAD and MDE of the peak temperature and cooling rate predictions for the tuned LAM model are calculated and reported in Table 6-9. Similar to the tuned LHT model, the deviations and errors of the model for the LAM system are also negligible, since they are very close to the measurement error of the thermal infrared camera. The range of error for the model melt pool temperature predictions for all of the three models with the different BC types is between ±3.96 % and ±12.6 %, and the range of error for the cooling rate predictions lies between ±9.15 % and ±16.05 %, which indicates an accurate estimation of the system. The errors of the nonlinear model with real-time adaptive BCs and the linearized model with fixed adaptive BCs are comparable and in some instances better compared to the tuned model for the LHT process. The only difference is the higher error of the fixed constant BC condition, which indicates a greater importance of a BC conditions for the LAM thermal process compared to the LHT thermal system. This issue may be resolved by selecting a bigger nodal network (increased size of M and N), which will result in boundary nodes with greater temperature independency.
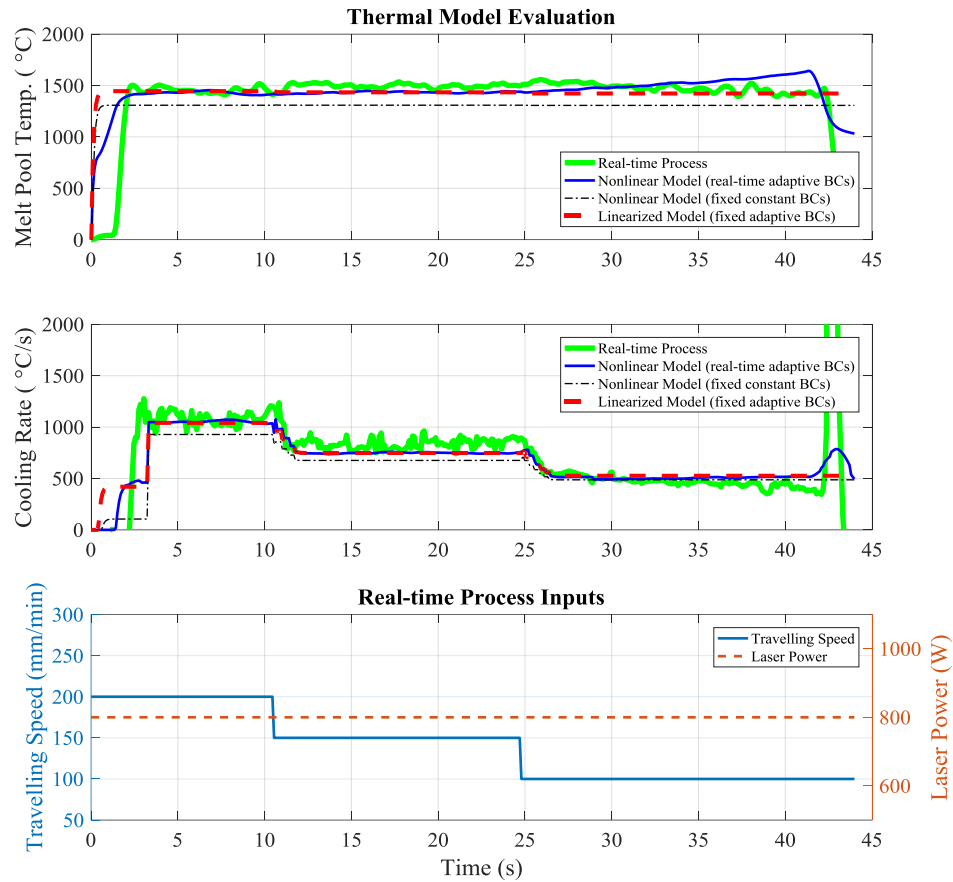
Figure 6-29 Thermal model validation and tuning for LAM sample *F1*.

Table 6-9 Mean Absolute Deviation (MAD) and Mean Deviation Error (MDE) for sample *F1*.

	Nonlinear Model (real-time adaptive BCs)	Nonlinear Model (fixed constant BCs)	Linearized Model (fixed adaptive BCs)
Peak Temperature Deviation (℃)	59.34	189.64	68.26
Peak Temperature Error (%)	3.96	12.66	4.55
Cooling Rate Deviation (℃/s)	67.68	118.77	73.92
Cooling Rate Error (%)	9.15	16.05	9.99

To further evaluate the model for the LAM thermal prediction, the tuned model was evaluated in real-time for sample *F2*, during which the system is excited with a decreasing ramp signal for the

135

travelling speed from 200 to 100 mm/min. The real-time process thermal data and model predictions for samples *F2* is illustrated in Figure 6-30. The MAD and MDE calculations of the model predictions for this sample excitation are also reported in Table 6-10. According to the real-time model estimations and calculated errors which are even lower compared to the tuned data, the developed dynamic model provides a very accurate estimation of the LAM thermal dynamics in terms of estimating the dynamic behavior and thermal value of the melt pool temperature and cooling rate.
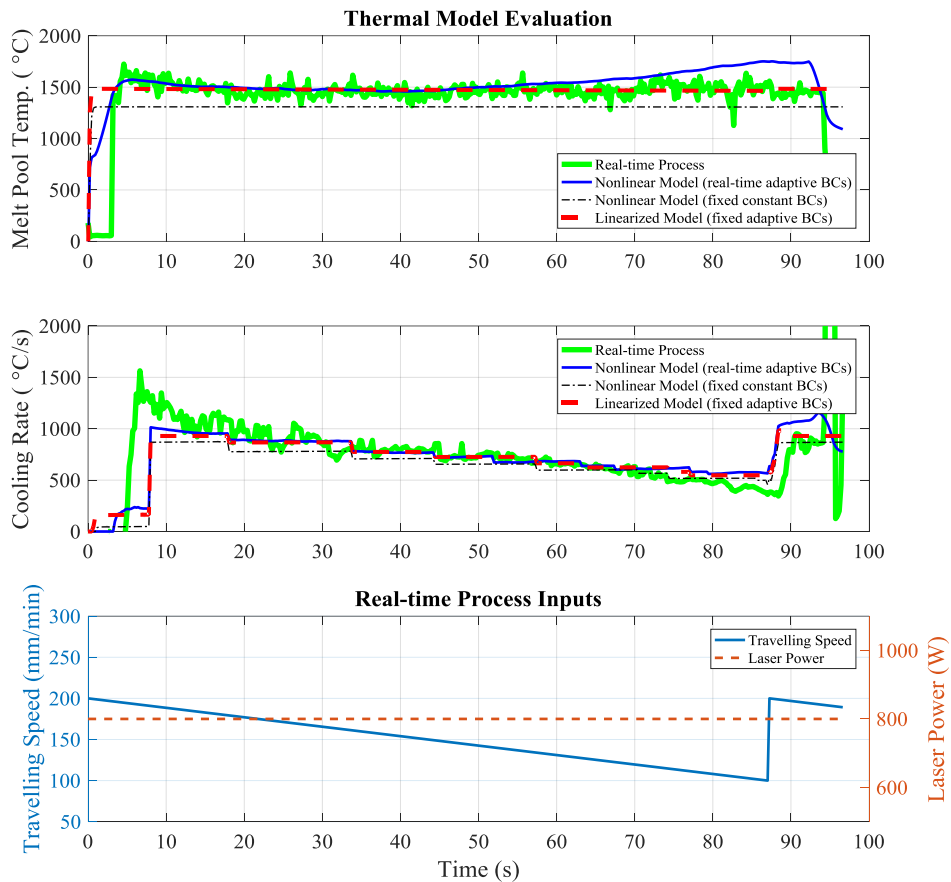
Figure 6-30 Thermal model evaluation for LAM sample *F2*.

Table 6-10 Mean Absolute Deviation (MAD) and Mean Deviation Error (MDE) for sample *F2*.

	Nonlinear Model (real-time adaptive BCs)	Nonlinear Model (fixed constant BCs)	Linearized Model (fixed adaptive BCs)
Peak Temperature Deviation (℃)	59.42	142.67	26.88
Peak Temperature Error (%)	4.09	9.83	1.85
Cooling Rate Deviation (℃/*s*)	41.55	72.47	38.30
Cooling Rate Error (%)	5.63	9.82	5.19

6.3 Real-Time Closed-Loop Control of Microstructure and Geometry

The ultimate goal of the current research is to develop a fully automated LMP system in the sense that all desired material and geometry properties of the final product can be locally tailored to the required engineering specifications. Development and validation of such an automated monitoring and control system will significantly reduce the required offline and passive inspections, while increasing the consistency and quality of the final product. Consequently, the thermal-geometry monitoring and control module developed and discussed in Section 3.2, was implemented in a fully automated closed-loop LMP process illustrated schematically in Figure 3-2. The intelligent closed-loop system was used to control multi-objective output properties of the LHT and LAM processes for a variety of different case studies, to demonstrate the potential of real-time microstructure and geometry control in the developed module.

   In this section, the final results are presented for closed-loop experiments designed in Section 5.4, which demonstrate intelligent real-time control of thermal dynamics and geometry variables by adaptive real-time adjustments of the process inputs. These experiments were designed based on the observations obtained from the microstructure, geometry and thermal dynamics analyses provided in Sections 6.1 and 6.2. Closed-loop control of the peak temperature for the LHT process is evaluated for real-time local hardness control. Additionally, two controllers are developed to control the cooling rate and clad height individually during the LAM process, for scenarios in which either a consistent microstructure or geometry is required. Finally, the individual cooling rate and clad height controllers are integrated into a unified multi-input-multi-output MIMO control system to provide integrated microstructure and geometry control in real-time. For each case study, an identical open-loop experiment is also studied in order to study the benefits of closed-loop control compared to the open-loop process.

6.3.1 Closed-Loop Laser Heat Treatment Process

It was observed in Section 6.1.1.3 that the real-time peak temperature of the LHT process has a significant effect on the austenization and martensite formation of steel, and subsequently the local achieved hardness during the laser heat treatment process. In the following two sections we will examine the variations of the real-time peak temperature under steady-state process input and common process disturbance conditions. The effects of these variations will be studied on the deviation of the final hardness values. Finally, it will be assessed whether these undesired hardness deviations can be addressed online through real-time control of the peak temperature. In order to evaluate and compare the performance of empirical error-based controllers with the state observer feedback control system, two types of controllers are applied for closed-loop control of the peak temperature. The first controller type used is an empirical error-based PID controller described in Section 4.6, which utilizes the direct measurements of the thermal dynamics in the closed-loop process shown in Figure 3-12. The second type of controller is the LQT state observer feedback control system illustrated in Figure 4-4, which utilizes the estimations of the thermal model observer to control the peak temperature of the LHT process in real-time.

6.3.1.1 Peak Temperature Control of Multi-Track Laser Heat Treatment (with PID controller)

The most common laser heat treatment procedure is the heat treatment of a surface, which requires multiple consecutive LHT tracks besides each other. While the hardness value of a single LHT track is dependent upon process and environmental conditions, the introduction of additional tracks besides each track brings about several other disturbances that require to be controlled and dealt with during or after the process. In order to observe the influence of these disturbances on the thermal, geometry and microstructure outputs of a heat treated surface, the open-loop sample *G1-o* was developed with three LHT tracks besides each other. As described in Section 5.2.1 and illustrated in Table 5-6, the travelling speed of each individual track has a two-step signal profile to study the disturbance effects of multi-track LHT at different travelling speeds.

The heat treated *G1-o* sample is shown in Figure 6-31. The monitored thermal dynamics and process inputs of this open-loop sample are also shown in Figure 6-32.
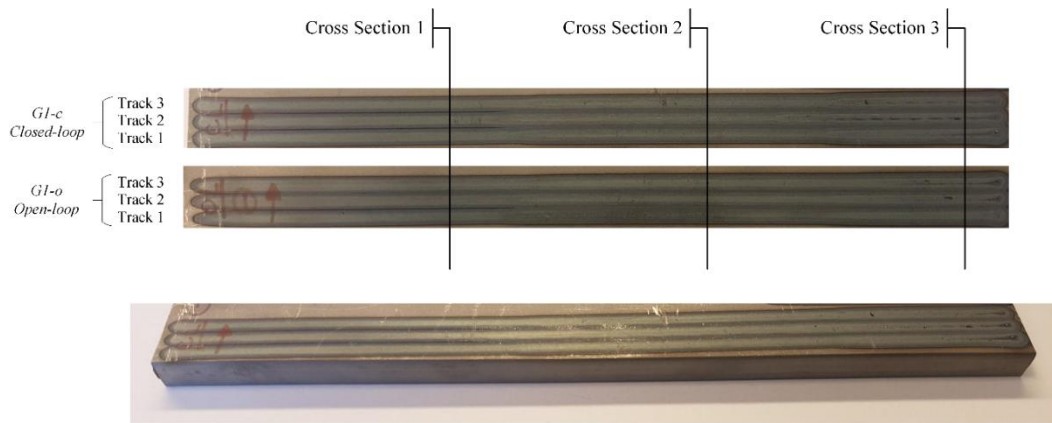
Figure 6-31 Open-loop and closed-loop multi-track LHT sample *G1*.
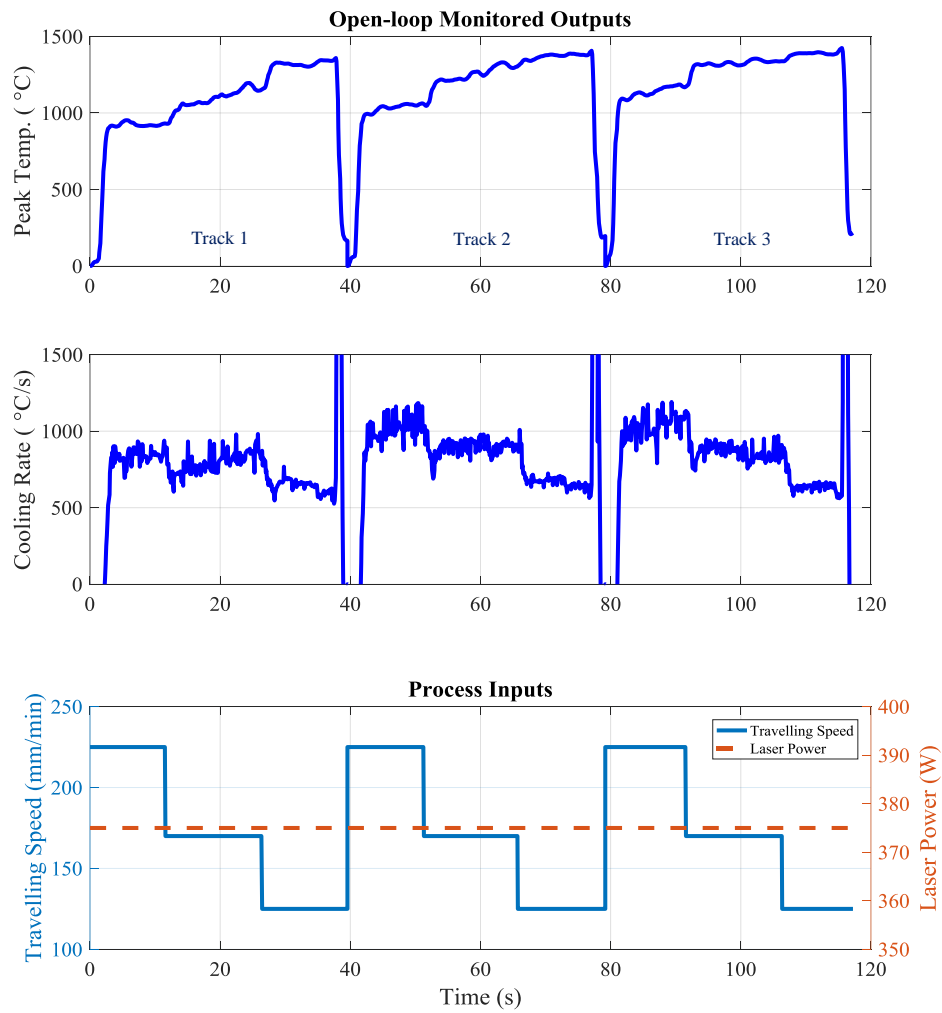
Figure 6-32 Open-loop thermal dynamics and process inputs of multi-track LHT sample *G1-o*.

139

According to Figure 6-32, although the processing parameters (travelling speed and laser power) of all three tracks are the same, the peak temperature profile of each track increases with respect to the previous track. The heat accumulation and preheat disturbance of the previous track(s), develops a deviation in the real-time thermal dynamics profiles of multiple tracks. This thermal inconsistency is observed for the peak temperature and cooling rate profiles of the respective open-loop tracks of sample *G1-o*, in Figure 6-32.

In order to evaluate the effect of these thermal dynamics variations on the developed microstructure and hardness of the heat treated surface, the open-loop *G1-o* sample was cross sectioned at three locations, as shown in Figure 6-31. Since the travelling speed profile of each track is a two-step travelling speed signal with three constant travelling speeds at $225, 175$ and $125 \; mm/min$, as shown in Figure 6-32, the cross sections were located on each constant travelling speed region to study the effect of the thermal disturbances at respective speeds. Thus, at each cross section, the respective three tracks for each constant travelling speed region are present. The micrographs of each track at each cross section (with constant travelling speed region) are shown in Figure 6-33. It is expected to have three similar microstructures at each cross section since the processing parameters at each cross section are the same. However, by comparing the micrographs at each cross section, it is evident that the microstructures formed at each track are different from one another. In general, it is observed that the amount of martensite (dark regions) increases from track 1 to track 3, for all three cross sections. Such variation is the result of deviation in the peak temperature profiles of the tracks compared to one another. This deviation can be clearly observed by comparing the peak temperature profiles of the three tracks Figure 6-33.

Vickers microhardness measurements were also taken from two points on top of each track using a large $1 \; kg$ indentation force. The average measured hardness of each track in the three cross sections are provided in Table 6-11. Similar to the different microstructures, the hardness values of each track are also different, although the processing conditions were the same. This inconsistency in the hardness profile of the surface is caused because of two phenomena. First, the real-time thermal dynamics and specifically the peak temperature of each track are different. Based on observations made in Section 6.1.1.3, the hardness value of LHT tracks is defined by the thermal dynamics and most importantly the real-time peak temperature. Consequently, in Table 6-11, the hardness of the three tracks at each cross section increases as the peak temperatures of the tracks increase (see Figure 6-32). The second reason behind the reduction of hardness in tracks 1 and 2 is the tempering phenomena in

steels caused by post heating of heat treated regions. During the multi-track LHT process, the second track post heats and tempers the first track, and subsequently the third track post heats and tempers the first and second tracks. This tempering reduces some of the excess hardness from the first and second tracks. Therefore, the first track, which has the lowest peak temperature and is under higher tempering conditions, obtains the lowest hardness, whereas, the third track, which has the highest peak temperature and experiences no tempering, has the highest hardness. The second track in each cross section, has an average hardness between the other two tracks, since it experiences intermediate peak temperature and tempering conditions.
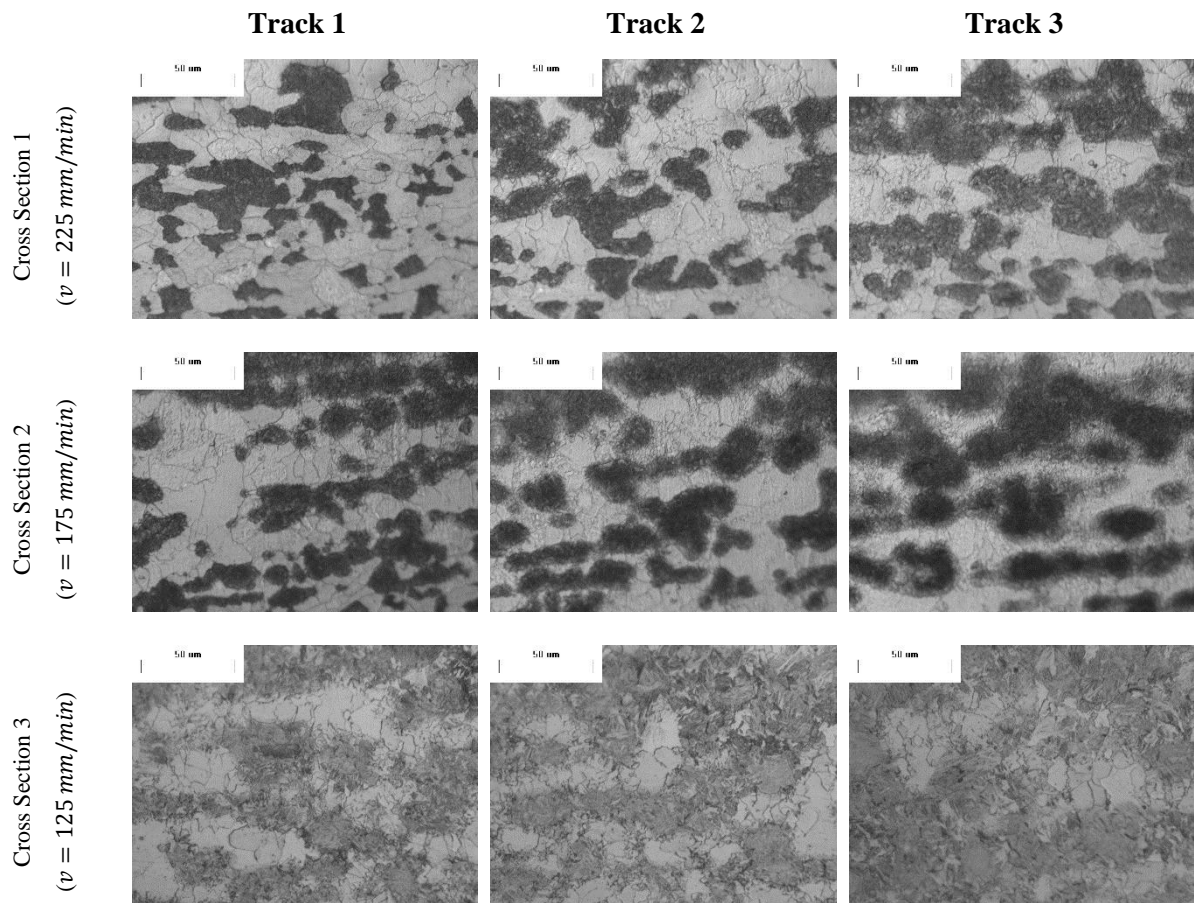
Figure 6-33 Micrographs of open-loop LHT sample *G1-o*.

Table 6-11 Hardness measurements of open-loop *G1-o* LHT sample.

	Average Hardness [Standard Deviation] (HV1.00)		
	Track 1	**Track 2**	**Track 3**
Cross Section 1 ($v = 225\ mm/min$)	225.55 [±0.15]	256.95 [±0.55]	278.85 [±7.75]
Cross Section 2 ($v = 175\ mm/min$)	274.10 [±3.20]	294.10 [±17.70]	299.00 [±0.60]
Cross Section 3 ($v = 125\ mm/min$)	325.90 [±3.00]	367.90 [±9.10]	389.10 [±2.80]

According to the observations obtained from the thermal dynamic, microstructure and hardness data of sample *G1-o*, peak temperature variations in multi-track LHT samples result in a differentiating microstructure and inconsistent surface hardness profile. In order to address these inconsistencies, the developed controller module was utilized to control the peak temperature of each track in a closed-loop LHT process by adaptively adjusting the travelling speed. In order to evaluate the local hardness control capability of the closed-loop process, the setpoint peak temperature for each track was set to three different peak temperature setpoints, as shown in Figure 6-34. Thus, the controller provided three desired peak temperature values at 1000, 1200 and 1400 ℃ in each track. The closed-loop response of the peak temperature and process inputs for sample *G1-c* are shown in Figure 6-34. As illustrated in this figure, the peak temperature in each LHT track, follows the desired setpoint profile very precisely by adaptively adjusting the real-time travelling speed throughout the process. Consequently, each track experiences the exact same peak temperature profile.

As shown in Figure 6-31, the closed-loop sample *G1-c* was also cross-sectioned at three regions with controlled constant peak temperature values of 1000, 1200 and 1400 ℃. The micrographs and average hardness of the closed-loop controlled tracks in each cross section are provided in Figure 6-35 and Table 6-12, respectively. It can be clearly observed in Figure 6-35 that the microstructure and amount of martensite in the three tracks of each cross section are very similar, which is the result of experiencing a consistent peak temperature profile. The tracks of the first cross section have the lowest amount of martensite since they have all been controlled at a lower peak temperature of 1000 ℃, whereas the tracks in the third cross section have the highest amount of martensite, since their peak temperature has been set to a higher value of 1400 ℃.

Most importantly, the hardness of each closed-loop section are tightly controlled and consistent, as shown in Table 6-12. The three tracks of each cross section have identical hardness values with minimum deviations. The closed-loop control of a unique peak temperature in each cross section, has

resulted in a specific consistent hardness profile for each local region. Therefore, through closed-loop control of the peak temperature, local microstructure and hardness can be controlled to desired setpoint values.
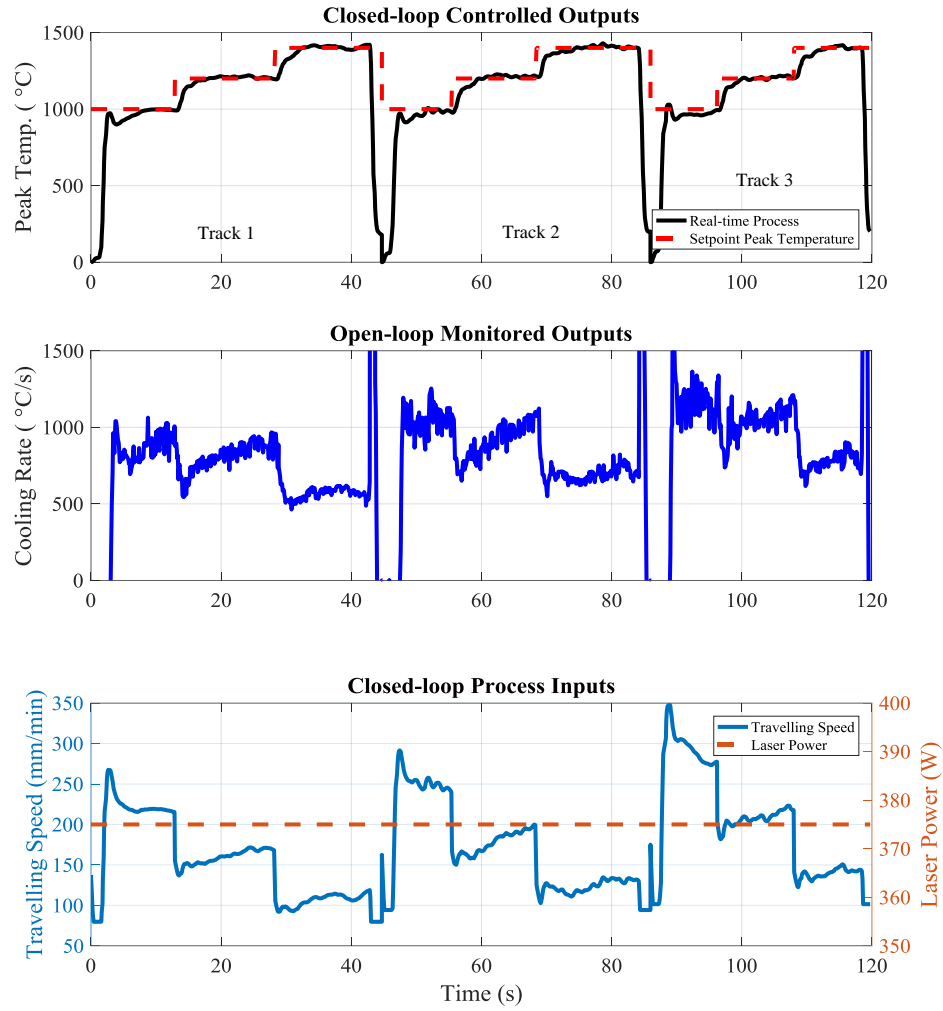
Figure 6-34 Closed-loop thermal dynamics and process inputs of multi-track LHT sample *G1-c*.
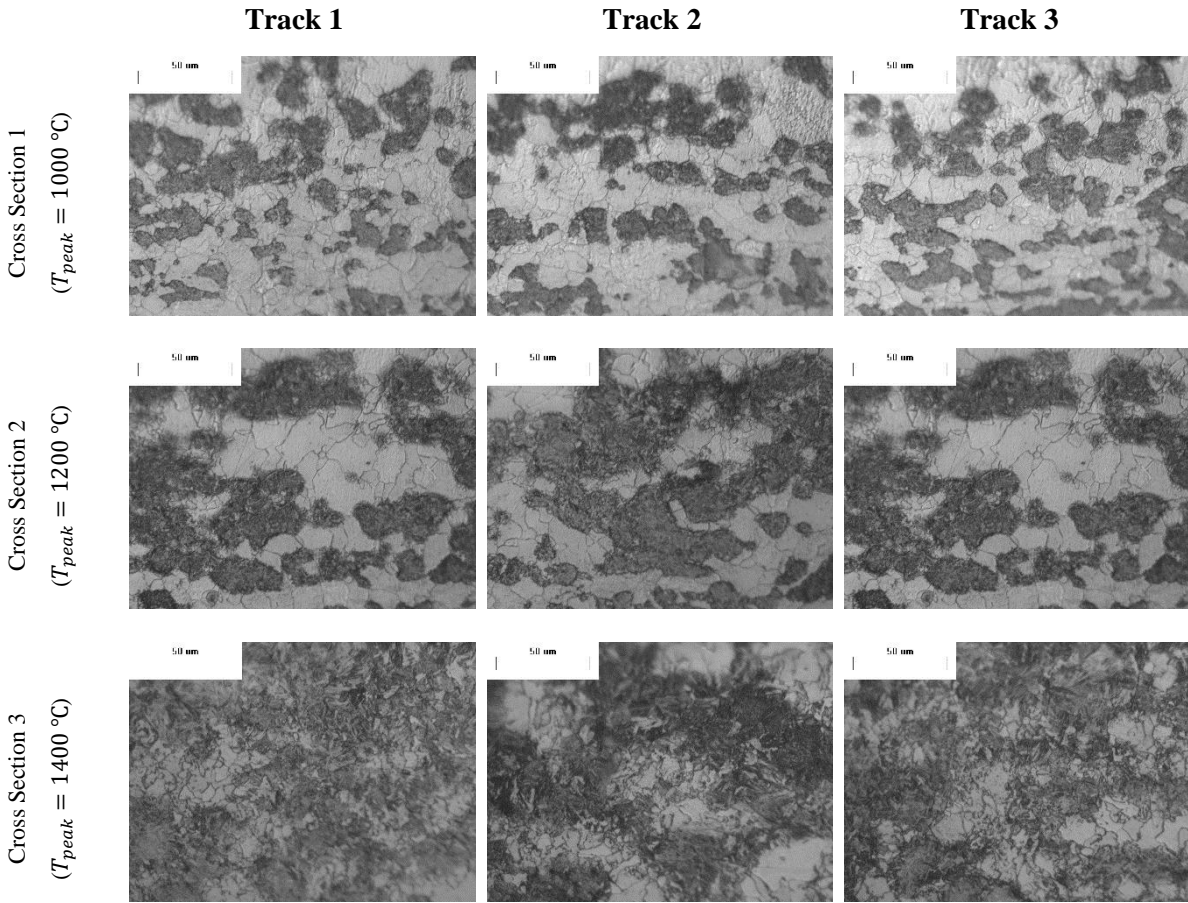
Figure 6-35 Micrographs of closed-loop LHT sample *G1-c*.

Table 6-12 Hardness measurements of closed-loop LHT sample *G1-c*.

	Average Hardness [Standard Deviation] (HV1.00)		
	Track 1	**Track 2**	**Track 3**
Cross Section 1 ($T_{peak} = 1000$ ℃)	234.50 [±2.00]	239.80 [±0.50]	231.30 [±7.80]
Cross Section 2 ($T_{peak} = 1200$ ℃)	271.80 [±3.70]	277.55 [±0.85]	273.80 [±4.70]
Cross Section 3 ($T_{peak} = 1400$ ℃)	339.90 [±0.80]	346.15 [±9.85]	338.05 [±7.95]

6.3.1.2 Peak Temperature Control of Single-track Laser Heat Treatment of a Stepped Workpiece (with PID controller)

The next set of experiments conducted were single-track laser heat treatment of straight lines on a workpiece with changing surface thickness, as shown in Figure 6-36. These conditions are very common in industrial applications where the geometry of the heat treated workpiece has several irregularities. Conventionally these geometry variations in the workpiece are addressed by offline modifications to the G-code programming, which require extensive hours of offline measurements and coding. Nonetheless, in order to evaluate the effects of these geometry irregularities on the microstructure of the LHT process, and to understand whether the closed-loop peak temperature control can overcome any inconsistencies caused by these geometry disturbances in real-time, a set of open-loop and closed-loop single-track laser heat treatment lines were developed on a stepped workpiece, as shown in Figure 6-36. The step on the workpiece has a length of $3.175\ mm$. As described in Section (Table 5-6 and Table 5-7), the first three tracks (samples *G2-o, G3-o* and *G4-o*) have been heat treated under open-loop process conditions with constant travelling speed and laser power, whereas, the next three tracks (samples *G2-c, G3-c* and *G4-c*), have been heat treated under closed-loop process conditions, with controlled peak temperatures obtained by adaptive adjustment to the travelling speed of the CNC machine.

The open-loop and closed-loop thermal dynamics response and process inputs of the *G1, G2* and *G3* samples are shown in Figure 6-37, Figure 6-38 and Figure 6-39, respectively. In these figures, the sudden oscillation in the middle of each peak temperature profile indicates the location of the step on the workpiece. As the thickness of the workpiece reduces, the focal point of the laser beam increases, which results in reduction of the laser beam spot size and increased heat input from the laser heat source. Consequently, it is observed that the peak temperatures of all open-loop samples (with constant travelling speed) increase right after the step on the workpiece. On the other hand, the implementation of a closed-loop control process for the peak temperature cancels out the geometry disturbance effect on the peak temperature, by adaptively increasing the travelling speed for the second part of the heat treatment in order to reduce the amount of heat input to the system. This real-time adjustment to the travelling speed results in a consistent controlled peak temperature for all samples at different desired setpoints. Hence, the tuned PID controller provides a highly accurate response for a broad range of desired peak temperatures.
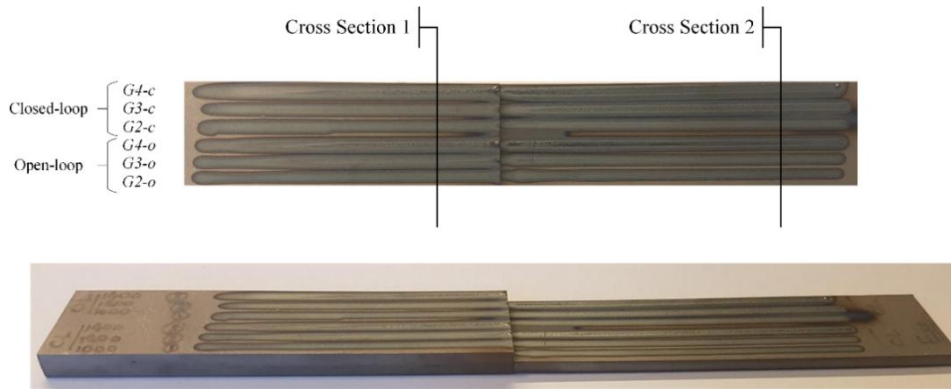
Figure 6-36 Open-loop and closed-loop single-track LHT samples *G2-G4* on stepped workpiece.
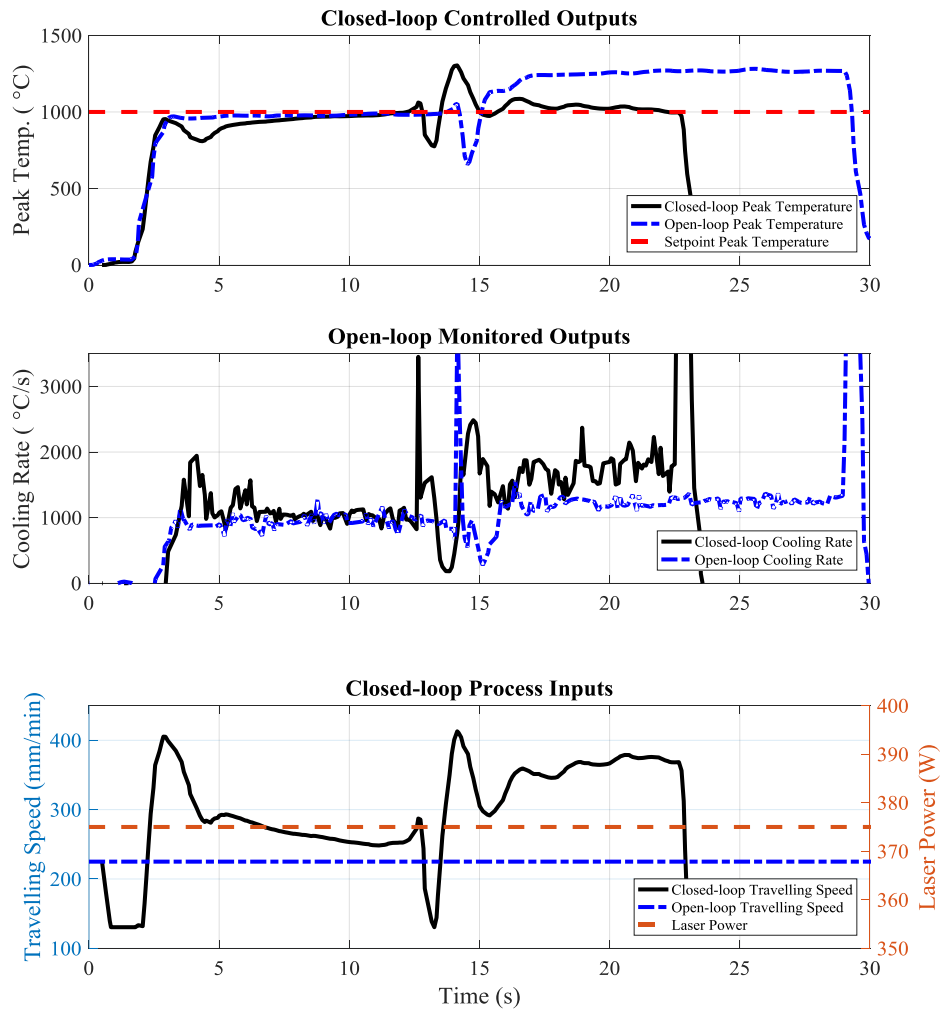
Figure 6-37 Closed-loop and open-loop thermal dynamics and process inputs of single-track LHT sample *G2* on a stepped workpiece.

146
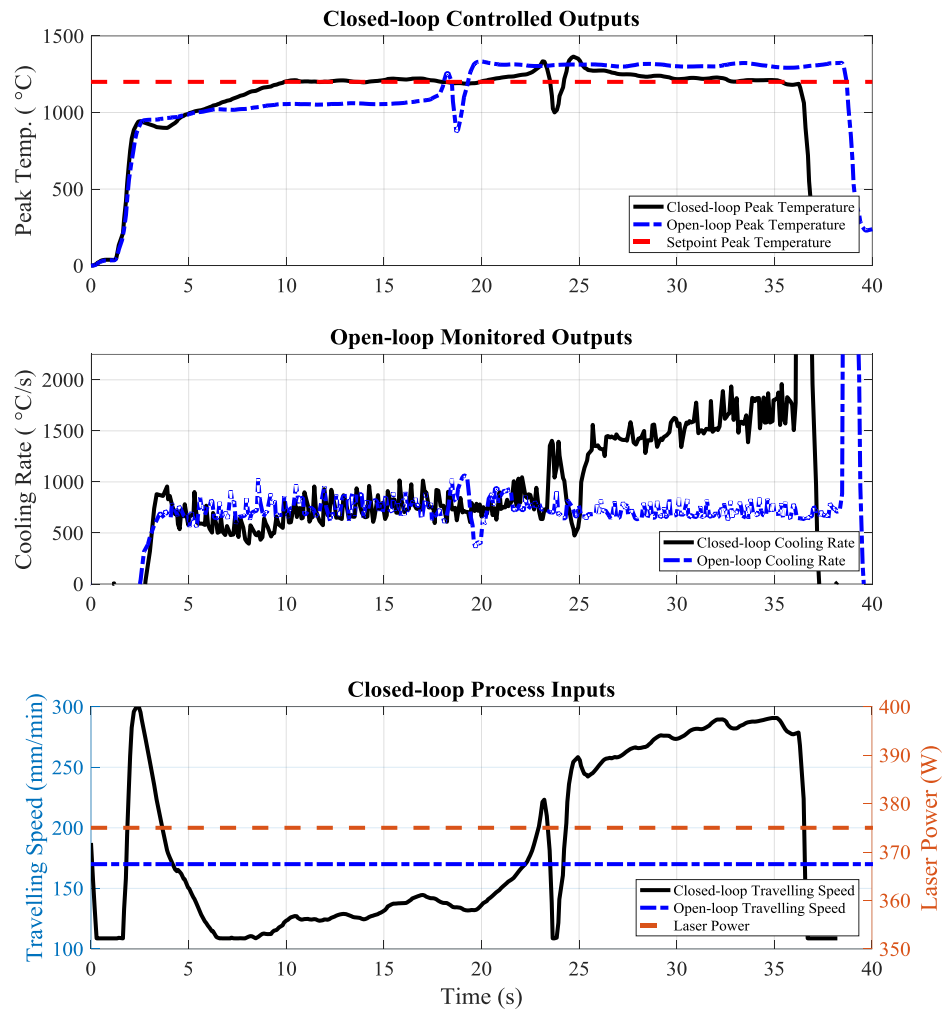
Figure 6-38 Closed-loop and open-loop thermal dynamics and process inputs of single-track LHT sample *G3* on a stepped workpiece.
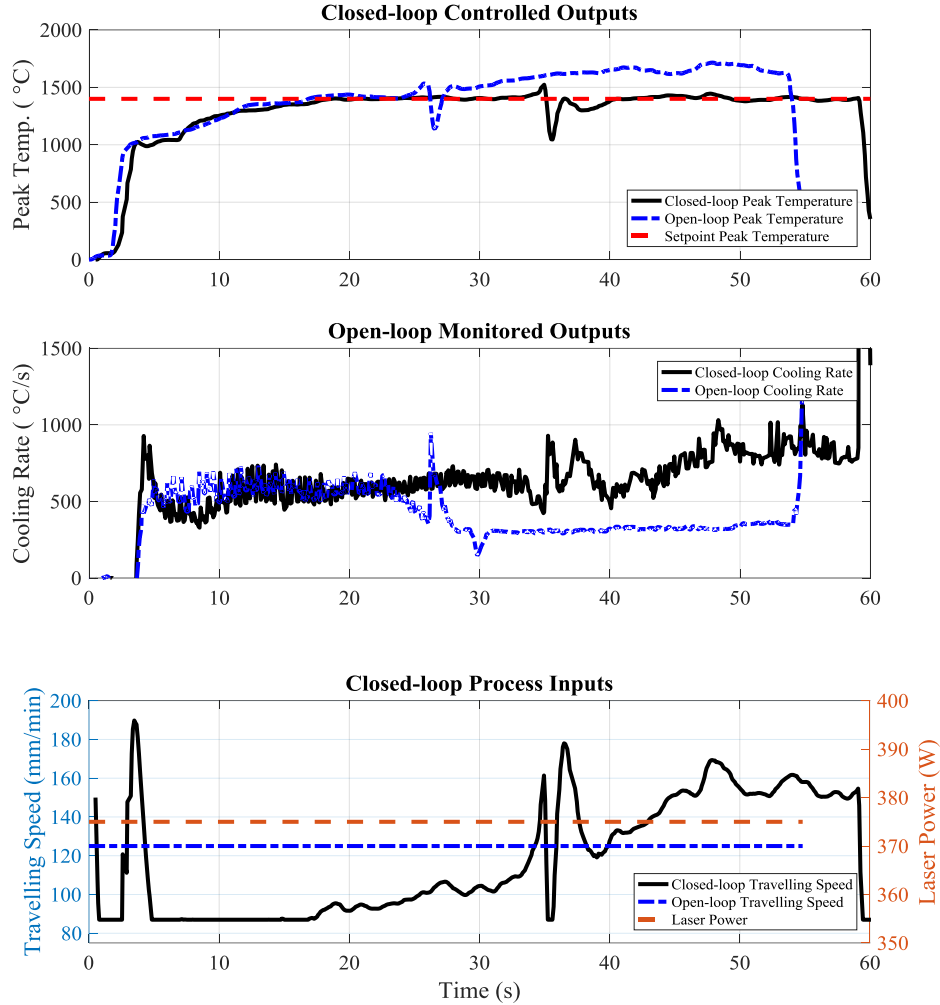
Figure 6-39 Closed-loop and open-loop thermal dynamics and process inputs of single-track LHT sample *G4* on a stepped workpiece.

In order to evaluate the consistency of the microstructures and hardness values of the open-loop and closed-loop conditions, each sample was cross sectioned at two locations on the workpiece, as indicated in Figure 6-36. The first cross section was located on the thicker section of the workpiece and the second cross section was located on the thinner section of the workpiece, after the step. The micrographs of the open-loop and closed-loop samples are illustrated in Figure 6-40 and Figure 6-41, respectively. The hardness measurements of each sample at its' two corresponding cross sections are also listed in Table 6-13.

G2-o $(v = 225\frac{mm}{min})$ **G3-o** $(v = 175\frac{mm}{min})$ **G4-o** $(v = 125\frac{mm}{min})$

Cross Section 1 (Thick Workpiece)

Cross Section 2 (Thin Workpiece)
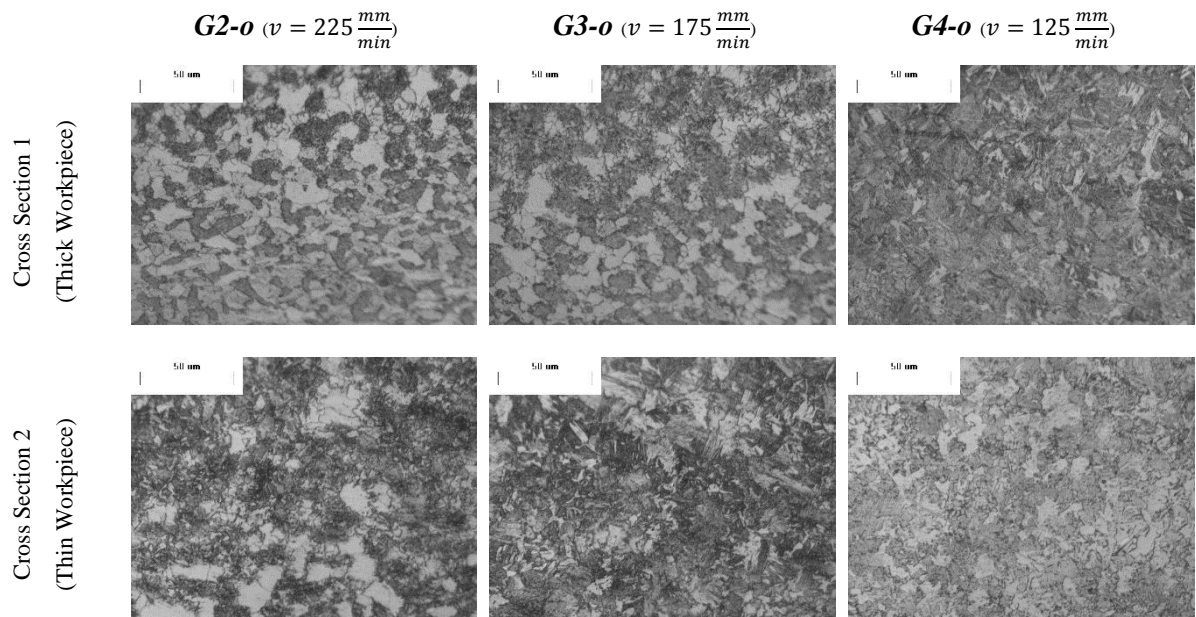
Figure 6-40 Micrographs of open-loop (constant travelling speed) single-track LHT samples *G2-o, G3-o* and *G4-o* on a stepped workpiece.

G2-c $(T_{peak} = 1000℃)$ **G3-c** $(T_{peak} = 1200℃)$ **G4-c** $(T_{peak} = 1400℃)$

Cross Section 1 (Thick Workpiece)

Cross Section 2 (Thin Workpiece)
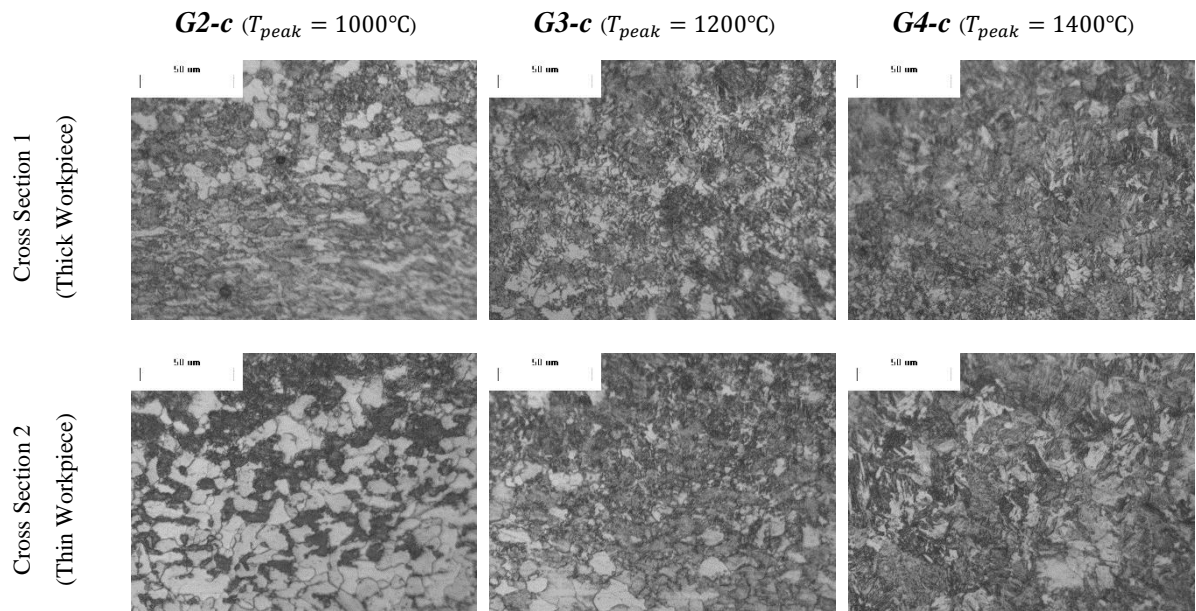
Figure 6-41 Micrographs of closed-loop (controlled peak temperature) single-track LHT samples *G2-c, G3-c* and *G4-c* on a stepped workpiece.

Table 6-13 Hardness measurements of open-loop and closed-loop single-track LHT samples *G2*, *G3* and *G4* on stepped workpiece.

	Average Hardness [Standard Deviation] (HV1.00)					
	Open-loop Samples			Closed-loop Samples		
	G2-o	*G3-o*	*G4-o*	*G2-c*	*G3-c*	*G4-c*
	$(v = 225\frac{mm}{min})$	$(v = 175\frac{mm}{min})$	$(v = 125\frac{mm}{min})$	$(T_{peak} = 1000℃)$	$(T_{peak} = 1200℃)$	$(T_{peak} = 1400℃)$
Cross Section 1 (Thick Workpiece)	245.15 [±5.45]	296.80 [±1.70]	411.90 [±0.00]	262.25 [±1.25]	371.15 [±6.85]	397.85 [±2.15]
Cross Section 2 (Thin Workpiece)	318.70 [±1.30]	382.50 [±0.50]	309.15 [±15.05]	273.25 [±9.05]	366.70 [±2.00]	394.60 [±6.90]

It is observed in Figure 6-40 that the microstructures of the open-loop heat treated lines are totally inconsistent and different in terms of martensite formation and overall morphology. For open-loop samples *G2-o* and *G3-o*, the microstructure at the thinner section of the workpiece contains more martensite, which is the result of increased peak temperature after the step on the workpiece (Figure 6-37 and Figure 6-38). For sample *G4-o* however, since the open-loop peak temperature after the step is above the liquidus temperature (Figure 6-39), the microstructure at the thinner region represents a partially melted cross section. In contrast to the open-loop samples, the microstructures of the closed-loop samples illustrated in Figure 6-41, are exactly the same and consistent at both cross sections and throughout the heat treatment. The closed-loop control of the peak temperature has resulted in a consistent controlled microstructure at different desired setpoints.

Looking at the hardness measurements provided in Table 6-13, one can also understand the consequences of the inconsistent microstructures obtained from open-loop conditions. It is evident that hardness values of the open-loop samples are completely different at each cross section, which is the result of different developed microstructures in these samples. Samples *G2-o* and *G3-o* have an increased hardness because of the increased martensite formation, whereas, sample *G4-o* has a reduced hardness value because of the partial melting. Alternatively, the hardness of the closed-loop samples are controlled by a very tight tolerance as a result of the consistent peak temperature. Therefore, the closed-loop control of the peak temperature can provide controlled local hardness and microstructure, and eliminate the effect of geometry disturbances in real-time, without the need for further manual tuning or adjustments.

6.3.1.3 State Observer Feedback Control of the Peak Temperature

The final set of closed-loop experiments conducted for the LHT process includes the state observer feedback control of the peak temperature using the closed-loop system illustrated in Figure 4-4. In this section, we will be implementing the optimal Linear Quadratic Tracking (LQT) controller system designed in Section 4.4, instead of the PID controller, to control the peak temperature during the LHT process. The control system is based on the thermal dynamics feedback estimation provided by the state observer finite difference model developed in Section 4.3. The capability of using model-based controllers is another advantage of the thermal-geometry monitoring and control module, since these type of controllers require less amount of trial and error and tuning time. Most importantly, the state observer feedback control system can provide closed-loop thermal dynamics control with limited thermal information of the melt pool boundaries rather than complete measurements of the thermal dynamics. Thus, in the current closed-loop control process, measurement of the melt pool temperature boundaries are only obtained from the infrared camera for the state observer to estimate the thermal dynamics in real-time. In order to evaluate the performance of the designed LQT state observer feedback control system, the controller was evaluated for two closed-loop control case studies. The first sample controlled with the LQT state observer feedback controller is the *H1-c* sample, which is a closed-loop multi-track laser heat treated surface, as described in Section 5.4.1.2. The heat treated sample and its' corresponding closed-loop thermal dynamics and process inputs are shown in Figure 6-42 and Figure 6-43, respectively.
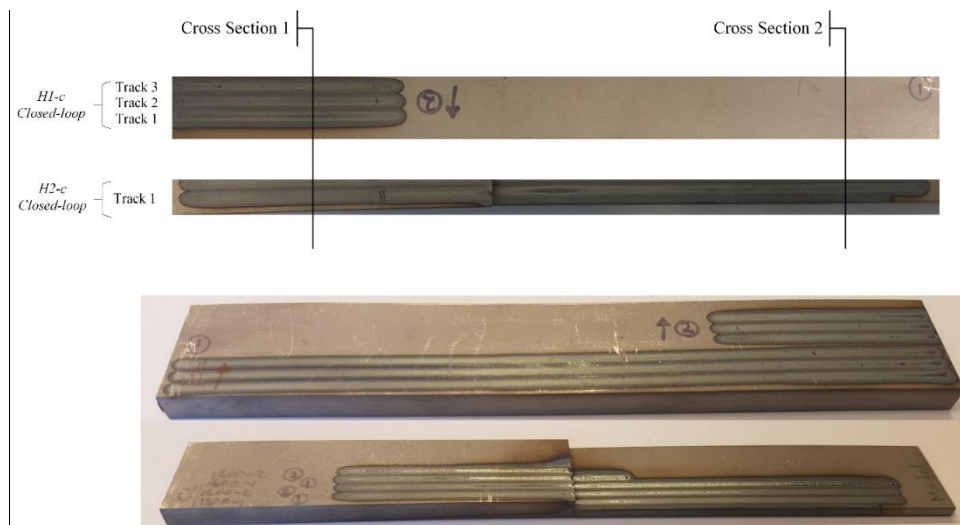
Figure 6-42 Closed-loop multi-track and single-track LHT samples *H1-c* and *H2-c* controlled with stated observer feedback controller.

It is observed in Figure 6-42 that the state observer controller has perfectly controlled the peak temperature of all three tracks to a constant setpoint peak temperature of 1400 °C, in spite of the thermal heat input disturbance caused by the previous tracks. The final jumps on the closed-loop travelling speed profile on each track are just measurement errors caused by the shutting off of the laser at the end of each track, which should be disregarded. In order to evaluate the consistency of microstructure and material properties along the surface, the *H1-c* sample was cross sectioned on one location as indicated in Figure 6-42. Very similar microstructures were observed, resulting in very consistent controlled hardness profiles in all three tracks, which are reported in Table 6-14.
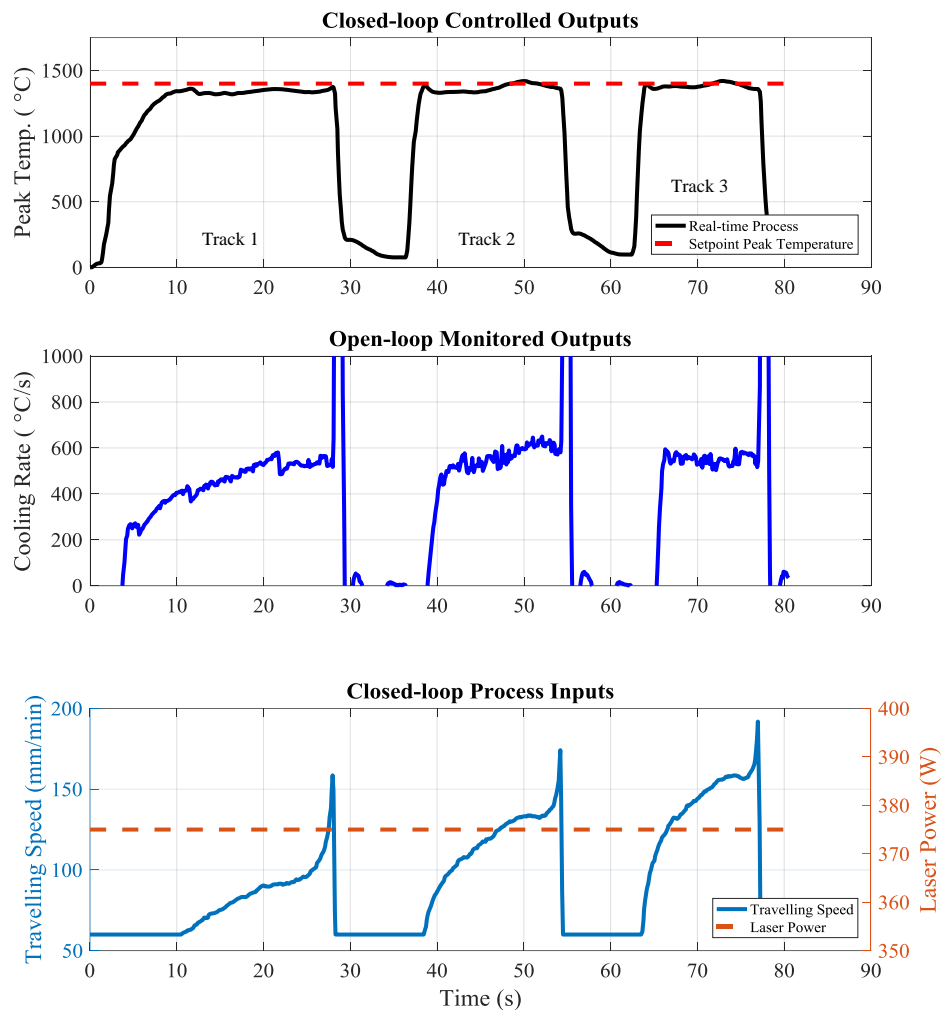
Figure 6-43 Closed-loop thermal dynamics and process inputs of multi-track LHT sample *H1-c* controlled with state observer feedback controller.

Table 6-14 Hardness measurements of closed-loop LHT samples *H1-c* and *H2-c* controlled with state observer feedback controller.

	Average Hardness [Standard Deviation] (HV1.00)			
	H1-c			*H2-c*
	Track 1	**Track 2**	**Track 3**	
Cross Section 1	305.20 [±13.00]	335.70 [±0.70]	333.65 [±7.25]	396.50 [±2.20]
Cross Section 2	-	-	-	385.75 [±2.95]

The second sample controlled with the state observer controller is the *H2-c* sample, which is a closed-loop single-track laser heat treated line on a stepped surface, as described in Section 5.4.1.2. The step on the workpiece has a length of 3.175 mm, similar to the PID closed-loop samples. This heat treated sample and its' corresponding closed-loop thermal dynamics and process inputs are illustrated in Figure 6-42 and Figure 6-44, respectively. It is evident from Figure 6-44 that the peak temperature of the workpiece is controlled at a constant temperature of 1400 ℃, even after the deviation in the thickness of the workpiece and laser focal point. The LQT state observer controller removes the excess heat of the smaller laser spot size (after the step in the workpiece), by adaptively increasing the travelling speed in real-time. Sample *H2-c* was cross sectioned at two locations; one before the workpiece step and one after, to understand whether the closed-loop control was able to develop controlled material properties. As a result of the consistent peak temperature, the microstructures of both cross sections were exactly similar in terms of amount of martensite and morphology. Subsequently, the hardness of the *H2-c* track were consistently controlled at both cross sections.

Accordingly, the developed state observer control system is able to provide a precise closed-loop peak temperature control for the LHT process, while only measurements of the melt pool temperature boundaries are provided to the system. The controller can eliminate the effect of different thermal and geometry disturbances. This closed-loop control of the peak temperature develops very consistent microstructure properties during the heat treatment process. More importantly, compared to the PID controller, the state observer control system required less experimentation, tuning and cost of implementation.
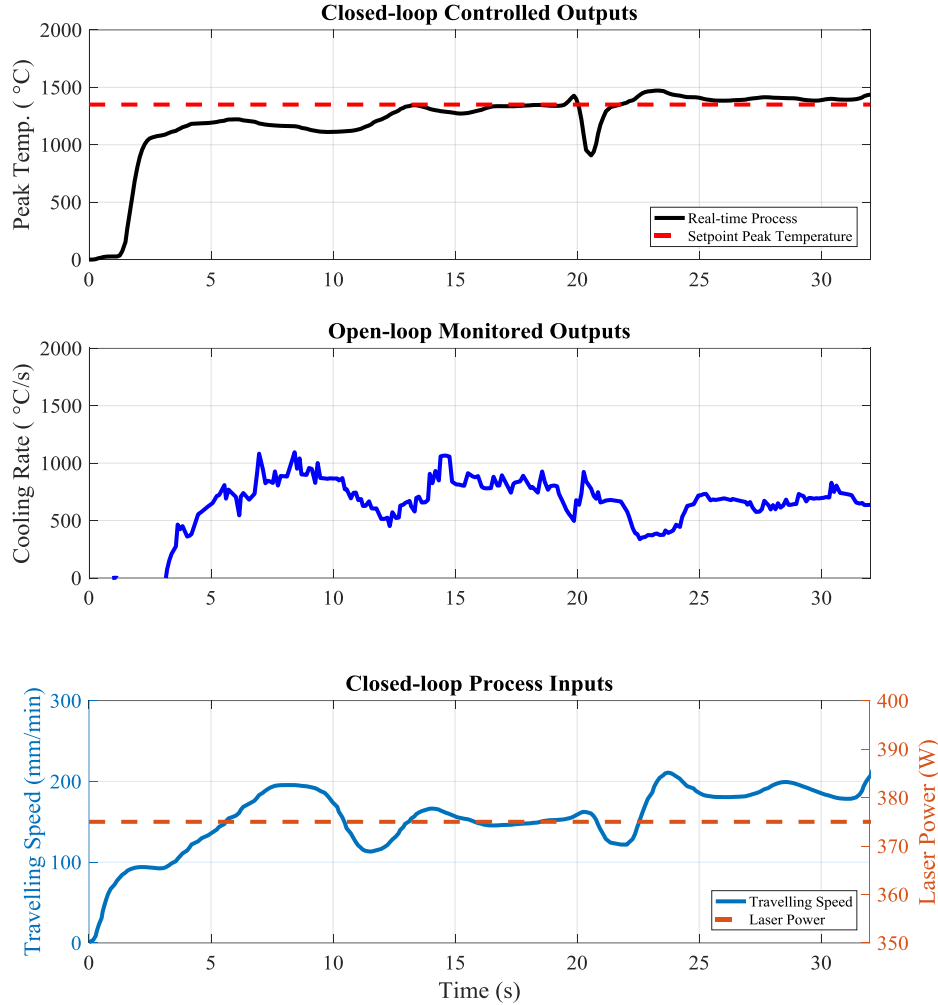
Figure 6-44 Closed-loop loop thermal dynamics and process inputs of single-track LHT sample H2-c on stepped workpiece, controlled with state observer feedback controller.

6.3.2 Closed-Loop Laser Additive Manufacturing Process

It was observed in Section 6.1.2 that the microstructure and geometry of the LAM depositions is defined by the thermal dynamics of the process. While the clad height can be monitored directly through CCD imaging, the microstructure can be monitored indirectly through thermal dynamics monitoring of the infrared camera. Results of the indirect microstructure monitoring in Sections 6.1.2.2 and 6.1.2.3 indicated that open-loop process conditions result in inconsistent microstructures and hardness profiles, specifically for multi-track depositions. In the following sections, examine variations of the real-time clad height, cooling rate and melt pool temperature under steady-state process input and common

154

process disturbance conditions. The effects of these variations will be studied on the deviation of the final clad height, microstructure and hardness properties. To eliminate the effect of these disturbances, closed-loop process conditions are developed in order to control the clad height and cooling rate through adaptive real-time adjustments of the process inputs. Individual single-input-single-output control systems are tested for individual control of each of these output properties. Finally, a multi-input-multi-output control system is developed to control integrated real-time cooling rate and clad height in order to achieve desired local microstructures, while keeping a consistent clad height.

6.3.2.1 Clad Height Control of Multi-Track Laser Additive Manufacturing Depositions (with PID controller)

Geometry of the LAM deposition is critically important in development of three-dimensional structures or protective coatings. Hence, it is essential to obtain consistent desired geometry and clad height during deposition of each track and layer. The CCD camera of the thermal-geometry monitoring and control module, was implemented to provide real-time feedback of the clad height using the algorithm and image processing techniques discussed in Section 3.2.1. The real-time clad height was controlled to a desired setpoint profile through autonomous real-time modification of the travelling speed.

The described closed-loop geometry process was used to control the clad height of the multi-track LAM sample *I1-c*, to a step setpoint clad height profile, which is schematically shown in Table 5-9. The closed-loop laser additive manufactured sample and its' corresponding thermal dynamics and process inputs are shown in Figure 6-45 and Figure 6-46, respectively.
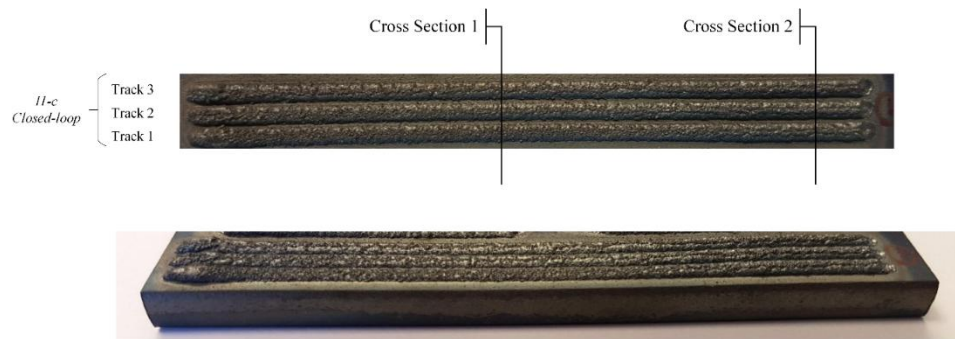
Figure 6-45 Multi-track LAM sample *I1-c* with closed-loop clad height control.

155
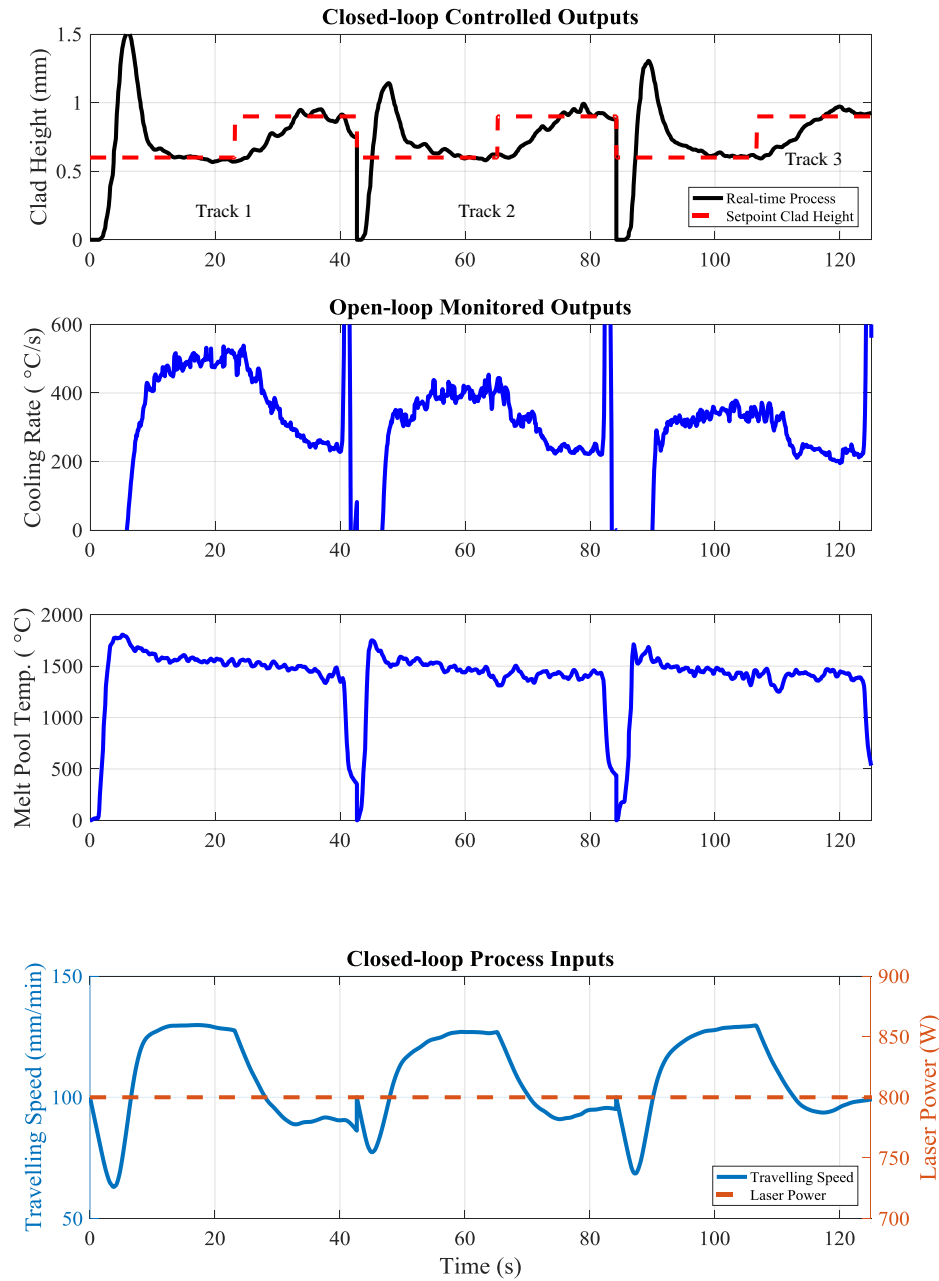
Figure 6-46 Thermal dynamics, geometry and process inputs of closed-loop clad height control of multi-track LAM sample *I1-c*.

The closed-loop clad height control delivers a precisely controlled step clad height profile as shown in Figure 6-46. Although, the clad height is controlled in sample *I1-c*, the adaptive adjustment of the travelling speed has resulted in different cooling rate profiles for the three tracks. The cooling rate drops

from the first track to the third. In order to study the effect of this cooling rate variation on the material properties of the deposition, the sample was cross sectioned at two locations located at the different constant travelling speeds, indicated in Figure 6-45. The microstructure and hardness of each track at the two cross sections are shown in Figure 6-47 and Table 6-15, respectively. It is expected to have similar microstructures at each cross section, however, the microstructures at each cross section are different, specifically for the third track. This variation of the microstructure is further justified by the diverging hardness profile of each cross section, reported in Table 6-15. These microstructure inconsistencies are similar to the results of open-loop multi-track LAM depositions, presented in Section 6.1.2.3. This inconsistency, is the result of experiencing a different cooling rate profile and tempering of the initial tracks. Nonetheless, it was observed that clad height control did not result in microstructure consistency and control.
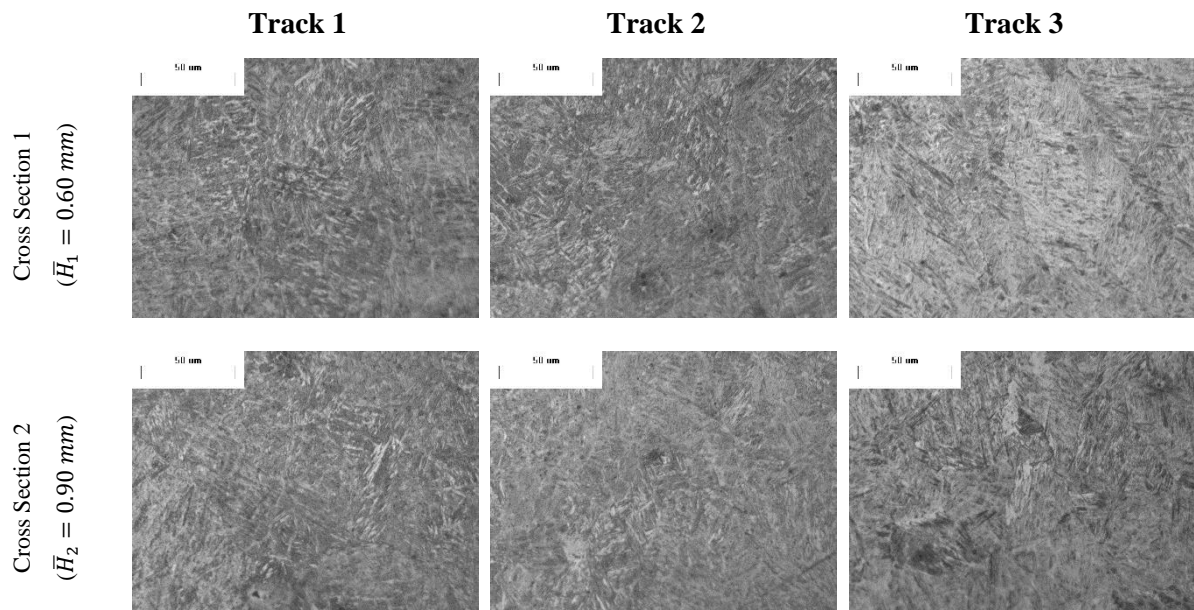
Figure 6-47 Microstructures of closed-loop clad height control of multi-track LAM sample *I1-c*.

157

Table 6-15 Hardness of closed-loop clad height control of multi-track LAM sample *I1-c*.

	Average Hardness [Standard Deviation] (HV1.00)		
	Track 1	**Track 2**	**Track 3**
Cross Section 1 ($\bar{H}_1 = 0.60\ mm$)	416.40 [±7.40]	412.35 [±6.65]	514.65 [±0.75]
Cross Section 2 ($\bar{H}_2 = 0.90\ mm$)	396.30 [±9.90]	379.75 [±14.05]	526.65 [±2.65]

6.3.2.2 Cooling Rate Control of Single-Track and Multi-Track Laser Additive Manufacturing Depositions (with PID controller)

The microstructure inconsistencies and hardness variations observed during open-loop and closed-loop clad height control (Sections 6.1.2.3 and 6.3.2.1), are the result of inconsistent thermal dynamics variations. In order to address these inconsistencies, closed-loop control of the cooling rate is investigated during LAM depositions. To realize the effect of closed-loop cooling rate control on achieved microstructure, an open-loop multi-track sample *J1-o* was initially developed. As described in Section 5.4.2.2, this sample has a step travelling speed profile for each track. The open-loop laser additive manufactured sample and its' corresponding thermal dynamics and process inputs are shown in Figure 6-48 and Figure 6-49, respectively.
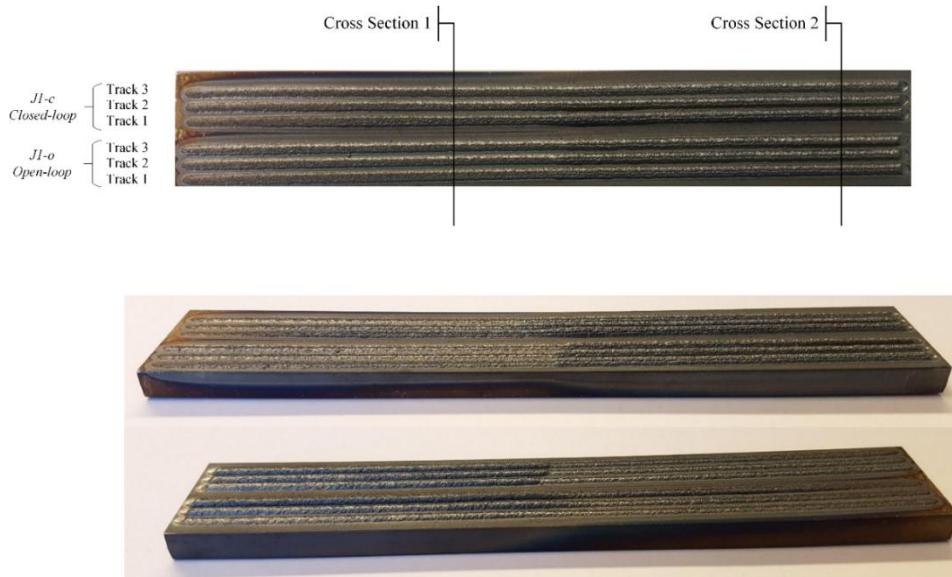
Figure 6-48 Multi-track LAM sample *J1* with closed-loop and open-loop cooling rate.
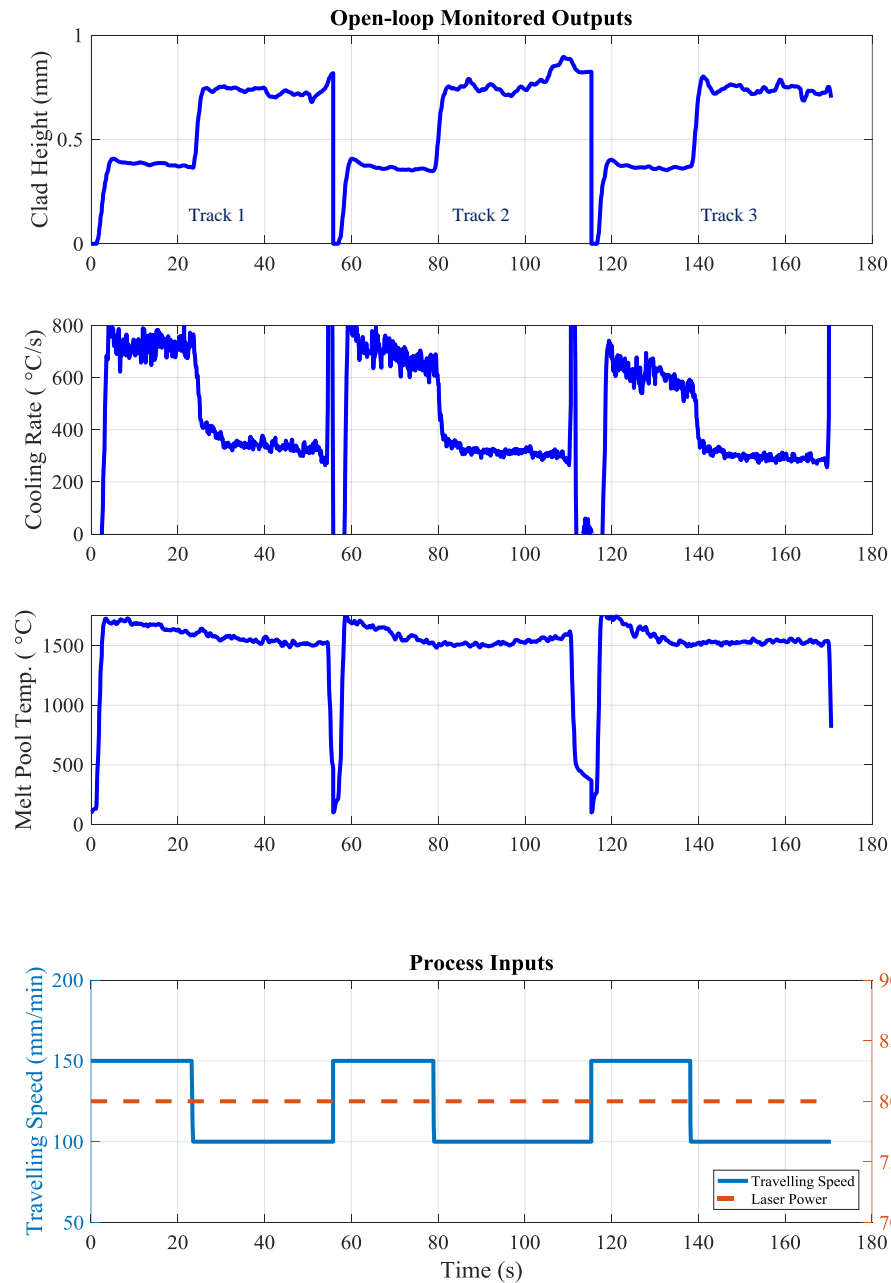
Figure 6-49 Thermal dynamics, geometry and process inputs of open-loop cooling rate control of multi-track LAM sample *J1-o*.

According to Figure 6-49, the cooling rate profile of each deposition track in sample *J1-o* differs because of the preheat effect caused by deposition of the initial tracks. The cooling rate drops for the second and third tracks as a result of this preheat effect. Subsequently, by cross sectioning the sample

at two the locations shown in Figure 6-48, the microstructures of the tracks at each cross section were examined. As illustrated in Figure 6-50, the microstructures of the open-loop multi-track LAM process are different at each cross section, although a constant set of processing parameters are used. This difference is also observed in the hardness values of each track, which is reported in Table 6-16. As explained earlier, this change of microstructure is the result of two main phenomena. The first reason behind this variation is the different thermal dynamics history and specifically the different cooling experienced by each track. The second reason behind this inconsistency is the effect of tempering caused by prior tracks on the subsequent ones.
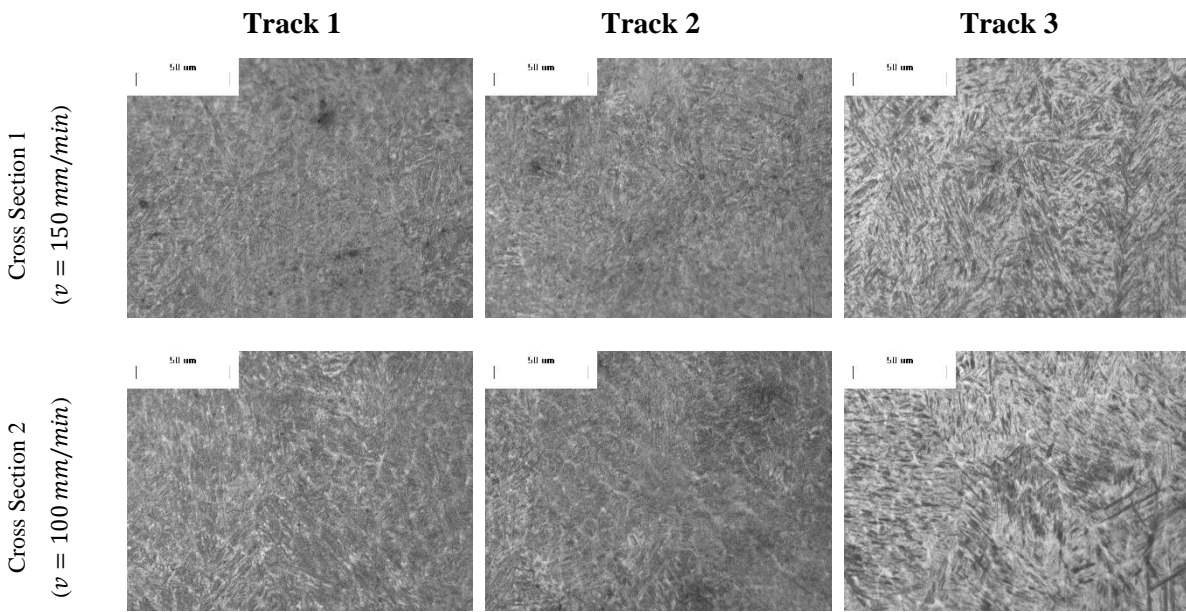
Figure 6-50 Microstructures of open-loop cooling rate control of multi-track LAM sample *J1-o*.

To eliminate the undesired cooling rate variations during the process, a closed-loop system was used to control the cooling rate in a multi-track LAM process. The closed-loop multi-track sample *J1-c*, which is shown in Figure 6-48, was controlled at a step cooling rate profile. The recorded closed-loop thermal dynamics, clad height and process inputs of this sample are shown in Figure 6-51. Unlike the open-loop sample *J1-o*, in the closed-loop process, all three tracks experience similar cooling rate profile.

160

Figure 6-51 Thermal dynamics, geometry and process inputs of closed-loop cooling rate control of multi-track step LAM sample *J1-c*.
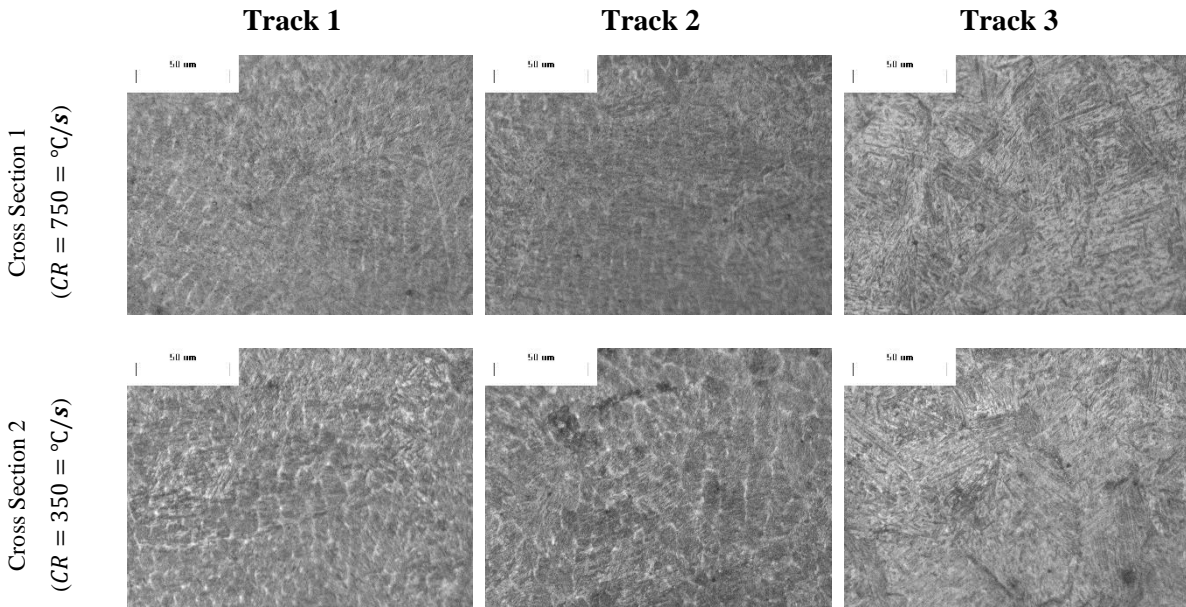
Figure 6-52 Microstructure of closed-loop cooling rate control of multi-track LAM sample *J1-c*.

Table 6-16 Hardness of open-loop and closed-loop cooling rate control of multi-track step LAM sample *J1*.

	Average Hardness					
	[Standard Deviation] (HV1.00)					
	Open-loop Samples			Closed-loop Samples		
	Track 1	**Track 2**	**Track 3**	**Track 1**	**Track 2**	**Track 3**
Cross Section 1	447.75	444.95	551.70	481.00	477.90	502.70
	[±0.05]	[±0.55]	[±8.80]	[±7.20]	[±10.60]	[±1.10]
Cross Section 2	389.65	396.65	571.55	420.10	417.20	435.15
	[±4.45]	[±3.45]	[±1.35]	[±5.30]	[±1.30]	[±4.15]

As a result of cooling rate control, the microstructures of each cross section have a greater consistency, which is shown in Figure 6-52. The hardness measurements of the closed-loop sample are also reported in Table 6-16. In the closed-loop sample, the three tracks in each cross section have very similar hardness values, in contrast to the open-loop sample. Yet, the final track in each cross section of the closed-loop sample has a slightly higher hardness value with respect to other tracks at each constant cooling section. As indicated earlier, hardness measurements for each track were taken at similar locations at the center of each deposition. The hardness values are an average of two points in

162

the center of each clad. Since the workpiece undergoes a pre-heating of at least 200 ℃ during each deposition track, the lower hardness of the initial tracks exemplifies the effect of tempering, which reduces the hardness of these tracks during deposition of subsequent ones. Although, the tempering phenomena cannot be prevented by any means in multi-track depositions, a controlled cooling rate will ensure that all tracks experience the same amount of tempering. Thus, the closed-loop cooling rate control, will control the thermal histories and tempering effects during the multi-track LAM process, which results in consistent mechanical and material properties. However, observing the clad height profile in Figure 6-51, it is evident that employment of a single-input-single-output cooling rate control system will not obtain a controlled geometry. In fact, the clad height of each track in sample *J1-c*, reduces significantly with respect to the previous track, as a result of the real-time adjustment to the travelling speed. This variation in the geometry can be even observed in Figure 6-48.

In order to further examine the effect cooling rate control on the achieved clad height, instead of a multi-track sample, a single-track LAM deposition was controlled at two cooling rate values as shown in Figure 6-53. Even in this sample, the measured clad height at the lower controlled cooling is different to the measured clad height at the higher controlled cooling. This is caused by the reduced travelling speed in the second section of the deposition, which will result in increased feed rate and melted material. Therefore, while the closed-loop control of the cooling rate will enable local microstructure control to desired characteristics, it will introduce a deviation in the clad height profile of the system. The same goes for single-input-single-output control of the clad height, which resulted in variation of the cooling rate and microstructure.
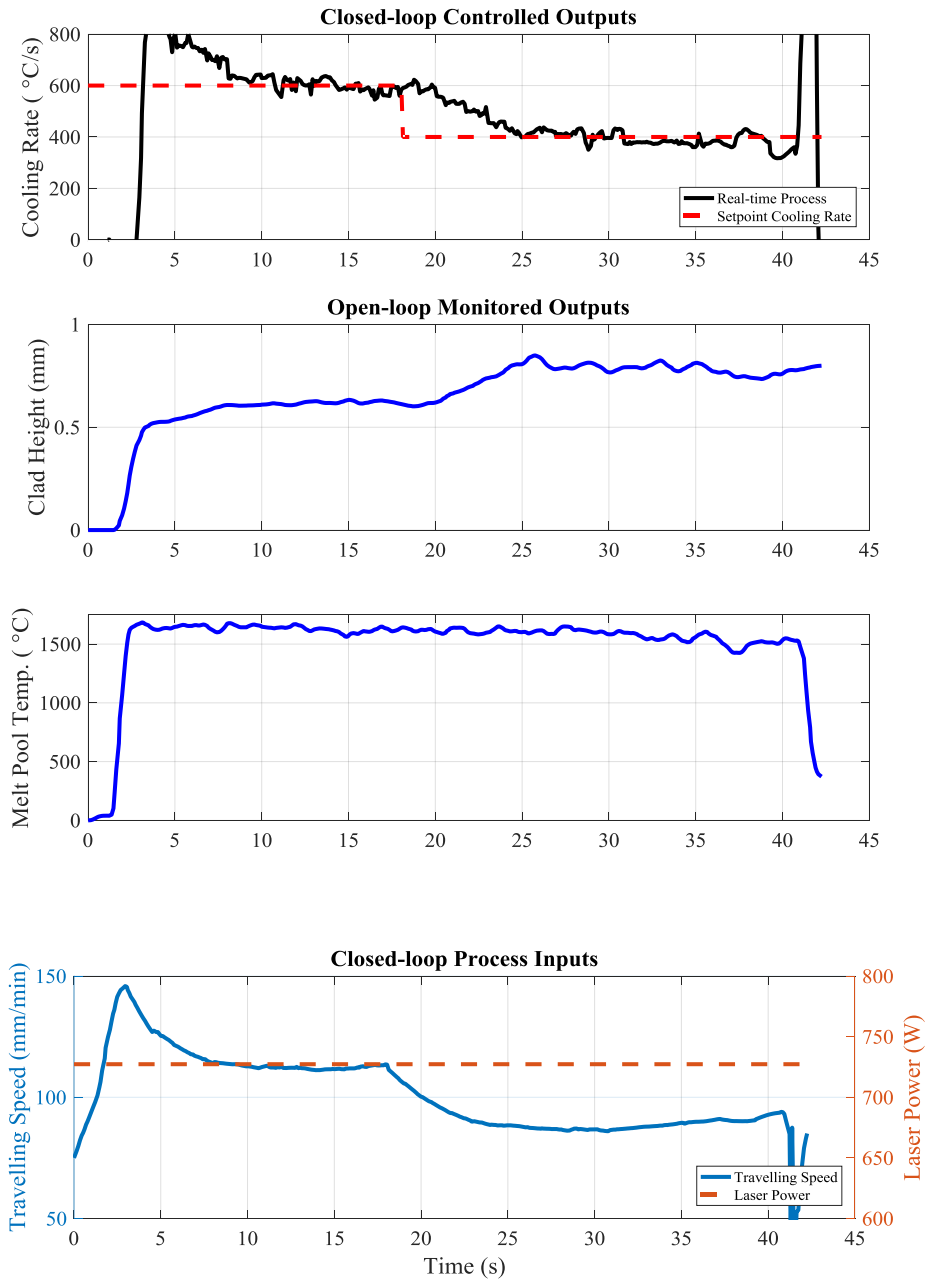
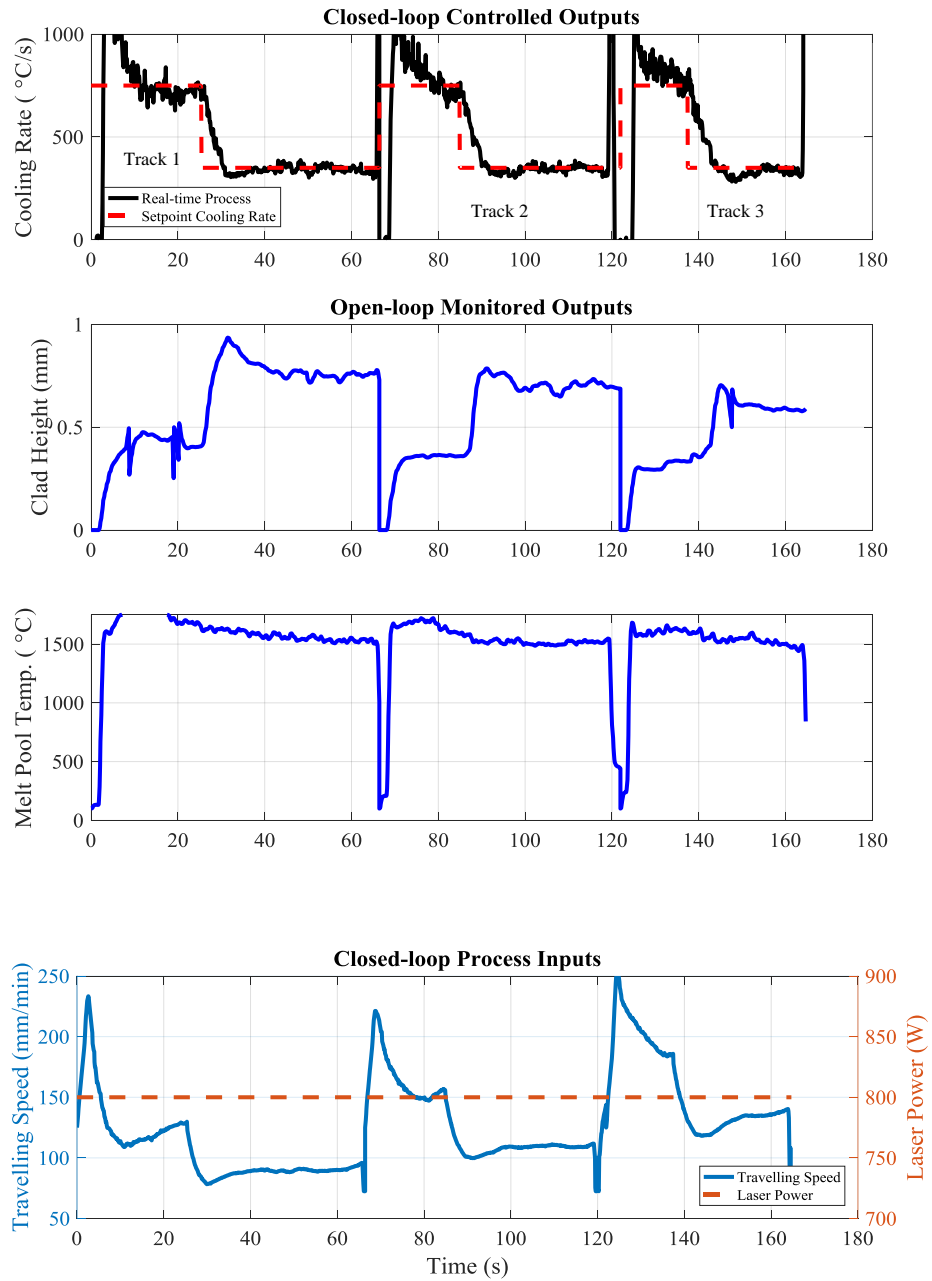**Figure 6-53 Thermal dynamics, geometry and process inputs of closed-loop cooling rate control of single-track LAM sample *J2-c*.**

6.3.2.3 Integrated Closed-loop Control of Cooling Rate and Clad Height in Single-Track and Multi-Track Laser Additive Manufacturing Depositions (with PID controller)

The previous single-input-single-output (SISO) control systems, for either the clad height or cooling rate, will provide the control of only one output parameter, whereas, the other parameter will undergo variation during the process. Nonetheless, as indicated in the prior chapters, the ultimate advantage of a fully automated LMP process is the capability of achieving integrated geometry and microstructure characteristics locally in the final product. Such complete automation requires a multi-input-multi-output (MIMO) control system that controls the cooling rate and clad height both at the same time. In such a system, two or more control actions are required to be adjusted in real-time rather than one. Thus, in addition to the travelling speed that has been used as the main control action up to now, the laser power is also required to be adjusted in real-time to compensate for the variation of the second output parameter.

The first integrated closed-loop sample developed in this research is the MIMO control of a two-step cooling rate profile for a single-track LAM deposition similar to sample *J2-c*. In addition to the cooling rate control, a constant setpoint is also assigned for the clad height, which is achieved through additional real-time adjustment of the laser power. The laser processing conditions of the closed-loop MIMO sample *K1-c*, are described in Section 5.4.2.3 and Table 5-12.

The integrated closed-loop sample *K1-c* is shown in Figure 6-54. The real-time thermal dynamics, clad height and controlled process inputs of the deposition are also illustrated in Figure 6-55. Unlike the previous SISO control systems that provided only clad height or cooling rate control, the MIMO control system develops a desired step cooling rate profile while keeping the clad height of the deposition consistent. This integrated control is obtained through real-time adjustments of both the laser power and travelling, as shown by the monitored process inputs in Figure 6-54.

The thermal dynamics control of sample *J2-c* shown in Figure 6-53, is similar to *K1-c* however, without the inclusion of a clad height control system. Comparing the two closed-loop systems, it is clear that the travelling speed in the *J2-c* sample changes differently compared to the *K1-c* sample. Most notably, as illustrated in Figure 6-54, instead of using a constant laser power, the laser power gradually increases to compensate for the change in clad height.
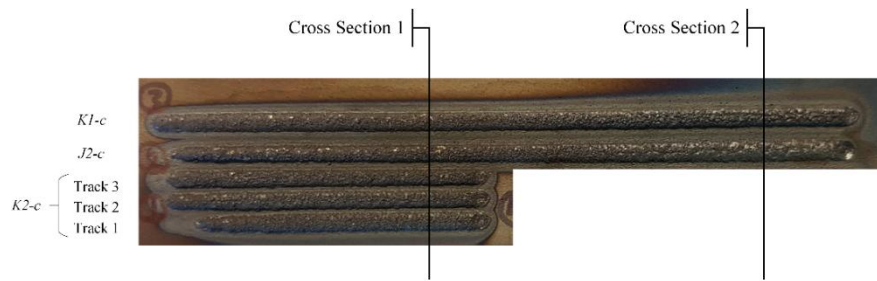
Figure 6-54 Single-track and multi-track LAM samples *K1-c* and *K2-c* with closed-loop integrated cooling rate and clad height control.

In order to compare the microstructures and material properties of the closed-loop cooling rate process versus the integrated closed-loop cooling rate and clad height process, they were both cross sectioned at two locations as indicated in Figure 6-54. The microstructures of each sample at the two cross sections are illustrated in Figure 6-56. The first section of both samples is controlled at a higher cooling of $750\ ℃/s$ compared to the second section with a cooling rate of $350\ ℃/s$. Accordingly, for each sample the microstructure of the first section is finer compared to the second section. Most notably, although the processing parameters of each sample are completely different, their microstructures at each section are very similar because of the similar closed-loop controlled cooling rate for both samples.
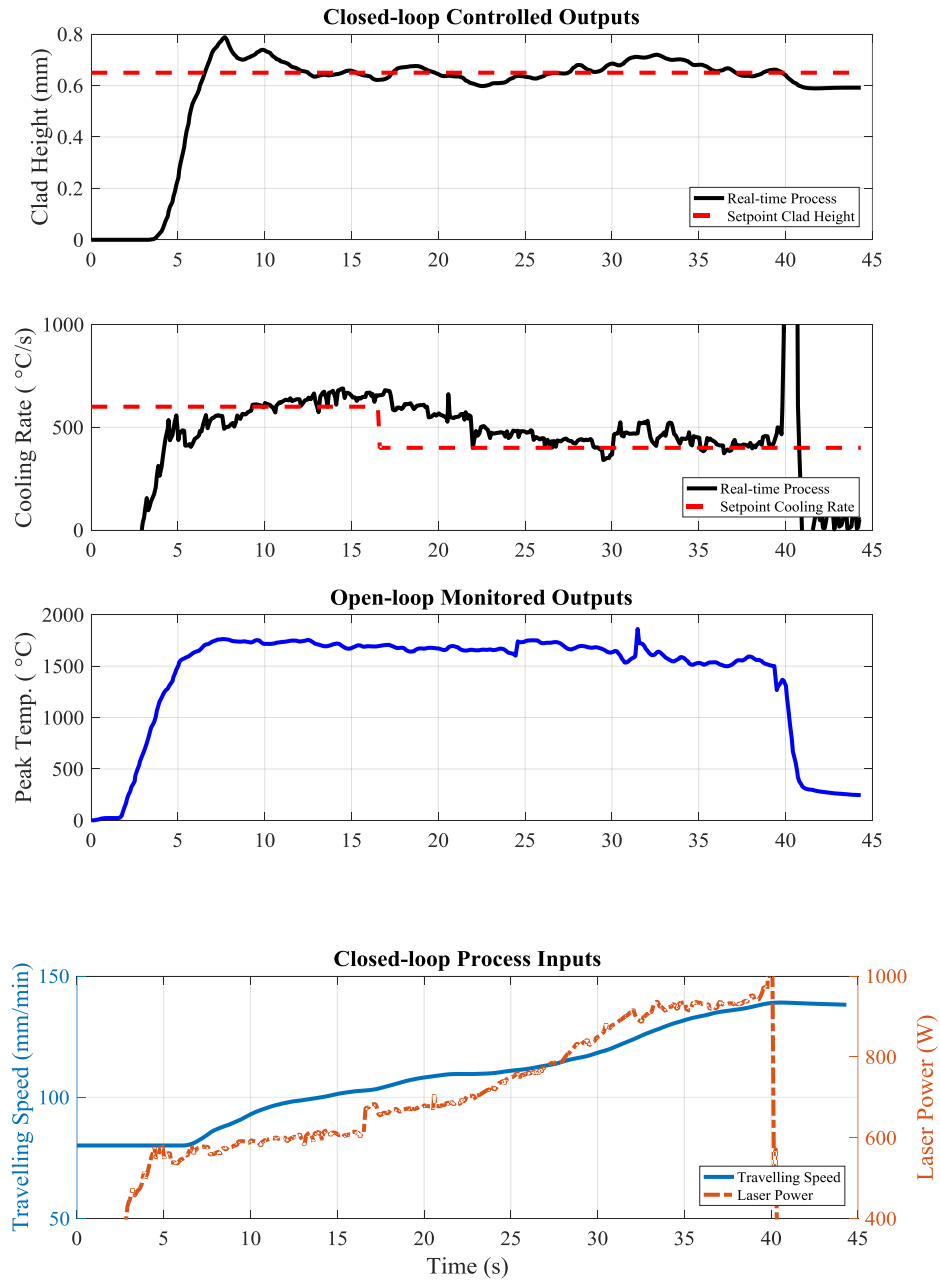
Figure 6-55 Thermal dynamics, geometry and process inputs of closed-loop integrated cooling rate and geometry control of single-track LAM sample *K1-c*.

Figure 6-56 Microstructures of SISO closed-loop cooling rate control sample *J2-c* and MIMO integrated cooling rate and clad height control LAM sample *K1-c*.

In order to further investigate the quantitative material properties of the SISO and MIMO closed-loop samples, their hardness values were measured and listed in Table 6-17. It can be seen that both samples have similar hardness values at each cross section as a result of the cooling rate control. Nonetheless, the clad height of the SISO cooling rate control sample has a deviation of $0.21\ mm$, as a result of the controlled cooling, while the MIMO integrated control sample has the same controlled clad height at both cross sections. Therefore, the MIMO integrated closed-loop control of the cooling rate and clad height, provides a consistent deposition with desired microstructure and geometry in real-time.

Table 6-17 Hardness of SISO closed-loop cooling rate control sample *J2-c* and MIMO integrated cooling rate and clad height control LAM sample *K1-c*.

	Average Hardness [Standard Deviation] (HV1.00)		Clad Height (*mm*)	
	J2-c	*K2-c*	*J2-c*	*K2-c*
Cross Section 1	589.45 [±4.25]	601.70 [±1.30]	0.62	0.65
Cross Section 2	422.90 [±4.20]	436.60 [±2.00]	0.83	0.66

To extend the results of the integrated MIMO microstructure and geometry control system to three dimensional structures developed with LAM, a closed-loop multi-track LAM sample was developed using the integrated control system. Sample *K2-c* is shown in Figure 6-54. The predefined laser processing conditions of the closed-loop MIMO sample *K2-c*, are described in Section 5.4.2.3 and Table 5-12. The closed-loop controlled thermal dynamics, clad height and process inputs of this sample are shown in Figure 6-57. According to this figure, the clad height and cooling rate of all three tracks are controlled to their predefined set values. Thus, each track experiences the same thermal history and cooling, while its geometry also remains consistent with its desired setpoint value. This complete consistency is in contrast to the SISO clad height and cooling rate control responses shown in Figure 6-46 and Figure 6-52, respectively. In the closed-loop clad height control system (Figure 6-46), the control of the clad height resulted in variations in the cooling rate. Similarly, the SISO control of the cooling rate (Figure 6-46), resulted in change of geometry in the multi-track deposition. On the other hand, the integrated MIMO control of the cooling rate and clad height develop a geometryly uniform layer of deposition with a consistent cooling rate history.
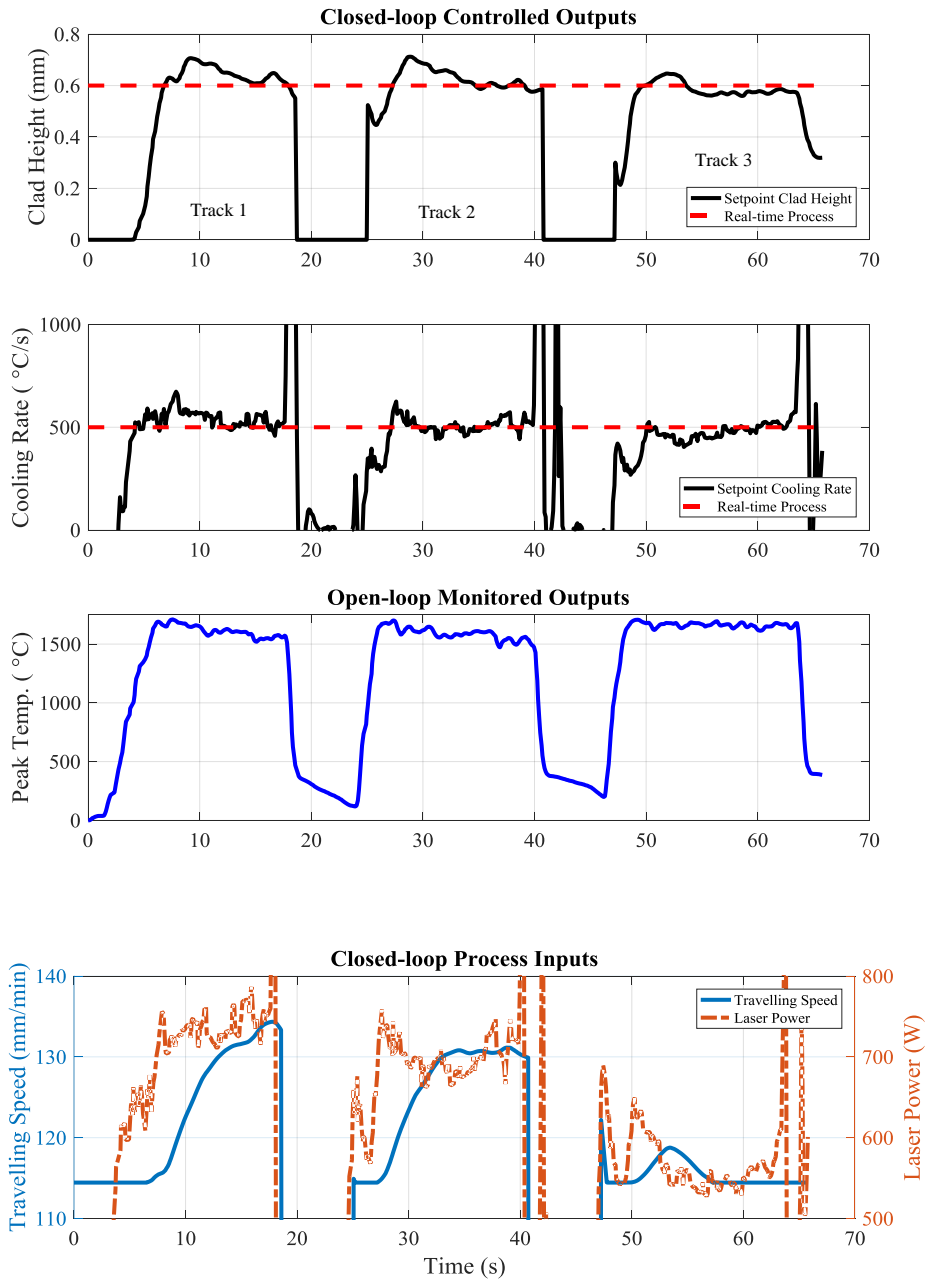
Figure 6-57 Thermal dynamics, geometry and process inputs of closed-loop integrated cooling rate and geometry control of multi-track LAM sample *K2-c*.

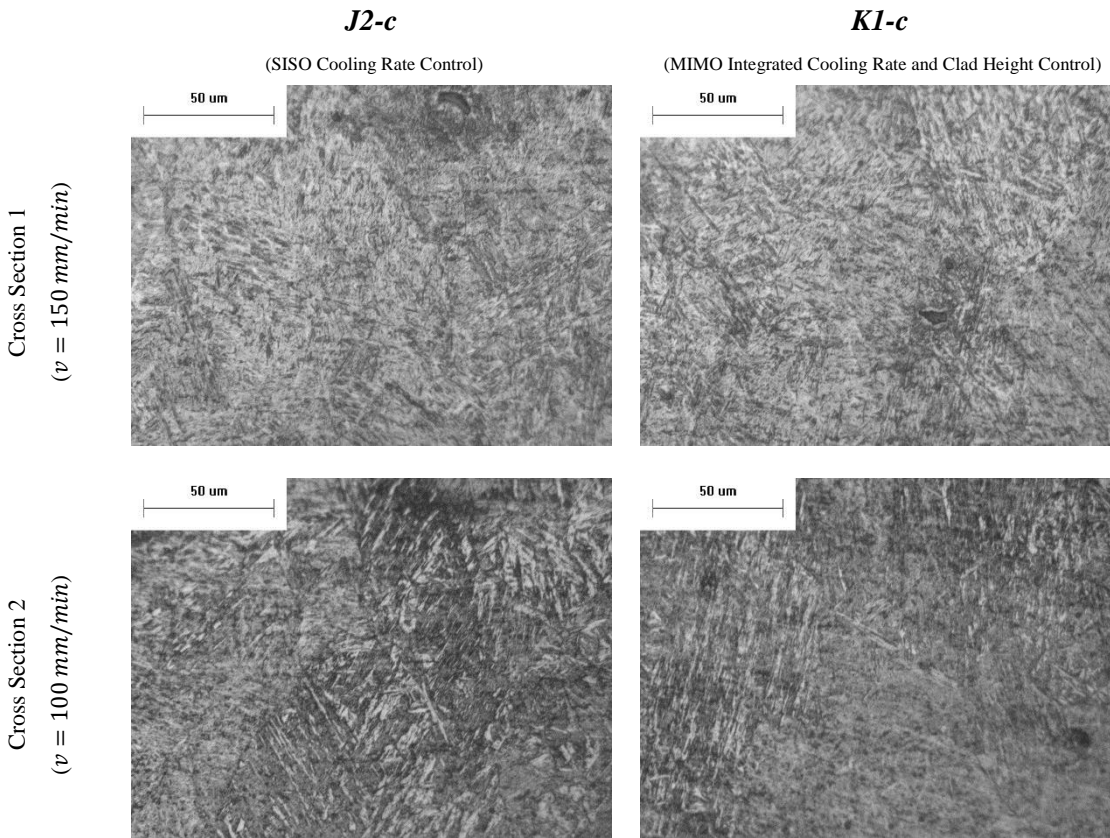To study the material properties of the integrated closed-loop controlled sample, the multi-track sample was cross sectioned at one location, as indicated in Figure 6-54. The microstructures and hardness values of each track are shown in Figure 6-58 and Table 6-18, respectively. The controlled cooling rate has produced a consistently controlled microstructure and hardness profile in all tracks. These consistent microstructure and material characteristics are achieved under consistent geometry control unlike the results of SISO control systems. Hence, by implementing a MIMO integrated closed-loop process for controlling the geometry and cooling rate, consistent desired microstructure and geometry properties are achieved at the same time.
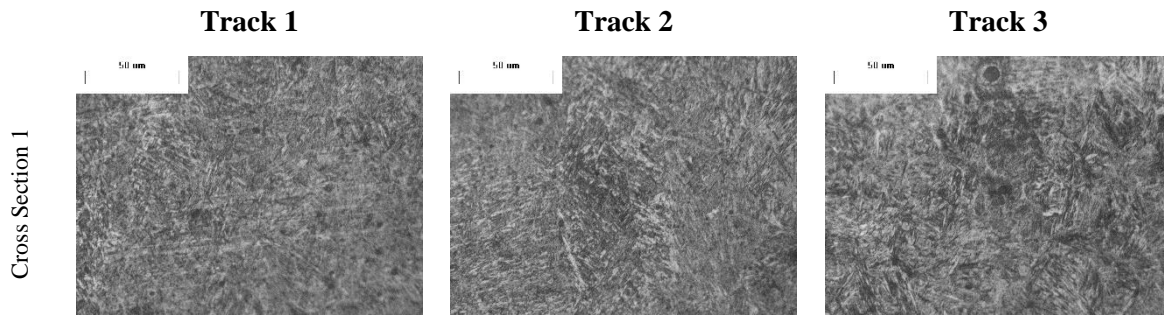
Figure 6-58 Microstructures of closed-loop integrated cooling rate and geometry control of multi-track LAM sample *K2-c*.

Table 6-18 Hardness of closed-loop integrated cooling rate and geometry control of multi-track LAM sample *K2-c*.

	Average Hardness [Standard Deviation] (HV1.00)		
	Track 1	Track 2	Track 3
Cross Section 1	444.20 [±3.50]	441.35 [±0.65]	468.00 [±1.52]

6.4 Summary

The current chapter summarized the benefits of the developed thermal-geometry monitoring and control module in three different set of applications: (1) online prediction of material and mechanical properties, (2) adaptive thermal dynamics estimation of LMP processes, and (3) real-time closed-loop control of microstructure and geometry in LMP processes. Initially, the module capabilities were

evaluated for real-time monitoring of different geometry and material/mechanical properties during the LAM and LHT processes. The percentage of martensite formation in low carbon steels such as AISI 1020 and 1018 during the laser hardening process was found to be in positive correlation with the real-time peak temperature signal measured by the module. While the cooling rate and heating rate of the LHT process increased, the reducing peak temperature resulted in lower martensite formation. According to CHT diagrams, at higher heating rates a higher peak temperature is required for homogenous austenization and final martensite formation. Consequently, the real-time monitoring of the combined thermal dynamics provides a reliable insight into the amount and consistency of the developed martensite microstructure during the process. Since the percentage of martensite defines the hardness of a heat treated layer, the final hardness value of the LHT process was also governed and monitored by the real-time peak temperature signal. Finally, it was also revealed that the hardening depth during the LHT process can be predicted with the value of the peak temperature during the process. The monitoring capabilities of the module were also evaluated for the LAM process for AISI 4340 depositions. It was observed that the martensite percentage, overall morphology size, hardness and deposition height of the LAM process could be monitored and predicted in real-time using the monitoring module.

The developed adaptive thermal model was tuned and verified for real-time estimation of the thermal dynamics during LHT and LAM processes. The nonlinear and linear formulations of the model provided highly accurate estimations of the cooling rate and peak temperature for both processes under different excitation signals for the laser power and travelling speed. Although the LHT and LAM processes displayed different dynamic responses towards similar excitation signals, the model provided accurate dynamic estimations of both processes. The adaptive adjustment of the equivalent thermal conductivity term enabled such highly accurate dynamic predictions for two completely different processes, with the same thermal model. Different set of boundary condition types were also validated for the model, which verified the different boundary assumptions considered during the modelling process.

Finally, a set of open-loop and closed-loop experiments were conducted to evaluate the effect of closed-loop control of the thermal dynamics and geometry on production consistency of LHT and LAM processes. Open-loop multi-track LHT resulted in hardness deviations as large as 70 $HV1.00$ in the heat treated surface, due to the inconsistency of martensite in each track, which was caused by peak temperature variation during the process. The closed-loop peak temperature control of a similar multi-

172

track LHT sample resulted in highly consistent martensite formation and hardness profile throughout the surface. Moreover, closed-loop control of the peak temperature at three different levels during the process provided a desired gradient hardness profile in a small surface area. Open-loop and closed-loop peak temperature control of single-track laser heat treated samples on a $3\ mm$ step workpiece were evaluated. It was observed that due to smaller laser beam size and increased peak temperature after the step profile, the hardness of the workpiece increased drastically up to $100\ HV1.00$. The microstructure and hardness deviation was resolved by closed-loop control of the peak temperature with adaptive change of the travelling speed during the process. In addition to closed-loop control of the peak temperature by PID controllers, a thermal dynamics state observer feedback control system was developed to control the peak temperature with only limited thermal information of the melt pool boundaries rather than complete thermal dynamics measurements. The estimation of thermal dynamics was provided through the adaptive thermal model in real-time. The state observer feedback control system provided highly consistent and controlled hardness profiles before and after the step profile during single-track and multi-track laser heat treated profiles.

Finally, a multi-input-multi-output controller was used to provide integrated clad height and cooling rate control during the LAM process with adaptive adjustments of the travelling speed and laser power. This integrated closed-loop process delivered highly consistent microstructure/mechanical properties while providing a consistent desired deposition geometry. The integrated geometry and microstructure control system was evaluated for single-track and multi-track LAM depositions to develop tailored in-layer mechanical properties with consistent in-layer clad height.

Chapter 7

Conclusions and Future Work

7.1 Conclusions

In this research, a closed-loop system was developed for real-time monitoring and control of microstructure and geometry properties, during Laser Materials Processing (LMP) procedures. The closed-loop system significantly increases the production consistency and quality of the final LMP-manufactured product. Most LMP process disturbances can be eliminated as a result of the closed-loop control procedure. Therefore, the implementation of such an automated system, will considerably reduce the extensive amount of time and effort required for manual tuning of LMP setups, and will also equip machine operators with an essential tool for obtaining rare in-process knowledge of the LMP manufacturing process. Finally, the current developed closed-loop process will enable selective local control of material properties, such as morphology and hardness, to a predefined desired values. Closed-loop Laser Additive Manufacturing (LAM) and Laser Heat Treatment (LHT) experiments were designed and conducted to demonstrate the performance and benefits of the developed real-time closed-loop control process. The major findings and contributions of this research are summarized below.

A multi-objective thermal-geometry monitoring and control module was developed in this research to control the microstructure and geometry of the LMP product. Although, individual thermal or geometry vision-based monitoring systems are already available for in-process monitoring of the LMP process, integration of these systems into one unified module has been seldom achieved. A CCD-based vision camera and a thermal infrared camera were integrated to provide vision-based monitoring of the melt pool geometry and thermal process. A thermal dynamics monitoring scheme was established to extract the three main thermal dynamics of the LMP thermal process in real-time, which include the cooling rate, peak temperature and heating rate. Measurement of the peak temperature is common in industry and literature, whereas, cooling rate and heating rate calculations are limited to offline and passive methods. Therefore, the real-time extraction of the cooling and heating rates by the module, provides an exciting new perspective into LMP thermal monitoring and control. While, no direct monitoring approach is available for understanding microstructure evolutions during the LMP process,

174

an indirect method was proposed to predict microstructure variations based on real-time thermal dynamics measurements. The geometry and thermal dynamics monitoring schemes of the module were incorporated as feedback signals for a multi-input-multi-output (MIMO) controller system, to construct a fully automated closed-loop LMP process. The closed-loop LMP process will be able to deliver integrated microstructure and geometry control for different LMP procedures.

A novel adaptive dynamic thermal model was developed for the purpose of real-time estimation and control. The finite difference approach was used to create an accurate dynamic representation of the LMP thermal process. The model provides real-time estimations of the two-dimensional temperature nodes on the surface of the heated workpiece. Each temperature node is a state of the dynamic system, and can be observed and verified by the thermal pixel measurements of the infrared camera. Since the original model was nonlinear, a linearized state space formulation of the thermal model was also proposed for the purpose of feedback control implementation. The model calculations can be restricted to any specific region of interest around the melt pool area, in order to reduce online computational time, so that it can be easily implemented for real-time applications. An adaptive equivalent thermal conductivity term was introduced into the model to compensate for any simplifying assumption and real-time process error. The boundary temperatures of the dynamic model can be updated by real-time measurements of any thermal monitoring device. Finally, an adaptive tuning method was proposed for the model, to provide accurate estimations of the process thermal dynamics in real-time.

A thermal dynamics state observer feedback control system was also designed in this research for closed-loop thermal dynamics control of systems with limited thermal observability. An optimal Linear Quadratic Tracking (LQT) controller was designed and developed based on the thermal dynamics model. The optimal controller minimizes the closed-loop error with a minimum control effort and minimum variations of the control action. While, the general closed-loop microstructure control is only possible if direct measurements of the thermal dynamics are available, many LMP setups may not be able to provide real-time thermal dynamics measurements, due to the costly expenses of a high-resolution and high-temperature thermal infrared camera. Consequently, a model-based state observer feedback control system was developed, which enables closed-loop thermal dynamics control of the LMP process with limited thermal information of the melt pool boundaries rather than the melt pool itself. One can use the temperature measurements of the boundaries obtained from a low-cost pyrometer or thermal camera, to obtain the unobservable peak temperatures, cooling rates and heating rates in real-time, using the developed thermal model as a reliable observer system. Compared with the general

closed-loop control system, the state observer feedback control has a much lower hardware cost, however, it requires the implementation of a highly reliable and accurate observer model.

Experiments were designed to evaluate the performance of the developed thermal-geometry monitoring and control module for three main applications: indirect online microstructure prediction, thermal dynamics model validation, and closed-loop control of microstructure and geometry. The indirect online microstructure prediction experiments verified the module as a highly reliable source for online prediction of microstructure variations during LMP processes. LHT experiments were conducted on AISI 1020 low carbon steel to provide predictions of relative changes in hardness/microstructure based on real-time thermal dynamics variations. It was observed that general microstructure properties of the LHT process including the amount of martensite formation, hardness value and hardening depth, can be predicted to a good degree by analyzing the real-time cooling rate, peak temperature and heating rate data. There was a maximum limit for the heating rate and cooling rate to prevent non-homogenized austenization and partial martensite formation, and it is suggested these limits can be defined, monitored and controlled by the real-time thermal monitoring system. The real-time thermal history also governed the hardness profile of each heat treated track. It was also observed that the hardened depth had a positive correlation with the peak temperature, which can be used as a feedback control signal during closed-loop depth control. In addition, AISI 4340 LAM experiments were also monitored with the developed module to enable a relative understanding and estimation of the microstructure/hardness under the influence of real-time perturbations. The general microstructure and hardness of the LAM process could be predicted specifically by the real-time recorded cooling rate data.

Therefore, the thermal-geometry monitoring and control module was found to be a highly effective instrument for indirect monitoring of the microstructure and geometry during the LHT and LAM processes. This is a significant discovery for automation of LMP procedures, since microstructure properties cannot be monitored directly online by means of any instrument due to the harsh environment of the LMP thermal process or highly expensive instrumentation.

The developed dynamic model was validated experimentally for estimation of the LHT and LAM processes, using a combination of different excitation signals for the laser power and travelling speed. The model was evaluated in real-time for four sets of LHT thermal excitations, which included ramp and multi-step change of the travelling speed and laser power. Results indicated a highly accurate model with an average error of $\pm 4.00\ \%$ (or $\pm 45.00\ ℃$) error for peak temperature estimations, and $\pm 8.00\ \%$

(or $\pm 57.00 \, °C/s$) error for cooling rate estimations. The model was also tuned and evaluated for the LAM process which resulted in similar degree of high accuracy. These amount of errors are completely acceptable for microstructure and geometry identification and control purposes, since these properties do not change significantly within these temperature and cooling rate deviations. More importantly, the model error was found to be even comparable to the measurement error, which is $\pm 2.00 \, \%$ for temperature measurements and $\pm 4.00 \, \%$ for cooling rate measurements.

Thus, the developed adaptive thermal model was found to be highly accurate and at the same time computationally fast for real-time closed-loop estimation and control purposes. Therefore, in the case of limited observability and unmeasurable thermal dynamics data, one can use the model for thermal dynamics estimation and microstructure control inside a state observer feedback control system. This state observer model would be a huge cost saver for closed-loop microstructure control applications.

Finally, closed-loop control of the LMP process was studied using the developed thermal-geometry monitoring and control module. Several closed-loop case studies were investigated to demonstrate the generality and performance of the proposed integrated microstructure and geometry control system.

Initially, the microstructure and hardness of multi-track heat treated lines were investigated in open-loop conditions. It was realized that due to preheating effect of the initial tracks, every track in a multi-track heat treatment process experiences a different peak temperature profile. Consequently, this deviation resulted in an inconsistent hardness profile in the surface with deviating hardness values of approximately $70 \, HV 1.00$ (Vickers hardness values measured at $1 \, kgf$). However, by implementing a closed-loop control process for the peak temperature, and keeping the temperature of all three tracks at the same value through adaptive adjustment of the laser travelling speed, highly consistent material properties were observed. The hardness value of all tracks in the closed-loop controlled process were very similar. In another set of experiments, a single-track heat treated line was tested on a workpiece with a $3.175 \, mm$ stepped surface, which resulted in change of laser spot size during the process. Open-loop experimentation of this case study indicated a significant deviation of around $100 \, HV 1.00$ for the heat treated line before and after the step, while keeping the processing parameters consistent. On the other hand, by implementing the closed-loop control process for the peak temperature and automatically changing the travelling speed during the process, complete identical hardness values were obtained for the track before and after the step. Microscopy of closed-loop samples indicated that the microstructures of the samples were controlled to a highly accurate degree, since very similar microstructures were observed during the peak temperature control.

The thermal dynamics LQT state observer feedback control system was also evaluated for closed-loop peak temperature control. The controller was tested for a multi-track LHT sample and single-track LHT sample on a stepped workpiece. Both closed-loop samples yielded perfectly controlled material properties as a consequence of using the state observer feedback control system.

A final set of closed-loop experiments were conducted regarding the control of microstructure and geometry in the LAM process. A closed-loop clad height control system was evaluated for multi-track LAM depositions. The material analyses showed that while the clad height was controlled to an extensive degree, the hardness and material properties of each track were different. This variation was predicted online, since clear deviation was observed for the cooling rate during closed-loop clad height control. Subsequently, closed-loop cooling rate experiments were conducted for multi-track and single-track LAM depositions. Hardness measurements and microscopy implied that the microstructure and hardness were very much controlled and consistent in closed-loop cooling rate process versus open-loop conditions. Nonetheless, during closed-loop cooling rate control deviations were observed in the clad height of the deposition. Therefore, a multi-input-multi-output controller was designed and tested for integrated clad height and cooling rate control during LAM depositions, by simultaneous adjustment to the laser power and travelling speed in real-time. Initially, a single track deposition was tested for a step cooling rate setpoint profile and a constant clad height profile. Microstructure analyses revealed that the morphology and hardness values of each section were completely controlled as predefined by the cooling rate value, meanwhile the clad height of the deposition also remained consistent to its predefined setpoint value. A multi-track deposition was also developed using the integrated closed-loop control system. It was observed that every track had a consistent controlled clad height and cooling rate, which was achieved by simultaneous adaptive adjustments to the laser power and travelling speed. Subsequently, because of the integrated closed-loop control condition, all three track had the same consistent microstructure, hardness and clad height values.

The above closed-loop control results indicate a significant breakthrough in development of a fully automated LMP process. As explored by these results, the closed-loop process can increase the consistency of the final material and mechanical properties of an LMP product to an extremely high degree. Such automation and manufacturing consistency will enable LMP machines and setups to be used in mainstream manufacturing.

178

7.2 Future Work

In order to improve the performance and reliability of the developed closed-loop LMP system, a few suggestions are provided in this section to advance the primary work done in this research.

- Further validation of the closed-loop LMP process for different materials and processing conditions: The current general closed-loop control system was tested for three different type of steels. There are other type of materials that may react differently in terms of thermal dynamics and microstructure behavior. Nonetheless, the developed closed-loop microstructure system provides a general scheme, which can be easily extended to any material and any processing conditions. Therefore, it is important to study and evaluate other different materials under different processing conditions to extend the general microstructure and geometry control method.

- Evaluation of the real time closed-loop integrated microstructure and geometry control process for development of three-dimensional LAM structures: Integrated microstructure and geometry control was evaluated for development of consistent single-track and multi-track horizontal layers during the LAM process. Although, these cases cover broad applications in the LAM technology, many industrial LAM applications involve construction of complete three-dimensional objects. Therefore, it is critically important to extend the developed thermal dynamics monitoring and closed-loop process for microstructure and geometry control of three-dimensional objects produced by the LAM process. In three-dimensional depositions, each layer experiences multiple thermal cycles rather than one. The first thermal cycle is experienced during the solidification and deposition of the respective track, whereas, the same track experiences lower-temperature thermal cycles while consecutive tracks are deposited on top. In order to provide correct measurement and control of microstructure/mechanical properties of each track, the current concept of thermal dynamics monitoring can be extended. Since each track experiences multiple thermal cycles, it is required to expand the system to monitor the thermal dynamics of all these thermal cycles during the process. Integrated control of these different sets of thermal dynamics develops consistent microstructure properties throughout a three-dimensional structure. However, since multiple sets of thermal dynamics have to be controlled, it is required to utilize multiple control actions rather than on or two.

- Employment of a secondary dual-emissivity monitoring device for increased accuracy of thermal measurements: A thermal infrared camera was used for extracting thermal dynamics measurements of the LMP process. The temperature measurements of an infrared camera are defined by the emissivity value of the material, which is on its own dependent on the material temperature and process conditions. However, in the experiments, a constant thermal emissivity was assumed since thermal information was used for control purposes, and a relative measurement would be acceptable. Nonetheless, it was observed during experiments that the thermal infrared camera provided obvious incorrect temperature measurements in specific experimental cases, which were most probably caused by the variation of the process emissivity in the harsh environmental conditions. A dual-emissivity monitoring device such as a dual emissivity pyrometer will remove the effect of changing emissivity. Therefore, it is highly advantageous to implement a dual-emissivity monitoring device in the system to adaptively correct the emissivity value of the thermal infrared camera for higher accuracy and true temperature measurements.

- Evaluation of the thermal dynamics state observer feedback control with low-cost point measurement devices: The state observer feedback control system controlled the peak temperature of the LHT process only through thermal information of the boundary conditions obtained from the thermal infrared camera. The state observer feedback control system has the capability of controlling microstructure properties even assuming fixed constant boundary temperatures, which will reduce the required amount of thermal measurement, and subsequently reduce the cost of close-loop control implementation. However, before being implemented in such scenarios, it is required to verify the fixed constant boundary temperature assumption, more extensively. One method is to utilize a low-cost point measurement device such as a pyrometer to provide a constant measurement of one boundary node for the observer and compare the estimation results with the complete measured thermal information of the infrared camera. By validating such a fixed constant boundary condition assumption, this allows one to implement the state observer feedback control in systems without infrared thermal measurements.

- Further validation of the developed model for multi-track LHT and LAM depositions: The current developed model was only verified for single-track LHT and LAM depositions, whereas estimating the thermal dynamics of multi-track processing conditions may represent

a more generalized condition. Thus, it is recommended to construct evaluation schemes for which the current thermal model is tuned and verified for multi-track LHT and LAM depositions. Such validation will increase the generality of the developed model and will also further justify its implementation as a state observer in the state observer feedback control system.

- Development of more accurate and versatile model-based controllers: In the current research an LQT model-based controller was used for controlling the estimated peak temperature. Nonetheless, there may be more versatile model-based controller designs such as model predictive control techniques that may provide better closed-loop responses in a state observer feedback control system. Hence, it is recommended to compared the response of such model-based controllers for obtaining the most suitable control technique for the process.

- Development of an adaptive real-time algorithm for online updating of the thermal model adaptive parameters: In the developed model, the equivalent thermal conductivity coefficients and temperature bias terms were introduced as two adaptive parameters to eliminate the effect of simplifying assumptions and model error. In the current research, the values of these parameters were defined through manual tuning. However, development of a real-time algorithm that can automatically and adaptively identify these values online, will increase the accuracy of the modeling technique. Moreover, online adaptive parameter identification will provide a great opportunity for further elimination of process noise and increased performance of the state observer feedback control system.

Bibliography

[1]   T. H. MAIMAN, "Stimulated Optical Radiation in Ruby," *Nature*, vol. 187, no. 4736, pp. 493–494, Aug. 1960.

[2]   L. Garwin and T. Lincoln, "A Century of Nature: Twenty-One Discoveries that Changed Science and the World." [Online]. Available: http://www.press.uchicago.edu/Misc/Chicago/284158_townes.html.

[3]   E. Toyserkani, A. Khajepour, and S. Corbin, *Laser Cladding*. Florida: CRC Press, 2005.

[4]   D. D. Gu, W. Meiners, K. Wissenbach, and R. Poprawe, "Laser additive manufacturing of metallic components: materials, processes and mechanisms," *Int. Mater. Rev.*, vol. 57, no. 3, pp. 133–164, May 2012.

[5]   S. Kou, *Welding Metallurgy*, Second., vol. 822. Hoboken: John Wiley and Sons, 2003.

[6]   T. S. Plaskett and W. C. Winegard, "No Title," *Can. J. Physiol.*, no. 38, p. 1077, 1960.

[7]   M. C. Flemings, *Solidification processing*, vol. 8. McGraw-Hill, 1974.

[8]   a. Munitz, "Microstructure of rapidly solidified laser molten AI-4.5 Wt Pct cu surfaces," *Metall. Trans. B*, vol. 16, no. March, pp. 149–161, 1985.

[9]   A. J. Paul and T. DebRoy, "No Title," *Rev. Mod. Phys.*, no. 67, p. 85, 1995.

[10]   S. Kou and Y. Le, "No Title," *Met. Trans.*, no. 13A, p. 1141, 1982.

[11]   W. D. Callister, *Materials Science and Engineering*. New York: John Wiley & Sons, 2007.

[12]   G. E. Totten, *Steel Heat Treatment Handbook*, Second. Boca Raton: Taylor and Francis, 2007.

[13]   J. Orlich, A. Rose, and P. Wiest, *Atlas zur Warmebehandlung der Stahle*. Dusseldorf: Verlag Stahleisen, 1973.

[14]   J. W. Elmer, T. a Palmer, S. S. Babu, W. Zhang, and T. DebRoy, "Direct Observations of Austenite , Bainite and Martensite Formation During Arc Welding of 1045 Steel using Time Resolved X-Ray Diffraction," *Weld. J.*, pp. 244–253, 2004.

[15]   A. K. Sinha, *Physical Metallurgy Handbook*. McGraw-Hill, 2003.

[16]   D. Rosenthal, "The Theory of Moving Sources of Heat and its Application to Metal Treatments," *Trans. ASME*, vol. 68, pp. 849–866, 1946.

[17] V. Gregson, *Laser Heat Treatment in Laser Materials Processing*. Amsterdam: North-Holland, 1983.

[18] H. S. Carslaw and J. C. Jaeger, *Conduction of Heat in Solids*. Oxford: Oxford Press, 1959.

[19] H. E. Cline and T. R. Anthony, "Heat treating and melting material with a scanning laser or electron beam," *J. Appl. Phys.*, vol. 48, no. 9, p. 3895, 1977.

[20] R. Festa, O. Manca, and V. Naso, "A comparison between models of thermal fields in laser and electron beam surface processing," *Int. J. Heat Mass Transf.*, vol. 31, no. 1, pp. 99–106, 1988.

[21] R. Festa, O. Manca, and V. Naso, "Simplified thermal models in laser and electron beam surface hardening," *Int. J. Heat Mass Transf.*, vol. 33, no. 11, pp. 2511–2518, 1990.

[22] M. F. Ashby and K. E. Easterling, "The transformation hardening of steel surfaces by laser beams—I. Hypo-eutectoid steels," *Acta Metall.*, vol. 32, no. 11, pp. 1935–1948, 1984.

[23] H. R. Shercliff and M. F. Ashby, "The prediction of case depth in laser transformation hardening," *Metall. Trans. A*, vol. 22, no. 10, pp. 2459–2466, 1991.

[24] K. a. Chiang and Y. C. Chen, "Laser surface hardening of H13 steel in the melt case," *Mater. Lett.*, vol. 59, no. 14–15, pp. 1919–1923, 2005.

[25] R. R. Dehoff, M. M. Kirka, W. J. Sames, H. Bilheux, A. S. Tremsin, L. E. Lowe, and S. S. Babu, "Site specific control of crystallographic grain orientation through electron beam additive manufacturing," *Mater. Sci. Technol.*, vol. 31, no. 8, pp. 931–938, May 2015.

[26] J. Isenberg and S. Malkin, "Effects of Variable Thermal Properties on Moving-Band-Source Temperatures," *J. Eng. Ind.*, vol. 97, no. 3, pp. 1074–1078, 1975.

[27] S. KOU, D. K. SUN, and Y. P. LE, "A Fundamental Study of Laser Transformation Hardening," *Metall. Trans. A*, vol. 14, no. April, pp. 643–653, 1983.

[28] R. Komanduri and Z. B. Hou, "Thermal analysis of the laser surface transformation hardening process," *Int. J. Heat Mass Transf.*, vol. 44, no. 15, pp. 2845–2862, 2001.

[29] K. POORHAYDARI, B. M. PATCHETT, and D. G. IVEY, "Estimation of Cooling Rate in the Welding of Plates with Intermediate Thickness," *Suppl. TO Weld. J.*, no. October, pp. 149–155, 2005.

[30] E. O. Hall, "The Deformation and Ageing of Mild Steel: III Discussion of Results," *Proc. Phys.*

Soc. Sect. B, vol. 64, pp. 747–753, 1951.

[31]   B. Petersen and H. W. Kerr, "Fine Grained Weld Structures," *Weld. Res. Suppl.*, 1973.

[32]   A. Emamian, S. F. Corbin, and A. Khajepour, "Tribology characteristics of in-situ laser deposition of Fe-TiC," *Surf. Coatings Technol.*, vol. 206, no. 22, pp. 4495–4501, Jun. 2012.

[33]   X. C. Li, J. Stampfl, and F. B. Prinz, "Mechanical and thermal expansion behavior of laser deposited metal matrix composites of Invar and TiC," *Mater. Sci. Eng. A*, vol. 282, no. 1–2, pp. 86–90, 2000.

[34]   J. M. L. Griffith, M. T. Ensz, J. D. Puskar, C. V. Robino, J. A. Brooks, J. A. Philliber and W. H. H. E. Smugeresky, "UNDERSTANDING THE MICROSTRUCTURE AND PROPERTIES OF COMPONENTS FABRICATED BY LASER ENGINEERED NET SHAPING," in *Proceedings of the Solid Freeform and Additive Fabrication Conference*, 2000, pp. 9–20.

[35]   S. Mitzner, S. Liu, M. Domack, and R. Hafley, "Grain Refinement of Freeform Fabricated Ti-6Al-4V Alloy Using Beam/Arc Modulation," *23rd Annu. Int. Solid Free. Fabr. Symp. 6-8 Aug 2012; Austin, TX; United States*, pp. 536–555, 2012.

[36]   Yunja, Frost, Olson, and Edwards, "Grain Refinement of Aluminium Weld Metal," vol. 68, no. July, p. 280s, 1989.

[37]   S. Sundaresan, G. D. Janaki Ram, R. Murugesan, and N. Viswanathan, "Combined effect of inoculation and magnetic arc oscillation on microstructure and tensile behaviour of type 2090 Al–Li alloy weld fusion zones," *Sci. Technol. Weld. Join.*, vol. 5, no. 4, pp. 257–264, Aug. 2000.

[38]   P. Cao, M. Qian, and D. H. StJohn, "Effect of iron on grain refinement of high-purity Mg-Al alloys," *Scr. Mater.*, vol. 51, pp. 125–129, 2004.

[39]   A. Emamian, S. F. Corbin, and A. Khajepour, "The effect of powder composition on the morphology of in situ TiC composite coating deposited by Laser-Assisted Powder Deposition (LAPD)," *Appl. Surf. Sci.*, vol. 261, pp. 201–208, Nov. 2012.

[40]   B. Grabas, "Vibration-assisted laser surface texturing of metals as a passive method for heat transfer enhancement," *Exp. Therm. Fluid Sci.*, vol. 68, pp. 499–508, 2015.

[41]   S. Bhattacharya, G. P. Dinda, a. K. Dasgupta, and J. Mazumder, "Microstructural evolution of AISI 4340 steel during Direct Metal Deposition process," *Mater. Sci. Eng. A*, vol. 528, no. 6, pp. 2309–2318, 2011.

[42] K. Putatunda, M. Nambiar, and N. Clark, "INFLUENCE OF LASER HARDENING ON MECHANICAL PROPERTIES OF A lOW AllOY STEEL," *Surf. Eng.*, vol. 13, no. 5, pp. 407–414, 1997.

[43] Qiu, "Laser transformation hardening of carbon steel: microhardness analysis on microstructural phases," *Surf. Eng.*, vol. 29, no. 1, 2012.

[44] W.-S. Lee and T.-T. Su, "Mechanical properties and microstructural features of AISI 4340 high-strength alloy steel under quenched and tempered conditions," *J. Mater. Process. Technol.*, vol. 87, no. 1–3, pp. 198–206, 1999.

[45] M. Fastow, M. Bamberger, N. Nir, and M. Landkof, "Laser surface melting of AISI 4340 steel," vol. 6, no. September, pp. 900–904, 1990.

[46] J. Beuth, J. Fox, J. Gockel, C. Montgomery, R. Yang, H. Qiao, P. Reeseewatt, A. Anvari, S. Narra, and N. Klingbeil, "Process Mapping for Qualification Across Multiple Direct Metal Additive Manufacturing Processes," in *Proceedings 2013 Solid Freeform Fabrication Symposium*, 2013, no. August, pp. 655–665.

[47] S. Bontha and N. W. Klingbeil, "Thermal Process Maps for Controlling Microstructure in Laser-Based Solid Freeform Fabrication," in *Proceedings 2003 Solid Freeform Fabrication Symposium*, 2003, pp. 219–226.

[48] Y. Cao and J. Choi, "Multiscale modeling of solidification during laser cladding process," *J. Laser Appl.*, vol. 18, no. 3, p. 245, 2006.

[49] H. Ki and S. So, "Process map for laser heat treatment of carbon steels," *Opt. Laser Technol.*, vol. 44, no. 7, pp. 2106–2114, 2012.

[50] P. . Kobryn and S. . Semiatin, "Microstructure and texture evolution during solidification processing of Ti–6Al–4V," *J. Mater. Process. Technol.*, vol. 135, no. 2–3, pp. 330–339, Apr. 2003.

[51] M. Doubenskaia, P. Bertrand, and I. Smurov, "Pyrometry in laser surface treatment," *Surf. Coatings Technol.*, vol. 201, no. 5, pp. 1955–1961, Oct. 2006.

[52] C. Doumanidis and Y.-M. Kwak, "Geometry Modeling and Control by Infrared and Laser Sensing in Thermal Manufacturing with Material Deposition," *J. Manuf. Sci. Eng.*, vol. 123, no. 1, p. 45, 2001.

[53]   Y. P. Kathuria and A. Tsuboi, "The effect of beam interaction time on laser cladding process," in *Lasers and Electro-Optics*, 1996, pp. 351–352.

[54]   I. Smurov, "Pyrometry applications in laser machining," vol. 4157, pp. 55–66, 2001.

[55]   I. Smurov and M. Ignatiev, "Real Time Pyrometry in Laser Surface Treatment," *Laser Process. Surf. Treat. Film Depos.*, vol. 307, pp. 529–564, 1996.

[56]   W. M. Steen and J. Mazumder, *Laser Material Processing*, 4th ed. London: Springer-Verlag, 2010.

[57]   M. . Griffith, M. . Schlienger, L. . Harwell, M. . Oliver, M. . Baldwin, M. . Ensz, M. Essien, J. Brooks, C. . Robino, J. . Smugeresky, W. . Hofmeister, M. . Wert, and D. . Nelson, "Understanding thermal behavior in the LENS process," *Mater. Des.*, vol. 20, no. 2–3, pp. 107–113, Jun. 1999.

[58]   W. Hofmeister and M. Griffith, "Solidification in direct metal deposition by LENS processing," *JOM*, vol. 53, no. 9, pp. 30–34, Sep. 2001.

[59]   M. Doubenskaia, P. Bertrand, and I. Y. Smurov, "Temperature Monitoring of Nd:YAG Laser Cladding (CW and PP) by Advanced Pyrometry and CCD-Camera based Diagnostic Tool," *Laser-Assisted Micro- and Nanotechnologies*, vol. 5399, pp. 212–219, Apr. 2004.

[60]   M. Pavlov, D. Novichenko, and M. Doubenskaia, "Optical Diagnostics of Deposition of Metal Matrix Composites by Laser Cladding," *Phys. Procedia*, vol. 12, pp. 674–682, Jan. 2011.

[61]   T. Hua, C. Jing, L. Xin, Z. Fengying, and H. Weidong, "Research on molten pool temperature in the process of laser rapid forming," *J. Mater. Process. Technol.*, vol. 198, no. 1–3, pp. 454–462, Mar. 2008.

[62]   Y. Zhang, G. Yu, X. He, W. Ning, and C. Zheng, "Numerical and experimental investigation of multilayer SS410 thin wall built by laser direct metal deposition," *J. Mater. Process. Technol.*, vol. 212, no. 1, pp. 106–112, Jan. 2012.

[63]   S. Lhospitalier, P. Bourges, A. Bert, J. Quesada, and M. Lambertin, "Temperature measurement inside and near the weld pool during laser welding," *J. Laser Appl.*, vol. 11, no. 1, p. 32, 1999.

[64]   G. Bi, A. Gasser, K. Wissenbach, A. Drenker, and R. Poprawe, "Investigation on the direct laser metallic powder deposition process via temperature measurement," *Appl. Surf. Sci.*, vol. 253, no. 3, pp. 1411–1416, Nov. 2006.

[65] M. Vasudevan, N. Chandrasekhar, V. Maduraimuthu, a. K. Bhaduri, and B. Raj, "Real-Time Monitoring of Weld Pool during GTAW using Infra-Red Thermography and analysis of Infra-Red thermal images," *Weld. World*, vol. 55, no. 7–8, pp. 83–89, Mar. 2013.

[66] H. Ki, S. So, and S. Kim, "Laser transformation hardening of carbon steel sheets using a heat sink," *J. Mater. Process. Technol.*, vol. 214, no. 11, pp. 2693–2705, 2014.

[67] F. Lusquiños, J. C. Conde, S. Bonss, A. Riveiro, F. Quintero, R. Comesaña, and J. Pou, "Theoretical and experimental analysis of high power diode laser (HPDL) hardening of AISI 1045 steel," *Appl. Surf. Sci.*, vol. 254, no. 4, pp. 948–954, 2007.

[68] R. K. Shiue and C. Chen, "Laser Transformation Hardening of Tempered 4340 Steel," *Metall. Trans. A*, 1992.

[69] H. Pantsar, "Relationship between processing parameters, alloy atom diffusion distance and surface hardness in laser hardening of tool steel," *J. Mater. Process. Technol.*, vol. 189, no. 1–3, pp. 435–440, 2007.

[70] S. Santhanakrishnan and R. Kovacevic, "Hardness prediction in multi-pass direct diode laser heat treatment by on-line surface temperature monitoring," *J. Mater. Process. Technol.*, vol. 212, no. 11, pp. 2261–2271, 2012.

[71] J. W. Elmer, S. M. Allen, and T. W. Eagar, "The influence of cooling rate on ferrite content of stainless steel alloys," in *Proceedings of the 2nd International Conference on Trends in Welding Research*, 1989, pp. 165–170.

[72] J. W. Elmer, S. M. Allen, and T. W. Eagar, "Microstructural Development during Solidification of Stainless Steel Alloys," *Metall. Trans. A*, vol. 20A, no. October, pp. 1989–2117, 1989.

[73] J. Mazumder, A. Schifferer, and J. Choi, "Direct materials deposition: designed macro and microstructure," *Mater. Res. Innov.*, vol. 3, no. 3, pp. 118–131, Oct. 1999.

[74] L. Wang, S. D. Felicelli, and J. E. Craig, "Thermal Modeling and Experimental Validation in the LENS TM Process," in *Proceedings 2007 Solid Freeform Fabrication Symposium*, 2007, pp. 100–111.

[75] S. Yamashita, A. Fujinaga, M. Yamamoto, K. Shinozaki, and K. Kadoi, "In-situ Temperature Measurement using Monochrome High-speed Sensors during Laser Welding," pp. 0–3, 2012.

[76] J. Yu, X. Lin, J. Wang, J. Chen, and W. Huang, "Mechanics and energy analysis on molten pool

spreading during laser solid forming," *Appl. Surf. Sci.*, vol. 256, no. 14, pp. 4612–4620, May 2010.

[77]   T. Mioković, V. Schulze, O. Vöhringer, and D. Löhe, "Influence of cyclic temperature changes on the microstructure of AISI 4140 after laser surface hardening," *Acta Mater.*, vol. 55, no. 2, pp. 589–599, 2007.

[78]   T. Mioković, V. Schulze, O. Vöhringer, and D. Löhe, "Prediction of phase transformations during laser surface hardening of AISI 4140 including the effects of inhomogeneous austenite formation," *Mater. Sci. Eng. A*, vol. 435–436, pp. 547–555, 2006.

[79]   L. Song and J. Mazumder, "Feedback Control of Melt Pool Temperature During Laser Cladding Process," *IEEE Trans. Control Syst. Technol.*, vol. 19, no. 6, pp. 1349–1356, Nov. 2011.

[80]   D. Salehi and M. Brandt, "Melt pool temperature control using LabVIEW in Nd:YAG laser blown powder cladding process," *Int. J. Adv. Manuf. Technol.*, vol. 29, no. 3–4, pp. 273–278, Dec. 2005.

[81]   M. H. Farshidianfar, "Control of Microstructure in Laser Additive Manufacturing," University of Waterloo, 2014.

[82]   M. H. Farshidianfar, A. Khajepour, and A. Gerlich, "Real-time control of microstructure in laser additive manufacturing," *Int. J. Adv. Manuf. Technol.*, vol. 82, no. 5, pp. 1173–1186, 2015.

[83]   M. H. Farshidianfar, A. Khajepour, and A. P. Gerlich, "Effect of real-time cooling rate on microstructure in Laser Additive Manufacturing," *J. Mater. Process. Technol.*, vol. 231, pp. 468–478, 2016.

[84]   M. H. Farshidianfar, A. Khajepouhor, and A. Gerlich, "Real-time monitoring and prediction of martensite formation and hardening depth during laser heat treatment," *Surf. Coatings Technol.*, vol. 315, pp. 326–334, Apr. 2017.

[85]   A. Emamian, M. H. Farshidianfar, and A. Khajepour, "Thermal monitoring of microstructure and carbide morphology in direct metal deposition of Fe-Ti-C metal matrix composites," *J. Alloys Compd.*, vol. 710, pp. 20–28, 2017.

[86]   F. Meriaudeau and F. Truchetet, "Control and optimization of the laser cladding process using matrix cameras and image processing," *J. Laser Appl.*, vol. 8, no. 6, p. 317, 1996.

[87]   J. Mazumder, D. Dutta, N. Kikuchi, and A. Ghosh, "Closed loop direct metal deposition: art to

part," *Opt. Lasers Eng.*, vol. 34, no. 4–6, pp. 397–414, Oct. 2000.

[88]   E. Toyserkani and A. Khajepour, "A mechatronics approach to laser powder deposition process," *Mechatronics*, vol. 16, no. 10, pp. 631–641, Dec. 2006.

[89]   A. Fathi, A. Khajepour, E. Toyserkani, and M. Durali, "Clad height control in laser solid freeform fabrication using a feedforward PID controller," *Int. J. Adv. Manuf. Technol.*, vol. 35, no. 3–4, pp. 280–292, Oct. 2006.

[90]   Y. Hua and J. Choi, "Adaptive direct metal/material deposition process using a fuzzy logic-based controller," *J. Laser Appl.*, vol. 17, no. 4, p. 200, 2005.

[91]   M. Zeinali and A. Khajepour, "Development of an adaptive fuzzy logic-based inverse dynamic model for laser cladding process," *Eng. Appl. Artif. Intell.*, vol. 23, no. 8, pp. 1408–1419, 2010.

[92]   M. Zeinali and A. Khajepour, "Height Control in Laser Cladding Using Adaptive Sliding Mode Technique: Theory and Experiment," *J. Manuf. Sci. Eng.*, vol. 132, no. 4, p. 41016, 2010.

[93]   D. Hu and R. Kovacevic, "Sensing , modeling and control for laser-based additive manufacturing," *Int. J. Mach. Tools Manuf.*, vol. 43, pp. 51–60, 2003.

[94]   J. Grum and T. Kek, "The influence of different conditions of laser-beam interaction in laser surface hardening of steels," *Thin Solid Films*, vol. 453–454, pp. 94–99, 2004.

[95]   Z. Xu, K. H. Leong, and C. B. Reed, "Nondestructive evaluation and real-time monitoring of laser surface hardening," *J. Mater. Process. Technol.*, vol. 206, no. 1–3, pp. 120–125, 2008.

[96]   D. Hömberg and W. Weiss, "PID Control of Laser Surface Hardening of Steel," vol. 14, no. 5, pp. 896–904, 2006.

[97]   "DM3D." [Online]. Available: http://www.pomgroup.com/.

[98]   M. Iravani-tabrizipour, "Image-Based Feature Tracking Algorithms for Real-Time Clad Height Detection in Laser Cladding," 2007.

[99]   H. Sadiq, M. B. Wong, X.-L. Zhao, and R. Al-Mahaidi, "Effect of high temperature oxidation on the emissivity of steel," in *1st World Congress on Advances in Structural Engineering and Mechanics*, 2011, pp. 3839–3849.

[100] R. Felice, "Pyrometry for Liquid Metals," *Adv. Mater. Process.*, vol. July, pp. 31–33, 2008.

[101] M. N. Ozisik, *Heat Conduction*, Second. John Wiley & Sons, Inc., 1993.

[102] F. P. Incropera, D. P. DeWitt, T. L. Bergman, and A. S. Lavine, *Fundamentals of Heat and Mass Transfer*, vol. 6th. John Wiley & Sons, 2007.

[103] D. S. Naidu, *Optimal Control Systems*. CRC Press, 2003.

[104] "NI Labview PID." [Online]. Available: http://www.ni.com/white-paper/3782/en/.